Contributions to instrumental developments for the XEMIS2 camera, on-board ionization and scintillation measurements

Dingbang Cai

COLLEGE DOCTORAL PAYS DE LA LOIRE
ED MATIERE, MOLECULES MATERIAUX ET GEOSCIENCES

IMT Atlantique
Bretagne-Pays de la Loire
École Mines-Télécom

THèSE DE DOCTORAT DE

L'ÉCOLE NATIONALE SUPÉRIEURE
MINES-TÉLÉCOM ATLANTIQUE BRETAGNE PAYS DE LA LOIRE –
IMT ATLANTIQUE

ECOLE DOCTORALE N° 596
Matière, Molécules, Matériaux et Géosciences
Spécialité : *Physique subatomique (nucléaire et des particules)*

Par

Dingbang CAI

Contributions to the instrumental developments of the XEMIS2 camera, on-board ionization and scintillation measurements

Thèse présentée et soutenue à IMT Atlantique, Nantes, le 7 juillet 2024
Unité de recherche : SUBATECH - UMR 6457
Thèse N° : 2024IMTA0408

Rapporteurs avant soutenance :

Damien NEYRET — Directeur de Recherche CEA
Marie-Laure GALLIN-MARTEL — Directrice de Recherche CNRS

Composition du Jury :

Président :	Ginès MARTINEZ	Directeur de recherche CNRS
Examinateurs :	Damien NEYRET	Directeur de Recherche CEA
	Etienne TESTA	Maître de conférences-HDR
	Mariangela SETTIMO	Chargée de recherche-HDR CNRS
	Marie-Laure GALLIN-MARTEL	Directrice de Recherche CNRS
Dir. de thèse :	Dominique THERS	Professeur SUBATECH, IMT–Atlantique

Invité(s)
Nicolas BEAUPÈRE — Maître de conférences, IMT–Atlantique

Acknowledgments

The research presented in this dissertation was conducted within the Xenon group at the Subatech laboratory, under the expert guidance of Dr. Jean-Pierre Cussonneau and the inspiring supervision of Prof. Dominique Thers. As I arrive at the culmination of my Ph.D. journey, I find myself reflecting with deep gratitude on the many individuals who have contributed to this project and helped transform it from a vision into a reality.

First and foremost, I want to extend my deepest gratitude to my supervisors, Dominique Thers and Jean-Pierre Cussonneau, as well as my colleague Nicolas Beaupère. Their unwavering guidance, consistent encouragement, and steadfast support have been the foundation of my research journey. Their unique ability to blend rigorous scientific advice with genuine enthusiasm and trust has been incredibly inspiring. I am especially grateful for their extraordinary patience in addressing my countless questions—often repeated in various forms—always with calm and insightful responses. The example they have set as exceptional researchers in experimental physics will continue to inspire and guide me as I advance in my career.

I am also deeply appreciative of the defense committee members, whose expertise and generosity have greatly enriched my work. I owe special thanks to the thesis reviewers, Dr. Marie-Laure Gallin-Martel and Dr. Damien Neyret, for their careful and thorough review of my thesis. Their insightful comments and suggestions have sparked new ideas and inspired me in ways I hadn't anticipated. I am especially grateful to Dr. Etienne Testa and Dr. Laurent Aphecetche for their ongoing support as the member of my thesis monitoring committee, always offering invaluable advice. My sincere thanks also go to Dr. Mariangela Settimo and Dr. Ginès Martinez for taking the time to evaluate my work and for the kindness and expertise they brought to the process.

During my time at the Subatech laboratory, the members of the XENON team contributed immensely to both my personal and professional growth. I would like to particularly thank Eric Morteau for his guidance on using experimental devices and his technical support with electronics. His willingness to answer my countless questions and to reveal the intricacies of electronics was invaluable. I am sincerely grateful to Sara Diglio for her immense help and constructive advice, always being responsive when needed. Special thanks to Jean-Sébastien

Stutzmann for his technical support on mechanical aspects and their good humor, even during the challenging times of my Ph.D. journey. I am also thankful to Jean-Luc Béney, for his technical support with electronics. Additionally, I extend my special gratitude to Yuwei Zhu, Yajing Xing, Maxime Pierre, Loizeau Johan, Bazyk Marina for their support throughout these years as office mates. My gratitude also extends to Julien Masbou, Semenov Evgenii and Principe Lorenzo for their kindness and for sharing memorable moments in the laboratory. I am also grateful to the administrative team, the information team, and the leadership team for their support over the years.

I am forever indebted to my dear family and my friends for their understanding, continuous support, endless encouragement, and unconditional love throughout my life. Special thanks to my close friend, yihua HE, who has consistently encouraged me, lightened my load in difficult times, and supported me throughout these years.

Table of Contents

Introduction

In the exploration of nuclear medical imaging, the journey from conceptual foundations to the current technology has a vast array of advancements and innovations. Each contribution is significant to the field's evolution. This thesis meticulously tells the story of nuclear medical imaging through a structured discourse, beginning with the development of foundational imaging techniques and progressing towards groundbreaking innovations. Additionally, this thesis focus on the current development of XEMIS2 camera and its favorable performance.

Chapter 1: Development of Medical Imaging takes readers into the world of nuclear medical imaging. It begins with a historical overview, showing how early diagnostic methods evolved into the advanced imaging techniques we use today. The thesis explains the important milestones and innovations in the field, helping readers understand how these developments have improved medical diagnosis and treatment over time. This chapter delineates the journey of Single Photon Emission Computed Tomography (SPECT) and Positron Emission Tomography (PET), highlighting the crucial role of radiopharmaceuticals and the technological advancements in scintillation cameras that have driven the field forward. The chapiter then shifts to modern image reconstruction techniques for SPECT and PET. It provides a detailed overview of the principles that form the foundation of these crucial parts of nuclear imaging.

Chapter 2: Xemis2: A Liquid Xenon Compton Camera for Small Animals delves into the specifics of the XEMIS2 camera, an exemplar of innovation in the application of liquid xenon (LXe) as a detection medium. The chapter starts by elucidating the physical properties of liquid xenon and its advantages as a detection medium, including interactions with photons and charged particles, and the generation of ionization and scintillation signals. It then explores the design and operational principles of liquid xenon time projection chambers (LXeTPCs), providing insights into the historical development and the breakthroughs that led to the conceptualization and realization of the XEMIS2 camera.

Chapter 3: Frisch Grid Simulation introduces the concept of the Frisch grid and its application in enhancing the performance of liquid xenon ionization chambers. This chapter

provides a foundational description of the Frisch grid, including the theoretical underpinnings such as the Shockley-Ramo theorem, and delves into the simulation studies aimed at optimizing the grid design for XEMIS2. The chapter will then provide a detailed introduction to the simulation tools we used and the results obtained from my work.

Chapter 4: Scintillation Signal Detection in XEMIS2 focuses on the intricate process of scintillation signal detection within the XEMIS2 system, a critical aspect of achieving high-resolution images. This chapter covers the comprehensive development and optimization efforts of the scintillation signal detection chain, from the motivation behind developing a high-efficiency readout system to the detailed analysis of calibration methods. It elucidates the principles of photomultiplier tubes (PMTs), their key characteristics, and their role in advancing the capabilities of the XEMIS2 system.

Chapter 5: Calibration Results Optimization addresses the challenges and strategies in optimizing calibration results, a crucial step in enhancing the accuracy and reliability of imaging data. This chapter delves into the propagation and characterization of scintillation light in liquid xenon, detailing the efforts to correct and improve Time Over Threshold (TOT) calibration, and the sophisticated simulation studies conducted to refine time measurement techniques.

Through these chapters, the thesis not only chronicles the technological advancements and innovations in nuclear medical imaging but also provides a detailed exposition of the principles, methodologies, and challenges inherent in the development of cutting-edge imaging systems – XEMIS2 camera. It aims to offer both a historical perspective and a forward-looking analysis of the potential impacts of these technologies on medical diagnostics and research.

1 Development of medical imaging

The motivation behind medical imaging is to enhance patient care by providing accurate disease diagnosis, facilitating treatment planning and monitoring, enabling early disease detection, supporting minimally invasive procedures, driving medical research, and improving patient communication. Medical imaging techniques offer detailed visualization of internal structures, aiding in the identification and characterization of diseases, guiding interventions, and evaluating treatment outcomes. By harnessing the power of medical imaging, healthcare professionals can make informed decisions, improve patient outcomes, and contribute to the overall well-being of individuals[1–4]. Some medical imaging milestones or technologies will be listed:

- **Discovery of X-rays**

The history of medical imaging dates back to the discovery of X-rays by Wilhelm Conrad Roentgen in 1895. Roentgen accidentally discovered X-rays while experimenting with cathode rays. He noticed that a fluorescent screen in his lab started to glow even when it was not in the direct path of the cathode rays. He realized that a new type of ray was being emitted, which he called X-rays. Roentgen's discovery revolutionized medical diagnostics. Physicians could now visualize the internal structures of the human body without invasive procedures. X-rays became widely used for diagnosing bone fractures, lung diseases, and other conditions. The first X-ray machine was developed in the same year as Roentgen's discovery[4,5].

- **Angiography**

In the early 20th century, other imaging techniques began to emerge. In 1927, the use of iodine as a contrast agent for X-rays was introduced, allowing better visualization of blood vessels[6]. This technique, known as angiography, laid the foundation for modern vascular imaging, especially in the field of coronary angiography[7] and diabetic retinopathy diagnostic[8].

- **Ultrasound**

The 1930s saw the advent of another important imaging modality: ultrasound. The use of ultrasound waves to generate images of soft tissues inside the body was pioneered by Karl Theodore Dussik in 1937[9–13]. However, it took several decades for ultrasound technology to become widely accessible and practical for medical imaging.

- **CT and MRI**

In the 1950s, computed tomography (CT) scanning was developed. CT scans use X-rays and advanced computer processing to create detailed cross-sectional images of the body. This imaging technique provided a significant advancement in diagnosing various diseases and conditions[3,14,15]. Magnetic resonance imaging (MRI) emerged in the 1970s and 1980s. MRI utilizes powerful magnets and radio waves to generate detailed images of the body's internal structures. It provides excellent soft tissue contrast and has become a versatile imaging tool for a wide range of medical conditions[16–18].

- **Nuclear medicine imaging**[19–22]

Nuclear medicine imaging also developed during the mid-20th century. It involves the use of radioactive tracers, which are injected into the patient's body. The tracers emit gamma rays that can be detected by special cameras to create images of organ function and metabolism. In recent years, there have been significant advancements in medical imaging technology, such as the development of 3D imaging techniques, functional imaging modalities like Single Photon Emission Computed Tomography (SPECT), Positron Emission Tomography (PET), and 3γ medical imaging technologies.

Overall, the history of medical imaging has been marked by continuous innovation and the development of various techniques that have greatly improved the ability to diagnose and treat medical conditions. **In this chapter, we will mainly delve into advanced nuclear medicine imaging techniques, including Single Photon Emission Computed Tomography (SPECT), Positron Emission Tomography (PET), and 3γ medical imaging technologies.**

1.1 Single photon emission computed tomography

Single Photon Emission Computed Tomography (SPECT) is a nuclear imaging technique used in medical diagnostics to obtain three-dimensional images of the internal organs and tissues of the body. It is based on the detection of gamma rays emitted by a radioactive tracer, typically a radiopharmaceutical, that is administered to the patient.

The main concepts of SPECT[23–25]:

1. **Radiopharmaceutical administration :** A small amount of a radioactive tracer is injected into the patient's bloodstream, swallowed, or inhaled, depending on the specific diagnostic procedure. The tracer is designed to accumulate in the organ or tissue being examined.

2. **Gamma ray emission and detection :** Once inside the body, the radioactive tracer emits gamma rays. Gamma rays are high-energy photons that can be detected by specialized cameras called gamma cameras. The emitted gamma rays are generally single photons, which means they are released individually. The gamma camera consists of a scintillation crystal, a collimator, and a photo-detector. When a gamma ray interacts with the scintillation crystal, it produces flashes of light. The collimator, with its array of lead or tungsten holes, allows only a specific direction of gamma rays to reach the crystal, ensuring that the emitted photons are detected accurately. The photo-detector converts the light flashes into electrical signals.

3. **Image reconstruction :** The electrical signals generated by the photo-detector are processed and analyzed by a computer. The computer performs complex mathematical calculations to reconstruct the distribution of the radiopharmaceutical in the body. By analyzing the patterns and intensity of gamma ray emissions, the computer generates a three-dimensional image of the target organ or tissue.

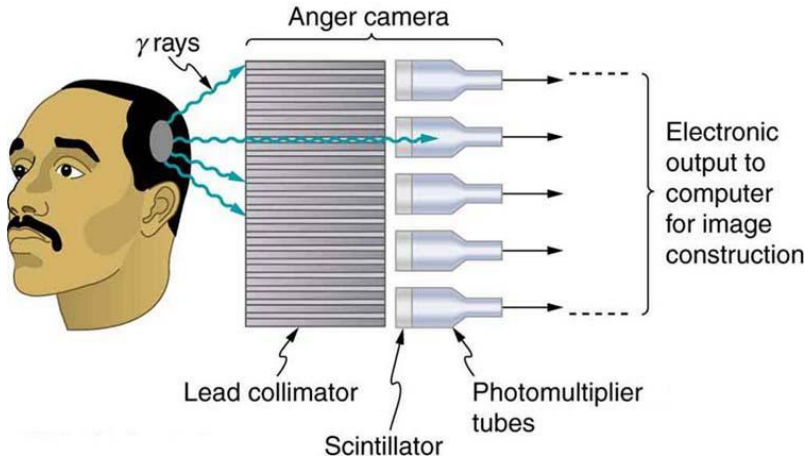

Fig. 1.1: Principle of SPECT image.

SPECT is particularly useful for studying the functional aspects of organs and tissues. It is commonly used in various medical fields, including cardiology, neurology, oncology, and psychiatry. SPECT scans can help diagnose conditions such as coronary artery disease[7,26], brain disorders (e.g., Alzheimer's disease[27], epilepsy[28]), and certain types of cancer[29–31]. As previously discussed, SPECT encompasses three essential steps: radiopharmaceutical administration, gamma ray emission and detection, and image reconstruction. The following sub-section will delve into significant aspects related to these steps. Section 1.1.1 will provide a comprehensive exploration of the historical background and evolutionary trajectory of radiopharmaceuticals. In Section 1.1.2, the development of scintillation cameras in the field will be presented. Furthermore, Section 1.1.3 will offer an in-depth analysis of state-of-the-art techniques employed for image reconstruction in SPECT.

1.1.1 Historical evolution of radiopharmaceuticals for SPECT

The field of radiopharmaceuticals for Single Photon Emission Computed Tomography (SPECT) imaging has evolved significantly over the years. SPECT is a nuclear medicine imaging technique that uses radiopharmaceuticals to produce three-dimensional images of the distribution of radioactive tracers in the body. These tracers emit gamma rays that are detected by a gamma camera, allowing for the visualization of biological processes and the diagnosis of various medical conditions. Here is a brief historical evolution of radiopharmaceuticals for SPECT:

- **Early radiopharmaceuticals (1960s-1970s):**

In the 1960s and 1970s, the field of nuclear medicine was in its early stages, and the development of radiopharmaceuticals for imaging techniques like SPECT was underway. During this time, iodine-131 (^{131}I) and technetium-99m-labeled (Tc-99m) sulfur colloid were commonly used radiopharmaceuticals for specific imaging purposes.

- I-131 is a radioactive isotope of iodine, which was primarily used for thyroid imaging, particularly in cases of thyroid dysfunction and thyroid cancer. It is taken up by the thyroid gland, allowing visualization and evaluation of its structure and function[32–34].
- Tc-99m is a widely used radioisotope in nuclear medicine due to its favorable imaging characteristics. It emits gamma rays of suitable energy for imaging and has a relatively short half-life, allowing for convenient use in medical settings. Sulfur colloid, when labeled with Tc-99m, was used for liver and spleen imaging. It is injected intravenously, and the radiotracer is taken up by the reticuloendothelial (mononuclear phagocyte) cells in the liver and spleen, providing information about their anatomy and function[35–38].
- Ga-67 (gallium-67) is another radiopharmaceutical used in SPECT imaging. Ga-67 is primarily used for oncological imaging, particularly in the evaluation of various types of tumors and inflammatory conditions. It has a high affinity for certain tumor cells and inflammatory sites, allowing for the visualization and characterization of these areas[39,40].

These early radiopharmaceuticals laid the foundation for the development and advancement of nuclear medicine imaging techniques. Over time, the field has witnessed significant progress with the introduction of a wide range of radiopharmaceuticals for various diagnostic purposes.

- **Technetium-99m radiopharmaceuticals (1970s-present):**

In 1970s, Tc-99m has become the workhorse of SPECT imaging, revolutionizing nuclear medicine due to its advantageous nuclear properties and the development of reliable generator systems for its production. Tc-99m radiopharmaceuticals have found wide application in various SPECT imaging studies.

- Tc-99m Sestamibi[41,42] and Tc-99m Tetrofosmin[43–45] are commonly used

radiopharmaceuticals for myocardial perfusion imaging, a technique used to assess blood flow to the heart muscle. These radiotracers are taken up by healthy heart muscle cells, allowing the visualization of areas with reduced blood flow, which may indicate ischemic heart disease or coronary artery blockages.

- Tc-99m MDP[46,47] (Methylene diphosphonate) is extensively used for bone imaging, specifically in the detection of bone metastases, evaluation of bone infections, and assessment of various bone disorders. Tc-99m MDP is preferentially taken up by areas of increased bone turnover, providing information about bone metabolism and any pathological changes.
- Tc-99m HMPAO[48,49] (Hexamethyl propylene amine oxime) and Tc-99m ECD[50,51] (Ethyl cysteinate dimer) are radiopharmaceuticals employed in brain imaging studies. They are used for cerebral blood flow studies and the evaluation of brain perfusion. These radiotracers are taken up by brain tissue in proportion to regional blood flow, enabling the detection of abnormalities such as ischemic strokes, brain tumors, and neurodegenerative disorders.

These examples highlight the versatility and widespread use of Tc-99m radiopharmaceuticals in various SPECT imaging applications. The availability of Tc-99m through generator systems, along with its desirable nuclear properties, has significantly contributed to the advancement of diagnostic imaging in nuclear medicine.

➢ **Hybrid imaging agents (1990s-present):**

With the advancement of imaging technologies, the integration of SPECT with other modalities such as CT or MRI has become possible, leading to the development of hybrid imaging agents. These agents combine the strengths of different modalities to enhance diagnostic accuracy and provide comprehensive imaging information. A few examples of SPECT/CT hybrid imaging agents will be presented:

- Tc-99m Sestamibi or Tetrofosmin with CT Contrast Agent[52,53] : Tc-99m sestamibi or tetrofosmin can combine with a CT contrast agent (such as iodine-based contrast), which can be used in SPECT/CT hybrid systems to assess myocardial perfusion while simultaneously providing anatomical information about the coronary arteries and parathyroid glands.

- Tc-99m MDP with CT Contrast Agent[54] : Tc-99m MDP is a radiopharmaceutical used for bone imaging in SPECT. When combined with a CT contrast agent, it allows for the fusion of functional bone scans with high-resolution CT images. This combination helps in the accurate localization of bone lesions and evaluation of bone pathology.
- Indium-111 (In-111) Octreotide or Pentetreotide (DTPA-conjugated form of octreotide) with CT Contrast Agent[55,56] : In-111 octreotide is used in SPECT imaging for the detection of neuroendocrine tumors, particularly those expressing somatostatin receptors. When combined with a CT contrast agent, it facilitates the fusion of functional SPECT images with detailed anatomical CT images, aiding in the localization and characterization of neuroendocrine tumors.
- Iodine-123 (I-123) Ioflupane with CT[57,58] : I-123 Ioflupane (also known as DaTscan) is used in SPECT imaging to evaluate the integrity of dopamine transporters in the brain. When combined with a CT scan, it allows for the precise localization of functional abnormalities seen in SPECT and provides anatomical context in the assessment of neurodegenerative disorders such as Parkinson's disease.

The integration of SPECT with other imaging modalities through hybrid imaging agents has significantly advanced the field of nuclear medicine and improved diagnostic capabilities. These hybrid systems provide clinicians with a more complete and accurate assessment of diseases, leading to better treatment decisions and patient care.

- **Theranostic radiopharmaceuticals (2010s-present):**

Theranostics is an emerging field in nuclear medicine that combines diagnostic and therapeutic capabilities using the same radiopharmaceutical agent. By employing specific radionuclides, it allows for personalized and targeted treatment based on individual patient characteristics. In SPECT-based theranostics, diagnostic radionuclides, such as Tc-99m, are used for imaging, while therapeutic radionuclides, such as lutetium-177 (Lu-177), are used for targeted radiation therapy[59,60].

Another case in point, Tc-99m/Re-188 labeled radiopharmaceuticals[61] are examples of theranostic agents used for targeted radiotherapy of various tumors, where Rhenium-188, a therapeutic radionuclide, is used to deliver targeted radiation to the tumor cells more

precisely. The concept of theranostics enables physicians to assess the specific characteristics of a tumor using the diagnostic radionuclide and then tailor the treatment approach by selecting the appropriate therapeutic radionuclide for effective radiation therapy. This approach offers the potential for personalized medicine, as it allows for treatment optimization based on individual patient response and tumor characteristics.

It's worth noting that theranostic radiopharmaceuticals are continually being developed and researched, and new agents are emerging for various applications, including targeted therapy for neuroendocrine tumors, prostate cancer, and other malignancies. Theranostics holds great promise in improving treatment outcomes and reducing side effects by delivering targeted therapy based on individual patient needs.

Table 1.1 List of common radionuclides in SPECT diagnostic

Isotope	Associated agent	Organ/Disease diagnostic
I-131 (Half-life = 8 d)	Sulfur colloid	Thyroid
I-123 (Half-life = 13.2 h)	Ioflupane	Brain
In-111 (Half-life = 2.81 days)	Octreotide or Pentetreotide	Neuroendocrine tumors
Ga-67 (Half-life = 3.26 days)	Citrate	Lymphoma
Tc-99m (Half-life = 6.01 h)	Sulfur colloid	Liver, spleen
	Sestamibi	Heart, parathyroid glands, breast
	Tetrofosmin	Heart, parathyroid glands
	Methylene diphosphonate	Bone
	Hexamethyl propylene amine oxime	Brain
	Ethyl cysteinate dimer	Brain

The field of radiopharmaceuticals for SPECT imaging continues to evolve with ongoing research and technological advancements, aiming to improve diagnostic accuracy and treatment outcomes for various medical conditions.

1.1.2 Historical evolution of scintillation cameras for SPECT

The evolution of scintillation cameras for SPECT imaging has spanned several decades, witnessing significant advancements in technology and design. Here is a brief overview of the historical evolution of scintillation cameras for SPECT[22]:

- **Anger Scintillation Camera (1950s)[62–64] :**

The Anger camera, invented by Hal Anger in the 1950s, was the first scintillation camera used for SPECT imaging. It consisted of a large scintillation crystal coupled to an array of photomultiplier tubes (PMTs). The camera allowed for the detection of gamma rays emitted from radiopharmaceuticals and provided planar images.

The basic design of the Anger camera involved a large scintillation crystal, typically made of sodium iodide (NaI) or cesium iodide (CsI), which acted as a gamma ray detector. When a gamma ray interacted with the crystal, it produced flashes of light known as scintillations. These scintillations were then detected by an array of PMTs that were coupled to the crystal. The PMTs converted the light flashes into electrical signals, which were then amplified and processed to produce an image. By analyzing the pattern and intensity of the signals received by the PMTs, the camera was able to reconstruct the distribution of the radioactive tracer within the patient's body. However, Single-head cameras acquired images one at a time, leading to time-consuming processes and limiting patient throughput.

- **Multi-head Scintillation Cameras (1950s - 1960s)[24,65]:**

In the 1970s, a significant advancement in nuclear medicine imaging came with the introduction of multi-head scintillation cameras using the discrete detector approaches. These cameras allowed for the simultaneous acquisition of images from multiple detectors, thereby improving imaging efficiency and reducing acquisition time. This development played a crucial role in enhancing the practicality and clinical utility of SPECT imaging.

Multi-head cameras typically featured two or more detector heads, each consisting of a scintillation crystal coupled to an array of photomultiplier tubes (PMTs). These detector heads were positioned around the patient, allowing for simultaneous detection of gamma rays emitted from the radiopharmaceuticals. The outputs from the detector heads were then

combined to produce a composite image. The use of multiple detector heads offered several advantages. Firstly, it significantly reduced the acquisition time since multiple images could be acquired simultaneously. This was particularly beneficial for imaging dynamic processes or when scanning a large number of patients. Secondly, it improved image quality by providing more data points for image reconstruction, resulting in enhanced spatial resolution and better visualization of structures and functions within the body.

Multi-head scintillation cameras played a crucial role in advancing SPECT imaging and contributed to its widespread adoption in clinical practice. However, multi-head cameras typically have a fixed arrangement of detector heads positioned around the patient. This fixed geometry results in a limited number of angular views for image acquisition and limit their flexibility in terms of imaging different anatomical regions or accommodating patients of varying sizes. What's more, multi-head cameras require multiple detector heads, each with its own set of PMTs and associated electronics. This complexity can make the system more challenging to operate and more expensive.

- **Rotating Gamma Camera (1960s - 1980s)**[66–68]**:**

The rotating gamma camera, introduced in the 1970s, represented a significant advancement in SPECT imaging. It offered improved capabilities for three-dimensional image reconstruction by acquiring multiple projections from various angles. The rotating gamma camera typically consisted of one or two detector heads mounted on a gantry that could rotate around the patient. Each detector head comprised a scintillation crystal coupled to an array of PMTs or solid-state detectors. As the camera rotated, it captured images from different angles, providing a more comprehensive sampling of the gamma rays emitted from the radiopharmaceuticals.

The ability to acquire multiple projections allowed for the reconstruction of three-dimensional images using advanced image reconstruction algorithms. By combining the information from different angles, the rotating gamma camera improved the spatial resolution, image quality, and accuracy of SPECT imaging. The rotating gantry also offered flexibility in patient positioning, allowing for imaging of various anatomical regions. It provided the ability to adjust the distance between the detector and patient, optimizing image acquisition for patients of different sizes. The introduction of the rotating gamma camera greatly expanded the clinical applications of SPECT imaging. It enabled more accurate and detailed

visualization of the distribution of radioactive tracers within the body, enhancing the diagnosis and management of various diseases and conditions. The ability to reconstruct three-dimensional images improved the sensitivity and specificity of SPECT imaging, making it a valuable tool in nuclear medicine. Since its introduction, rotating gamma cameras have undergone further advancements, including the integration of hybrid imaging technologies such as SPECT/CT (computed tomography) or SPECT/MRI (magnetic resonance imaging). These hybrid systems combine functional and anatomical information, further enhancing diagnostic capabilities in nuclear medicine.

- **Hybrid SPECT/CT Systems (1990s-present)**[69–71] **:**

The integration of SPECT with CT imaging has led to the development of hybrid SPECT/CT systems. These systems have been in use since the 1990s and continue to be utilized in present-day nuclear medicine. Hybrid SPECT/CT systems combine the functional information obtained from SPECT with the anatomical localization provided by CT imaging. The integration of these modalities offers several advantages in terms of improved accuracy, precise anatomical correlation, and enhanced lesion localization.

By acquiring both SPECT and CT images in a single examination, the hybrid system enables the fusion of functional and anatomical data. This fusion allows for a more comprehensive assessment of the patient's condition. The SPECT component provides information about the functional aspects of the body, such as the distribution of radioactive tracers, while the CT component offers detailed anatomical images, showcasing the structures and tissues. The fusion of functional and anatomical information leads to improved accuracy in lesion localization and a better understanding of the relationship between functional abnormalities and anatomical structures. It enables clinicians to precisely pinpoint areas of interest and facilitates more accurate diagnoses, treatment planning, and monitoring of various diseases and conditions. Moreover, the integration of SPECT and CT also offers several practical benefits. Patients undergoing a hybrid SPECT/CT examination experience reduced examination time and inconvenience compared to separate SPECT and CT scans. The combined system streamlines the imaging process and provides a comprehensive data-set for analysis.

Hybrid SPECT/CT systems have found widespread applications in various fields of medicine, including oncology, cardiology, neurology, and orthopedics, among others. They have become valuable tools for precise disease staging, therapy response assessment, surgical

planning, and localization of functional abnormalities within the anatomical context.

As technology advances, hybrid SPECT/CT systems continue to evolve with improved image quality, faster acquisition times, and enhanced software algorithms for image reconstruction and fusion. These advancements contribute to even greater accuracy and clinical utility, making hybrid SPECT/CT an essential component of modern nuclear medicine imaging.

- **Hybrid SPECT/MRI Systems**[72–75] **(2000s-present) :**

SPECT/MRI systems employ a combination of SPECT detectors and an MRI scanner within a single device. The SPECT component utilizes radioactive tracers to provide functional information about the targeted organ or tissue, while the MRI component captures high-resolution anatomical images based on magnetic field and radio-frequency signals.

The SPECT/MRI system and SPECT/CT systems share similarities in their ability to integrate functional and anatomical data, resulting in improved diagnostic accuracy. These systems enable simultaneous image acquisition and provide precise anatomical correlation. Both SPECT/CT and SPECT/MRI offer valuable anatomical context for functional abnormalities. CT scans deliver high-resolution images of bony structures and calcifications, while MRI provides excellent soft tissue contrast and detailed anatomical information. This correlation between functional and anatomical data facilitates accurate localization of functional abnormalities within their specific anatomical context. SPECT/CT and SPECT/MRI have found applications in various clinical fields, including oncology, neurology, cardiology, and orthopedics. They assist in disease diagnosis, treatment planning, response assessment, and monitoring. Both modalities offer valuable insights and aid in delivering personalized patient care. It's worth mentioning that despite these similarities, the choice between SPECT/CT and SPECT/MRI depends on factors such as the specific clinical scenario, available resources, and the clinical information required. The selection should be made based on individual patient needs and the desired imaging outcomes.

- **Advanced Detector Technologies**[76–79] **(2000s-present):**

In recent years, there have been significant advancements in detector technologies for scintillation cameras used in SPECT imaging. These advancements have introduced new

possibilities and improved the performance of SPECT systems. One notable development is the use of solid-state detectors, particularly cadmium zinc telluride (CZT) detectors. CZT detectors have gained popularity in the field of nuclear medicine due to their unique properties and advantages over traditional scintillation crystals. Some key advancements and benefits of CZT detectors include:

- Improved energy resolution: CZT detectors offer superior energy resolution compared to traditional scintillation crystals, such as sodium iodide (NaI) or cesium iodide (CsI). This improved energy resolution allows for better discrimination between different energy levels, resulting in enhanced image quality and more accurate quantification of radiotracer uptake.
- Faster acquisition times: CZT detectors exhibit faster scintillation decay times compared to scintillation crystals, leading to reduced dead time and faster data acquisition. This allows for shorter acquisition times during SPECT imaging, improving patient throughput and reducing motion artifacts.
- Enhanced spatial resolution: CZT detectors provide improved spatial resolution compared to scintillation crystals. The smaller pixel sizes and better intrinsic spatial resolution of CZT detectors allow for the visualization of fine anatomical details and smaller structures, enhancing the diagnostic capabilities of SPECT imaging.
- Compact and versatile design: CZT detectors have a compact and modular design, allowing for flexible detector configurations and easier integration into existing SPECT systems. Their smaller size and reduced weight make them more practical and convenient for clinical use.

The use of CZT detectors in SPECT imaging has shown promising results in various clinical applications, including oncology, cardiology, and neurology. They have the potential to improve lesion detection and localization, enhance image quality, and provide more accurate quantitative measurements. In addition to CZT, other advanced detector technologies, such as silicon photomultiplier (SiPM) arrays and hybrid semiconductor detectors, are also being explored and developed for SPECT imaging. These technologies offer further improvements in energy resolution, sensitivity, and compactness, opening up new avenues for enhancing the performance of SPECT systems.

As detector technologies continue to advance, the field of SPECT imaging is expected to benefit from improved image quality, reduced operational time, increased sensitivity, and

enhanced diagnostic accuracy. These advancements have the potential to further optimize patient care and contribute to the ongoing evolution of nuclear medicine.

1.1.3 State-of-the-art techniques for image reconstruction in SPECT

Image reconstruction in SPECT involves processing the acquired projection data to generate a three-dimensional image of the patient's internal structures. Over the years, several state-of-the-art techniques have been developed to improve the quality and accuracy of SPECT image reconstruction. Here are some of the notable techniques:

- **Statistical Iterative Reconstruction**[80–83] **:**

Statistical iterative reconstruction methods, such as the Maximum Likelihood Expectation Maximization (MLEM) algorithm and its variants, are widely used in SPECT image reconstruction. These techniques model the statistical properties of the data, including Poisson noise, to iteratively estimate the image. They incorporate system modeling, geometric corrections, and statistical regularization to improve image quality and reduce noise.

Regularization plays a vital role in balancing noise reduction and preserving image details in SPECT reconstruction. Various regularization techniques, such as total variation regularization, wavelet-based regularization, and non-local means, have been employed to enhance image quality and reduce noise artifacts[84].

- **Model-based Iterative Reconstruction**[82]**:**

Model-based iterative reconstruction (MBIR) techniques have emerged as a promising approach in SPECT. These methods incorporate a detailed system model that includes accurate modeling of physical processes, system geometry, and noise statistics. By explicitly incorporating system-specific information, MBIR techniques can achieve superior image quality and reduced artifacts compared to traditional methods.

- **Resolution Recovery Techniques**[85] **:**

SPECT suffers from limited spatial resolution due to factors like collimator blurring and detector response. Resolution recovery techniques aim to mitigate this limitation by

incorporating a priori knowledge of the system's point spread function (PSF). Methods like the Ordered Subset Expectation Maximization (OSEM) algorithm and its variants use deconvolution techniques to recover the lost resolution and enhance image details.

- **Monte Carlo-based Techniques**[86,87]**:**

Monte Carlo simulation methods have gained popularity in SPECT image reconstruction. These techniques involve simulating the photon transport within the imaging system and patient using mathematical models. By simulating multiple photon paths, Monte Carlo methods can accurately model the complex interactions of photons with matter, leading to more accurate image reconstructions.

- **Deep Learning-based Techniques**[88]**:**

Deep learning has made significant strides in medical image reconstruction, including SPECT. Convolutional neural networks (CNNs) and generative adversarial networks (GANs) have been utilized to learn complex image features and generate high-quality reconstructions. These techniques often require large-scale training datasets and can effectively handle noise, limited-angle data, and missing projections.

These state-of-the-art techniques have advanced SPECT image reconstruction, improving the quality, resolution, and diagnostic accuracy of SPECT images. Ongoing research continues to explore novel algorithms and approaches to further enhance the capabilities of SPECT imaging.

1.2 Positron emission tomography

Positron Emission Tomography (PET) is a medical imaging technique that allows for the visualization and measurement of metabolic processes in the body. It involves the use of a radioactive tracer called a radiopharmaceutical, which emits positrons, the antiparticles of electrons. The transition from SPECT to PET imaging represents a significant leap in medical imaging capabilities. PET's improved spatial resolution, sensitivity, quantitative analysis and availability of specialized radiotracers have revolutionized the field. These advancements have enhanced our ability to diagnose diseases, monitor treatment responses, and explore complex biological processes, leading to better patient care and improved outcomes.

The main concepts of PET[20,21,88,89]**:**

1. **Radiopharmaceutical administration:** A radiopharmaceutical is introduced into the patient's body, typically by injection into a vein. The radiopharmaceutical is designed to be taken up by specific tissues or organs, depending on the medical purpose of the PET scan.
2. **Positron emission and annihilation:** Once inside the body, the radiopharmaceutical undergoes radioactive decay and emits positrons. Positrons are positively charged particles that quickly encounter electrons within the tissue. When a positron encounters an electron, both particles annihilate each other, resulting in the simultaneous release of two gamma photons. These photons are emitted in opposite directions and have a specific energy of 511 keV each.
3. **Gamma camera detection:** Specialized detectors called gamma cameras or positron detectors are used to detect the emitted gamma photons. These detectors consist of scintillation crystals that convert the gamma photons into flashes of light, which are then detected by photo-multiplier tubes or other light sensors.
4. **Data acquisition and image reconstruction:** The gamma detectors surrounding the patient's body capture the emitted photons from multiple directions. This data is recorded by the PET scanner, which measures the time of arrival and location of each detected photon. The recorded data is processed by a computer to reconstruct a three-dimensional image of the distribution and concentration of the radiopharmaceutical within the body. The computer employs sophisticated algorithms to analyze the data and generate detailed images of the metabolic activity in different organs and tissues.

PET scans are widely used in various medical disciplines, including oncology, cardiology,

neurology, and psychiatry. They provide valuable information about the function and metabolism of organs and tissues, allowing for the detection and characterization of diseases. For example, PET can help in diagnosing and staging cancers, evaluating brain disorders such as Alzheimer's disease or epilepsy, and assessing cardiac function and blood flow. The principle of PET image is shown in the figure 1.2.

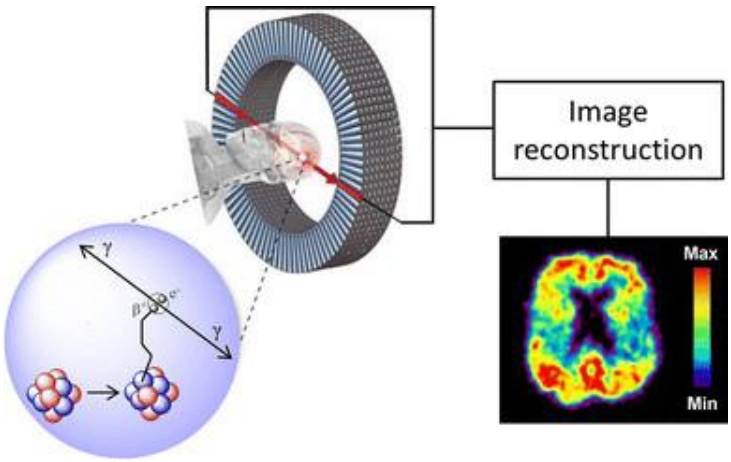

Fig. 1.2: Principle of PET image. [89] © 2024 Springer Nature

The following subsequent section of this thesis will encompass three distinct parts. Firstly, in Section 1.2.1, a thorough exploration of the historical background and evolutionary trajectory of radiopharmaceuticals employed in PET will be undertaken. This examination aims to provide a comprehensive understanding of the development and progression of these specialized pharmaceuticals. Moving forward, Section 1.2.2 will focus on the development of PET scintillation cameras, specifically tailored for the purpose of PET imaging. This section will shed light on the advancements made in the design and functionality of scintillation cameras to enhance PET imaging capabilities. Lastly, Section 1.2.3 will delve into an extensive analysis of state-of-the-art techniques utilized for PET image reconstruction. This comprehensive investigation will emphasize the latest advancements in the field, showcasing cutting-edge approaches and methodologies employed to reconstruct PET images with superior accuracy and clarity.

1.2.1 Evolutionary trajectory of PET radiopharmaceuticals

The evolution of PET radiopharmaceuticals has followed a trajectory of advancements in

tracer design, development, and clinical application. Over the years, there have been notable improvements in tracer properties, targeting strategies, and imaging applications. Let's explore the evolutionary trajectory of PET radiopharmaceuticals:

- **First-generation PET radiopharmaceuticals[39]:**

The initial PET radiopharmaceuticals primarily consisted of simple, small molecules labeled with short-lived positron-emitting isotopes like carbon-11 (^{11}C), nitrogen-13 (^{13}N) or oxygen-15 (^{15}O). These tracers were often used to study basic physiological processes such as blood flow, metabolism, and receptor binding. Examples include ^{11}C-methionine, ^{11}C-raclopride, and ^{11}C-flumazenil.

- **Second-generation PET radiopharmaceuticals[39,90]:**

As PET imaging gained popularity, researchers began focusing on developing more specialized and target-specific radiopharmaceuticals. This led to the emergence of second-generation PET tracers, which involved labeling bio-molecules like peptides, proteins, and antibodies with positron-emitting isotopes. These radiopharmaceuticals enabled the visualization and quantification of specific molecular targets, such as receptors, enzymes, and transporters. Examples include FDG (^{18}F-fluorodeoxyglucose) for glucose metabolism imaging[91,92] and ^{18}F-fluorothymidine for cell proliferation imaging[92,93].

- **Third-generation PET radiopharmaceuticals[39]:**

The evolution continued with the development of third-generation PET radiopharmaceuticals, which incorporated advancements in tracer design and imaging strategies. This generation saw the introduction of more complex radiotracers, such as radio-labeled nanoparticles, antibody fragments, and engineered bio-molecules. These tracers offered improved target specificity, enhanced pharmacokinetics, and increased stability. Examples include ^{68}Ga-PSMA-11 for prostate cancer imaging[94,95] and ^{18}F-fluciclovine for amino acid transport imaging[96,97].

- **Theranostic radiopharmaceuticals[37,39]:**

In recent years, there has been a growing emphasis on theranostic radiopharmaceuticals, which combine diagnostic and therapeutic capabilities. These radiopharmaceuticals are designed to enable both imaging and targeted radionuclide therapy using the same or similar molecular targets. This approach allows for personalized medicine, where patients can be

selected for specific treatments based on the imaging data obtained with the diagnostic radiotracer. Examples include [^{68}Ga/^{177}Lu]DOTA-TATE for neuroendocrine tumor imaging and therapy[98] and [^{68}Ga/^{177}Lu]PSMA-617 for prostate cancer imaging and therapy[59,99].

- **Novel imaging modalities[100,101]:**

Advancements in PET technology have also led to the development of novel imaging modalities. For instance, simultaneous PET/MRI scanners have become more prevalent, enabling the combination of PET molecular information with the anatomical and functional details provided by MRI. Additionally, new imaging techniques like dynamic PET and parametric imaging have emerged, allowing for quantitative analysis of physiological processes and better characterization of disease states.

Table 1.2 List of common radionuclides in PET diagnostic

Isotope	Associated agent	Organ/Disease diagnostic
C-11 (Half-life = 20.37 min)	Methionine	Brain tumors
	Raclopride	Parkinson's disease, schizophrenia, addiction.
	Flumazenil	Epilepsy, anxiety disorders, dementia
N-13 (Half-life = 9.97 min)	$^{13}NH_3$	Coronary artery disease
	$^{13}N_2$	Epilepsy and Alzheimer's disease
O-15 (Half-life = 2.04 min)	$^{15}O_2$	Heart
	$^{15}H_2O$	Brain
F-18 (Half-life = 109.7 min)	Fluorodeoxyglucose	Cancer (Glucose metabolism)
	Fluorothymidine	Tumors (Cell proliferation)
	Fluciclovine	Cancer (amino acid transport)
Ga-68 (Half-life = 68 min)	PSMA-11	Prostate cancer

The evolutionary trajectory of PET radiopharmaceuticals has witnessed a transition from simple small molecules to more complex and target-specific tracers. The development of

theranostic radiopharmaceuticals and the integration of PET with other imaging modalities have expanded the diagnostic and therapeutic capabilities of PET imaging, paving the way for personalized medicine and improved patient care. With ongoing research and technological advancements, the future holds even more promising prospects for the field of PET radiopharmaceuticals.

1.2.2 Historical advancements in PET scintillation cameras:

Historical advancements in PET (Positron Emission Tomography) scintillation cameras[102–106] have paved the way for the development and improvement of PET imaging technology. Here are some notable historical advancements in PET scintillation cameras:

- **Coincidence detection**[19,107–109] **:**

Starting in the 1960s, the development of coincidence detection techniques was a major advancement. Coincidence detection involves detecting two gamma-ray photons emitted simultaneously from a positron annihilation event. This technique improves spatial resolution and reduces background noise, leading to better image quality. The development of coincidence detection techniques in the 1970s is a significant milestone in PET. This approach involves the detection of two gamma-ray photons emitted simultaneously from a positron annihilation event, resulting in a range of benefits that have greatly improved PET imaging.

Coincidence detection has played a crucial role in enhancing spatial resolution in PET. By precisely measuring the arrival times of the two gamma-ray photons at different detectors, it becomes possible to determine the line of response (LOR) along which the annihilation event occurred. This information helps localize the positron emission within the patient's body more accurately, resulting in sharper and more detailed images. Improved spatial resolution allows for better visualization and characterization of small structures and abnormalities, leading to enhanced diagnostic capabilities.

Furthermore, coincidence detection contributes to the reduction of background noise in PET images. By requiring both gamma-ray photons to be detected within a specific time window, the detection system can effectively distinguish between true coincidence events (those originating from the annihilation event) and random or scattered events. This discrimination

helps eliminate unwanted noise, improving the signal-to-noise ratio and enhancing image quality. Reduced background noise leads to clearer and more accurate PET images, enabling more precise interpretation by clinicians.

- **Block detectors**[102,103,110] **:**

Starting in the 1984, Block detectors are key components in PET scanners. They are used to detect the gamma-ray photons emitted from the patient after the administration of a radiotracer. A block detector consists of an array of individual scintillation crystals arranged in a grid pattern. These crystals are typically made of materials such as lutetium oxyorthosilicate (LSO), lutetium-yttrium oxyorthosilicate (LYSO), or bismuth germanate (BGO). Each crystal is coupled to a photosensor, usually a photomultiplier tube (PMT) or silicon photomultiplier (SiPM), which converts the scintillation light into an electrical signal.

The purpose of using block detectors is to improve the spatial resolution and sensitivity of PET scanners. With a block detector design, each crystal in the array acts as an individual detector element. This allows for more precise localization of the gamma-ray interaction within the patient's body, resulting in improved image quality. Block detectors also help in reducing the so-called "parallax error" in PET imaging. Parallax error occurs when the true position of an annihilation event is incorrectly determined due to differences in the depth of interaction within the crystal. By using block detectors, the depth of interaction can be better estimated and corrected, leading to more accurate image reconstruction.

- **Time-of-Flight (TOF) PET**[111–115] **:**

Another significant milestone in PET is the emergence of Time-of-Flight (TOF) PET technology in the 2000s. Since then, TOF PET has gained widespread adoption due to its numerous advantages. This innovative technology measures the time difference between the detection of two annihilation photons, leading to remarkable improvements in image quality, noise reduction, and scan times.

By incorporating TOF information, the precise location of the annihilation event can be determined more accurately. This enhanced localization capability translates into sharper and more detailed images, enabling better visualization and characterization of biological structures and abnormalities. Moreover, the improved accuracy provided by TOF PET allows

for more precise quantification of radiotracer uptake, enhancing the reliability and usefulness of PET imaging in various clinical applications.

Additionally, TOF PET offers the advantage of reducing image noise. By incorporating time information, the scanner can differentiate between true coincidence events and random coincidences, which are more likely to occur by chance. This discrimination leads to a reduction in noise levels and improves the signal-to-noise ratio, resulting in clearer and more accurate PET images.

Furthermore, TOF PET technology enables faster scan times compared to conventional PET scanners. The ability to measure the time of flight of annihilation photons allows for more efficient data acquisition, reducing the duration of imaging sessions. This not only improves patient comfort but also increases the throughput of PET imaging facilities, enabling more efficient utilization of resources and potentially enhancing patient access to this valuable diagnostic modality.

Due to its significant advantages, TOF PET has become a standard feature in modern PET scanners. Its widespread adoption has revolutionized PET imaging by providing clinicians with improved image quality, reduced noise, faster scan times, and enhanced diagnostic capabilities. As a result, TOF PET technology continues to play a pivotal role in advancing molecular imaging and contributing to improved patient care.

- **Depth-of-Interaction (DOI) detectors**[116–118] **:**

Traditional PET detectors have typically been limited to measuring only the X and Y coordinates of detected photons. However, in recent decades, researchers have made significant advancements in the development of Depth-of-Interaction (DOI) detectors.

These innovative detectors aim to enhance spatial resolution across the field of view by providing depth information. DOI detectors employ various approaches to achieve this goal. One such approach involves using multiple scintillator layers with different light output properties. By analyzing the variation in light output, DOI detectors can ascertain the depth at which a photon interaction occurs, thus providing valuable depth information. Another technique utilized in DOI detectors is the use of position-sensitive photodetectors within crystal arrays. This configuration allows for precise localization of the interaction point along

both the X and Y coordinates, as well as the depth axis. By capturing three-dimensional information, DOI detectors can correct for parallax error and improve spatial resolution across the entire field of view.

- **Silicon photomultipliers (SiPMs) PET**[119–121] **:**

Since the early 2010s, solid-state photodetectors called Silicon Photomultipliers (SiPMs) have gained significant popularity in the design of PET cameras. SiPMs have emerged as a promising alternative to traditional PMTs and have introduced a range of advantages to PET imaging systems.

SiPMs are known for their compact size, making them well-suited for applications where space is limited. Their small form factor allows for more flexible camera designs and the development of smaller and more portable PET scanners. This portability opens up new possibilities for point-of-care imaging, mobile applications, and imaging in challenging environments.

Additionally, SiPMs offer high photon detection efficiency. They are capable of efficiently detecting individual photons, leading to improved sensitivity in PET imaging. This increased efficiency enhances the signal-to-noise ratio and allows for better image quality, enabling more accurate detection and quantification of radiotracer uptake in tissues.

Another advantage of SiPMs is their low operating voltage. Compared to PMTs, SiPMs operate at lower voltages, reducing power consumption and heat generation. This lower operating voltage simplifies the overall system design and improves energy efficiency, which is particularly beneficial for portable and battery-operated PET scanners.

Moreover, SiPMs exhibit excellent timing resolution, which refers to their ability to accurately measure the arrival time of photons. The precise timing information provided by SiPMs enables advanced imaging techniques such as TOF-PET, further enhancing image quality and enabling faster and more accurate image reconstruction.

The advantages offered by SiPMs have led to their adoption in PET camera design, and in some cases, they have replaced traditional PMTs. The compact size, high photon detection efficiency, low operating voltage, and excellent timing resolution of SiPMs have

revolutionized PET systems, enabling the development of smaller, more portable scanners without compromising imaging performance.

- **Total-Body PET**[122,123] **:**

In recent years, there have been advancements in PET technology that have led to the development of total-body PET scanners capable of capturing the entire body in a single acquisition. Traditional PET scanners had a limited axial field of view, which meant that multiple bed positions and image stitching were required to obtain a whole-body image. However, with the introduction of total-body PET scanners, this limitation has been overcome.

Total-body PET scanners utilize long axial field of view detector designs, which means that the detectors cover a larger portion of the patient's body along the axial direction. This allows for the imaging of the entire body without the need for bed repositioning. These scanners also incorporate continuous bed motion, where the patient is moved smoothly and continuously through the scanner during the acquisition. This eliminates the need for stopping and repositioning the patient, resulting in a more efficient scanning process.

Advanced image reconstruction algorithms are also employed in total-body PET scanners to process the acquired data and generate high-quality whole-body images. These algorithms account for the continuous bed motion and the long axial field of view, ensuring accurate image reconstruction and comprehensive visualization of the body.

Total-body PET scanners have significantly improved the efficiency and convenience of whole-body imaging in clinical practice. They have streamlined the scanning process, reduced patient discomfort, and provided comprehensive imaging in a single acquisition, offering a more complete assessment of the patient's condition.

- **Integrated PET/MRI**[100,124–126] **and PET/CT Systems**[127–131] **:**

Over the past two decades, there has been significant progress in the integration of PET with other imaging modalities such as MRI or CT. This development has resulted in the emergence of integrated PET/MRI systems in the early 2000s and PET/CT systems in the late 1990s.

The integration of PET with other imaging modalities aims to combine their respective strengths and provide complementary information. By combining PET with MRI or CT, integrated systems enable the simultaneous acquisition of anatomical and functional data, leading to enhanced diagnostic capabilities.

PET/MRI systems offer the advantage of capturing both metabolic activity (PET) and detailed anatomical structures (MRI) in a single imaging session. The high soft tissue contrast and excellent spatial resolution of MRI complement the functional information provided by PET, allowing for a more comprehensive understanding of the underlying pathology. This integration enables precise localization of PET findings within the anatomical context, aiding in accurate diagnosis, treatment planning, and monitoring of diseases.

On the other hand, PET/CT systems combine the functional information from PET with the anatomical information obtained from CT scans. CT provides detailed structural images of the body, including bones, organs, and other tissues, while PET reveals metabolic activity and functional abnormalities. By combining PET and CT in a single examination, clinicians can correlate metabolic changes with the precise anatomical location, enabling improved detection and characterization of diseases. PET/CT systems have become widely adopted in clinical practice and have significantly contributed to oncology, cardiology, and neurology, among other fields.

The integration of PET with other imaging modalities has revolutionized medical imaging, enabling a more comprehensive and multidimensional evaluation of diseases. Whether it is PET/MRI or PET/CT, these hybrid systems provide valuable insights by combining functional and anatomical information, leading to improved diagnostic accuracy and better patient care.

These historical advancements have significantly improved the performance, image quality, and diagnostic capabilities of PET scintillation cameras, leading to broader applications in clinical research and patient care.

These historical advancements in PET scintillation cameras have played a crucial role in enhancing the capabilities of PET imaging. They have contributed to improved image quality, better spatial resolution, increased sensitivity, and expanded clinical applications, making PET a valuable tool in various fields such as oncology, cardiology, neurology, and molecular

imaging.

1.2.3 Techniques for PET Image Reconstruction

PET (Positron Emission Tomography) image reconstruction is a critical step in generating accurate and high-quality PET images from acquired raw data. Several techniques have been developed to improve the image quality, quantitative accuracy, and clinical utility of PET imaging. Here are some commonly used techniques for PET image reconstruction:

- **Filtered back projection (FBP)**[132] **:**

FBP is a widely used technique for PET image reconstruction. It involves two main steps: back projection and filtering. In back projection, the measured projection data is back-projected onto the image space. The filtered back projection step then applies a filter to reduce noise and enhance image sharpness. FBP is computationally efficient but may result in lower image quality compared to iterative methods.

- **Iterative reconstruction**[133,134] **:**

Iterative methods aim to iteratively refine an initial estimate of the PET image based on a mathematical model that describes the acquisition process. These methods typically incorporate system modeling, statistical modeling, and regularization techniques to improve image quality. Common iterative algorithms include Ordered Subset Expectation Maximization (OSEM) and Maximum Likelihood Expectation Maximization (MLEM). Iterative reconstruction tends to produce better image quality and quantitative accuracy but requires more computational resources.

- **Statistical reconstruction**[135–137] **:**

Statistical reconstruction methods take into account the statistical nature of PET data to improve image quality. One such technique is the Penalized Likelihood (PL) reconstruction, which combines statistical modeling with regularization to promote image smoothness while preserving details. This approach helps reduce noise and improve lesion detectability.

- **Time-of-Flight (TOF) reconstruction**[114,138,139] **:**

TOF PET scanners provide time information of the detected annihilation events, allowing for more accurate localization of the emission source. TOF reconstruction algorithms leverage

this additional timing information to improve image quality, increase signal-to-noise ratio, and enhance lesion detectability. TOF data can be incorporated into both FBP and iterative reconstruction methods.

- **Resolution modeling**[133,140] **:**

PET scanners have limited spatial resolution due to factors like positron range, detector size, and system blurring. Resolution modeling techniques aim to compensate for these limitations and improve spatial resolution in the reconstructed images. Point Spread Function (PSF) modeling is a common approach where the system blurring is modeled and incorporated into the reconstruction algorithm, resulting in sharper images.

- **Attenuation correction**[139,141–143] **:**

Accurate attenuation correction is crucial for quantitative PET imaging. Techniques for attenuation correction include transmission-based methods, where a transmission scan is acquired using a separate radioactive source, and CT-based methods, where attenuation maps are derived from co-registered CT images. Attenuation correction is typically performed as a preprocessing step before image reconstruction. These techniques for PET image reconstruction have evolved over the years, and researchers continue to develop novel approaches to further improve image quality, quantitative accuracy, and clinical applications of PET imaging. The choice of reconstruction technique depends on various factors such as imaging goals, available computational resources, and specific scanner characteristics.

1.3 3γ imaging: a Novel Modality for Advanced Nuclear Medical Imaging

3γ imaging is an innovative approach to low-dose nuclear medical imaging that has gained attention in recent years. Unlike traditional nuclear imaging techniques, 3γ imaging utilizes the detection of three gamma rays simultaneously[144–146]. This technique utilizes a (β+, γ) radionuclide emitter, such as ^{44}Sc, which emits a positron and a third γ ray in quasi-coincidence in terms of time and position. By incorporating the information from all three coincident gamma rays, 3γ imaging offers several advantages :

- Improved Image Quality: The additional information from the coincidence photon allows

for better localization and reconstruction of the radiotracer distribution, leading to improved image quality.

- Reduced Radiation Dose: Since 3γ imaging relies on a (β+, γ) radionuclide emitter, it requires a lower administered activity compared to traditional imaging techniques. This results in reduced radiation exposure for patients.
- Enhanced Image Quantification: The incorporation of the coincidence photon improves the accuracy of quantitative measurements, allowing for better assessment of physiological processes.

3γ imaging is still an emerging technique and it will be investigated in preclinical and clinical research studies in the future. It offers promising potential for reducing radiation dose and improving image quality in nuclear medical imaging[145,147]. However, further research and development are needed to optimize the technique, establish standardized protocols, and determine its clinical applicability in different areas of medicine.

In the upcoming subsection of this thesis, specifically in Section 1.3.1, the principle of 3 gamma imaging will be elucidated. This technique leverages the annihilation of a positron to generate two photons, which are then used to construct a Line of Response, similar to PET imaging discussed in the preceding section. Furthermore, the subsequent section, Section 1.3.2, will delve into the presentation of the Compton telescope, the instrument responsible for detecting the third photon. Lastly, Section 1.3.3 will focus on the introduction of the pharmaceuticals utilized in 3γ imaging.

1.3.1 Principle of 3γ imaging technique

Figure 1.3 illustrates the imaging principle of the 3-gamma modality, showcasing how the three gamma rays are utilized for imaging purposes. The process begins with the annihilation of a positron, resulting in the emission of a pair of back-to-back photons. These annihilation photons are used to construct a Line of Response (LOR), which is a standard technique employed in conventional PET imaging.

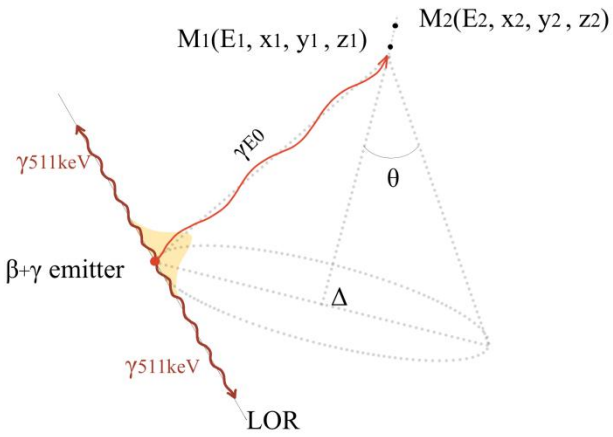

Fig. 1.3: Principle of 3γ imaging technique.

In addition to the annihilation photons, there is a third quasi-coincident single photon that is detected through electronic collimation, typically utilizing a Compton telescope. The Compton telescope allows for the detection of this third photon, which is not directly related to the annihilation process but occurs in quasi-coincidence with it.

The 3-gamma event is then reconstructed by determining the intersections of the LOR (defined by the annihilation photons) with the surface of the Compton cone. Typically, there are two intersection points, but in most cases, only one of them is well located within the region of interest within the field of view (FOV).

Due to the inherent uncertainties in the measurements, the localization of an emitter can be obtained from a single radiation decay event. However, the deviation in this case is a result of the energy and angular resolution of the Compton telescope, rather than the precision of the TOF information. Therefore, the 3-gamma imaging modality can be considered a pseudo-TOF-PET approach[148].

This approach utilizing the 3-gamma modality provides the potential to localize radioactive decays with high precision, similar to TOF-PET, but with the key difference being the reliance on the energy and angular resolution of the Compton telescope. This modality offers promising capabilities for precise localization and imaging, with potential applications in nuclear medicine and other fields that require accurate gamma-ray localization[149].

1.3.2 The Compton Camera: A Key Instrument for 3γ Imaging

The Compton Camera represents a significant advancement in the field of gamma ray imaging, marking a departure from conventional imaging technologies towards a more precise and versatile approach. At the heart of its operation lies the principle of Compton scattering, a phenomenon first described by Arthur H. Compton, which involves the scattering of gamma rays by electrons. This fundamental principle has been harnessed to create a camera capable of three-dimensional imaging, offering unparalleled insights into the distribution of radioactive tracers or sources within a target object. The camera's unique ability to detect and localize gamma rays emitted from various processes, including positron annihilation events, has made it an indispensable tool in a wide range of applications. From nuclear medicine, where it enhances the precision of diagnostics and treatment monitoring, to environmental monitoring and homeland security, the Compton Camera's impact is broad and significant. Its development reflects a blend of historical scientific discoveries and modern technological advancements, culminating in a device that significantly enhances our capability to visualize and understand complex gamma ray emissions.

1.3.2.1 History of Compton Camera

The development of the Compton camera can be traced back to the pioneering work of Arthur H. Compton, an American physicist who won the Nobel Prize in Physics in 1927 for his discovery of the Compton scattering effect. Compton's experiments in the 1920s involved investigating the scattering of X-rays by electrons. He observed that when X-rays interacted with electrons, they underwent a change in wavelength and scattered in different directions. This phenomenon, known as the Compton effect, provided evidence for the particle-like nature of electromagnetic radiation.

The concept of using the Compton effect for imaging purposes was proposed in the 1970s[150]. Significant advancements in detector technology, specifically the development of high-resolution position-sensitive detectors, paved the way for the practical realization of Compton cameras in the late 20th century. The use of semiconductor detectors, such as cadmium telluride[151] (CdTe) and cadmium zinc telluride[79,152] (CZT), provided improved energy resolution and position sensitivity required for Compton imaging. In the early 1990s, several research groups started developing prototype Compton cameras. One notable example is the work done by researchers at the University of California, Berkeley, led by Robert E. Wagner.

They built a Compton camera using position-sensitive CZT detectors and demonstrated its feasibility for imaging gamma rays in medical and scientific applications. Over the years, the development of Compton cameras continued, with advancements in detector technology, image reconstruction algorithms, and system integration. Researchers focused on improving energy resolution, spatial resolution, and overall system efficiency. Various research institutions and companies worldwide contributed to the progress of Compton camera technology.

Today, Compton cameras have become a valuable instrument in the field of nuclear medicine and medical imaging. They are used for a range of applications, including gamma ray imaging in nuclear medicine, particle therapy monitoring, environmental monitoring, and homeland security. The ongoing research and development efforts aim to further enhance the performance of Compton cameras, making them more compact, cost-effective, and suitable for various imaging scenarios. With continued advancements, the future of Compton cameras holds promise for even more precise and detailed imaging of gamma ray sources.

1.3.2.2 Principle of compton camera

The Compton camera operates based on the principle of Compton scattering, which is the scattering of gamma rays by electrons. The camera takes advantage of this scattering effect to detect and localize gamma rays emitted from a source. The principle of the Compton camera can be summarized in the following steps[144,145,148,153,154]:

- **Gamma Ray Interaction:** When a gamma ray interacts with an electron in a material, it can undergo Compton scattering. The gamma ray transfers a portion of its energy and changes direction due to the collision with the electron.
- **Scatter Detection:** The Compton camera consists of a scatter detector, typically made of a high-Z material like cadmium zinc telluride (CZT). The scatter detector is responsible for detecting the scattered gamma ray. When the gamma ray interacts with the scatter detector, it scatters off an electron, changing its direction.
- **Energy and Position Measurement:** The scatter detector measures the energy and position of the scattered gamma ray. By analyzing the energy and position information, the camera can determine the scattering angle of the gamma ray.
- **Absorber Detection:** After scattering in the scatter detector, the gamma ray continues its

path and enters the absorber detector, typically made of a thicker material like thallium-doped sodium iodide (NaI(Tl)). The absorber detector measures the final position and energy of the gamma ray.

- **Coincidence Detection:** By correlating the information from the scatter and absorber detectors, the Compton camera can identify coincident events where the same gamma ray scattered in the scatter detector and deposited energy in the absorber detector.
- **Image Reconstruction:** Image reconstruction techniques are used to analyze the coincident events and reconstruct the origin of the gamma rays within the imaged object. The reconstruction process aims to determine the position and intensity distribution of gamma ray sources within the imaged volume.

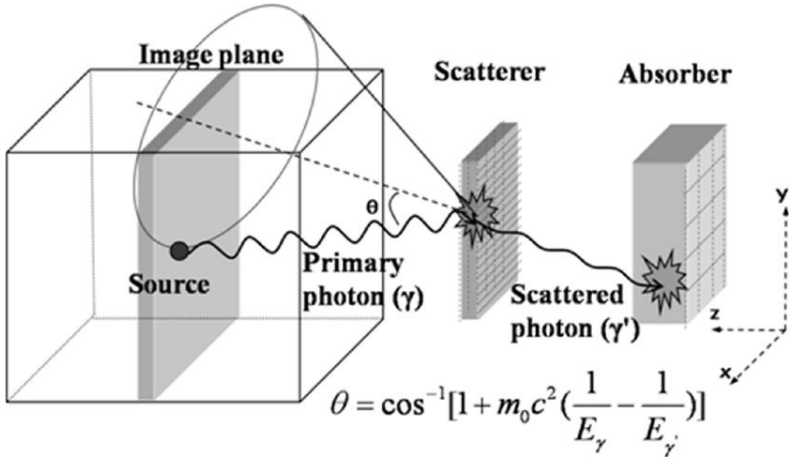

Fig. 1.4: Principle of a Compton camera. [154] © [2008] IEEE

By detecting and localizing the gamma rays based on their scattering behavior, the Compton camera can generate three-dimensional images that provide information about the distribution and concentration of radioactive tracers or sources within the imaged object. The advantage of the Compton camera is its ability to detect multiple coincident gamma rays emitted from positron annihilation events, enabling applications in positron emission tomography (PET) imaging. Furthermore, the camera offers improved spatial resolution compared to traditional gamma cameras, enhancing the accuracy of image reconstruction.

1.3.3 Pharmaceuticals in 3 gamma imaging: A comprehensive overview

Selecting a specific (β+, γ) radionuclide is crucial for enhancing the capabilities of 3γ imaging. The chosen radionuclide must have the ability to detect the positron and the third γ

ray in temporal coincidence. This means that it should emit a positron with precise energy. Additionally, to favor Compton scattering and improve detection capabilities, the daughter nuclide should rapidly de-excite to the ground state while emitting a γ ray. This ensures that the positron and third γ ray emissions can occur in temporal and spatial quasi-coincidence.

Several criteria related to nuclear medicine should also be satisfied by this specific radionuclide. Ideally, the branching ratios of the positron and the third γ ray should be as close to 100% as possible, as this improves the efficiency of signal detection. Furthermore, to reduce detector noise and the dose administered to the patient, the de-excitation of the daughter nuclide should preferably be accompanied by the emission of a single γ ray radionuclide. Lastly, the radionuclide should have a suitable half-life for clinical applications and be easily producible.

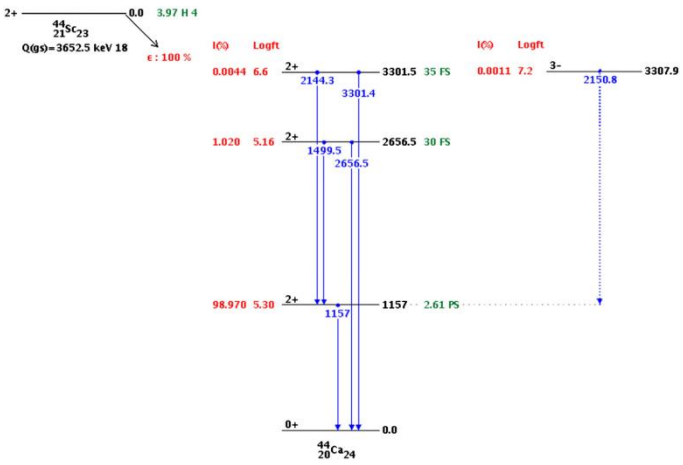

Fig. 1.5: Decay scheme of ^{44}Sc . © NuDat

Numerous radionuclides have the potential to be suitable candidates for 3γ imaging feasibility. Among them, 34mCl, 44gSc, 48V, 52mMn, 55Co, 60Cu, 66Ga, 69Ge, 72As, 76Br, 82gRb, 86gY, 94mTc, 110mIn, 124I, 22Na, 10C, and 14O have been identified[155]. Among the listed radionuclides, 44gSc (scandium-44g) has been identified as the best candidate for enhancing the capabilities of 3γ imaging. It possesses the necessary characteristics to detect the positron and the third γ ray in temporal coincidence and favor Compton scattering in liquid xenon detectors. Here are the reasons why 44gSc is considered a suitable radionuclide for 3γ imaging[148,149]:

- **Precise Positron Energy:** Scandium-44g emits a positron with a precise energy, allowing for accurate detection and localization of the positron annihilation event.
- **Efficient De-excitation:** The daughter nuclide of 44gSc rapidly de-excites to the ground state while emitting a γ ray of around 1 MeV. This ensures that the positron and third γ ray emissions occur in time and spatial quasi-coincidence, enhancing the imaging capabilities.
- **High Branching Ratios:** The branching ratios of the positron and the third γ ray emissions of 44gSc are close to 100%. This high branching ratio improves the efficiency of signal detection.
- **Single γ ray Emission:** The de-excitation of the daughter nuclide of 44gSc is accompanied by the emission of a single γ ray radionuclide. This reduces detector noise and the dose injected to the patient, improving the image quality.
- **Feasible Half-Life:** Scandium-44g has a half-life suitable for clinical applications. It decays with a half-life of about 3.97 hours, allowing for sufficient imaging time.
- **Production Availability:** Scandium-44g is relatively easily produced, which is advantageous for its widespread use in clinical settings.

Due to these favorable physical and chemical properties, 44gSc is being investigated for the development of innovative radiopharmaceuticals labeled with DOTAT peptides. Studies are being conducted at various research institutions and hospitals to explore its potential applications in 3γ imaging, including SUBATECH laboratory, ARRONAX GIP, CRCI2NA, and *Centre Hospitalier Universitaire (CHU) de Nantes*.

1.4 Conclusion

In conclusion, Section 1 has taken us on a captivating journey through the development of medical imaging, tracing the historical evolution and recent advancements in SPECT, PET, and the emerging 3γ imaging modality.

Over the course of more than a century, the diligent work of countless pioneers has paved the way for the successful integration of SPECT and PET into medical practice. These imaging modalities have revolutionized diagnostics, enabling healthcare professionals to gain crucial insights into various medical conditions and improve patient outcomes. The continuous dedication of researchers in this field reflects the unwavering commitment to enhancing

imaging quality and efficiency, making medical imaging an indispensable tool in modern healthcare.

In the midst of these established imaging techniques, the emergence of 3γ imaging stands as a promising development. With a relatively shorter period of 20 years in development, 3γ imaging holds the potential to usher in a new era of nuclear medical imaging. While it is still undergoing validation and realization, the principles and instrumentation behind 3γ imaging have sparked considerable excitement within the scientific community.

Looking ahead, the prospect of 3γ imaging replacing SPECT and PET as the mainstream modality for nuclear medical imaging is an intriguing possibility. The continuous refinement and validation of this novel technique could potentially lead to enhanced spatial resolution, sensitivity, and reduced radiation exposure, revolutionizing medical imaging practices.

As our understanding of these imaging modalities deepens, and as new technologies like Xemis2, the liquid xenon Compton camera, emerge, we are presented with boundless opportunities to push the boundaries of medical imaging. The fusion of historical knowledge and cutting-edge innovations holds the potential to reshape medical diagnostics, enabling more accurate and earlier detection of diseases, and ultimately, providing better care for patients worldwide.

2 Xemis2 : a liquid xenon Compton camera for small animals

Introducing XEMIS (Xenon Medical Imaging System), an innovative liquid xenon Compton camera project aiming to revolutionize medical imaging with its groundbreaking 3γ imaging technique using ultra-low activity. The project comprises three key stages, each contributing to its ultimate vision.

- ✓ The initial phase, XEMIS1, stands as a small-scale single-phase LXe Compton camera prototype that showcased the capabilities of LXeTPC (Liquid Xenon Time Projection Chamber) in 3γ imaging.

- ✓ Building upon this success, the XEMIS2 system emerged, featuring a larger cylindrical LXe Compton camera dedicated to imaging small animals. This step marks a significant milestone in preclinical applications within hospital centers. XEMIS2's primary objective revolves around 3D localization of radiopharmaceuticals labeled with specific radionuclides, like Sc^{44g}, and optimizing administered radiotracer activity while preserving image quality in oncology diagnosis. Excitingly, preliminary full GATE/Geant4[156,157]simulations demonstrated the feasibility of obtaining high-quality images of small animals using a mere 20 kBq of Sc^{44g} over a 20-minute exposure period[148,149,158]. Compared to conventional functional imaging systems, XEMIS2 exhibited a remarkable sensitivity of approximately 7%, equivalent to 70 cps/kBq. This performance highlights XEMIS2's potential impact in the medical imaging landscape. XEMIS2 is characterized as a monolithic single-phase detector, boasting a large axial FOV capable of handling nearly 200 kg of ultra-high-purity liquid xenon. Its development has been successfully carried out at the renowned SUBATECH laboratory.

- ✓ Looking ahead, XEMIS aims to materialize the ambitious XEMIS3—a large FOV LXe Compton camera designed for whole human body imaging and hadron-therapy monitoring applications. With XEMIS leading the way, the future of medical imaging holds promising advancements and potential benefits for humanity.

In Section 2, we will explore three key aspects. Firstly, we will delve into the rationale behind utilizing liquid xenon as the detection medium for XEMIS. Next, we will discuss the reasons that led to the selection of the time projection chamber technology. Lastly, we will provide a concise yet informative overview of the XEMIS2 camera.

2.1 Liquid xenon: a promising detection medium

Noble gas detectors offer numerous advantages, including non-reactivity, stability, high sensitivity, selectivity, and safety, making them invaluable across diverse applications. Their chemically inert nature ensures minimal interference with target materials or environments, while their stability enables reliable and consistent long-term operation. Noble gas detectors' ability to detect trace amounts of specific substances is crucial for environmental monitoring and leak detection. Additionally, their use in radiation detection applications, alongside their non-toxic and non-flammable properties, further highlights their importance in fields such as medical imaging, industrial safety, and scientific research[159–161].

Liquid xenon, a noble gas, stands out as a highly promising detection medium, finding extensive use in scientific and technological domains, especially in particle physics and astrophysics. Its distinctive properties make it exceptionally well-suited for sensitive and high-resolution detection applications. In Section 2.1.1, we will explore the physical properties of liquid xenon and highlight its exceptional qualities as a detection medium. Following that, in Section 2.1.2, we will present an overview of the historical applications of liquid xenon in the field of medical imaging.

2.1.1 Investigating the physical properties and advantages of liquid xenon

Liquid xenon proves to be an exceptional high-performance detection medium, owing to its remarkable physical properties. In this section, we shall delve into various physical attributes and benefits that make liquid xenon stand out as a detection medium[159,162].

- **High stopping power and small radiation length:**

Table 2.1 summarizes the essential properties of liquid noble gases as a compelling detection medium. Among all liquefied noble gases, LXe stands out as an ideal candidate for highly

sensitive detection in both γ ray calorimeters and position-sensitive detectors. While liquid radon (LRn) possesses a higher atomic number and density akin to LXe, offering greater stopping power for ionizing particles, but its significant intrinsic radioactivity renders it unsuitable for use as a radiation detection medium. Thus, apart from LRn, LXe boasts the highest density (2.953 g/cm³) and largest atomic number (54) among liquid rare gases, resulting in the most substantial radiative stopping power for ionizing particles across a broad energy range, spanning from several tens of keV to tens of MeV. Beyond its high atomic number and density, LXe also features a small radiation length (approximately 2.872 cm), making it highly attractive for electromagnetic calorimeters.

Table 2.1 Physical properties of liquid noble gases*

Noble Gas	Atomic Number Z	Average Atomic Weight A(g/mol)	Liquid Density (g/cm³) at 164K, 1 atm	Boiling Point Tb (K) at 1 atm	Melting Point Tm (K) at 1 atm	Radiation Length X0 (cm)
Helium (He)	2	4.0026	0.125	4.220	0.950	755.2
Neon (Ne)	10	20.180	1.207	27.07	24.56	24.03
Argon (Ar)	18	39.948	1.395	87.30	83.80	14.00
Krypton (Kr)	36	83.798	2.413	119.9	115.8	4.703
Xenon (Xe)	54	131.29	2.953	165.0	161.4	2.872
Radon (Rn)	86	222.02	4.400	211.40	202.0	1.533

* Data taken from: https://pdg.lbl.gov/2023/AtomicNuclearProperties/index.html

- **Rapid response and high light yield:**

From a scintillation perspective, LXe demonstrates rapid response times on the order of several tens of nanoseconds. This characteristic ensures excellent coincidence timing resolution and a high-count-rate capability, making it ideal for Time-of-Flight PET applications. Additionally, LXe boasts the highest scintillation light yield among liquefied rare gases, meaning it emits a significant amount of light per unit of deposited energy. This light can be detected and used to reconstruct the interactions. Table 2.2 summarizes the essential scintillation properties of liquid xenon.

Table 2.2 Scintillation properties of liquid xenon

Scintillation properties of LXe	Value & Unit
Scintillation light emission peak (at 160 K)[163,164]	178 ± 1 nm
Peak width (FWHM) (at 160 K)[163]	14 ± 2 nm
Fast decay time (singlet state τs) for electrons[165]	2.2 ± 0.3 ns
Slow decay time (triplet state τt) for electrons[165]	27 ± 1 ns
Recombination time constant (τr) for electrons[165]	45 ns
Scintillation yield for 1 MeV electrons[166]	46300 photons/MeV
Work function (W_{ph}) for 1 MeV electrons without electric field[166]	21.6 eV

- **Dual Signal Response:**

In addition to scintillation light, liquid xenon also produces ionization signals when particles interact with it. This dual signal response allows for a complementary method of event reconstruction and background rejection. Regarding ionization properties, LXe stands out with the highest ionization yield compared to all other liquid rare gases. Only a small amount of energy, approximately 15.6 eV, is needed to produce an electron-ion pair. The high electron mobility further enhances LXe's potential as an ionization detector medium, capable of generating a detectable ionization signal by producing sufficient free electrons per unit length. Details of LXe's ionization properties can be found in Table 2.3.

Table 2.3 Ionization properties of liquid xenon

Ionization properties of LXe	Value & Unit
Average ionization energy W-value[167]	15.6 ± 0.3 eV
Electron drift velocity (v_e) at 1 kV/cm[168]	2.25×10^5 cm/s
Electron drift velocity (v_e) at 10 kV/cm[168]	2.8×10^5 cm/s
Electron transverse diffusion coefficient (D_T) at 1 kV/cm[159]	80 cm^2/s
Electron transverse diffusion coefficient (D_T) at 10 kV/cm[159]	50 cm^2/s
Electron longitudinal diffusion coefficient (D_L)[159]	$0.1D_T$

- **Low intrinsic background radiation:**

Xenon (Xe) stands out as the superior choice over argon (Ar) and krypton (Kr) in various applications due to its remarkably low intrinsic background radiation. Unlike argon and krypton, xenon lacks long-lived natural radionuclides, rendering it an excellent candidate for sensitive experiments in fields like particle physics, dark matter searches, neutrino studies and medical imaging.

Argon contains the radioactive isotope ^{39}Ar, produced through cosmic ray interactions with potassium in the Earth's atmosphere, and krypton harbors the radioactive isotope ^{85}Kr, released into the environment via nuclear fuel reprocessing, both isotopes contribute to background radiation in detectors employing argon or krypton. Exploiting xenon as the detection medium allows researchers to capitalize on its low intrinsic background, reducing unwanted interference and facilitating the precise identification of the target particles. The utility of xenon extends to liquid xenon detectors, exemplified by the XENON and LUX experiments, boasting exceptional sensitivity to dark matter interactions as a result of xenon's low intrinsic background and innate self-shielding capabilities.

The absence of long-lived natural radionuclides in xenon not only makes it a preferred option for sensitive experiments but also positions it as an ideal choice in medical imaging and other applications where minimizing background radiation is paramount. Xenon's prowess in offering reliable and accurate data in various fields underscores its crucial role in the advancement of cutting-edge research in fundamental physics, astrophysics, and medical diagnostics.

2.1.2 Interactions of photons with liquid xenon

Interactions of photons with liquid xenon are of great importance in various scientific and technological applications. When photons interact with liquid xenon, several processes can occur, each contributing to the overall response of the medium. Here are some of the main interactions:

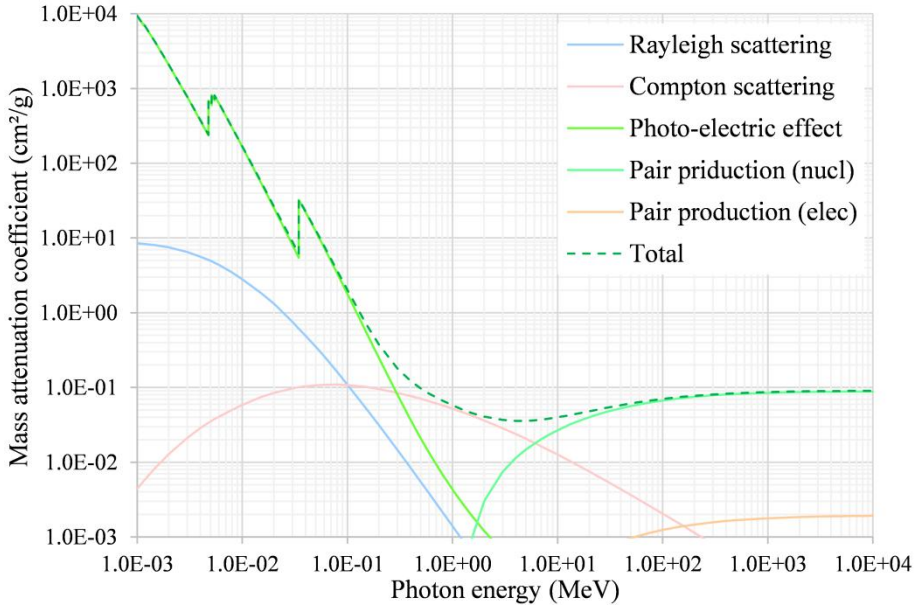

Fig. 2.1: The photon energy dependency of computed mass attenuation coefficients for diffusion, Rayleigh scattering, Compton scattering, photoelectric effect, and pair production in xenon was analyzed.

- **Photoelectric Effect:**

The photoelectric effect is a fascinating phenomenon that occurs when a photon interacts with an atom, causing an electron to be expelled from its bound state within the atom. If the photon's energy surpasses the binding energy of the electron (the energy required to keep it in its orbit), the excess energy becomes the kinetic energy of the ejected electron. This process is particularly notable in liquid xenon (LXe), as shown in Figure 2.1.

TABLE 2.4 Electron binding energies of xenon in electron volts*

K 1s	L12s	L22p1/2	L32p3/2	M13s	M23p1/2
34,561.00	5,453.00	5,107.00	4,786.00	1,148.70	1,002.10
M33p3/2	M43d3/2	M53d5/2	N14s	N24p1/2	N34p3/2
940.6	689	676.4	213.2	146.7	145.5

* Data taken from: https://xdb.lbl.gov/Section1/Periodic_Table/Xe_Web_data.htm *Al Thompson. ©2000.*

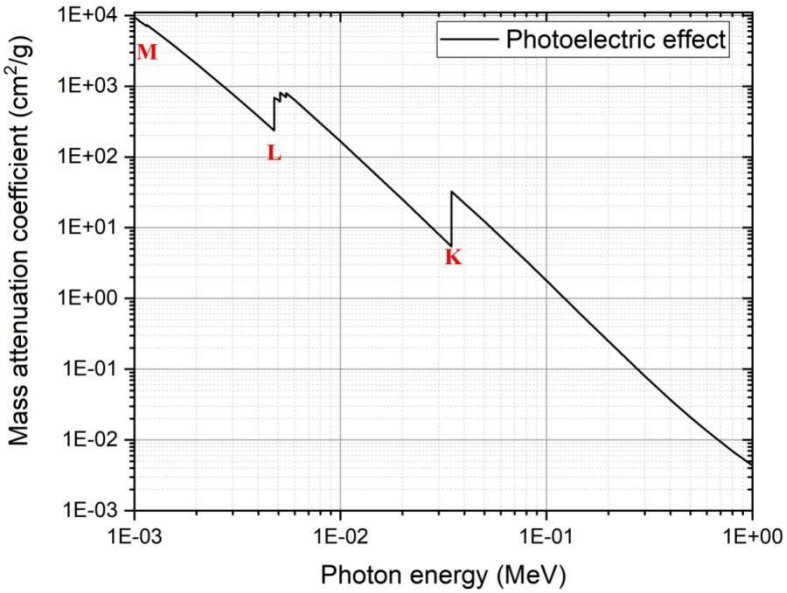

Fig. 2.2 The photon energy dependency of computed mass attenuation coefficients for photoelectric effect, and pair production in xenon was analyzed using data obtained from https://www.nist.gov/pml/xcom-photon-cross-sections-database. © 1990, 1998 copyright by the U.S. Secretary of Commerce on behalf of the United States of America.

In the realm of LXe, the photoelectric effect overwhelmingly dominates other interaction processes at low photon energies. In simpler terms, when low-energy photons interact with LXe, the most probable outcome is the photoelectric effect. This results in photons being absorbed, and electrons being ejected from the inner shells of xenon atoms. The drops observed around 1 keV, 5 keV and 30 keV in the Figure 2.2 correspond to the absorption edges of atomic shells (M,L and K). These edges represent specific photon energy levels where the probability of photoelectric interactions significantly increases due to resonant absorption. Table 2.4 illustrates the electron binding energies of xenon.

- **Rayleigh Scattering**[159,169]**:**

Rayleigh scattering, alternatively referred to as coherent scattering, is a fascinating occurrence where photons engage with atoms or molecules and scatter in various directions while maintaining their original energy. This phenomenon is particularly influential for visible light in the atmosphere; however, its relevance diminishes as the wavelength becomes shorter, such as in the case of ultraviolet or X-rays.

- **Compton Scattering**[159,170]**:**

Compton Scattering, also known as incoherent scattering, involves the collision of high-energy photons with electrons, resulting in the transfer of some energy to the electrons. This transfer causes the electrons to recoil, and the photons are scattered in different directions with reduced energy. The significance of Compton scattering lies in its application in high-energy physics and gamma-ray astronomy. Scientists utilize this phenomenon to measure the energy and direction of incoming gamma rays, making it a valuable tool in these fields.

- **Pair Production**[171]**:**

At photon energies surpassing 1.02 MeV, a fascinating phenomenon called pair production occurs. In this process, photons interact with the intense electric field of a nucleus, resulting in the transformation of the photons into an electron-positron pair. This event holds significant importance in high-energy physics experiments and offers valuable insights into the absorption of high-energy gamma rays in dense materials. Furthermore, pair production can also be initiated when high-energy photons interact with the electric field of neighboring electrons, but in such instances, a higher energy level of photons is necessary to trigger this effect.

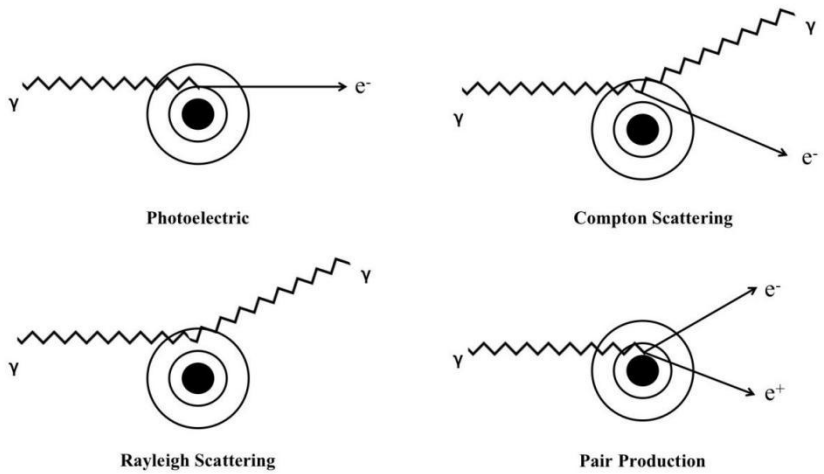

Fig. 2.3 Schematic description of main processes accounting for γ-ray interaction and absorption.

Conclusion:

In 3γ medical imaging, the photon energy typically ranges from keV to 1 MeV. As shown in Figure 2.1, we can infer that in this energy range, the dominant processes are the

photoelectric effect and Compton scattering. These interactions result in the production of electrons. Consequently, in the next subsection 2.1.3, we will discuss the interactions of charged particles with liquid xenon.

2.1.3 Interactions of charged particles with liquid xenon

Charged particles, including α-particles, protons, or electrons, primarily dissipate their energy through two processes: ionization and atomic excitation. When a charged particle traverses through liquid xenon (LXe), it undergoes interactions with the electrons and nuclei within the material, driven by the Coulomb force.

Charged particles have the ability to transfer only a small portion of their total energy during an individual electronic collision. Consequently, they engage in continuous interactions with numerous electrons in the surrounding medium, resulting in a gradual loss of energy until they come to a stop. In the case of heavy charged particles, their collisions with atomic electrons do not cause a significant deviation from their original trajectory. As a result, the trajectory of a heavy charged particle, representing the average distance it travels before coming to rest, can be approximated as a straight line. In contrast, electrons and positrons are less ionizing than heavy charged particles, allowing them to travel longer distances before slowing down. Due to their reduced ionizing nature, they can cover greater distances before their energy is substantially depleted. In following section, we will discuss some typical interactions between electrons and xenon[148,149].

- **Elastic Scattering[172,173]:**

Elastic scattering is a type of interaction between an incident electron and a xenon atom or nucleus in which the electron transfers energy to the target without experiencing any energy loss. During the collision, the direction of the electron is changed, but its kinetic energy remains unchanged. This process is termed "elastic" because the total kinetic energy of the system (incident electron and xenon target) is conserved before and after the collision. In other words, the incident electron rebounds from the target without losing energy. Elastic scattering is an important phenomenon in understanding the behavior of charged particles and their interactions with matter.

- **Inelastic Scattering**[174]**:**

Inelastic scattering is similar to elastic scattering in that an incident electron interacts with a xenon atom or nucleus, causing a change in direction. However, in the case of inelastic scattering, the incident electron transfers some of its energy to the xenon target during the collision, resulting in energy loss. The energy transferred to the xenon atom or nucleus can lead to different outcomes, such as atomic excitation or ionization. In atomic excitation, the xenon atom is temporarily raised to a higher energy state, with one of its electrons occupying a higher energy level. On the other hand, in ionization, the xenon atom may lose one or more of its electrons, forming positively charged ions. In some cases, inelastic scattering can also induce nuclear reactions, where the xenon nucleus undergoes a transformation, resulting in the emission of particles or radiation.

- **Bremsstrahlung**[175]**:**

When high-energy electrons are deflected by the Coulomb force of the nuclei within xenon atoms, they can undergo acceleration. This acceleration of charged particles leads to the emission of electromagnetic radiation in the form of photons. This phenomenon is called bremsstrahlung, a German term meaning "braking radiation". In the context of electron interactions with xenon, bremsstrahlung radiation occurs when the electrons experience significant deceleration due to the attraction of the positively charged xenon nuclei. As a result, they emit photons with energies corresponding to the amount of energy lost during the deceleration process.

- **Auger Effect**[176–178]**:**

The Auger effect is a type of electron-electron interaction that can occur in certain situations when an electron is ejected from the inner shell of an atom, leaving a vacancy in that shell. After the inner shell electron is ejected, there is now an energy level vacancy in the atom. To stabilize, an electron from an outer shell may transition into the inner shell, filling the vacancy. When this outer shell electron fills the vacancy in the inner shell, it releases energy in the form of an Auger electron. The Auger electron carries away the excess energy from the transition between the outer and inner shells. In the context of xenon, the Auger effect can occur when an electron is ejected from one of the inner electron shells (e.g., K or L shells), and an outer shell electron transitions into the vacant inner shell, releasing an Auger electron.

Conclusion:

At lower incident electron energies, such as 3γ medical imaging, the primary interactions are ionization and excitation. However, as the energy of incident electrons rises, processes like Bremsstrahlung gain significance. Higher-energy electrons are more prone to elastic and inelastic scattering as they traverse through the medium, resulting in a greater production of radiation, including Bremsstrahlung. These phenomena provide essential understanding of electron-medium interactions across various energy ranges.

2.1.4 Ionization and scintillation signals generation

Upon interaction with liquid xenon (LXe), incident photons give rise to one or more recoil electrons, typically caused by either the photoelectric effect or Compton scattering. Subsequently, these primary electrons lose their energy primarily through ionization and atomic excitation as explained in section 2.1.3 . Consequently, this energy deposited by the recoil electron leads to the generation of ionization and scintillation signals within LXe, as depicted in Figure 2.4. Both signals are produced simultaneously and can be utilized independently or in combination for detecting radiation particles[159,179].

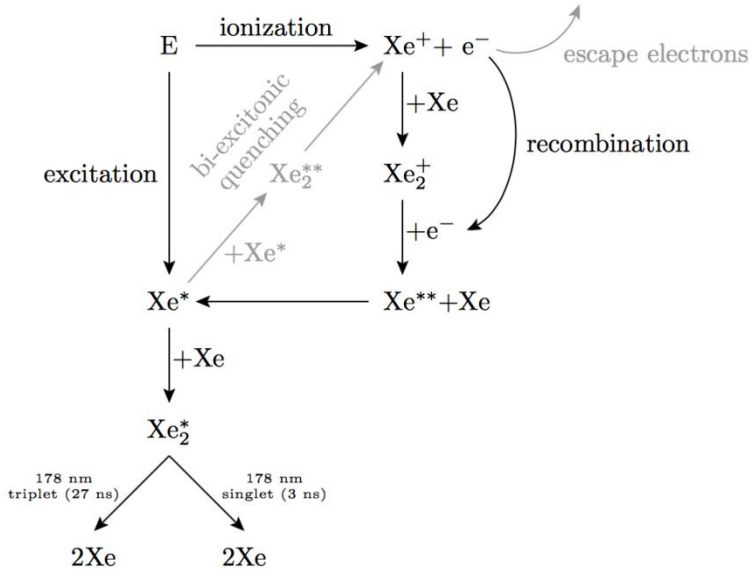

Fig. 2.4 Scintillation mechanism in LXe.

- **Ionization Signals:**

When a charged particle, such as an electron, enters the liquid xenon, it deposits energy by colliding with xenon atoms. These collisions can ionize the xenon atoms, liberating electrons from their orbits, and creating positively charged xenon ions. The liberated electrons are then free to move through the liquid xenon due to the applied electric field. The ionization process leads to the creation of ionization tracks along the path of the charged particle. These tracks consist of the ionized xenon atoms and free electrons. The pattern of these ionization tracks is an essential part of the information used to reconstruct the particle's trajectory.

- **Scintillation Signals:**

In addition to ionization, the interaction of a charged particle with the liquid xenon can also lead to scintillation. Scintillation is the process by which the xenon atoms are excited to higher energy levels during the particle interaction, and then they subsequently return to their ground state, emitting photons in the process.

Conclusion:

The emitted photons carry information about the amount of energy deposited by the charged particle. The number of photons emitted is proportional to the energy of the incoming particle. This scintillation light is detected by sensitive photodetectors, typically positioned at the top and/or bottom of the LXeTPC, and it helps in the determination of the energy of the particle.

2.2 Liquid xenon time projection chambers

The 3γ imaging technique requires a detector with high spatial and energy resolutions to accurately determine the interaction position and deposited energy. Additionally, the detector must have high sensitivity and detection efficiency to distinguish between single Compton scattering and multiple scattering events. To detect gamma-ray energies around 1 MeV, a suitable detection medium is required, preferably one capable of producing at least one Compton scattering with subsequent photoelectric interaction. The single-phase Time Projection Chamber (TPC) with LXe (liquid xenon) as the detection medium, known as LXeTPC, fits these criteria perfectly[180].

LXeTPC has widespread applications in dark matter direct detection, gamma-ray astrophysics, and neutrino-less double-beta decay experiments. It offers precise spatial information on interaction positions, accurate energy measurement for each interaction, and

effective particle identification. The dedicated medical imaging system XEMIS, developed at the SUBATECH laboratory, utilizes LXeTPC's scintillation light and charge carriers response to ionizing particle interactions, making it a promising choice for medical imaging using gamma rays.

2.2.1 Principles of LXeTPC

The LXeTPC (Liquid Xenon Time Projection Chamber) is a type of particle detector used in experimental physics and astrophysics research. Its basic principle involves the use of liquid xenon as a detection medium to observe interactions between particles and xenon atoms. Figure 2.5 shows the schematic description of LXeTPC[148,149].

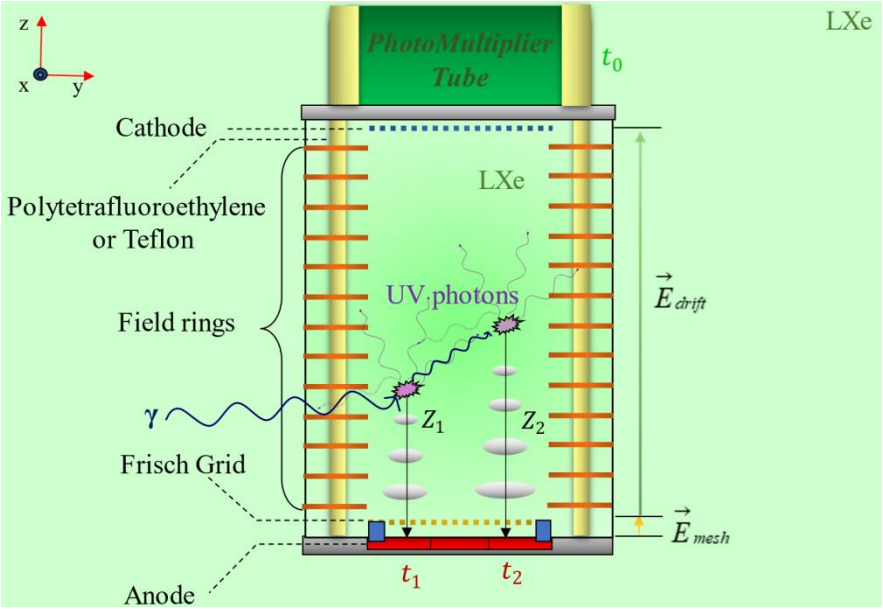

Fig. 2.5 Schematic description of LXeTPC principle.

- **Liquid Xenon Medium:**

The LXeTPC consists of a volume filled with liquid xenon at cryogenic temperatures (around -106°C). Xenon is a noble gas with excellent scintillation and ionization properties, making it suitable for detecting various types of particles, including neutrinos, dark matter candidates, and other rare events.

- **Drift of Charged Particles:**

When charged particles pass through the gas-filled volume of a TPC, they ionize the gas atoms or molecules along their path, creating free electrons and positively charged ions. An

electric field is applied within the TPC, causing the charged particles (electrons and ions) to drift towards the readout plane.

- **Readout Plane (Anode):**

The readout plane is located perpendicular to the drift direction and typically consists of a two-dimensional array of sensitive elements. These elements can be wire electrodes or pixel pads that detect the arriving charged particles.

- **Drift Time Measurement:**

By measuring the time it takes for the charged particles to drift to the readout plane, one can determine their position in the drift direction. The drift time is usually measured with high precision, allowing for precise reconstruction of particle tracks.

- **Frisch grid:**

For a traditional TPC, the readout plane often incorporates Multi-wire Proportional Chambers or Micro-Pattern Gaseous Detectors. MWPCs consist of a large number of closely spaced parallel wires that amplify the charge as it passes through, while Micro-Pattern Gaseous Detectors use micro-structures to achieve a similar amplification. These technologies help to improve the spatial resolution of the TPC.

In the case of XEMIS, a new grille structure was proposed, named as MEMILI(Micro-Mesh for Liquid Ionization Chamber). The detail description will be presented in the Section 4.

- **Photomultiplier Tubes (PMTs):**

The scintillation light is detected using arrays of sensitive photomultiplier tubes (PMTs) that surround the LXeTPC volume. These PMTs convert the scintillation photons into electrical signals.

- **Event Reconstruction:**

The signals from PMTs are processed, and the arrival times of electrons and ions are recorded. By analyzing this data, researchers can reconstruct the energy and trajectory of the initial particle that interacted with the liquid xenon.

The LXeTPC is a versatile and sensitive detector that can be used for various experiments to study rare and low-energy particle interactions. It has applications in astrophysics, dark matter searches, neutrino experiments, and other studies in fundamental physics.

2.2.2 Historical overview of LXeTPC

The history of LXeTPC dates back to the early 1980s when researchers started exploring the use of liquid xenon as a medium for detecting and studying rare events and particle interactions. The concept of a TPC involves reconstructing particle tracks in three dimensions using the time and position information of the ionization electrons generated by the interactions.

- **Early Concepts:**

The idea of using liquid xenon as a particle detector was proposed in the 1980s, and initial experiments demonstrated its potential for use in rare event searches. The principle of the Time Projection Chamber (TPC) was first proposed by D. Nygren at the Lawrence Berkeley Laboratory in 1974. The concept aimed at detecting charged particles in a gas detector. Three years later, Rubbia[181] proposed the concept of a liquid Time Projection Chamber (TPC) as a large-scale liquid argon detector dedicated to studying proton decay, solar neutrinos, and other rare phenomena in particle physics. This detector design allows for three-dimensional (3D) event imaging, energy measurement, and particle identification[180].

- **LXeGRIT (A Liquid Xenon Gamma-Ray Imaging Telescope):**

In the 1990s and 2000s, the LXeGRIT experiment stood as a groundbreaking endeavor conducted on a balloon-borne platform, led by Aprile Elena[182,183]. This pioneering experiment utilized a liquid xenon time projection chamber (LXeTPC) to effectively detect and image gamma-ray emissions originating from cosmic sources. The energy range of interest spanned from 0.15 to 10 MeV. As a prototype developed at Columbia University, the primary goal of LXeGRIT was to demonstrate and highlight the immense potential of gamma-ray spectroscopy and imaging. The implementation of a liquid xenon time projection chamber with three-dimensional (3D) position sensitivity and a combined charge and light readout system allowed for precise spatial imaging and accurate energy measurements of gamma rays. Being carried on a balloon-borne platform provided LXeGRIT the advantage of conducting observations at high altitudes, away from most atmospheric interference. This pioneering experiment significantly advanced the technology of liquid xenon detectors for gamma-ray astrophysics, paving the way for future missions in high-energy astrophysics that utilize liquid xenon as a sensitive medium for detecting and studying gamma-ray emissions from cosmic sources.

➢ **EXO (Enriched Xenon Observatory) Experiment[184,185]:**

EXO is a significant particle physics experiment located near Carlsbad, New Mexico, U.S., specifically designed to search for neutrinoless double beta decay of xenon-136. The detection of neutrinoless double beta decay (0νββ) holds immense importance as it would provide evidence for the Majorana nature of neutrinos, and it could have a profound impact on our understanding of neutrino mass values and their ordering – two crucial and open topics in particle physics. EXO has already achieved success in detecting xenon double beta decay and has set limits for 0νββ, bringing us closer to unlocking the secrets of neutrinos and their role in the fundamental properties of the universe.

➢ **Dark Matter Searches:**

Liquid xenon time projection chambers have also been used in the search for dark matter particles. The XENON collaboration[186–188], starting with XENON10 and then XENON100 and XENON1T, utilized LXeTPC to detect possible interactions with dark matter particles. As of 2023, the field of LXeTPC technology continues to evolve, with larger and more sensitive experiments in planning or under construction, such as XENONnT[189] and the future DARWIN experiment[190].

2.3 Brief description of Xemis2 camera

The use of liquid xenon in the XEMIS2 detector adds complexity to the system. Liquid xenon operates at a temperature of 168 K and a pressure of 1.2 bar absolute, with a narrow operating range of 6.7 K under this pressure. To ensure proper and stable detector operations, a cryogenic facility is essential to control the liquid xenon environment. Since XEMIS2 is designed for preclinical research and will be installed at CIMA (Nantes Hotel Dieu hospital), its cryogenic infrastructure must comply with medical imaging facility standards. Compactness and safety are two critical characteristics that need to be considered in the design.

The XEMIS2 cryogenic facility comprises three sub-systems:

- ✓ TPC Container (Cryostat) - This houses the TPC and ensures the proper containment and temperature control of the liquid xenon.

- ✓ Recovery and Storage of Xenon (ReStoX) - This sub-system is responsible for the recovery and storage of xenon, which is essential for the efficient and economical use of the noble gas.

- ✓ Purification System - The purification system ensures the xenon is free from impurities and contaminants, maintaining the detector's performance over time.

Figure 2.6 illustrates the overall layout of the XEMIS2 cryogenic facility. This section provides an overview of the cryogenic facility's description and performance, highlighting its importance in enabling the successful operation of the liquid xenon-based XEMIS2 camera for preclinical research.

Fig. 2.6 XEMIS2 Cryogenics Facility: Overview of Detector Cryostat, TPCs, ReStoX, and Xenon Purification System.

2.3.1 XEMIS2 TPC

The XEMIS2 Compton camera is presently in the construction phase. It utilizes a single-phase liquid xenon Time Projection Chamber (TPC) approach, and you can see its transverse and longitudinal cutout views in Figure 2.6. This detector has been meticulously designed as a high-sensitivity cylindrical camera, monolithically constructed to hold approximately 200

kg of LXe. It boasts a remarkable geometrical acceptance for small animals, consistently exceeding 50% (reaching up to 75% at the center) across the entire field of view (FOV).

The XEMIS2 TPC consists of two identical cylindrical TPCs with a shared central cathode. A hollow tube runs through the center of the detector, facilitating the imaging of small animals during experiments. Each TPC has dimensions of 7 cm inner radius, 19 cm outer radius, and 12 cm drift length. Figure 2.8 illustrates a schematic diagram of the upper half TPC, representing one-quarter of the active region. To detect VUV scintillation light, the active volume is initially equipped with 64 PMTs distributed peripherally. However, for future research, the plan is to cover the entire lateral surface with 380 PMTs.

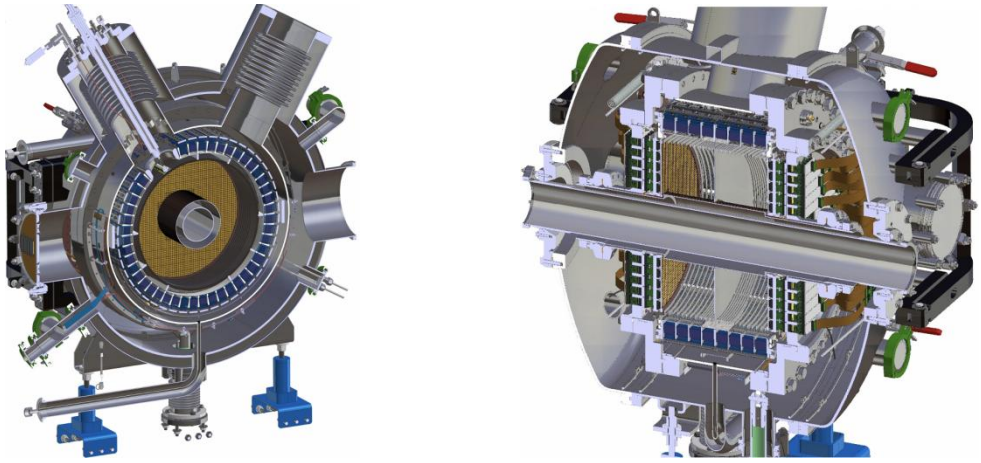

(a) (b)

Fig. 2.7 Design of XEMIS2 Camera: Longitudinal Section (a) and Transverse Cut View (b)

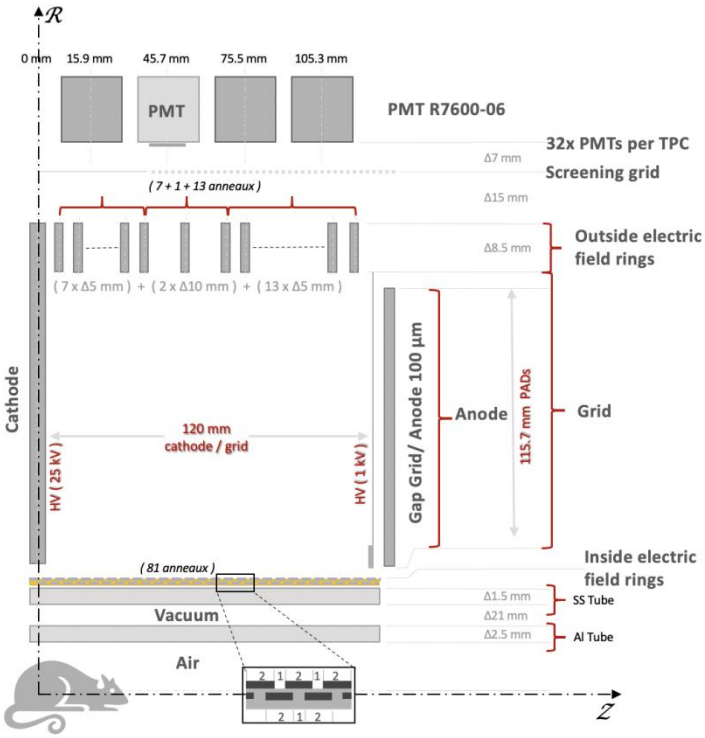

Fig. 2.8 Simplified Geometry of XEMIS2 ½ TPC.

The TPC features two segmented anodes symmetrically placed at both end-sides, opposite to the cathode. Each anode is divided into pixels measuring 3.1 x 3.1 mm². Above the anode, a micro-mesh is positioned at 120 µm, functioning as a Frisch grid. When ionizing radiation produces charges, they drift under the influence of the electric field and are subsequently collected by the anode. For a more comprehensive understanding of the light and charge collection systems, further details are provided in the next subsection.

2.3.1.1 Light detection system:

The XEMIS2 camera represents a cutting-edge advancement in the field of nuclear medical imaging, designed to detect and precisely image gamma rays emitted from objects using a LXe-based detector. A key component of this sophisticated imaging system is the highly optimized light detection system, which plays a crucial role in capturing and analyzing scintillation photons produced in the LXe. This subsection delves into the various aspects of the XEMIS2 light detection system, highlighting its innovative design, crucial components, and functional significance in enabling high-resolution imaging.

- **Scintillation light detection in XEMIS2**

The XEMIS2 camera operates as a single-phase monolithic detector, utilizing the LXe as the sensitive medium for capturing scintillation light. As explained in the section 2.1.4, when gamma rays interact with the LXe, recoil electrons are produced, leading to ionizations or excitations. As the excimers de-excite back to the ground state, VUV scintillation photons are emitted in a transition from the singlet or triplet states to the ground state. The detection of these scintillation photons is essential for determining the deposited energy and interaction positions of the incident gamma rays.

- **Photomultiplier tubes (PMTs) - The heart of light detection**

The core of the XEMIS2 light detection system comprises a set of VUV-sensitive PMTs, specifically developed in cooperation with Hamamatsu Photonics. These PMTs are equipped with an effective bialkali photocathode (Sb-Rb-Cs or Sb-K-Cs), situated on the vacuum side of the light entrance window, to convert scintillation photons into photoelectrons. The bialkali photocathode exhibits high sensitivity to Xe scintillation photons, boasting a relatively high quantum efficiency of approximately 30% at a wavelength of 175 nm. However, at low temperatures, the bialkali photocathode may experience electrical resistivity, which could lead to photocathode saturation. To mitigate this issue, conductive metal strips are employed under the quartz entrance window, rapidly compensating for the increased resistivity and preserving PMT sensitivity without losing efficacy due to photocathode charging.

Fig. 2.9 VUV-sensitive Hamamatsu R7600-06MOD-ASSY PMT used in XEMIS2.

To amplify the primary photoelectron into a measurable electronic signal, the PMTs in XEMIS2 employ a 10-stage dynode structure, achieving a short axial length of 21.25 mm using a metal channel dynode design. This configuration allows the PMTs to operate in a temperature range from -110 ℃ to 50 ℃. In XEMIS2, the PMTs are maintained at a

temperature of -105℃ (168 K) for a pressure of 1.2 bar abs, ensuring optimal performance and stability during operation.

- **Screening grids and mounting bracket**

To protect the PMTs from the impact of high voltage applied to the cathode and field shaping rings, the screening grids (also known as shielding grids) are electrically grounded and located 7 mm in front of the PMT entrance window (15 mm outside the external set of copper field shaping rings). These screening grids consist of two layers of welded copper wires, featuring a pitch size of 6.3 mm and providing 89% optical transparency, thus also serving as light screens.

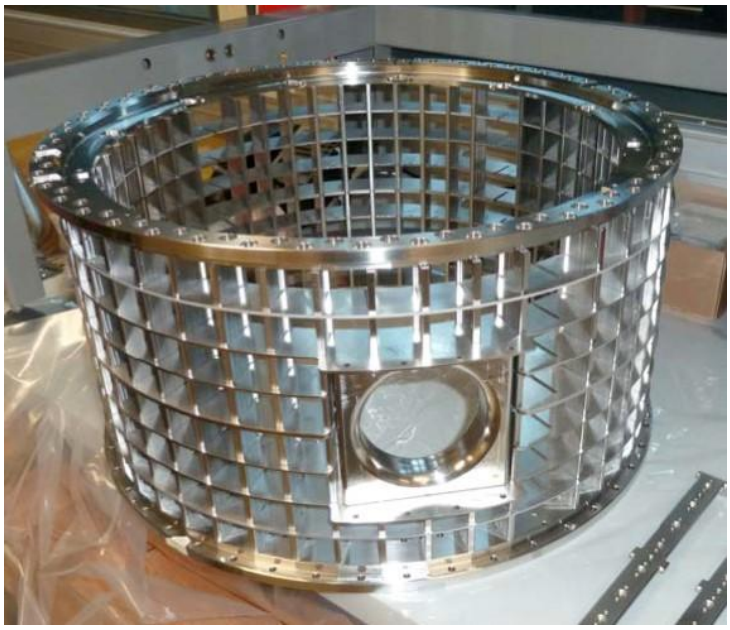

Fig. 2.10 Mechanical support for PMTs[148].

The PMTs are assembled around the XEMIS2 active zone using a stainless-steel mounting bracket, entirely immersed in the LXe. The mounting bracket can accommodate up to 368 PMTs, ensuring complete coverage of the active volume of XEMIS2. Separation structures set a 3 mm distance between each PMT position grid, leading to a small increase in the dead zone. Approximately 73% of the surface is covered by the 368 PMTs.

- **Cabling and arrangement**

In the first stage of the XEMIS2 project, 64 PMTs are arranged in two rows in Z and 32 sectors in φ around the TPC to measure VUV scintillation photons. This configuration

demonstrates the feasibility of realizing whole-body small animal imaging with only 20 kBq administered activity for a 20-minute exposure time. In the second stage of the project, 368 PMTs will be used to fully cover the active volume of XEMIS2, accommodating increased injected activity to shorten exposure time.

The PMT cabling in XEMIS2 is a critical aspect, given the relatively small dimensions of the camera and the numerous cables required for PMT signals and high voltage supply. All wires, including the PMT signal lines, PMT high supply voltage wires, and calibration and monitoring cables from the slow control sensors, are extended toward the top of the detector cryostat through exit tubes. These exit tubes are part of the cryostat design and provide a pathway for the cables to pass through the cap of the external vacuum enclosure to the outside of the cryostat. The tubes are then evacuated to remove impurities that may come from cable outgassing, ensuring the cleanliness and purity of the LXe.

- **Conclusion**

The light detection system of XEMIS2 is a carefully crafted and highly optimized setup that ensures efficient collection and detection of scintillation photons in LXe. Through the use of VUV-sensitive PMTs, effective bialkali photocathodes (Sb-Rb-Cs or Sb-K-Cs), screening grids, and precision mounting brackets, XEMIS2 achieves high-resolution imaging, making it a promising advancement in the field of nuclear medical imaging. The system's innovative design and comprehensive capabilities position

2.3.1.2 Charge collection system

The XEMIS2 system boasts an optimized charge collection system, a pivotal element within its LXeTPCs. This advanced system plays a fundamental role in the precise detection and collection of drifting electrons, enabling high-performance imaging for various scientific applications.

- **Central cathode**

At the heart of the charge collection system lies the central cathode, a shared component used in both LXeTPCs. Constructed from stainless steel, the cathode features specific dimensions, with a thickness of 2 mm, an inner radius of 76.5 mm, and an outer radius of 203.5 mm. It includes a central hole that allows the insertion of small animals during the imaging process.

Acting as a separation plane for the detector chamber, the cathode ensures no interference from Vacuum Ultraviolet (VUV) photons. With a high voltage of 25 kV applied during normal operation, the cathode establishes a drift electric field of 2 kV/cm, facilitating efficient charge collection.

Fig. 2.11 Front view of the cathode with the stainless steel field shaping rings.

- **Field shaping rings**

The XEMIS2 charge collection system incorporates two sets of field shaping rings, strategically positioned on the inner and outer sides of each TPC to ensure electric field uniformity in the drift volume. The internal set comprises 81 micro copper electrodes, each measuring 2 mm in width and 0.35 mm in thickness. These copper electrodes are printed directly on a Kapton insulation layer patched on the hollow middle tube. The external set consists of 21 stainless-steel field rings immersed in liquid xenon, carefully designed to shape a uniform electric field. These field rings are driven by a resistive divider chain, where the last resistor is connected to the ground via a 500 MΩ resistor, and the first one is connected to the high-voltage electrode. An extensive simulation study led to the expansion of the gap between the external field rings above the PMTs from 5 mm to 10 mm, optimizing light collection while preserving electric field uniformity.

- **Pixelated anodes and Frisch grids**

Efficient charge collection is achieved through pixelated anodes, placed symmetrically on both sides of the detector relative to the cathode. Each charge collecting electrode includes a

segmented anode and a micro-mesh serving as a Frisch grid, adopting the MIMELI technique. The segmented anode boasts over 10,000 pixels, each measuring 3.1 mm × 3.1 mm, equipped with micro-pillars of 130 µm. It is a four-layer ceramic circuit made of ROGERS RO4350B, with copper used for the pixels, strips between pixels, and pillars. At the back of the anode, 60-point connectors facilitate connection to the front-end electronics, while a passivation Ni-Au layer deposited on the copper surface imparts a golden appearance.

Above the segmented anode, the Frisch grid plays a vital role, comprising a 500 LPI copper micro-mesh, 5 µm thick, supported by a stainless-steel frame. A voltage of 300 V is applied during operation, ensuring a readable ionization signal that remains independent of the interaction position along the drift direction. Stretching and fixing the micro-mesh maintain its flatness and distance from the anode, generating a uniform electric field. A more detail description of Frisch grid will be presented in the section 3.

- **Conclusion**

The optimized charge collection system in XEMIS2 represents a pinnacle of precision engineering, enabling efficient and accurate charge carrier detection in the LXeTPC. With its strong drift electric field, uniform electric fields ensured by field shaping rings, and advanced pixelated anodes shielded by Frisch grids, XEMIS2 stands at the forefront of cutting-edge technology. This remarkable charge collection system propels advancements in imaging capabilities, holding great promise for diverse scientific frontiers. Furthermore, the cost-effectiveness of this direct ionization signal measurement makes XEMIS2 an attractive option for medical imaging applications, offering a transformative approach to Compton imaging with unparalleled accuracy.

2.3.2 ReStoX and purification systems

Incorporating liquid xenon into the XEMIS2 detector introduces complexity, necessitating a cryogenic facility to ensure stable and proper detector operations. The design must prioritize safety. Hence, a subsystem like ReStoX (Recovery and storage system of xenon) becomes vital, ensuring safe and reliable xenon storage, ultimately contributing to the success of medical research and treatments. Additionally, the purification system plays a crucial role in maintaining an ultra-high purity level of liquid xenon, a critical factor for achieving optimal imaging performance in XEMIS2..

- **Recovery and storage system of xenon**

ReStoX is a crucial cryogenic subsystem in the XEMIS2 system, designed for safe manipulation of xenon in medical applications. It features a walled vacuum-insulated stainless-steel tank with optimal operating temperatures and pressures. The system can store up to 280 L of gaseous xenon, with only 25% in liquid form for safety. Liquid nitrogen (LN2) is used for initial precooling, liquefaction, and continuous cooling. LN2 circulation maintains temperature and pressure stability, ensuring efficient xenon handling throughout the system's operation. ReStoX is a vital component, contributing to the success of medical research and treatments.

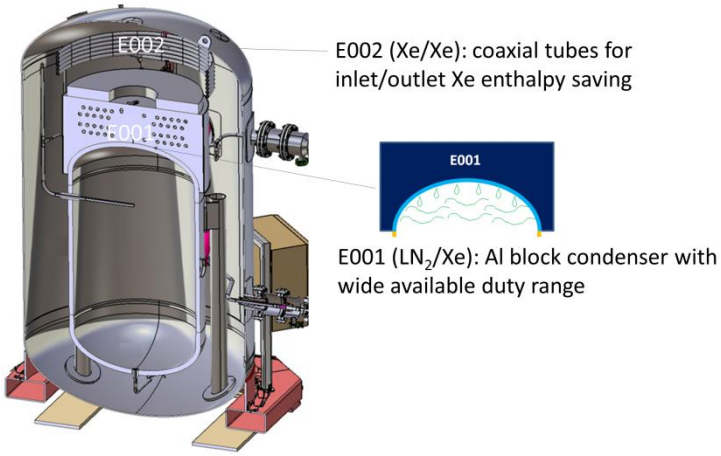

Fig. 2.12: A Basic overview of ReStoX.

- **The purification and circulation system:**

XEMIS2 utilizes a recirculation closed-loop to maintain an ultra-high purity level of liquid xenon (LXe). This high purity can enhance scintillation light performance, enable efficient ionization charge detection, improve the signal-to-noise ratio, and ensure long-term stability. The system incorporates two parallel purification branches, each equipped with a high-temperature SAES MonoTorr Phase II getter based on zirconium. This getter efficiently removes impurities, reducing O2 and N2 levels to below 1 ppb. The purification process involves evaporation of LXe to a gaseous state before passing through the getter. The purified xenon is then liquefied and recirculated back to the XEMIS2 TPC cryostat. Oil-free

membrane pumps maintain constant pressure during circulation, ensuring a continuous purification and recirculation process, vital for optimal imaging performance.

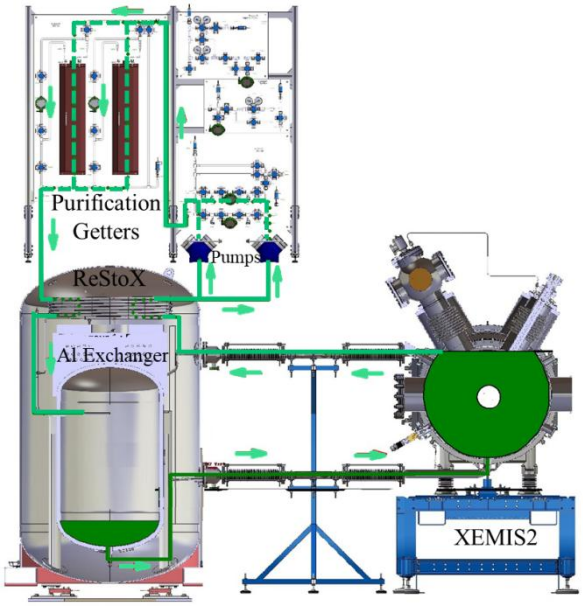

Fig. 2.13: A Basic overview of XEMIS2 purification and circulation system.

2.4 Conclusion

In summary, Section 2 provides a comprehensive and in-depth discussion of XEMIS2, a state-of-the-art liquid xenon Compton camera developed specifically for imaging small animals in nuclear medicine research. This section begins by exploring the physical properties and advantages of liquid xenon, demonstrating its potential as an efficient detection medium for capturing radiation signals. The unique interactions of photons and charged particles with liquid xenon are investigated in depth in this section, revealing the signal generation processes that make liquid xenon an ideal candidate for high-resolution imaging.

One of the highlights of Section 2 is a detailed discussion of the liquid xenon time projection chamber (LXeTPC). The principles of liquid xenon time projection chambers are carefully explained, showing how the technique enables precise tracking and imaging of radiation events, and an overview of the history of LXeTPC provides background information on the advances that have been made in the field, culminating in the development of XEMIS2.

An in-depth introduction to the Xemis2 camera itself, highlighting its innovative design and functionality, which utilises liquid xenon as the detection medium and employs the principle of the time-projection chamber to provide ultra-high spatial resolution and sensitivity, making it ideally suited to small animal imaging studies. The camera's ability to accurately capture and reconstruct radiation signals promises to greatly advance the understanding of various diseases and their treatments. In addition, the section highlights the integration of the ReStoX and purification systems in Xemis2, which play a crucial role in maintaining the purity and performance of liquid xenon, thus ensuring optimal functionality and long-term stability of the camera.

In summary, Section 2 not only provides an in-depth look at liquid xenon and its interaction with radiation, but also provides a comprehensive overview of XEMIS2, the groundbreaking liquid xenon Compton camera.

3 Frisch Grid Simulation

The Frisch grid is identified as an important component in gas-filled radiation detectors, including but not limited to Geiger-Müller tubes and proportional counters, especially those designed for the detection of charged particles. The Frisch grid's essential role is to obscure the anode wire from the electric fields generated by ionizing radiation events within the detector's peripheral areas. This configuration ensures that the pulse signals detected at the anode are independent of the location of the initial ionization event, thereby offering a consistent response to ionizing events across the detector's entire volume.

In the case of XEMIS2, the interaction of radiation with liquid xenon (LXe) prompts ionization, creating a path of electron-ion pairs. In the absence of an externally applied electric field, these charge carriers tend to recombine swiftly. However, the introduction of an electric field leads to the separation and opposite movement of electrons and ions. This movement is crucial for the detector's ability to gauge the energy deposited by the incident radiation through the detection of the charge carriers formed during the interaction.

Ionization detectors, including ionization chambers, Geiger-Müller tubes, and proportional counters, have been instrumental in the detection of ionizing particles since the early twentieth century. The signal in such a detector originates from the charge induced on one or more electrodes by the transit of electrons and positive ions through the medium. The basic architecture of an ionization detector consists of two parallel electrodes, separated by a specific distance and immersed in a dielectric medium, where the induced charge's magnitude is contingent on the traversed distance by the charges prior to their collection. This design leads to variations in signal strength based on the site of interaction within the detector's active zone relative to the collecting electrode. A Frisch grid, serving as a third electrode, is typically introduced between the main electrodes to address the issue of pulse amplitude variability contingent on the interaction location. Ionization chambers incorporating a Frisch grid are extensively used in nuclear and particle physics to quantify ionizing radiation. Moreover, the development of more sophisticated designs with strip electrodes or pixelated anodes has broadened the utility of these detectors, making them suitable for gamma spectroscopy and precise positional determination. Operating on the principle of a Frisch grid ionization chamber, the XEMIS camera exemplifies the advanced application of this technology. This chapter explores the underlying theory of signal induction within a parallel

plate ionization chamber, highlighting the critical role of the Frisch grid in enhancing detector performance and accuracy.

3.1 Fundamental description of Frisch grid

The Frisch grid is placed between the detection volume (where ionization occurs) and the anode wire. It acts as a shield, preventing the electric field from the anode wire from penetrating into the full volume of the detector. This means that ion pairs generated in the gas are initially unaffected by the presence of the anode wire. Only when the ions pass through the Frisch grid and move towards the anode do they experience the strong electric field necessary for their accelerated movement and subsequent signal generation. This setup ensures that the pulses measured at the anode are only influenced by the total number of ions created, not their initial location in the detector. Therefore, the detector's response becomes uniform for ionizing events throughout its volume.

3.1.1 Shockley-Ramo theorem

The Shockley-Ramo theorem offers a foundational principle for understanding charge induction in various types of detectors, ranging from gas ionization chambers to semiconductor detectors. Initially conceptualized for charge induction in vacuum tubes, the theorem has proven its applicability across a broad spectrum of detector configurations. According to the theorem, the instantaneous current (i) induced on an electrode by the motion of a single charge (q) within a detector is given by the equation:

where represents the velocity of the charge in the medium, and denotes the weighting field at the charge's location. The theorem further clarifies that the total charge (Q) induced on an electrode due to the displacement of a point charge (q) can be expressed as:

Here, signifies the difference in weighting potential. The weighting field and weighting potential are defined at the charge's position when the electrode intended for charge collection is set at a potential of 1 V, with all other electrodes grounded and absent of any

charges. These parameters are inherently dependent on the detector's geometry, and generally, they diverge from the actual electric field and potential applied, except in the simplest scenario of a two infinite parallel plate ionization chamber.

The Shockley-Ramo theorem elucidates that although the charge q moves according to the actual electric field lines (assuming diffusion is disregarded), the induced charge Q on a specific electrode can be determined through the weighting potential. This distribution of weighting potential doesn't affect the charge's trajectory; instead, it symbolizes the electrostatic interaction between the moving charge and the electrodes designated for charge collection. The calculation of the weighting potential involves solving the Laplace equation under spatial boundary conditions tailored to the detector's geometry :

Consequently, the magnitude of the charge induced by the movement of q is independent of the electrodes' applied potential, relying solely on the relative position of q to the collecting electrode.

3.1.2 Frisch Grid Ionization Chamber

Utilizing a parallel plate ionization chamber is among the most straightforward approaches to quantify the charge generated in a liquefied noble gas detector. This chamber's fundamental structure consists of two parallel plane electrodes—an anode and a cathode—spaced a certain distance d apart and encapsulated within an appropriate medium, typically a gas or liquid. These electrodes are subjected to a potential difference V_b , establishing an electric field between them. To ensure a uniform electric field, the distance between the electrodes is kept relatively small compared to their length and width. A schematic representation of this setup is shown in Figure 3.1(a). Typically, the cathode is set to a potential of $-V_b$, and the anode, serving as the collecting electrode, is grounded through a resistor R. The passage of radiation through the medium generates electrons and ions, which are swiftly separated due to the electric field's influence. The anode's induced current is then transformed into an electrical pulse through an external electronic sequence, generally comprising a charge-sensitive preamplifier.

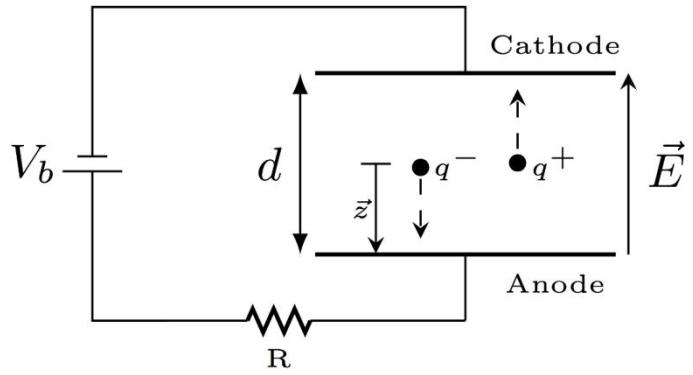

(a)

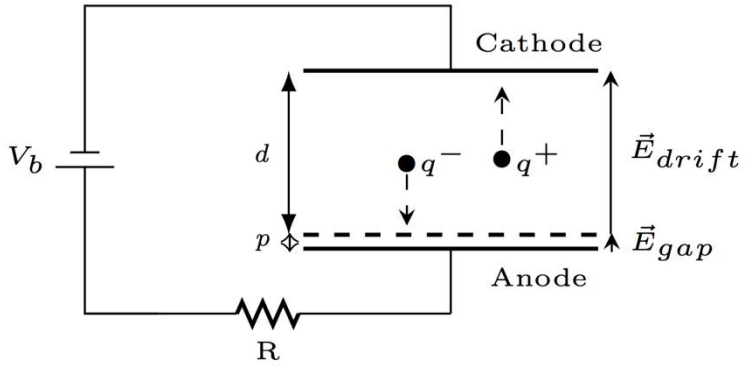

(b)

Fig. 3.1: Comparative Illustrations of Ionization Chambers: Traditional Parallel Plate (a) vs. Frisch Grid Configuration (b).

In practical experimental setups for the traditional parallel plate , the induced signal primarily captures the movement of electrons, with the contribution from positive ions typically being negligible due to the integration time of the external electronic readout system. Consequently, the total induced charge is influenced by the location of the interaction relative to the anode, as indicated by:

Where q is the elementary charge of an electron, N representes the number of electron-ion pairs created by the interaction and z is the distance of the interaction point from the anode. Here, Q is the amplitude of the induced pulse which can vary between 0 and $V_{max} \approx q \cdot N$, depending on the origin of the electron-ion pairs. Such variability in signal amplitude,

contingent upon the interaction's position, significantly impairs the detector's energy resolution. To counteract this issue of z-dependence in the induced signals, the introduction of a third electrode, positioned between the cathode and the anode, was suggested by Frisch. To enhance the functionality of an ionization chamber and eliminate the positional dependency of the signal induced by the movement of charge carriers, a gridded electrode, known as the Frisch grid, is introduced between the cathode and anode. This innovation, initially proposed by O. Frisch in 1944 for gas ionization chambers, involves positioning the Frisch grid a specific distance p from the anode, where it is set to a potential intermediate to that of the cathode and anode.

This arrangement effectively prevents the anode from detecting charges generated in the area between the cathode and the grid, thereby conceptually dividing the detector's active region into two separate zones: the drift region and the adjacent gap, as shown in Figure 3.1(b). Predominantly, interactions occur within the drift region, between the cathode and the grid, where electrons and ions generated migrate in opposite directions under the influence of the electric field. While positive ions generate a current at the cathode, electrons traverse the grid to induce a signal at the anode. This signal generation commences as electrons pass through the grid and ceases upon their arrival at the anode, with positive ions being effectively blocked by the grid from inducing any current at the anode.

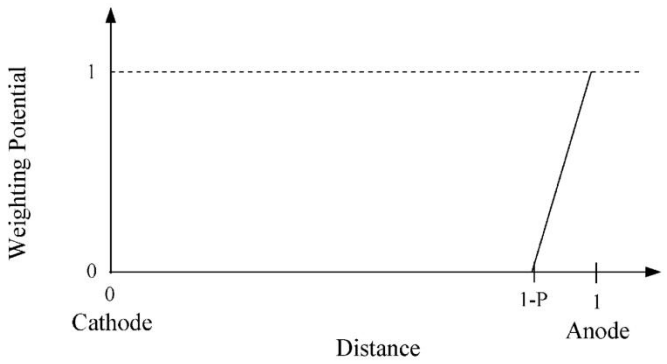

Fig. 3.2: Depiction of the anode's weighting potential in an ideal Frisch grid ionization chamber, where the grid is positioned at a distance 1−P from the anode.

The induced charge on the anode is further quantifiable through the Shockley-Ramo theorem, which involves setting the anode's potential to 1 V and grounding both the cathode and the Frisch grid. As shown in Fig 3.2, this setup yields a weighting potential for the anode that is

zero in the region between the cathode and the grid and increases linearly to 1 from the grid to the anode. Consequently, the total induced charge becomes independent of the interaction location, as electrons always traverse the same distance p within the detector. Illustrations depict the induced voltage in a Frisch grid ionization chamber, highlighting that the signal remains null as electrons approach the grid, followed by a swift increase as they pass through it. The signal's amplitude directly correlates with the number of electrons collected and is unaffected by the collection of positive ions. This independence results in the rise time of the induced pulse being solely determined by the distance between the Frisch grid and the anode, alongside the characteristics of the electronics used for current integration, with shorter gap distances typically leading to quicker rise times.

3.1.3 Discussion and Conclusion

Incorporating an ideal Frisch grid between the cathode and anode ensures that the amplitude of the induced signal correlates directly with the energy deposited within the detector, though the total induced charge remains a function of the electrons collected. The proportion of electrons reaching the anode is influenced by various factors, including the detector's design, the purity of the medium, and the strength of the applied electric field. Under actual experimental conditions, some electrons may be intercepted by the grid, diminishing the overall charge collection. This phenomenon is attributed to the grid's electron collection efficiency. Furthermore, the Frisch grid's ability to shield the movement of charges in the drift region is not absolute. Electrons can induce a current on the anode even before crossing through the grid, a limitation known as the Frisch grid's inefficiency, impacting both the total induced charge and the characteristics of the output signals.

In Lucia Gallego Manzano's thesis[158], a previous PhD student of XEMIS project, she emphasizes the critical role of understanding signal formation in detectors for optimizing the measurement of time, energy, and position of detected signals. Her thesis extends to the operational principles of a gridded ionization chamber and the consequential impact of the Frisch grid on signal collection, underlining how the grid's properties, particularly electron transparency, critically affect charge collection and, by extension, the detector's energy resolution, which provides an in-depth evaluation of two distinct grid designs, stressing the importance of achieving an optimal electric field ratio in the gap for enhanced electron transparency, dictated by the grid's physical dimensions. Gallego Manzano's findings are

instrumental in comprehending signal formation in a segmented anode-based gridded ionization chamber, laying a groundwork for XEMIS2 camera.

However, it is important to know that the simulations carried out by Lucia were exclusively centered around the geometric configurations of the XEMIS1 prototype. Given the significant dimensional discrepancies between the XEMIS1 and XEMIS2 prototypes, this thesis introduces an in-depth and tailored simulation study of the Frisch grid, specifically designed for the XEMIS2 architecture. In subsequent sections, we embark on a detailed investigation into the influence of grid pillars—integral components of the grid structure—on the overall performance and efficiency of the XEMIS2 detector system. This analysis is critical for understanding how these structural elements can affect signal quality and detection accuracy. Furthermore, this thesis expands its scope to include comprehensive simulations of various alternative grid geometries that are commercially available, evaluating their compatibility and efficacy within the XEMIS2 framework. Through these expanded simulations, we aim to identify optimal grid designs that enhance the detector's performance, taking into account the unique requirements and challenges presented by the XEMIS2 design parameters.

3.2 Simulation of Frisch grid for XEMIS2

The Simulation of the Frisch grid for XEMIS2 represents a pivotal component in the advancement of gamma ray imaging technologies, particularly in the context of monolithic Compton telescopes. This section delves into the intricate process of simulating the Frisch grid mechanism, a critical element designed to optimize the performance of liquid ionization chambers. The focus is on a novel micro-mesh technology, MIMELI (Micro-Mesh for Liquid Ionization Chamber), patented by the XEMIS group, which is aimed at enhancing the measurement accuracy of both energy and position of electron clouds within a dielectric medium. Through comprehensive finite element simulations, this segment explores the geometry and electrostatic dynamics of MIMELI, aiming to improve the efficiency of electron detection and minimize the influence of indirect currents on measurement accuracy. The simulation encompasses various aspects, including the design and implementation of the segmented anode, the construction of the grid, and the analysis of electric field distributions. This approach not only provides valuable insights into the optimization of ionization chambers for gamma ray detection but also showcases the potential of advanced simulation tools in refining the performance of complex detection systems like XEMIS2.

3.2.1 Micro-Mesh for Liquid Ionization Chamber (MIMELI)

The electrode geometry enabling the realization of a highly efficient segmented ionization chamber for measuring both the energy and position of an electron cloud is a crucial aspect for monolithic Compton telescopes such as XEMIS. In this context, a new microstructure have been envisioned by XEMIS group, which offers a fresh perspective on measuring low currents induced by the drift of charge carriers under the action of an electric field within a dielectric medium, preferably liquid. We have named this invention MIMELI (Micro-Mesh for Liquid Ionization Chamber), which is now patented.

MIMELI optimizes the efficiency of the "Frish grid" by providing electrostatic shielding of the electrodes located on the anode, while minimizing the intensity of indirect influence currents typically present on certain segmented elements of the anode that do not directly collect moving electrons. The invention is particularly effective in the context of its use with dense liquids as the dielectric medium within which charge carriers are mobile under the influence of an external electric field; thus, it has been characterized with XEMIS1 and liquid xenon of density close to 3. In such media, indeed, electrons can drift over a very long distance without being captured (due to the extremely low presence of electronegative impurities), while the presence of a strong electric field gradient over a small portion of their trajectory hardly generates parasitic phenomena such as electroluminescence or direct multiplication by avalanche. Therefore, it is particularly timely to identify the major potential of MIMELI for the family of instruments measuring ionization currents generated inside dense liquids and chemically inert to free electrons (such as noble gas liquids or organometallic liquids, in particular).

3.2.1.1 MIMELI Geometry Description

Technically, MIMELI is implemented using a segmented ceramic/insulating anode featuring surface conductor pixels isolated from each other, and also isolated from 4 micro-conductive posts of thin thicknesses located at each of the pixel's corners. Adjacent pixels share posts in common to define a periodic geometric pattern that forms a mesh in a large dimension plane, consisting of a pixel and a micro-post. The maximum size and shape of this plane are not restricted, but the covered surface can extend over several square meters, ideally outlined around a self-enclosed geometry (square, rectangular, round, perforated, etc.). The typical

mesh dimension is on the order of 1 mm x 1 mm, and the height of the micro-posts is about a hundred microns. This ratio between the lateral dimension of the pixels and the height of the micro-posts is advantageously as large as possible, preferably greater than 10. A particularly advantageous embodiment for creating this segmented anode involves adding a conductive track between each pixel, connecting all the posts to one another. A thin conductive grid is then placed in contact with the top surface of each of the conductive micro-posts. The pitch of this grid is advantageously smaller than the height of the micro-posts to maximize the efficiency of the "Frish" grid.

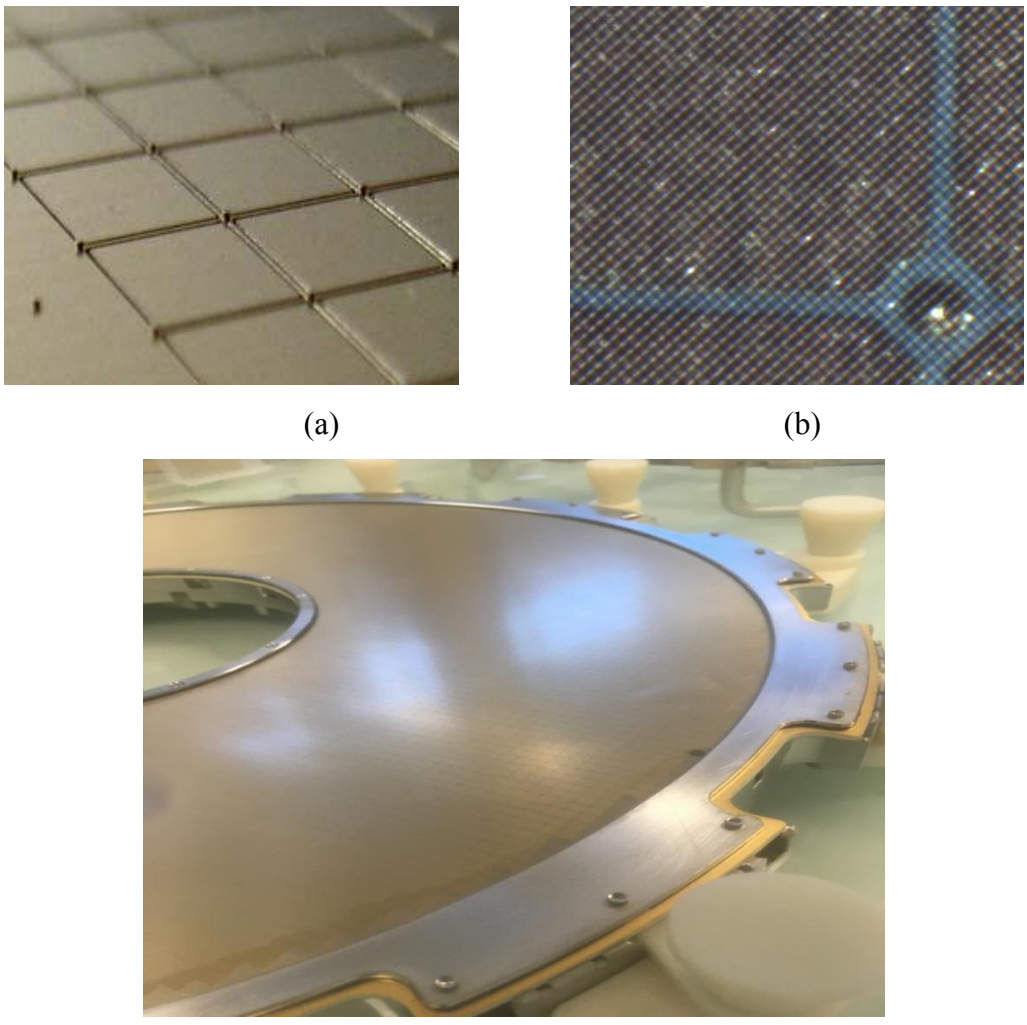

(a) (b)

(c)

Fig. 3.3: MIMELI system components for XEMIS2: (a) Anode structure; (b) Geometric layout; (c) Integrated grid assembly.

The optical transparency of this grid is maximally high, and its thickness is minimally low, to maximize its electronic transparency. A cathode is then mounted at a distance from the grid

much greater than the height of the micro-posts (typically several centimeters) to define a thick region of active liquid where the electric field is almost uniform, and within which the generated charges are measured by the principle of the ionization chamber. Each anode pixel is then biased at a voltage typically close to 0 V, the micro-grid has a voltage ranging from a few tens to a few hundred volts, and the cathode has a voltage sufficient to define an electric field from a few 100 V/cm to a few kV/cm depending on the implementation.

The experimental characterization of MIMELI was carried out using the XEMIS1 prototype and after a sufficient purification period to reduce the concentration of residual impurities to less than 1 ppb. The test prototype accommodates 64 patterns distributed in 8 x 8 pixels/micro-posts. The pattern is defined around a pitch of 3.175 mm, the posts measure 130 µm in height and 130 µm in width, and the tracks connecting the micro-posts in the x and y directions are 80 µm wide. The insulation present between the pixels and the tracks is 80 µm.

The MIMELI anode is a multilayer ceramic circuit (thick layer technology), with the pixels, tracks, and posts made of copper: 20 prototype circuits were produced with the same geometry, 3 have been tested so far and have given complete satisfaction. A photograph of the realization, showing the presence of tracks between the pixels as well as the presence of the micro-posts, is presented in Fig 3.3. The golden color of the circuit comes from the Ni-Au passivation layer that was deposited on the surface of the copper.

Metallographic cross-sections of the test circuit were also made to qualify the thickness of the metal posts. One of them is represented in Fig 3.4 : the posts are made using two layers of copper stacked on top of each other to achieve a total height of 130 µm.

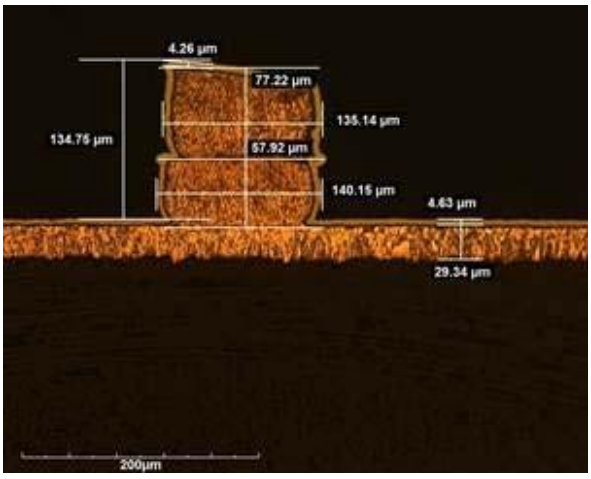

Fig. 3.4: Metallographic cross-section of a MIMELI pilar.

A grid was then mounted using a frame around the 64 patterns. Upon assembly, the grid does not touch all the conductive posts, its parallelism being very difficult to guarantee given the surfaces involved. However, in operation, when the grid is polarized, the electrostatic attraction force exerted between the grids and each pixel compensates for the geometric imperfections so that all the conductive posts of thickness 130 +/- 5 µm come into contact with the micro-grid. Several types of grids have been tested. Grids made of woven steel wires of ~20 µm diameter are difficult to use for this invention. These grids lack elasticity, and it is experimentally challenging to deform them to compensate for parallelism defects under the action of the electric field. However, copper micro-grids made by electrodeposition are good candidates. Although complex to handle, their contact with all the posts is observable by the experimenter in the open air as soon as a potential difference of a hundred volts is applied between the grid and the pixels. With this technology, two types of grids have been tested, both made of pure copper and 5 µm thick. The "200 LPI" grid contains holes of 103 µm and bars of 24 µm width, the "500 LPI" grid has holes of 39 µm and bars of 12 µm wide. This type of grid is also used with gas detectors with microstructures such as Micromegas and PIM. Finally, a conductive cathode placed at 6 cm from the grid defines the conversion zone. The polarization of this grid is defined for our tests so that the electric field is 1 kV/cm in this region for XEMIS1.

3.2.1.2 MIMELI Geometry Simulation

At the inception of this thesis, a comprehensive finite element simulation was initiated to delve into the intricate dynamics of the electric field spanning critical components including the cathode, grid, interstitial spacers, anode pixels, and the dielectric material resembling the ceramic structure opposite the anode.

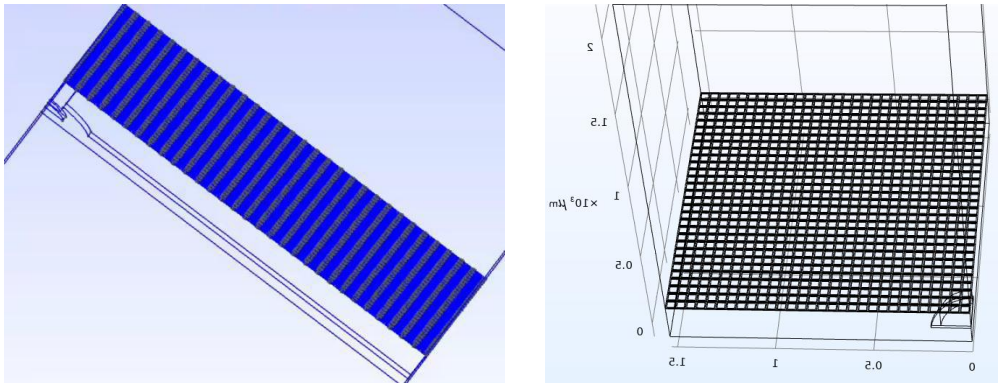

(a) (b)

Fig. 3.5: Simulation of MIMELI geometry using (a) GMESH; (b) COMSOL Multiphysics.

The primary aim of this simulation was to scrutinize the phenomenon of electron transparency within the grid, pivotal in shaping the behavior of induction signals captured at the pixel level. This transparency is contingent upon both the grid's geometric intricacies and the electrostatic field ratios on either side, dictating electron passage under specific conditions. Particularly notable are the two copper grids positioned over the XEMIS2 anodes, characterized by a mesh density of 500 lines per inch (LPI) and featuring bars measuring 10 microns in width and thickness. It was imperative to meticulously replicate these specifications within the simulation. Additionally, precise parameters were defined for the 3 mm square pixels, spaced 100 micrometers apart, along with the copper spacers discreetly positioned at the corners of each anode pixel, isolated from the main pixel body. The simulation encompassed an active area measuring one square centimeter, deemed sufficient for capturing the nuanced behaviors of numerous anodes, each housing over 10,000 pixels. To accurately represent the fine details of the grid, micron-level mesh definitions were employed. However, computational constraints imposed limitations on the simulation's scale. The geometric configurations essential to this investigation are thoughtfully illustrated in Figure 3.5.

3.2.2 GEM-modified grid geometry

The GEM-modified grid is constructed from a copper plate featuring circular holes each with a radius of 30 microns. The distance from the center of one hole to the center of an adjacent hole is 100 microns, as shown in Figure 3.6.

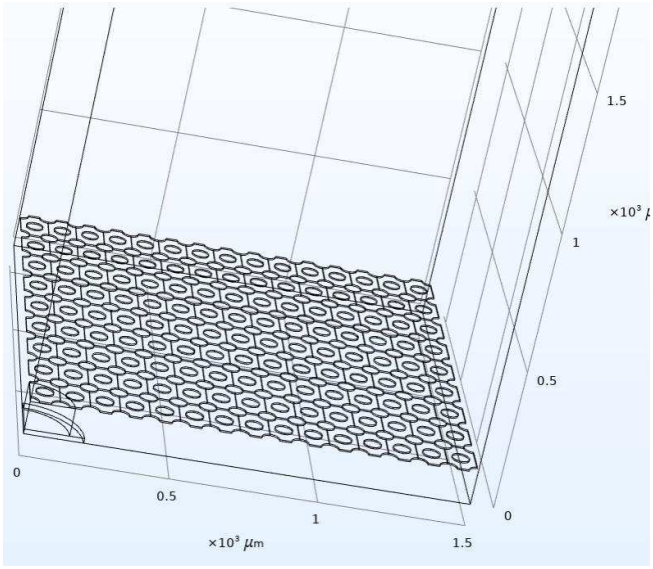

Fig. 3.6: Simulation of GEM-modified grid geometry using COMSOL Multiphysics.

3.2.3 Simulation tools

This simulation leveraged a carefully chosen suite of open-source tools for a detailed analysis. GMSH, a 3D finite element mesh generator, laid the groundwork by defining the simulation's geometry. Following this, Elmer software calculated the electric field distribution using the Finite Element Method (FEM), a crucial step for understanding the electric field's impact on charge carriers. For visualizing the electric field maps, Paraview was employed, allowing for the easy identification of significant patterns. Finally, Garfield++ was used for tracking electron trajectories based on the electric field data, playing a key role in assessing detector performance. This integrated set of tools facilitated a comprehensive examination of electric field and electron dynamics in the system.

In addition to the previously mentioned tools, COMSOL Multiphysics was also utilized to simulate both the geometry and the electric field. COMSOL, known for its powerful and intuitive interface for multiphysics simulations, further enhanced the analysis by providing detailed insights into the electric field's behavior and its interaction with the defined geometry. This addition ensured a more robust and versatile simulation environment, enriching the comprehensive analysis of the system's dynamics.

3.2.3.1 GMSH: Geometry Definition

GMSH serves as the foundational block in the simulation process, tasked with the creation and definition of the geometric model. As an advanced 3D finite element mesh generator, GMSH offers a user-friendly interface combined with powerful scripting capabilities, making it ideal for designing complex simulation geometries. Its flexibility allows for the creation of parametric models, which are essential for simulations that require variation in geometric parameters. GMSH supports a wide range of meshing algorithms, enabling the generation of high-quality meshes tailored to the needs of finite element analysis. This step is crucial, as the accuracy of the mesh directly influences the precision of the simulation outcomes. By providing a detailed representation of the simulation domain, GMSH lays the groundwork for subsequent calculations of physical phenomena.

3.2.3.2 Elmer: Electric Field Calculation

Following the establishment of the simulation geometry, Elmer software takes the stage to compute the electric field distribution using the Finite Element Method (FEM). Elmer is a comprehensive simulation package that specializes in solving multiphysical problems. Its core advantage lies in its ability to handle complex equations governing the behavior of electric fields within varied materials and conditions. Elmer's modular structure supports the simulation of a broad spectrum of physical processes, making it exceptionally versatile for applications beyond electric field calculations. In this specific simulation, Elmer processes the mesh generated by GMSH, applying boundary conditions and material properties to solve for the electric field vectors. The accuracy and reliability of Elmer's calculations are pivotal for understanding the electric field's influence on electron behavior in the simulation environment.

3.2.3.3 Paraview: Electric Field Map Analysis

Paraview offers a sophisticated platform for analyzing and visualizing the electric field maps produced by Elmer. Its strength lies in its ability to handle large datasets and produce clear, detailed visual representations of complex data. Paraview supports a variety of visualization techniques, including scalar and vector field visualization, which are instrumental in examining the electric field distributions within the simulation domain. Users can interact with the data, slicing, dicing, and manipulating the visualizations to uncover underlying

patterns and anomalies in the electric field behavior. This analytical phase is critical for interpreting the simulation results, providing insights that guide the optimization of the simulation model and the prediction of electron dynamics.

3.2.3.4 Garfield++: Electron Tracking

Garfield++ is a specialized toolkit designed for simulating the passage of particles through detectors, focusing on the tracking of electrons in the context of this simulation. It integrates the electric field maps and material properties to simulate the trajectories and interactions of electrons as they move through the simulated environment. Garfield++ employs a combination of Monte Carlo techniques and deterministic solvers to model the complex interactions between electrons and the electric field, including phenomena such as ionization, recombination, and scattering. This detailed simulation of electron behavior is essential for assessing the performance of detectors, allowing researchers to predict how changes in geometry, material properties, or electric field configurations might impact detector efficiency and resolution. Through Garfield++, the simulation achieves a comprehensive understanding of electron dynamics, providing valuable insights into the design and optimization of advanced detection systems.

3.2.3.5 COMSOL Multiphysics: Geometry Definition and Electric Field Calculation

COMSOL Multiphysics is a leading simulation software that specializes in the finite element method (FEM) for solving complex multiphysics problems. Its strength lies in the ability to model and analyze the interaction between different physical phenomena within a single platform. COMSOL is user-friendly, featuring an intuitive interface that guides users from geometry creation and meshing to solving and post-processing. With a vast library of physics interfaces and material properties, it streamlines the setup for a wide range of simulations. The software is highly regarded for its advanced visualization tools, enabling clear and detailed examination of simulation results. By integrating COMSOL into the simulation workflow, users enhance their analysis capabilities, gaining comprehensive insights into the behavior of electric fields and their effects on materials and devices.

3.2.4 Simulation results

In liquid xenon (LXe), an interaction with a 511 keV γ-ray typically generates approximately 30200 electrons if an electric drift field of 2 kV/cm is applied[191]. The total charge collected by the anode in an ideal scenario, where the Frisch grid's electron transparency is 100%, equals the number of electrons produced during the interaction. However, imperfect grid transport properties may result in a portion of electrons being collected by the grid before passing through, reducing the total induced charge on the anode. The transparency of a Frisch grid, influenced by the fraction of electric field lines it intercepts, is assessed by comparing the 511 keV photoelectric peak across different electric field ratios.

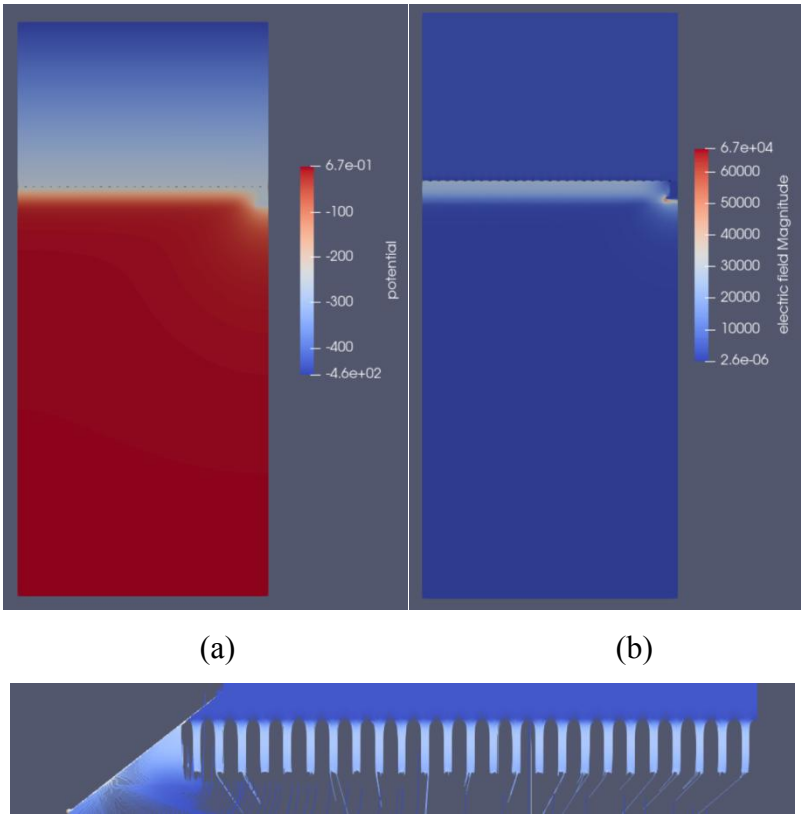

(a) (b)

(c)

Fig 3.7: Visualization of Electric Fields Using Paraview: (a) Intensity of Electric Potential, (b) Intensity of Electric Field, (c) Visualization of Electric Field Lines.

To determine the electron collection efficiency of a Frisch grid, the cathode's potential is kept constant to maintain the same electric drift field, with the anode grounded and varying the grid's applied potential. In the case of XEMIS2, varying the grid, cathode, and the first electric field ring's voltages while grounding the anode ensured a consistent electric field

along the drift region. This study was conducted with a constant electric drift field of 2 kV/cm in a 12cm TPC, biasing the cathode from -100 V to -1000 V and the Frisch grid's potential from -50 V to -500 V, achieving electric field ratios between 2 and 20. A 500 LPI metallic woven mesh, positioned 150 µm from the anode, served as the Frisch grid. The simulation results are shown in Figure 3.7.

The visualization of the electric fields in Figure 3.7, as analyzed in Paraview, provides insightful data regarding the performance of the Frisch grid in the 12cm TPC of XEMIS2. In part (a) of the figure, we observe the intensity of electric potential, which demonstrates a gradient influenced by the applied voltages across the cathode and Frisch grid. Notably, the potential gradient remains consistent with the expected behavior when the cathode is biased from -100 V to -1000 V. Part (b) of Figure 3.7 illustrates the intensity of the electric field, where the uniformity of the field within the drift region is evident, confirming the efficiency of the design in maintaining a constant electric drift field of 2 kV/cm as required for optimal electron transport. In part (c) of Figure 3.7, we see a more focused illustration that depicts the interaction of electric field lines with the grid structure. This precise mapping of the field lines in proximity to the grid allows us to understand the grid's impact on electron transport and field uniformity.

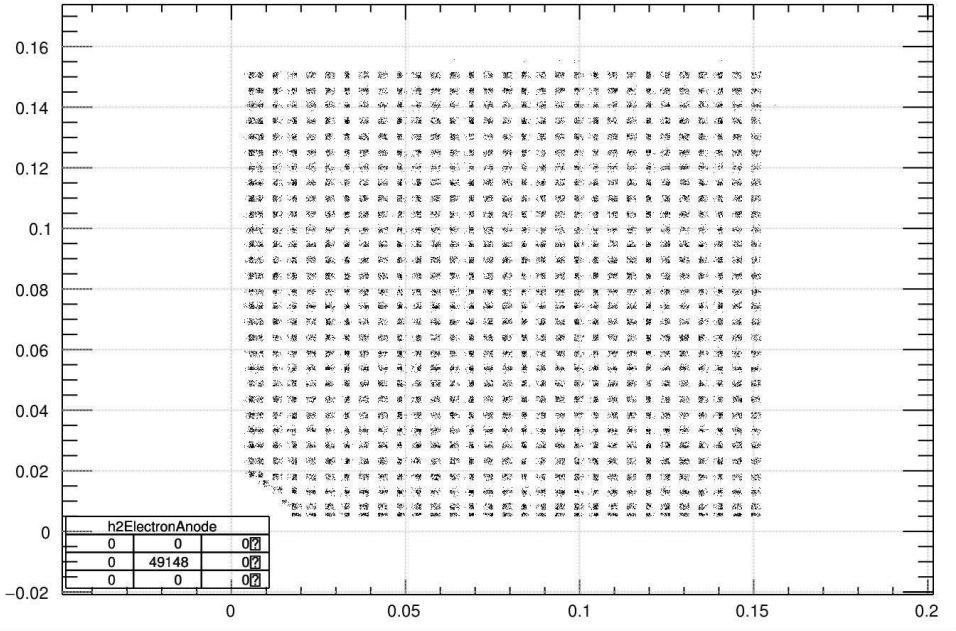

Fig 3.8: Spatial distribution of electrons collected at the anode with a electric field ratio of 12.

Figure 3.8 showcases the spatial distribution (plan x-y) of electrons upon their arrival at the anode surface in a time projection chamber (TPC) experiment. This distribution is the result of releasing 50,000 electrons from the cathode, with the x and y axes denoting the two-dimensional coordinates of the anode surface. Each mark represents the touchdown point of an electron, with the density of these marks reflecting the number of electrons that have congregated in various regions.

The plot reveals a relatively even distribution of electron arrivals, interspersed with areas of varied density that likely indicate the grid's influence on electron transit. Notably, the most populated area contains a substantial density of points, signifying the primary zone where electrons have been collected. This area of higher electron concentration could be indicative of the efficiency with which the electric field steers electrons toward this central region on the anode surface. The numerical label 49,148 on the plot specifies the exact count of electrons detected at the anode, which becomes a direct measure of the grid's transparency. To calculate this transparency, we take the number of electrons that reached the anode (49148) and divide it by the total number of electrons released from the cathode (50000). This yields a grid transparency calculation of 49148/50000 , which simplifies to approximately 98.29% for the electric field ratio of 12. Such a high percentage of electron collection efficiency is indicative of an exceptionally transparent grid, facilitating accurate charge measurement and enhancing the TPC's detection capabilities.

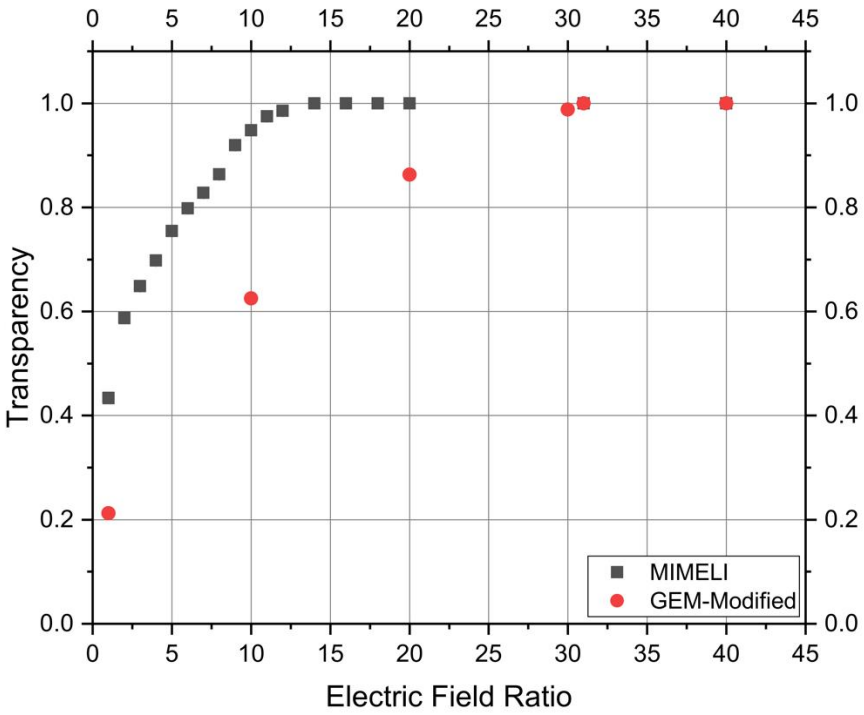

Fig 3.9: Transparence simulation results for MIMELI and GEM-Modified grid.

In light of the findings illustrated in Figure 3.9, the 'MIMELI' configuration demonstrates a superior and consistent electron transparency when subjected to varying electric field ratios. This transparency stabilizes at nearly 100% as the electric field ratio surpasses a threshold of 13. In stark contrast, the 'GEM-Modified' system exhibits suboptimal transparency at electric field ratios below 30, suggesting its limited applicability in environments where maintaining such elevated field ratios may be technically challenging or impractical. Therefore, the deployment of the 'GEM-Modified' system in operational settings must be carefully evaluated, particularly in scenarios where the creation of high electric field ratios is constrained by design or operational parameters.

3.2.5 Discussion and Conclusion

Detailed modelling of the MIMELI and GEM-Modified grids and their integration into the XEMIS2 time-projection chamber is a critical step towards improving gamma-ray imaging techniques. In this study, a comprehensive comparison of these two grid structures is performed to improve the accuracy of measuring ionization currents in liquid xenon media. This comparison is not just theoretical; it will also lead to a series of experiments with the XEMIS2 instrument. We plan to install half of the chamber using the GEM-Modified grid and the other half using MIMELI technology, but this decision has not yet been made.

The MIMELI grid has excellent electron transparency over a wide range of field ratios, demonstrating its robustness and versatility. Its performance peaks at an E-field ratio of 13, demonstrating that it provides reliable measurements even under varying operating conditions. In contrast, the GEM-Modified grid performs very differently, requiring a threshold E-field ratio of 30 to achieve a comparable level of transparency. This finding suggests that the use of GEM-Modified may be limited in cases where such a high electric field ratio cannot be sustained or achieved.

As both grids are now integral components of XEMIS2, their real-world performance will be closely scrutinized in the upcoming 2024 experimental run. This run is expected to yield empirical data that will either validate or challenge the simulations presented herein. The forthcoming experimental results will be pivotal in determining the practical efficacy of the MIMELI and GEM-Modified grids and their respective contributions to the enhancement of medical imaging.

3.3 Conclusion

The Frisch grid is a cornerstone in the field of inflatable radiation detectors and plays a key role in ensuring uniformity and accuracy of signal detection, especially in ionisation chambers used for ionising radiation quantification. By elucidating the fundamental working principles of the Frisch grid and exploring advanced simulation techniques tailored for contemporary detector architectures such as XEMIS2, this study sheds light on the complex dynamics of the Frisch grid and its impact on detector performance.

The theoretical foundations established through the discussion of the Shockley-Ramo theorem provide a fundamental understanding of the mechanisms of charge induction within ionisation detectors. By delving into the intricate interactions between charge motion and electric field, the theorem serves as a guiding principle for understanding the induced signals in the detector and lays the groundwork for the subsequent discussion of the functionality of the Frisch lattice.

In practical implementations, the Frisch grid ionization chamber has emerged as a sophisticated solution to address the issue of pulse amplitude variability inherent in traditional ionization chambers. By conceptually dividing the detector's active region into distinct zones and effectively shielding the anode from charges generated in the intermediate region, the Frisch grid ensures that the induced signals at the anode are solely influenced by the total number of ions created, rather than their initial location within the detector. This characteristic not only enhances the detector's energy resolution but also facilitates accurate quantification of ionizing radiation across its entire volume.

Furthermore, the simulation of the Frisch grid for XEMIS2, encompassing innovative designs such as the Micro-Mesh for Liquid Ionization Chamber (MIMELI) and GEM-modified grid geometry, offered valuable insights into their performance characteristics. Through a meticulous analysis facilitated by a suite of simulation tools, including GMSH, Elmer, Paraview, Garfield++, and COMSOL Multiphysics, researchers gained a comprehensive understanding of electron dynamics, electric field distributions, and grid efficiency. These insights are instrumental in optimizing detector design parameters, enhancing detection accuracy, and advancing the capabilities of next-generation detector systems like XEMIS2.

In summary, this study highlights the importance of the Frisch grid in the XEMIS2 detector, emphasising its role in mitigating signal variability and improving detector performance. By combining theoretical principles with advanced simulation techniques, researchers can open up new avenues of innovation, paving the way for the development of more sensitive, accurate and efficient radiation detection systems. As technology continues to evolve, the Frisch grid remains an integral component, driving advances in fields ranging from nuclear and particle physics to medical imaging and homeland security. With continued R&D efforts, the potential for Frisch grids to revolutionise radiation detection in a variety of applications is endless.

4 Scintillation signal detection in XEMIS2

Scintillation detection assumes a paramount role within the operational framework of the XEMIS2 camera[149], serving as a cornerstone for the acquisition and subsequent exploitation of crucial data pertaining to the interactions of gamma rays within the liquid xenon medium. This detection modality not only facilitates the precise determination of deposited energy and spatial coordinates attributed to incident gamma rays but also affords the means to perform intricate timing measurements, thanks to the expeditious emission of vacuum ultraviolet (VUV) scintillation photons. The temporal information gleaned from these emissions, in conjunction with simultaneous ionization signal measurements, affords a unique capability to reconstruct interaction depths with a striking degree of precision, approaching a spatial resolution of 100 μm. Furthermore, the scintillation detection mechanism assumes a pivotal role in the context of pre-localizing gamma ray interactions, thereby mitigating occupancy challenges encountered within the confines of the liquid xenon Time Projection Chamber (LXeTPC). These multifaceted contributions collectively augment the overall functionality and performance of the XEMIS2 camera.

In the subsequent section, we shall embark upon an exhaustive examination of the scintillation detection chain, extending and elaborating upon the foundational concepts elucidated in section 4.1. Following this, in section 4.2, some key information about the PMT will be detailly discussed. Subsequently, in section 4.3, we will systematically introduce and expound upon a rigorous calibration methodology meticulously developed for precise measurements. Finally, in section 4.4, we will present a comprehensive summary, drawing together the salient conclusions and insights gleaned from the extensive research and analysis presented in this chapter.

4.1 Comprehensive overview of the scintillation detection chain

In XEMIS2, the precise measurement of time relies heavily on the scintillation signal. This signal serves a crucial role in determining the interaction time of a γ-ray with liquid xenon (LXe) and aids in the preliminary localization of the interaction point, thereby mitigating the occupancy rate. To cater to these requirements, a scalable self-triggered scintillation signal

readout and data acquisition (DAQ) system has been purposefully designed for XEMIS2. This specialized system facilitates the measurement of interaction time and offers an approximate estimation of the number of photoelectrons detected by the photomultiplier tubes (PMTs). The scintillation light detection and measurement system consist of three fundamental components: VUV-sensitive PMTs, XSRETOT (XEMIS Scintillation Readout for Extraction of Time Over Threshold) front-end electronics, and XDC (XEMIS Data Collector), which streamlines the data readout and acquisition process. A comprehensive and detailed exposition of the detection chain will be provided in the subsequent subsection.

4.1.1 Motivation for developing a high-efficiency scintillation readout system

As mentioned previously, the scintillation signals play a crucial role in determining the interaction time of gamma rays. In addition, by correlating the scintillation signals with ionization signals, they assist in spatially locating gamma-ray interactions, facilitating the virtual delineation of the active volume. Given the multitude of PMTs involved, signal information extraction becomes paramount in reducing readout data flow. The system is meticulously designed to capture and digitize pertinent data from the scintillation signals, including the interaction time of gamma rays with liquid xenon and the approximate number of photoelectrons detected by the PMTs.

To achieve this goal, a novel approach is undertaken to enhance the accuracy and efficiency of signal acquisition during the detection of ionization and scintillation events. Unlike traditional methods that utilize external scintillation light to trigger ionization signal acquisition, which often introduces significant electron drift dead time, XEMIS2 employs two distinct yet synchronized detection chains for scintillation and ionization signals. This innovative approach enables concurrent and uninterrupted data collection, minimizing electronic dead time. By adopting this self-triggered data acquisition mode for both scintillation light and ionization charge measurements, the system eliminates the time-consuming process of triggering feedback control. This, in turn, prevents event loss during non-negligible electron drift dead times, ensuring maximum event efficiency. Consequently, the recorded signals from these two systems can be accurately synchronized and correlated to determine essential event parameters, such as charge carrier drift times, during offline data analysis. Additionally, the self-triggered data acquisition mode necessitates the

implementation of a threshold for discriminating pulses above a certain noise level. Setting this threshold too high would significantly degrade signal detection efficiency. To achieve precise 3D position and energy measurements for each gamma interaction, a relatively low threshold is essential. However, for applications like small animal imaging with low activity (e.g., 20 kBq used in XEMIS2), this low threshold can result in a substantial increase in data flow. Consequently, the PMT output signals may become inundated with noise signals. In response to these challenges, XEMIS2 employs a high-rate scintillation signal readout system to accommodate the increased data flow associated with low threshold triggering. This system effectively manages the data volume by extracting essential information from each signal, mitigating the potential overload of data storage and analysis capabilities.

4.1.2 Detail description of scintillation light detection chain

The scintillation light detection and measurement system comprises three essential components: VUV-sensitive PMTs (Vacuum Ultraviolet-sensitive Photomultiplier Tubes), XSRETOT (XEMIS Scintillation Readout for Extraction of Time Over Threshold) front-end electronics, and XDC (XEMIS data concentrator)[148], designed to facilitate the data readout and acquisition processes as illustrated in Figure 4.1.

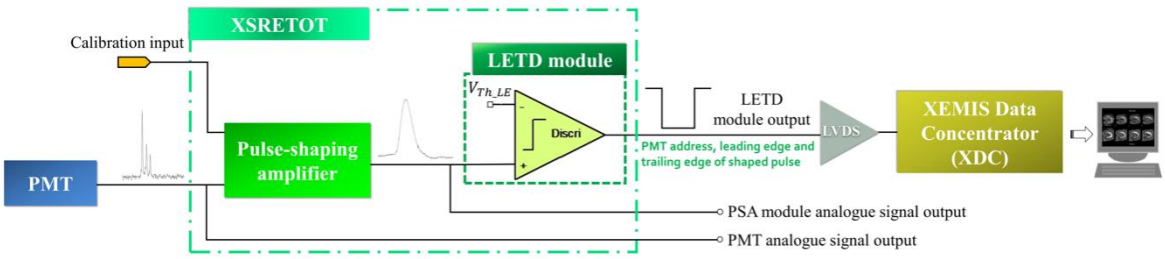

Fig. 4.1: Schematic diagram of the scintillation readout system in XEMIS2 for each PMT channel[149].

Initially, the scintillation signals, as introduced in section 2.3.1.1, are acquired by the VUV-sensitive PMTs. These signals undergo a rigorous processing and extraction process facilitated by the internally developed XSRETOT front-end readout electronics. XSRETOT is comprised of 16 identical self-triggered electronic circuits, each dedicated to concurrently processing the output signals from 16 PMT channels, as illustrated in Figure 4.2.

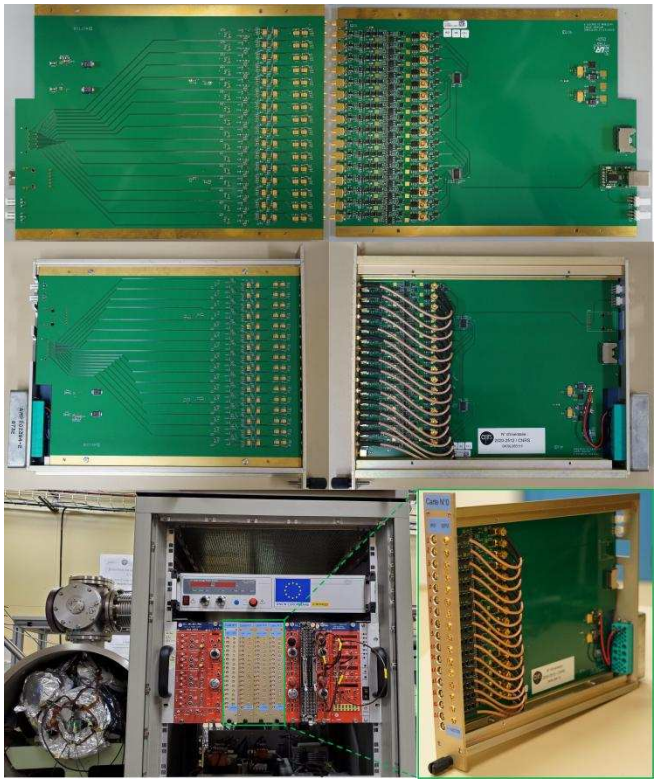

(a)

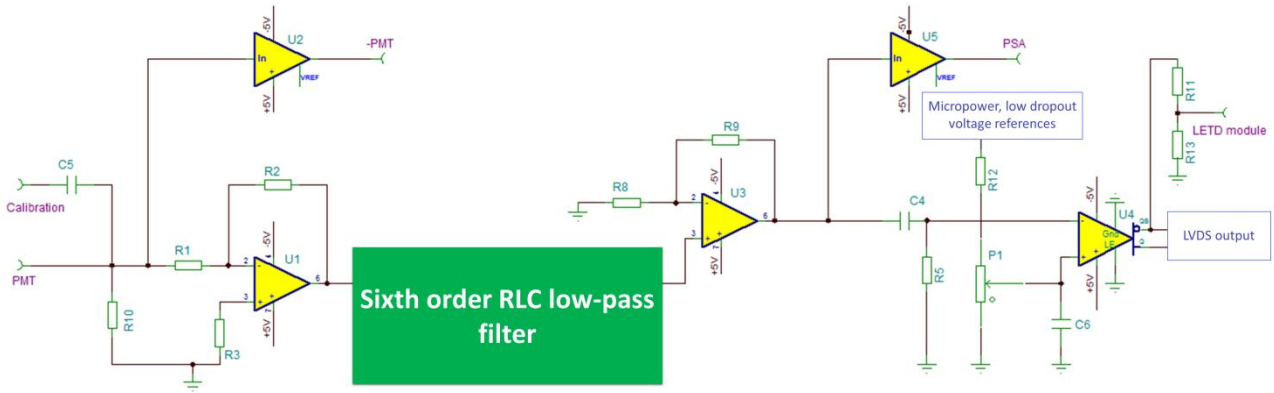

(b)

Fig. 4.2: (a) Image of XSRETOT front-end readout electronics. (b) Simplified schematic of the XSRETOT prototype PCB for each PMT channel[149].

Each elementary electronic circuit is equipped with a pulse-shaping amplifier and a discriminator, enabling the extraction of both the leading edge and the TOT (Time Over Threshold) of the shaped pulses. Subsequently, the digital information pertaining to the leading edge, TOT, and the PMT address for each channel is transmitted by the XDC via high-speed LVDS cables to streamline the data acquisition process. In the context of XEMIS2, which employs 64 PMTs, each half-LXeTPC (Liquid Xenon Time Projection

Chamber) efficiently processes the output signals of a total of 32 PMTs through a single XSRETOT unit. XEMIS2 is equipped with a total of 4 XSRETOT units and 4 XDC units. A more detail description will be provided in the following subsection.

4.1.2.1 Pulse-shaping amplifier

Within the PMT's response time range, the number of photons reaching the photocathode is directly proportional to the number of photoelectrons (p.e.s) they generate. However, due to varying intrinsic decay times of xenon scintillation light emitted during the same interaction, the arrival times of these photons at the PMT photocathode differ. This dispersion effect results in multiple peaks in the PMT's electrical signals, particularly pronounced when only a few p.e.s are detected (like XEMIS2 situation). This non-proportionality between detected p.e.s and pulse height complicates the direct inference of the number of scintillation photons produced during the interaction. In the absence of a global event trigger system, a self-triggering method with a low threshold is employed in XEMIS2's detection chain to select physical events. However, applying the threshold directly to the PMT output may lead to missed signals with only a few p.e.s, hampering the alignment of scintillation and ionization signals and event efficiency. To address these challenges, the electrical signals from the PMTs undergo effective shaping and integration using a PSA (Pulse-Shaping Amplifier), aiding in the estimation of the number of detected photoelectrons and the average arrival time of Xe scintillation light.

This advanced PSA primarily consists of a sixth-order low-pass RLC shaper, meticulously designed to enhance the measurement of interaction time and the accurate counting of photoelectrons detected by the PMTs. Given that PMT output pulses are initially negative signals, an inverting operational amplifier is employed to facilitate signal processing before entering the shaper. This amplifier not only ensures signal inversion but also delivers impedance matching to mitigate the influence of reflected waveforms from the large PMT signals. The dynamic range of PMT output signals in XEMIS2 varies from one to several tens of photoelectrons, and the use of a low-noise operational amplifier prior to the RLC shaper ensures precise amplification with minimal noise. The PSA, in conjunction with this amplification stage, shapes and integrates the pulses efficiently. To meet calibration requirements, a capacitor of 2.2 pF at the calibration input channel allows direct injection of charge, while the presence of the inverting amplifier enables electronics calibration without

affecting PSA characteristics. Overall, the PSA is a critical component that optimizes the signals for subsequent processing, aiding in the extraction of vital information such as time and TOT, ultimately contributing to the system's precision and sensitivity in detecting radiation events.

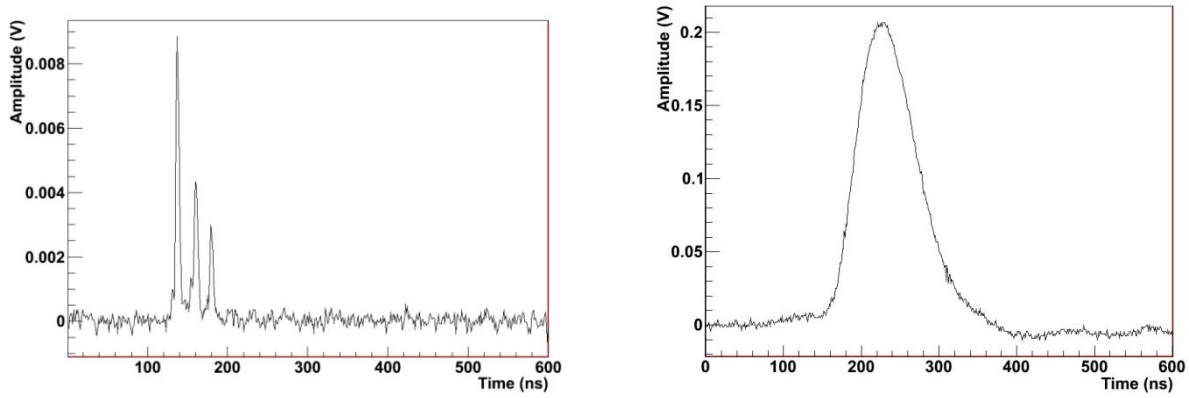

(a) (b)

Fig. 4.3: (a) Example of an output signal of the PMT; (b) Example of an output signal of the pulse-shaping amplifier[192].

4.1.2.2 LETD (Leading Edge Timing Discrimination) method

The Leading Edge Timing Discrimination (LETD) method is a crucial technique employed in radiation detection systems, specifically in the context of signal processing for PMT and scintillation light measurements. In LETD, the primary goal is to determine the arrival time and TOT of incoming signals accurately. This method utilizes a leading-edge discriminator with a fixed threshold voltage applied to shaped pulse signals. When a signal from the PSA surpasses this threshold, the discriminator generates a logic pulse signal, and the timing of this logic pulse's leading edge is used as the arrival time of the input PSA signal, as shown in Figure 4.4. Essentially, LETD converts an analog PSA signal into a digital logic pulse only when its amplitude exceeds the threshold level. The threshold level is typically set several times higher than the noise level to select only genuine physical events.

The LETD method, however, introduces a phenomenon known as time walk effect, as shown in Figure 4.5 (a). This effect arises because, when signals of varying amplitudes and peaking times cross the fixed threshold, they do so at different points along their leading edges. This results in variations in the recorded arrival times, introducing timing uncertainties. The magnitude of this uncertainty depends on the noise-to-slope ratio of the signal, where a larger

signal slope corresponds to smaller timing uncertainty. Consequently, selecting an optimal threshold value that aligns with the maximum slope of the input signal is crucial for minimizing time jitter and achieving precise time measurements. LETD is widely used in radiation detection due to its simplicity and efficiency, although careful consideration of threshold settings is essential to mitigate timing uncertainties caused by noise and variations in signal characteristics.

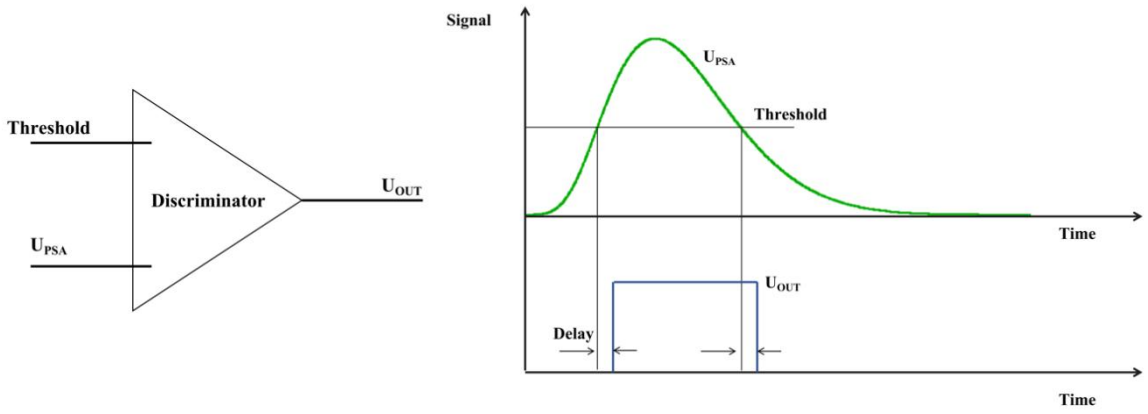

Fig. 4.4: Principe of leading edge timing discrimination method.

In addition to the time walk effect, timing errors within the system are influenced by two other factors: time jitter and time drift. Time jitter refers to the statistical fluctuations in time measurements, stemming from noise sources in the detector, the readout electronics and the noise impose in the threshold. These fluctuations are superimposed onto the output signals and introduce uncertainty into the time measurements. The fluctuations of the comparator and the fluctuations of signal are represented in the Figure 4.5 (b).

On the other hand, time drift represents a timing error resulting from components within the detector or time pick-off circuit that exhibit sensitivity to temperature variations and fluctuations in power supply voltage. Moreover, these components are susceptible to aging over time. Fortunately, mitigating time drift is feasible through the application of common electronic techniques.

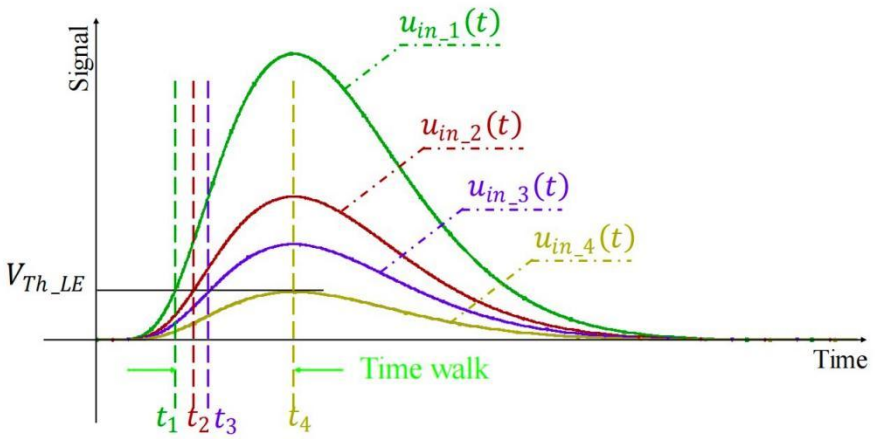

(a)

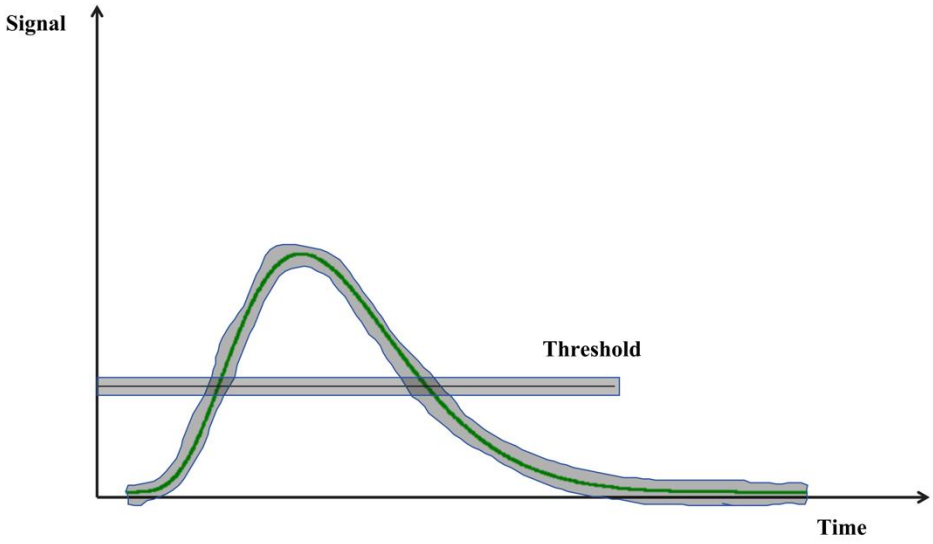

(b)

Fig. 4.5: (a) Illustration of the time walk effect. (b) Illustration of the time jitter effect.

4.1.2.3 XEMIS data concentrator card

The firmware for the prototype Spartan concentrator card in XEMIS2 is a critical digital component of the project's data processing system. This concentrator card is purpose-built to aggregate, process, and organize data from various detectors and sensors distributed throughout the experimental setup. The firmware is meticulously developed to ensure efficient and precise data acquisition for XEMIS2.

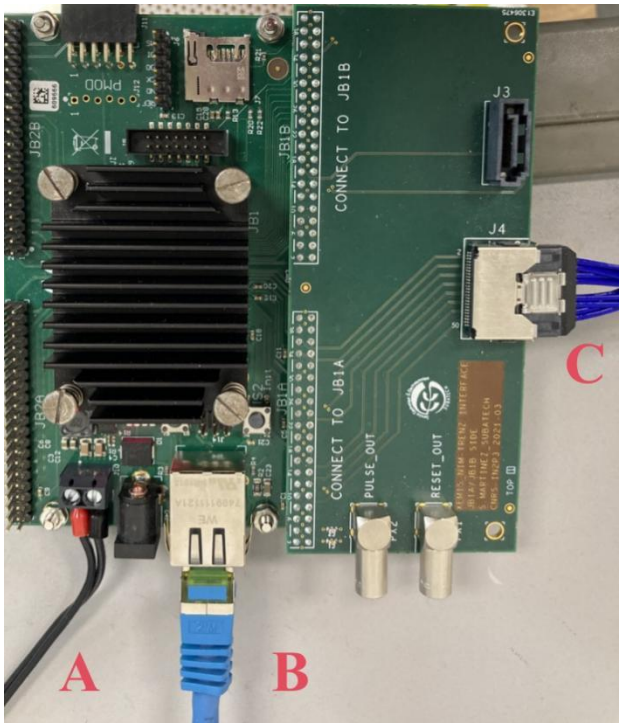

Fig. 4.6: Spartan card overview. (A) Voltage supply; (B) Serial communication port to computer ;
(C) Data flow from XSRETOT.

The firmware for the Spartan card incorporates advanced techniques, such as over-sampling (OVS), to optimize data acquisition quality. It leverages a clock frequency of 200 MHz (equivalent to a 5 ns period) for capturing high-frequency signals effectively. Additionally, it handles time-stamping and data compression, contributing to the efficiency of raw data processing.

The Spartan concentrator card plays a central role in XEMIS2's data acquisition system, ensuring that collected data is prepared optimally for subsequent analysis steps. Its firmware is designed to adapt to the specific requirements of the experiment, guaranteeing data accuracy and consistency. This, in turn, contributes to the overall success of the XEMIS2 project.

4.2 Principle of PMT

Photomultiplier tubes (PMTs) are integral components in the realm of LXe-based detectors, playing a pivotal role in detecting scintillation light. These devices comprise several essential

components, as depicted in Figure 4.7. The primary constituents of a PMT include a light entrance window, a photocathode, a set of focusing electrodes forming a photoelectron acceleration structure, an electron multiplying system (also known as a dynode structure), and an electron collection electrode or anode. These components are meticulously contained within a sealed vacuum tube to ensure their proper functioning.

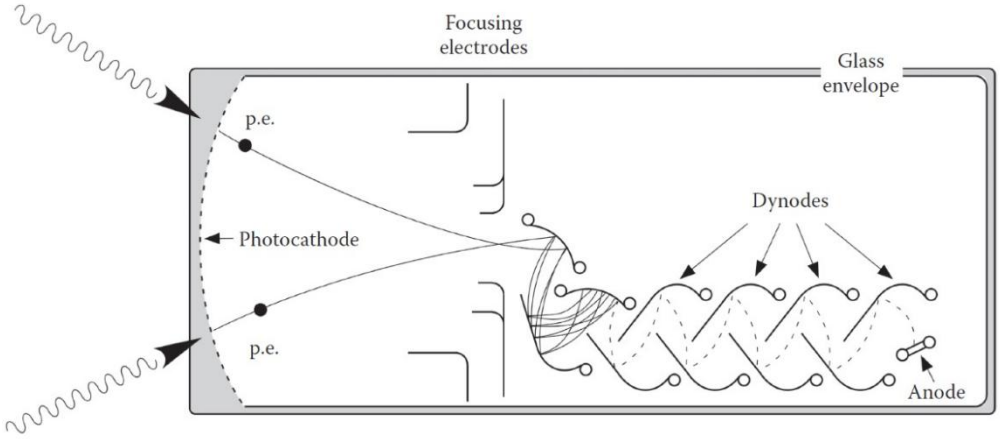

Fig. 4.7: Schematic Illustration of the Fundamental Principles of a Photomultiplier Tube (PMT)[193]. Copyright © Hamamatsu Photonics K.K. and its affiliates.

In the context of LXe-based detectors, where the direct detection of scintillation light is paramount, PMTs are required to be completely immersed in the liquid xenon. The fundamental operation of a PMT is illustrated in Figure 4.7. Initially, scintillation photons generated within the LXe medium enter the PMT through the light entrance window. This window is specifically designed to be transparent to the vacuum ultraviolet (VUV) scintillation light emitted by liquid xenon. Subsequently, these scintillation photons interact with the photocathode, which is coated with photosensitive materials capable of facilitating the photoelectric effect. The photocathode is typically located on the inner surface of the light entrance window or on an electrode positioned in front of it. When VUV photons are absorbed by the photocathode, they give rise to photoelectrons. Some of these photoelectrons migrate to the photocathode surface and are expelled into the vacuum.

The subsequent critical step involves harnessing a powerful electric field, generated by a series of precision-focused electrodes. This field serves a dual purpose: firstly, it accelerates the photoelectrons, propelling them toward the initial dynode within the electron multiplication system, and secondly, it precisely guides their path. Upon striking the first

dynode, the photoelectrons stimulate the emission of multiple secondary electrons, which are then promptly accelerated and directed towards the successive dynode. This cascade of events unfolds at each dynode, resulting in an exponential surge in electron quantities. Ultimately, these amplified electrons converge at the anode, marking the culmination of the electron amplification process. The resulting output signals from the PMT are then channeled to the front-end electronics, with signal pulse heights being converted into TOT values. In the subsequent subsection, we will conduct an in-depth exploration of the experimental setup for TOT calibration.

4.2.1 Fundamental elements of PMTs

The fundamental elements of Photomultiplier Tubes represent a cornerstone in the detection and amplification of weak light signals, playing an indispensable role in a myriad of scientific applications, from medical imaging to particle physics. A PMT capitalizes on the photoelectric effect to convert light photons into an electrical signal that can be quantified and analyzed. This process is achieved through a meticulously orchestrated interaction among several critical components, each designed to perform a unique function within the PMT structure. At the outset, the photocathode initiates the conversion of light to an electron signal. Subsequently, the dynode structure amplifies the electron signal through a series of stages, culminating in the electron collection at the anode. This ensemble of components not only amplifies weak light signals to measurable levels but also ensures the high sensitivity and specificity required for advanced scientific research.

- **Photocathode**

The photocathode, comprising photosensitive materials, serves the crucial role of converting scintillation photons into photoelectrons. Typically, it is either semi-transparent, deposited on the inner surface of the light entrance window facing the vacuum side, or reflective, placed on an electrode opposite the entrance window. Photocathode thickness varies, tailored to whether they are reflective or semi-transparent. Various materials sensitive to the VUV region, such as cesium iodide (CsI), cesium tellurium (CsTe), bialkali photocathodes (Sb-Rb-Cs or Sb-K-Cs), multialkali photocathodes (Na-K-Sb-Cs), and gallium arsenide photocathodes (GaAs), can be employed. Photocathodes for LXe scintillation light detection are typically composed of alkaline semiconductor materials, chosen for their low work function facilitating photo-extraction. While bialkali photocathodes are highly reactive and

often protected within the PMT's high vacuum tube, they exhibit sensitivity to low-temperature-induced electrical resistivity changes, leading to photocathode saturation and reduced PMT sensitivity. To mitigate this, many PMTs incorporate conductive metal strips beneath the photocathode, connecting the central region to a peripheral conducting ring, and some employ platinum backing to minimize charging. Despite the saturation risk, bialkali photocathodes remain popular in LXe-based detectors for their high quantum efficiency and low dark noise, with recent developments reducing sheet resistance and obviating the need for additional measures.

- **Light entrance window**

Within Photomultiplier Tubes, the critical component is the light entrance window, serving as the interface for scintillation light. Liquid xenon's VUV scintillation, with a 178 nm longest wavelength, demands a specific material choice. Quartz is favored due to its transparency in the xenon scintillation wavelength range. These windows can be placed at the PMT's top (head-on type) or on its side, with the head-on type prevalent in medical imaging. While quartz windows are slightly costlier than borosilicate glass, they can be made in larger sizes, ensuring efficient detector surface coverage. The refractive index of the entrance window is crucial for minimizing light loss via internal reflection. Synthetic silica (quartz), with a refractive index near 1.6, aligns well with liquid xenon's refractive index range of 1.54 to 1.72, making it an ideal choice. It also exhibits minimal photon attenuation and radioactivity, making quartz-windowed PMTs ideal for low-background experiments.

- **Dynode structure**

The dynode structure within a PMT plays a pivotal role in the amplification of photoelectrons. It is composed of a series of electrodes, each called a dynode, which are strategically positioned to facilitate a chain reaction of electron multiplication. When the photoelectrons ejected from the photocathode collide with the first dynode, they have enough energy to release several secondary electrons. These secondary electrons are then accelerated to the next dynode, and the process repeats. Each successive dynode is at a higher potential, ensuring that the electron multiplication effect is compounded with each stage. The types of dynodes, such as box-and-grid, linear-focused, Venetian blind or metal channel type, differ in shape and material, affecting the gain and other characteristics of the PMT. The choice of dynode material, like copper-beryllium or silver-magnesium, influences the secondary emission yield and ultimately the PMT's gain and resolution.

- **Electron collection electrode (anode)**

The anode is the final electrode in the PMT where the multiplied electrons, having passed through the entire dynode chain, are collected. It converts the amplified electron signal into a measurable current. The anode's design and material are crucial for the efficient collection of electrons and the minimization of signal loss. Usually made from materials with good electrical conductivity such as gold or silver, the anode must be robust enough to handle the high electron flux without deteriorating over time. The anode's signal is then fed into the front-end electronics, where it is processed and converted into a voltage pulse proportional to the initial number of scintillation photons that entered the PMT. This signal is what researchers use to analyze the properties of the detected radiation.

4.2.2 Some key characteristics of PMTs

Photomultiplier Tubes are renowned for their unparalleled sensitivity and precision in detecting and amplifying faint light signals, serving as the backbone of various scientific and medical imaging technologies. The performance and utility of PMTs are determined by a set of key characteristics that define their operational capabilities and application suitability. These include sensitivity, which gauges the efficiency of light-to-electron conversion; time response, indicating the speed and uniformity of the device's reaction to light stimuli; pulse linearity, ensuring the fidelity of signal output relative to input light intensity; dark current, which can impact the signal-to-noise ratio; after-pulsing, affecting timing resolution and signal clarity; quantum efficiency, which measures photocathode effectiveness; and gain, the degree of signal amplification. Each of these attributes plays a critical role in the functioning of PMTs, influencing their performance in a myriad of applications, from the detection of scintillation photons in high-energy physics experiments to the precise imaging required in nuclear medicine. Understanding these characteristics is essential for optimizing PMT operation and leveraging their capabilities to meet the demands of advanced scientific research and technological development.

- **Sensitivity**

The sensitivity of a PMT encompasses both the cathode and anode's responsiveness to light. For the cathode, it refers to the efficiency of converting photons to photoelectrons under standard lighting conditions, which is crucial in determining the lower limit of light detection capabilities. The anode sensitivity, on the other hand, indicates the output current generated in response to the light detected by the photocathode. This characteristic is key to assessing the PMT's amplification process and its ability to produce a measurable signal, even from low-light environments.

- **Time Response**

The time response of a PMT is a composite characteristic that includes the anode pulse rise time and the transit time spread (FWHM). The rise time is essential for understanding how swiftly the PMT can respond to incoming light, an important factor for applications requiring rapid signal detection. The transit time spread is equally critical as it signifies the uniformity of the photoelectron transit duration within the PMT, affecting the device's resolution and the precision of timing measurements.

- **Pulse Linearity**

Pulse linearity is the characteristic that describes how accurately the PMT's output signal reflects changes in light intensity. It ensures that the PMT provides a linear output over a wide range of light inputs, without saturation or signal distortion. Maintaining linearity is fundamental for quantitative measurements, as it allows for a direct correlation between the detected light and the output signal, facilitating the accurate interpretation of the PMT's readings across varying levels of light intensities.

- **Dark current**

Dark current is the current that flows through the PMT even in the absence of incident light. It originates from thermal electrons emitted from the photocathode and dynodes and from ionized residual gases within the tube, leading to noise that can affect the signal-to-noise ratio of the PMT. Reducing dark current is crucial for improving the PMT's performance, especially in applications requiring the detection of very low light levels. Various strategies, such as cooling the PMT, selecting materials with lower thermal electron emission for the photocathode and dynodes, and maintaining a high vacuum within the tube, are employed to minimize dark current.

- **After-pulsing**

After-pulsing is a phenomenon in PMTs where delayed secondary pulses follow the primary signal. These pulses are caused by ions produced in the multiplication process that travel back to the photocathode and release additional photoelectrons after a certain delay. After-pulsing can significantly affect the timing resolution and signal clarity of a PMT. To mitigate this, PMTs can be designed with ion barriers or focusing structures that minimize the likelihood of ions reaching the photocathode, or by using materials for dynodes that have lower ionization potentials.

- **Quantum efficiency**

Quantum efficiency (QE) is a critical parameter that quantifies the effectiveness of a photocathode in converting incident photons into photoelectrons. It is defined as the ratio of the number of photoelectrons emitted to the number of incident photons. High QE is advantageous as it results in more signal from the same amount of light, which is particularly important in low-light conditions like those encountered in LXe detectors. The QE depends on the photocathode material and its response to the specific wavelengths of the incident light. In the case of VUV scintillation light from LXe, materials with high QE at these wavelengths, such as bialkali photocathodes, are selected to maximize the PMT's sensitivity.

- **Gain**

Gain, denoted as G, is a fundamental parameter of PMTs that measures the degree of amplification of the photoelectron signal. The gain is the factor by which the number of photoelectrons produced at the photocathode is multiplied by the time they reach the anode. It is determined by the voltage applied to the PMT and the efficiency of the dynode chain at converting and multiplying electrons. High gain is essential for detecting low levels of light, as it ensures that the signal from the photocathode is amplified sufficiently to be detectable above the noise level. PMT gain is subject to fluctuations due to changes in temperature, voltage supply, and the aging of the tube, and therefore must be carefully calibrated to ensure accurate measurements. The gain of PMTs is expressed as[193]:

$$G = (a \times E^{k})^{n} \tag{4.1}$$

Here, a is a constant, k is a factor of structure and material of the dynode, E is the interstage voltage of dynodes and n is dynode stage. The next section, 4.2.5, will delve into the specifics of PMT gain calibration, detailing the procedures and considerations necessary to maintain the reliability and accuracy of PMT measurements in LXe-based detectors. This involves a series of steps including setting up a controlled light source, measuring the PMT response, and adjusting the PMT voltage to achieve the desired gain. The calibration ensures that the PMT performs optimally, with stable gain over time, which is essential for experiments requiring high sensitivity and precision.

4.2.3 The PMTs of XEMIS2 and future prospects

The selection and performance of Photomultiplier Tubes (PMTs) play a critical role in the success of the XEMIS2 project, a cutting-edge experiment designed to advance our understanding of xenon scintillation photon detection. The XEMIS2, as a continuation and enhancement of its predecessor XEMIS1, relies on highly specialized PMTs that are optimized for sensitivity to the Vacuum Ultraviolet (VUV) spectrum, crucial for capturing the 178 nm wavelength photons characteristic of xenon scintillation. This section delves into the specific PMTs employed in the XEMIS2 system—particularly the Hamamatsu R7600-06MOD-ASSY and the Hamamatsu R12699-406-M4 PMTs—highlighting their unique features, performance metrics, and how they align with the project's stringent requirements for high sensitivity, low background noise, and precise timing resolution. As the XEMIS2 project looks toward the future, the potential for further advancements and the adoption of new PMT technologies that promise even greater efficiency and accuracy in photon detection will be explored, underscoring the continuous evolution and innovation within the field of photomultiplier technology.

4.2.3.1 Hamamatsu R7600-06MOD-ASSY PMT

The Hamamatsu R7600-06MOD-ASSY PMT is suitable for the XEMIS1 and XEMIS2 systems, with capabilities suited to the precise demands of LXe scintillation photon detection. Its design is particularly sensitive to the VUV spectrum, crucial for detecting the 178 nm wavelength photons characteristic of xenon scintillation.

The photomultiplier tube (PMT) features a streamlined, square design with a 1-inch head-on type profile, specifically crafted to enable full submersion in liquid xenon (LXe). This design

is critical for enhanced efficiency in detection, as it ensures both stable operational conditions and proximity to the scintillation events for optimal photon capture. It boasts a transverse surface area of 25.7 mm by 25.7 mm, which is sufficiently large to gather scintillation photons effectively. The PMT utilizes a slice glass light entrance window of 24 mm by 24 mm, chosen for its VUV light transparency and its ability to withstand the high-pressure environment typical in LXe detectors. Within this PMT, a photocathode is positioned on the interior side of this window, facing the vacuum, which covers a minimum active area of 18 mm by 18 mm. The window's refractive index, at 1.6, is ideally matched to the optical characteristics of LXe, ensuring minimal photon loss through attenuation.

The photocathode of the Hamamatsu R7600-06MOD-ASSY PMT is composed of bialkali material, known for its high quantum efficiency at a wavelength of 175 nm. Despite the bialkali's inherent high electrical resistivity, which can increase at lower temperatures leading to potential saturation, the PMT addresses this by including conductive metal strips beneath the quartz window. These strips compensate for changes in resistivity, allowing the PMT to resist higher irradiances at LXe temperatures without a loss in sensitivity. A 10-stage dynode structure amplifies the photoelectron signal within a compact axial length of 21.25 mm, thanks to the metal channel design. This PMT can operate across a wide temperature range, which is from -110 ℃ to 50 ℃, making it suitable for the controlled environment of XEMIS2, where it operates at 168 K (-105 ℃) under a pressure of 1.2 bar abs. Voltage dividers and other circuit elements are carefully chosen to ensure reliability at LXe temperatures.

At the critical wavelength of 175 nm, pertinent to the VUV scintillation of liquid xenon, the PMT showcases an impressive quantum efficiency of 30%, highlighting its capability to efficiently convert incident photons into photoelectrons. Anode sensitivity mirrors this high standard, registering at 100 A per lumen, indicating robust signal amplification capabilities. In terms of reliability post-dormancy, the PMT maintains a low anode dark current between 2 to 20 nA after being in darkness for 30 minutes, a feature that underscores its precision in low-light conditions by minimizing background noise. The time response of this PMT is characterized by a swift anode pulse rise time of 1.4 ns, coupled with a transit time spread (FWHM) of just 0.35 ns, parameters that together ensure rapid and consistent signal processing. Furthermore, it maintains pulse linearity within ±2% deviation up to 30 mA,

demonstrating its ability to deliver accurate measurements across a range of light intensities. These characteristics are summarized in Table 4.1.

Table 4.1: Comparison of R7600-06MOD-ASSY PMT[194,195] and R12699-406-M4 PMT Features[193].

Feature	R7600-06MOD-ASSY PMT	R12699-406-M4 PMT
Design Type	metal channel type, square head-on, multi-anode	metal channel type, square head-on, multi-anode
Spectral Response	160 to 650 nm	160 to 650 nm
Photocathode Material	Bialkali	Bialkali
Quantum Efficiency at 175 nm	30%	30%
Dimensional outline	25.7 mm × 25.7 mm	56 mm × 56 mm
Effective Area	18 mm × 18 mm	48.5 mm × 48.5 mm
Packing density	49%	75%
Window Material	Silica glass	Silica glass
Window Thickness	1.2 mm	2.5 mm
Temperature Range	-110 ℃ to +50 ℃	-110 ℃ to +50 ℃
Gain	10^5 - 10^6	10^5 - 10^6
Anode Dark Current	2 nA per channel	1.5 nA per channel
Time Response	Anode pulse rise time of 1.4 ns	Anode pulse rise time of 1.2 ns
Transit Time Spread (FWHM)	0.35 ns	0.9 ns
Pulse Linearity Within ±2% deviation	30 mA	8 mA
Applications	Suited for XEMIS, optimized for LXe scintillation photon detection	Broad applications including dark matter detection, XEMIS

4.2.3.2 Hamamatsu R12699-406-M4 PMT

The Hamamatsu R12699-406-M4 is a flat panel type multi-anode photomultiplier tube designed for sensitive light detection across a wide spectral response range from 160 to 650 nm, with peak sensitivity at 400 nm. This device is particularly well-suited for low temperature operation, with an operating temperature range down to -110°C, making it ideal for applications such as academic research in dark matter detection and nuclear medicine equipment like PET scanners and XEMIS. These characteristics are also summarized in Table 4.1.

One of the standout features of this PMT is its large effective area of 48.5 mm by 48.5 mm, which allows for a significant capture volume for incident photons. This is complemented by a pixel size of 24.25 mm by 24.25 mm per anode, providing high resolution in the detection pattern. Additionally, the PMT boasts low radioactivity, ensuring minimal background noise in sensitive experiments. In terms of construction, the R12699-406-M4 uses a bialkali photocathode material known for its high quantum efficiency, particularly at the VUV wavelength of 175 nm, where it achieves approximately 30% efficiency. The window material is made of silica glass, with a thickness of 2.5 mm, offering both durability and excellent transmission of light to the photocathode. The PMT employs a metal channel dynode structure, which is highly effective for electron multiplication, resulting in a gain of 1.5×10^6. This high gain allows for the detection of even the weakest light signals. Each of the four anodes has a minimal dark current of just 1.5 nA, which contributes to the PMT's high signal-to-noise ratio. The time response characteristics of the R12699-406-M4 are fast, with an anode pulse rise time of just 1.2 ns and a transit time spread (FWHM) of 0.9 ns, ensuring precise timing in applications where timing resolution is critical. Pulse linearity is maintained within ±2% deviation, and the uniformity ratio between anodes is carefully controlled to ensure consistent response across the PMT's surface.

The device's maximum ratings allow for a supply voltage of up to 1100 V and an average anode output current in total of 0.1 mA. With its robust design and precise performance

metrics, the Hamamatsu R12699-406-M4 is well-positioned as a highly reliable and efficient solution for advanced photodetection needs.

4.3 In-depth analysis of scintillation detection calibration

An exhaustive calibration methodology has been meticulously devised to ensure the precise calibration of the scintillation light detection and measurement system. This multifaceted approach comprises five integral phases:

1. Initial Threshold Calibration: The establishment of initial threshold levels.
2. Unit Conversion: The conversion of threshold units from Least Significant Bit (LSB) to charge (e-).
3. Photoelectron Approximation: Estimating the approximate number of photoelectrons.
4. Time Measurement Correction: This phase includes time walk correction to enhance the precision of time measurements.
5. PMT Gain Calibration: A meticulous calibration of the PMT gain.

Collectively, these phases form a comprehensive framework, ensuring the utmost accuracy and reliability of the scintillation light measurement system.

4.3.1 Threshold calibration

As explained upon in Section 4.1, XEMIS2 employs the LETD method, also referred to as the TOT (Time Over Threshold) method, for light detection. The meticulous selection of an appropriate threshold is of paramount importance to ensure the optimal performance of the detection chain. This is due to the fact that noise not only exerts a discernible impact on both time and amplitude resolutions but also dictates the minimum detectable signal threshold. To strike a delicate balance, the discriminator threshold should ideally be configured to the lowest feasible value to guarantee superior resolution and maximize detection efficiency. Nonetheless, this setting must also be harmonized with an acceptable noise rate. Elevated background rates not only engender a substantial surge in the volume of readout data but can also markedly compromise the quality of the acquired data and exacerbate dead times.

In scenarios where the temporal gap between two consecutive triggers falls below the time required by the electronics to process the information from the preceding signal, the second pulse may be disregarded. This could potentially lead to the forfeiture of crucial information

stemming from a genuine interaction and the inadvertent inclusion of additional noise events. Consequently, the overarching objective of this section is to ascertain the optimal threshold level through a systematic assessment of electronic noise rates at varying discriminator threshold settings.

4.3.1.1 Method for approximating noise count rate calculation

Given the amplitude distribution of noise adheres to a Gaussian distribution, characterized by its standard deviation σ_{noise}, the dependency of the noise counting rate (f) on the applied threshold level (V_{th}) can be estimated through the utilization of Rice's formula[196]:

$$f = f_0 \times e^{\frac{-V_{th}{}^2}{2\times\sigma_{noise}{}^2}} \tag{4.2}$$

In this equation, f represents the noise count rate, Vth signifies the threshold level, and f_0 designates the noise frequency corresponding to a threshold setting of 0, whose is contingent upon the timing characteristics inherent to the electronics. Specifically, for a fast amplifier with a peaking time of τ_0, we have the approximate values of f_0 as follows:

$$f_0 = \frac{1}{2\times\tau_0} = \frac{1}{100ns} = 10^4\text{kHz} \tag{4.3}$$

At extremely low threshold levels, the noise counting rate escalates to an unacceptably high frequency, reaching around 10^4 kHz. This results in the registration of a considerable number of noise events and a substantial increase in system dead time. To achieve a harmonious equilibrium between sensitivity and noise mitigation, a minimum acceptable threshold level is established, slightly exceeding four times the noise level.

Supposed that the threshold level is equal to 4 times of the noise level :

$$V_{th} = 4\sigma_{noise}$$

$$f = f_0 \times e^{\frac{-V_{th}^2}{2\times\sigma_{noise}^2}} = 10^4\text{kHz} \times 3.4 \times 10^{-4} = 3.4\text{kHz} \quad (4.4)$$

For a threshold level slightly exceeding four times the noise level, which can translate to a noise rate of approximately 1000 triggers per second, a compromise that proves suitable. It allows for the capture of nearly all physical signals, even those with low amplitudes, without overwhelming or saturating the readout electronics.

4.3.1.2 Experimental setup

The objective of threshold calibration is to determine the specific threshold level that corresponds to a detection rate of 1000 triggers per second for each PMT channel within the defined experimental setup. In this configuration, a voltage of 50 V is supplied to the PMT and the output signal of PMT is served as the input signal for the XSRETOT, as depicted in Figure 4.8. Data acquisition is conducted using the Spartan card, systematically varying the threshold levels to analyze the resulting trigger rates.

In the context of threshold configuration for input channels, a comprehensive procedure is followed to ensure precise adjustments. This process initiates with the careful selection of the relevant channel by directing the Inter-Integrated Circuit (I2C) bus accordingly. Subsequently, a dual-channel digital potentiometer with an 8-bit resolution is meticulously fine-tuned. Each channel undergoes this configuration individually, with specific settings governed by the manipulation of registers within the I2C bus.

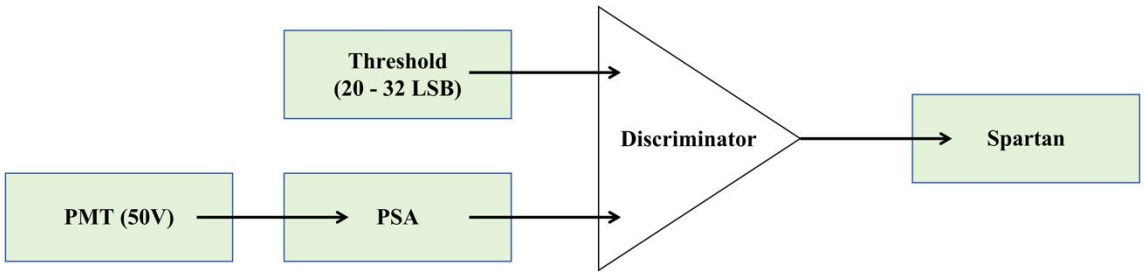

Fig. 4.8: Simplified schematic of experimental setup for threshold calibration.

The unit of LSB, as shown in Figure 4.8, representing "Least Significant Bit" which emerges as a key element in the intricacies of threshold configuration, significantly impacting the sensitivity of the detection system. This significance is rooted in the architecture of the 8-bit digital potentiometer, composed of 8 binary bits that collectively represent various threshold levels. Within this binary representation, the LSB holds particular importance as it signifies the smallest and most minute unit of change achievable in the threshold setting. In many cases, when dealing with an 8-bit digital potentiometer, the LSB translates to 1/256th of the complete threshold range, equating to approximately 0.4% of the total range. However, in the context of XEMIS2, an observed non-linear relationship exists between the small value of threshold and alterations in the digital value. Consequently, the necessity arises for a meticulously designed calibration process tailored to precisely convert digital values (LSB) into their respective charge equivalents. This pivotal calibration procedure is comprehensively expounded upon in Section 4.3.2.

4.3.1.3 Calibration results

The noise count rate in the PMT channels exhibits an exponential decline as the threshold level is increased, as shown in Figure 4.9, aligning with the fundamental principles elucidated in Rice's formula. Furthermore, due to the distinctive characteristics inherent to the electronic components, subtle variations in the threshold values are discernible across the different channels. Nevertheless, on average, the threshold value consistently approximates 24 to 26 LSB shown in Figure 4.9. Comprehensive threshold data for all 64 PMT channels is available in Table 4.2.

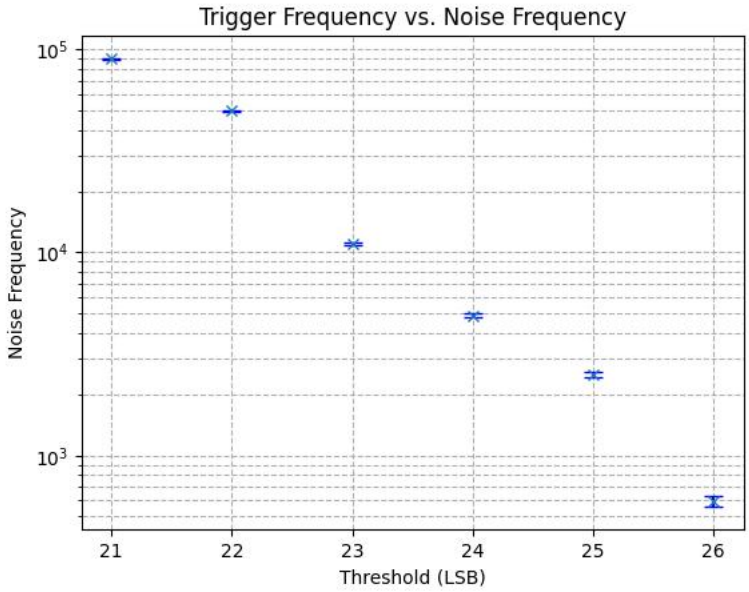

Fig. 4.9: Trigger frequency for PMT channel 0 on a logarithmic scale as a function of threshold in LSB.

Table 4.2. Comprehensive threshold data for all 64 PMT channels

Channel	Threshold (LSB)	Trigger (cps/s)	Channel	Threshold (LSB)	Trigger (cps/s)
0	26	595	32	26	825
1	26	771	33	26	951
2	25	1417	34	27	637
3	25	1165	35	27	533
4	25	1257	36	27	585
5	25	866	37	25	1337
6	26	601	38	25	1342
7	26	759	39	26	605
8	25	656	40	26	597
9	26	968	41	26	855
10	25	1317	42	27	573
11	25	942	43	26	1166
12	25	1006	44	26	659
13	25	1059	45	25	1637
14	25	1503	46	26	1350

15	26	975	47	26	809
16	26	512	48	25	1070
17	25	1290	49	26	553
18	26	648	50	25	1680
19	26	844	51	25	1106
20	26	1036	52	26	517
21	25	1515	53	25	1628
22	27	574	54	26	1133
23	26	656	55	26	647
24	26	581	56	26	760
25	26	568	57	24	1656
26	25	1799	58	25	987
27	24	1051	59	25	504
28	25	1192	60	26	730
29	25	1293	61	25	1555
30	26	654	62	26	946
31	25	650	63	25	1359

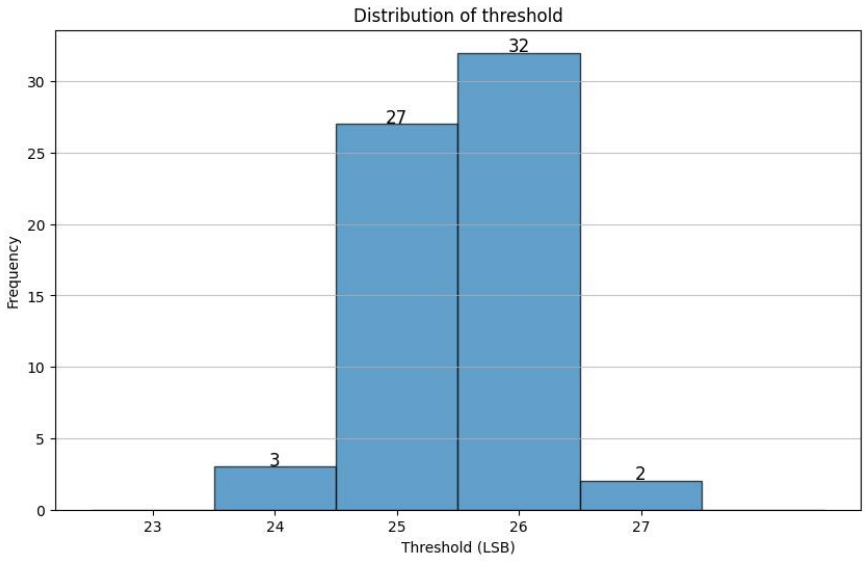

Fig. 4.10: Distribution of threshold for the 64 PMTs channels.

4.3.1.4 Discussion and Conclusion

The comprehensive examination and calibration of threshold levels within the XEMIS2 experiment have yielded critical insights into optimizing the detection efficiency and resolution of the PMT channels employed. Through the meticulous calibration process, an

optimal threshold range of 24 to 27 LSB has been established across the PMT channels, striking a delicate balance between minimizing noise and maximizing signal detection. This calibration effort underscores the intricate relationship between threshold settings, noise count rates, and the overall performance of the PMT detection system.

One significant observation from this calibration exercise is the exponential decrease in noise count rate with increasing threshold levels, consistent with the theoretical expectations outlined by Rice's formula. This finding validates the approach taken in threshold calibration, reinforcing the importance of careful threshold selection to achieve an optimal balance between signal sensitivity and noise reduction. The variations in threshold values across different channels highlight the inherent differences in the electronic components and necessitate a channel-specific approach to calibration to ensure uniform performance across the detector array.

The choice of a threshold level slightly above four times the noise level, resulting in a noise rate of approximately 1000 triggers per second, demonstrates a practical compromise. It effectively reduces background noise while retaining the sensitivity required to detect low-amplitude signals. This approach minimizes the risk of saturating the readout electronics and ensures the capture of meaningful physical interactions without excessive noise.

The experimental setup and calibration process also reveal the non-linear relationship between small threshold values and digital adjustments, necessitating a precise calibration method to convert digital values into charge equivalents accurately. This precision is crucial for maintaining the sensitivity and accuracy of the PMT channels in detecting scintillation photons, especially in complex experimental setups like XEMIS2.

4.3.2 Threshold unit conversion

Our primary objective is the determination of the threshold value in terms of electrons, rather than relying on LSB units. Therefore, the second phase of the calibration process is centered on the conversion of threshold units from Least Significant Byte (LSB) to voltage or charge units, a critical step in achieving accurate and precise calibration for our scintillation light detection and measurement system.

4.3.2.1 S-Curve Fit Method

The S-curve fit method assumes a pivotal role in calibrating the discriminator threshold. Its primary function is to ascertain the detection efficiency of XSRETOT, which denotes the ratio between the number of detected events and the total number of injected events. This efficiency parameter hinges on the input signal's amplitude within the LETD module and the specific threshold level employed.

For a given threshold level, considering that the electronic noise of the PSA signals follows a Gaussian distribution, the relationship between detection efficiency and input signal amplitude follows the pattern of a Gaussian error function.

$$S(x) = a \times \left[1 + \mathrm{erf}\left(\frac{x-b}{\sqrt{2}c}\right)\right],$$
$$\mathrm{erf}(x) = \frac{2}{\sqrt{\pi}}\int_0^x e^{-t^2}dt \tag{4.5}$$

Where, parameter 'a' represents the efficiency that corresponds to the prescribed level of applied tension. It is set to a default value of 50 % to ensure a maximal efficiency of 1; Parameter 'b' denotes the desired tension value at which the S-Curve fit function attains 50% of its peak magnitude. The default value of 'b' is determined dynamically and encompasses the entire spectrum of achievable tension values; Parameter 'c' characterizes the RMS of the noise distribution in the output signal of the LETD. This noise distribution arises from the convolution of the input signal noise with the electronic noise inherent to the discriminator. Figure 11 shows an illustrative example of the error function and S-curve.

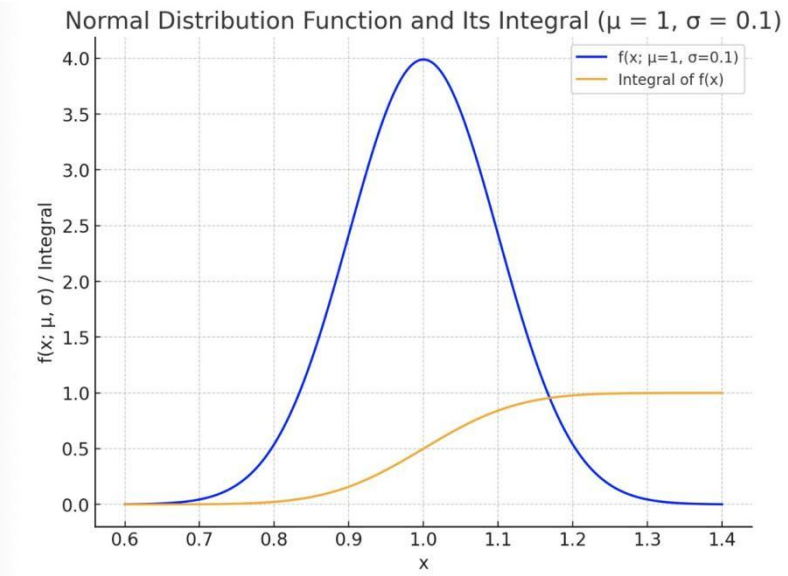

Fig. 4.11: An illustrative example of the error function and S-curve (parameters: a = 0.5, b (μ) = 1, c (σ) = 0.1).

A crucial insight is that the detection efficiency attains the 50% threshold precisely when the input signal's amplitude aligns with the threshold value. To provide further clarity, refer to Figure 4.12, where, at the point where the input signal's amplitude matches the threshold level, the presence of noise results in a 50% probability that the input signal will exceed the threshold. This phenomenon underscores that reaching a detection efficiency of 50% signifies a harmonious equilibrium between the input signal's amplitude and the threshold value.

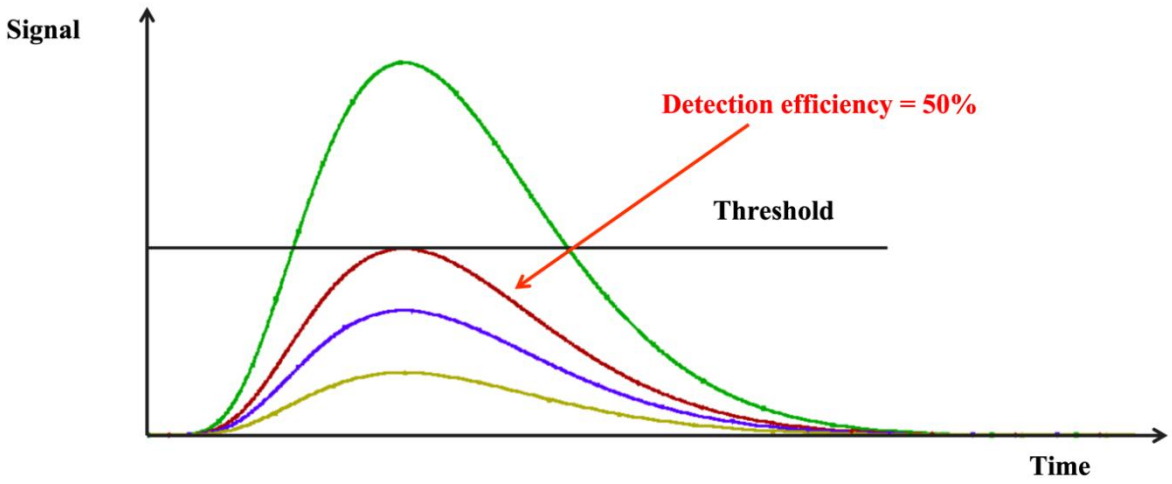

Fig. 4.12 Illustrative an example of signal

To construct the thresholds S-curve, a sequence of square wave signals with varying amplitudes from 1 mV to 50 mV is directed to the injection capacitor, characterized by a capacitance of 2.2 pF. Consequently, distinct charge quantities are injected into XSRETOT. For each injected voltage, a consistent injection event of 12000 is maintained. The Spartan card records the detected events in binary files. Analysis of these binary files yields the detected events, enabling the calculation of detection efficiency for each injected voltage. Subsequently, the S-Curve fit method is employed to analyze the detection efficiency data plotted against the injected voltage. This analytical approach provides precise insights into the conversion of digital values (LSB) into their respective charge equivalents, offering valuable information for system performance evaluation and calibration refinement. The results will be presented in the follwing section.

4.3.2.2 Optimizing noise strategies – Time windowing approach

As previously mentioned, the PMT channel 15 serves as our reference channel. Within this channel, a high threshold configuration has been applied to effectively mitigate all sources of noise interference. Furthermore, this channel has been subject to injection with a meticulously crafted simulated PMT response of significant amplitude. Consequently, this reference channel is dedicated solely to capturing physical events, acting as a temporal window through which we explore the behavior of PMT channel 0 as an representative example.

In the course of our study, we methodically introduced six distinct voltage levels (10 mV, 30 mV, 50 mV, 500 mV, 1000 mV and 4000 mV) into channel 0. Our primary objective was to identify an optimal time window that not only minimizes the impact of noise but also preserves all physical events. These voltage levels represent diverse signal scenarios: 10mV signifies signals falling below the detection threshold, 30mV corresponds to signals in close proximity to the threshold, 50mV denotes signals exceeding the threshold, while 500 mV, 1000 mV and 4000 mV represent the signals substantially surpassing the threshold.

Figure 4.13 serves as a visual representation of the temporal disparities between the two channels. For each trigger event recorded in the reference channel (about 12000 events), a meticulous process of identifying the nearest corresponding event in the test channel (channel 0) was undertaken, followed by precise calculation of the time difference. Subsequently,

histogram analysis was performed to provide a comprehensive visualization and quantitative assessment of these temporal differences.

In the case of small signals falling below the detection threshold, the temporal differences exhibit a Gaussian-like distribution. This distribution arises because, in such instances, there are almost no triggering events in the test channel capable of surpassing the threshold. Instead, the recorded events in the Spartan card predominantly consist of spurious noise-induced triggers.

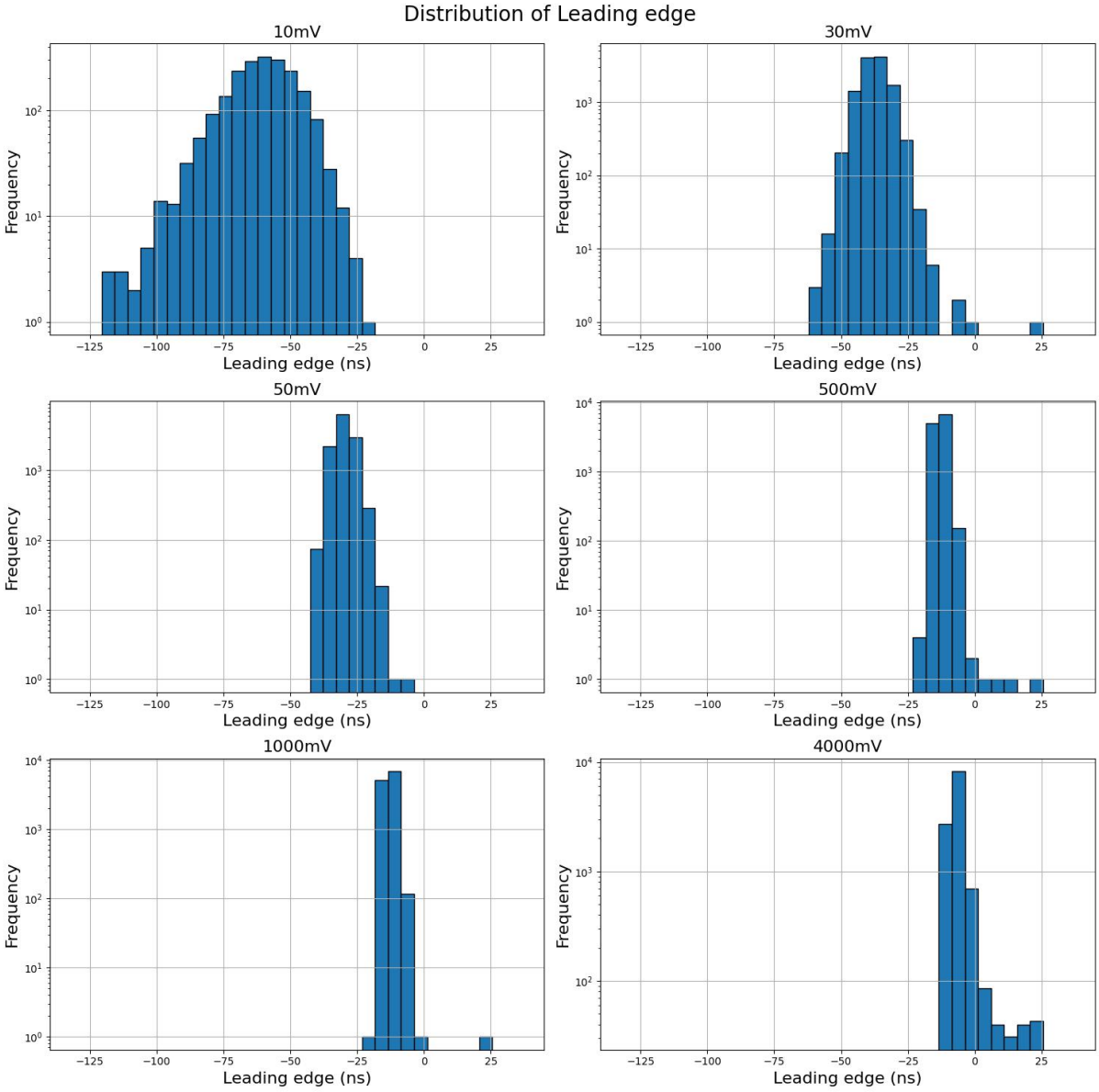

Fig. 4.13: Temporal Discrepancies Across Channels 15 and 0 (Voltage Settings for Channel 0: 10 mV, 30 mV, 50 mV, 500 mV, 1000 mV, 4000 mV - Corresponding electrons: 137,500; 412,500; 687,500; 6,875,000; 13,750,000; 55,000,000).

Conversely, for high-amplitude signals significantly surpassing the threshold, the temporal differences consistently cluster within a defined interval. This behavior emerges due to the achievement of a 100% detection efficiency, indicating that for every trigger event recorded in the reference channel, a corresponding trigger event is reliably observed in the test channel. In this context, we can establish a suitable time window length, for instance [-125 ns, 25 ns] effectively encompassing nearly all genuine physical triggers.

Furthermore, upon careful examination of the histograms depicted in Figure 4.13, we can readily identify the presence of a time walk effect. In the case of signals with the small charge like 10 mV, a noticeable time difference is concentrated around -75 ns for the mean. Conversely, for signals subjected to a substantial charge injection, a mean time difference of approximately -5 ns is observed for 4V. We will delve deeper into the discussion of this effect in Section 4.3.4.

4.3.2.3 Experimental setup

The experimental configuration, as depicted in Figure 4.14, involves the deliberate disconnection of all Photomultiplier Tubes (PMTs). Subsequently, a Function Generator (GBF) assumes the role of the PMT output and functions as the primary injection source. Initially, PMT channel 0 is configured with a threshold of 26 LSB, corresponding to a trigger rate of 1000 triggers per second, while PMT channel 15 is configured with a higher threshold of 50 LSB, effectively minimizing noise interference in this specific channel. All other channels are intentionally deactivated, with channel 0 singled out for meticulous examination, while channel 15 serves as a reference channel. Furthermore, the injection voltage applied to PMT channel 0 is systematically adjusted within a range of 1mV to 100mV, accounting for an electrical capacitance of 2.2 pF. PMT channel 15 is subjected to synchronous injection of the GBF and is passed through a custom-made circuit to replicate a high response characteristic similar to that of a PMT. The resulting trigger counts, generated through these carefully controlled adjustments, are diligently documented by Spartan card. Subsequently, these recorded counts are employed with precision in the calculation of detection efficiency.

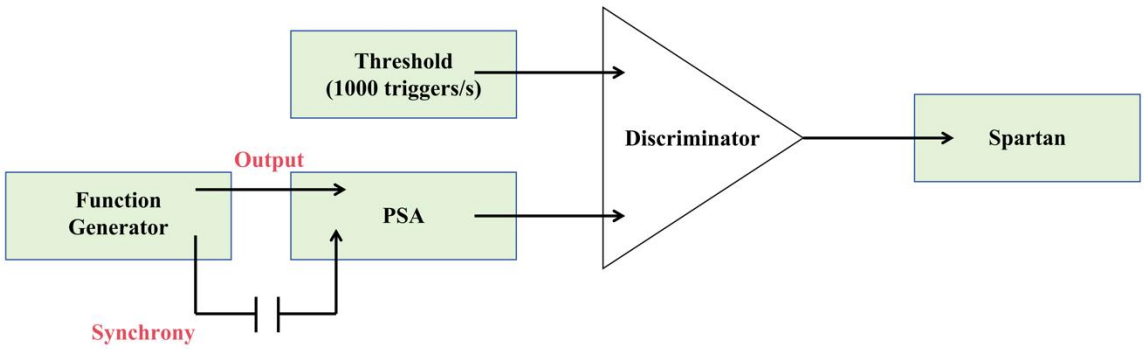

Fig. 4.14: Simplified schematic of experimental setup for threshold unit conversion.

The experimental configuration described here closely parallels the setup employed for TOT calibration, as elucidated in Section 4.3.3, and for time measurement optimization, which will be discussed in Section 4.3.4.

4.3.2.4 Threshold unit conversion results

In this section, we present the threshold unit conversion results. As previously discussed, parameter 'a' represents the efficiency corresponding to the specified applied tension level. It is initially set to a default value of 50% to ensure a maximum efficiency of 100%.

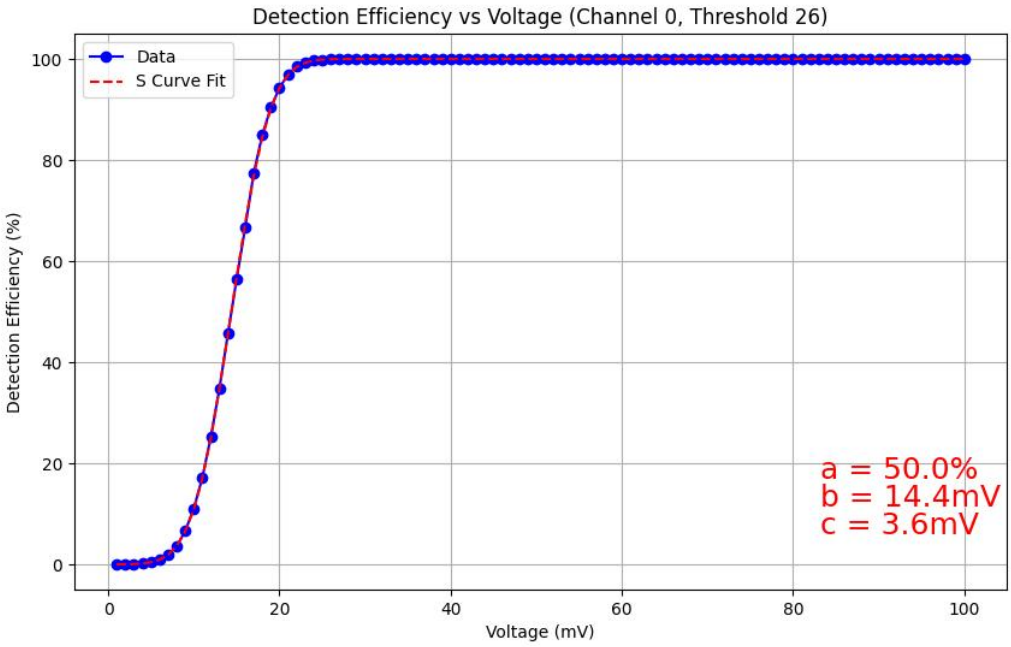

Fig. 4.15: S-curve for PMT channel 0.

From Figure 4.15, we indeed observe that it closely approximates 50%. Parameter 'b' signifies the target tension value at which the S-Curve fit function reaches 50% of its peak amplitude. For this particular channel, we determined a tension value of 14.4 mV to achieve a 50% detection efficiency. Lastly, parameter 'c' characterizes the Root Mean Square (RMS) of the noise distribution present in the output signal of the LETD, which we determined to be 3.6 mV. These findings provide valuable insights into the system's performance and calibration characteristics.

With a capacitance of 2.2 pF, we conducted calculations, and the results are as follows:

$$Q = C \times V = 2.2\,pF \times 14.4\,mV = 31.7\,fC = 198000\,electrons$$
$$Q_{RMS} = C \times V_{RMS} = 2.2\,pF \times 3.6\,mV = 7.7\,fC = 49500\,electrons \quad (4.6)$$

At a threshold setting of 26 LSB for channel 0, we determined an equivalent charge of 198000 electrons, with a noise level of 49500 electrons. We can deduce that the threshold is about 4 times of the noise level.

Figure 4.16 illustrates the threshold and noise distribution for the 64 channels. In Figure 4.16(a), the distribution of threshold levels is presented, revealing a range primarily clustered between 160,000 and 220,000 electrons, with a peak frequency occurring just above 190,000 electrons. Figure 4.16(b) displays the distribution of noise levels across the same channels. Here, the noise levels are mostly concentrated around the 40,000 to 60,000 electron mark. These two histograms can provide preliminary insights into the proper functioning of the 64 channels.

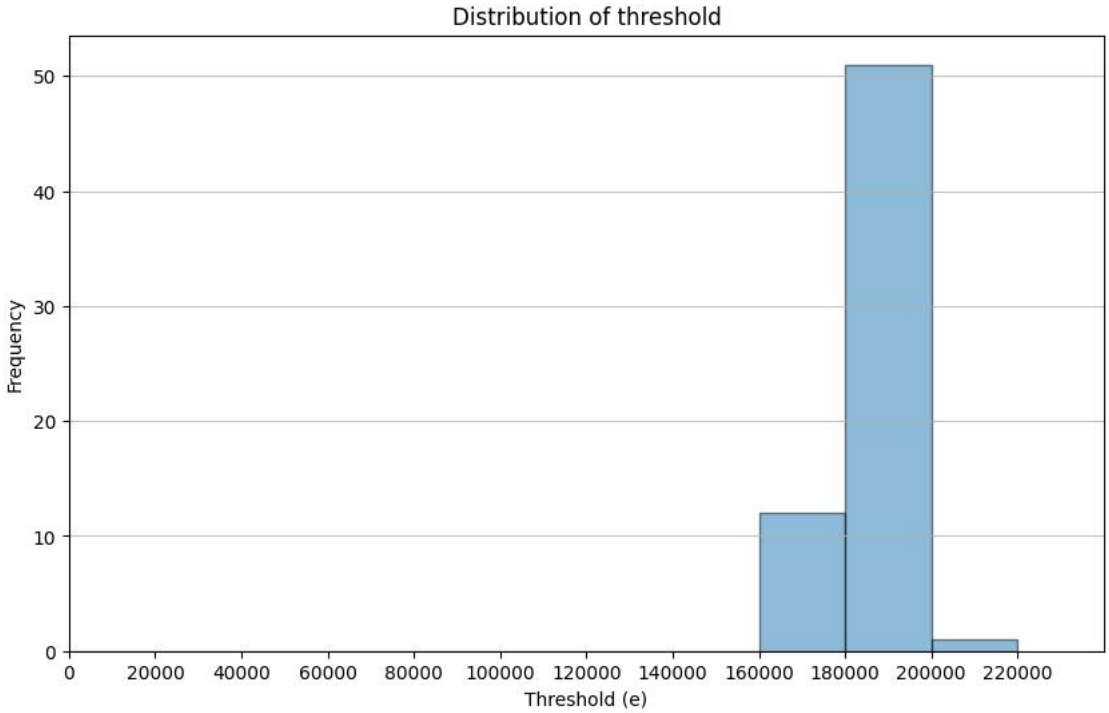

(a)

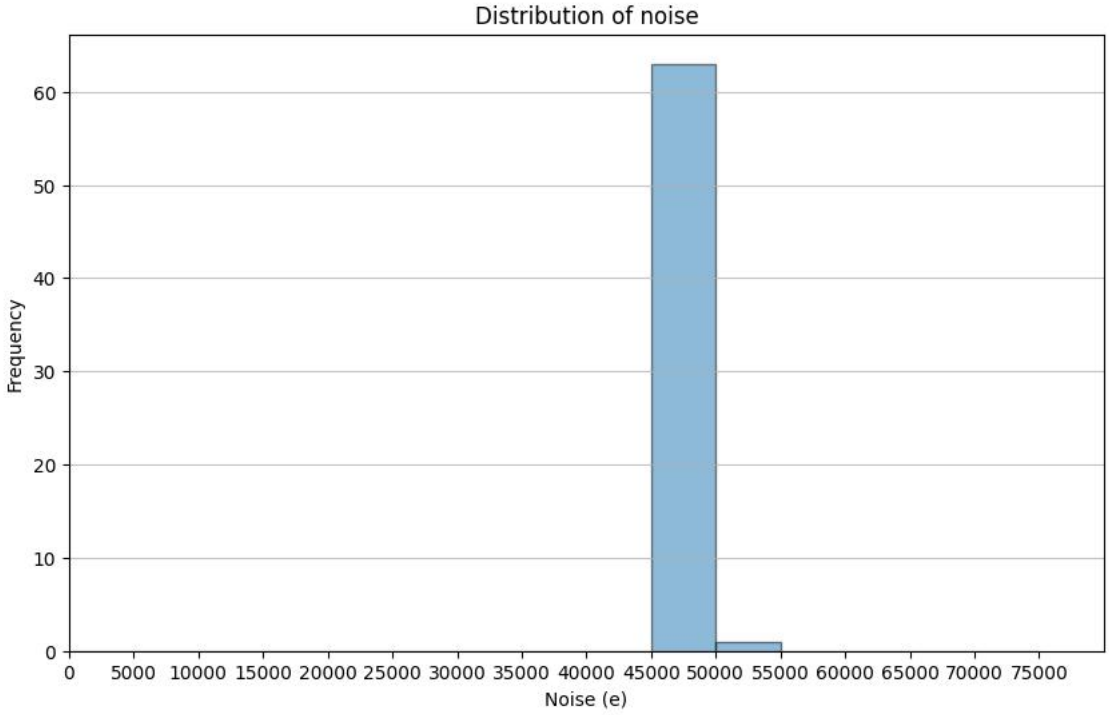

(b)

Fig. 4.16: (a) Distribution of threshold in electrons for 64 channels.

(b) Distribution of noise level in electrons for 64 channels.

Table 4.3 provides a comprehensive view of the threshold-to-charge conversion for all 64 channels. A close examination reveals that despite having the same threshold value in LSB, the resulting equivalent charge in electrons varies across channels. This variability signifies that the conversion relationship is not uniform but rather channel-specific, underscoring the necessity for individual calibration of each channel. Such calibration is critical to establish the precise relationship between the threshold and the equivalent charge for accurate and reliable measurements. The table also includes noise levels in electrons, further highlighting the distinct characteristics of each channel and the importance of tailored calibration to ensure optimal functionality of the PMT array.

Table 4.3: Threshold units conversion (64 PMTS)

Channel	Threshold (LSB)	Equivalent charge (e^-)	Noise (e^-)	Channel	Threshold (LSB)	Equivalent charge (e^-)	Noise (e^-)
0	26	198000	49500	32	26	188375	48125
1	26	189750	48125	33	26	189750	48125
2	25	181500	49500	34	27	196625	49500
3	25	182875	48125	35	27	181500	49500
4	25	189750	50875	36	27	187000	49500
5	25	185625	49500	37	25	182875	49500
6	26	199375	49500	38	25	177375	49500
7	26	196625	49500	39	26	193875	49500
8	25	189750	49500	40	26	198000	48125
9	26	191125	49500	41	26	189750	49500
10	25	182875	49500	42	27	199375	48125
11	25	188375	48125	43	26	184250	49500
12	25	184250	48125	44	26	196625	48125
13	25	187000	48125	45	25	178750	48125
14	25	191125	49500	46	26	195250	48125
15	26	182875	46750	47	26	191125	48125

16	26	178750	49500	48	25	178750	48125
17	25	184250	48125	49	26	192500	46750
18	26	189750	48125	50	25	174625	46750
19	26	187000	48125	51	25	184250	46750
20	26	182875	49500	52	26	195250	46750
21	25	180125	49500	53	25	177375	46750
22	27	187000	48125	54	26	178750	46750
23	26	192500	48125	55	26	184250	46750
24	26	195250	49500	56	26	193875	46750
25	26	141625	49500	57	24	171875	48125
26	25	178750	49500	58	25	181500	46750
27	24	185625	48125	59	25	170500	46750
28	25	180125	48125	60	26	185625	46750
29	25	181500	48125	61	25	173250	46750
30	26	200750	48125	62	26	196625	46750
31	25	184250	46750	63	25	178750	46750

4.3.2.5 Discussion and Conclusion

The threshold calibration and unit conversion process of the XEMIS2 project is a key way to improve the accuracy and efficiency of scintillation light detection. Through careful application of S-curve fitting methods and the use of noise optimisation strategies, we have succeeded in establishing a reliable framework for setting and interpreting discriminator thresholds in terms of units of charge rather than abstract LSB units. This shift helps to align the operational parameters of the detection system with the physical reality of the scintillation events it is intended to capture.

The experimental setup and methodology employed for the calibration emphasises the complexity and precision required to fine-tune the detection equipment. By converting the threshold units from LSB to charge, we not only enhanced the interpretability of the system's operating thresholds, but also significantly improved the sensitivity and specificity of detecting true scintillation events in noise. The calibration process shows that the optimal threshold setting balances sensitivity with noise mitigation in the range of about four times the noise level, i.e., the noise rate is within a manageable range and does not affect the detection of low-amplitude signals.

In addition, the experimental results emphasise the specificity of the whole PMT array, suggesting the need for channel-specific calibration to ensure consistent detection capability. Differences in the equivalent charge values for the same LSB threshold in different channels emphasise the impact of individual electronic properties and the importance of tailoring calibration procedures for each detector unit.

Overall, the calibration results show a relatively uniform distribution of threshold equivalent electron counts across the PMT array, indicating consistent sensitivity and noise levels across channels. Although there are individual variations that require calibration of specific channels, the overall trend indicates that the PMT maintains a uniform operating baseline. This consistency is critical to ensure that the entire detector array operates in concert, resulting in accurate and reliable measurements throughout the system. The consistency of the threshold settings corresponding to electron counts and noise levels suggests that with proper calibration, each PMT can be fine-tuned to meet the overall performance criteria of the system, thereby improving the accuracy and reliability of the XEMIS2 experiment.

4.3.3 TOT and number of photoelectron relation

In XEMIS2, our primary focus lies on extracting two critical pieces of information from the scintillation signal: the precise arrival times of photons and the quantity of photons arriving. These two pieces of data hold paramount significance as they serve as the foundation for image reconstruction processes.

In this section, our focus is on quantifying the number of arriving photons, and we present a dedicated calibration method designed for the conversion of TOT values into their corresponding count of detected photoelectrons. As previously mentioned, when photons interact with the PMT, they initiate the generation of an electronic signal at the PMT's output. The amplitude of this signal is directly proportional to the number of photons simultaneously reaching the PMT. By employing the Leading Edge Timing Discrimination (LETD) method, we establish a robust correlation between the signal's pulse height and TOT values. Consequently, TOT values serve as a dependable indicator of the quantity of photons incident on the PMT. Thus, the primary objective of this subsection is to elucidate the methodology utilized for converting TOT values into an accurate quantification of detected photons.

In the following section, we undertake an in-depth exploration of the experimental configuration, data processing procedures, and calibration outcomes, with a focus on a selected channel serving as an illustrative exemplar.

4.3.3.1 Data processing and calibration results

The experimental setup remains consistent with the one detailed in Section 4.2.2, as depicted in Figure 4.14. The sole modification is the adjustment of the injection charge, which has been increased from 1 mV to 4.6V for each tension step of 1 mV. In terms of data processing, a specific time window, spanning [-125 ns, 25ns] is applied to the raw data of the test channel to mitigate the occurrence of false triggers induced by noise. A Python-based code has been developed to verify that within each time window for the test channel, there are either 0 or 1 event detected, and no more than 2 events are detected in the time windows.

For each applied injection voltage, an approximate total of 12,000 events are recorded, resulting in a comprehensive dataset of 12,000 * 4600 events (1 mV to 4600 mV for tension step of 1 mV) for subsequent analysis. As established in Section 4.3.2, the defined threshold corresponds to 14.4 mV, equating to the charge equivalent of one photoelectron (p.e). By collecting the entirety of detected events, including their associated voltage and TOT values, and normalizing the voltage by the threshold, we derive critical insights into the relationship between TOT and the NPE (Number of Photonelectrons). This relationship represents the central objective of this section.

Figure 4.17 (a) provides a graphical representation that elucidates the correlation between TOT and the NPE for channel 0, while Figure 4.17(b) focuses on delineating the behavior of smaller NPE values derived from (a). It is observed that as TOT values increase, there is a correspondingly steep and accelerating increase in NPE, indicating a nonlinear relationship. Notably, beyond the threshold of 180 ns, the TOT-NPE curve assumes an exponential form, implying that small variations in TOT can lead to disproportionately large errors in the calculated NPE. This presents a significant challenge for accurate NPE quantification in high TOT regions. Conversely, at lower TOT levels, the NPE values are less sensitive to fluctuations in TOT, making it a more dependable measure for assessing the charge conveyed by Pulse Shape Analysis (PSA) signals. This dual behavior underscores the complexity of the

TOT-NPE relationship and the importance of careful calibration and analysis, especially in the high TOT regime.

An analogous conclusion is reached when reversing the perspective, treating NPE as the independent variable and TOT as the dependent variable (NPE as x and TOT as y). Here, we discern distinctive TOT patterns as NPE increases. TOT exhibits gradual growth with diminishing acceleration as NPE rises. When the PSA signal surpasses the preset threshold, TOT exhibits a noticeable upswing for lower NPE values. We define the effective conversion range of TOT as the NPE interval where substantial TOT variations occur. Within this range, TOT proves itself as a dependable indicator of the charge conveyed by PSA signals, facilitating precise charge measurements.

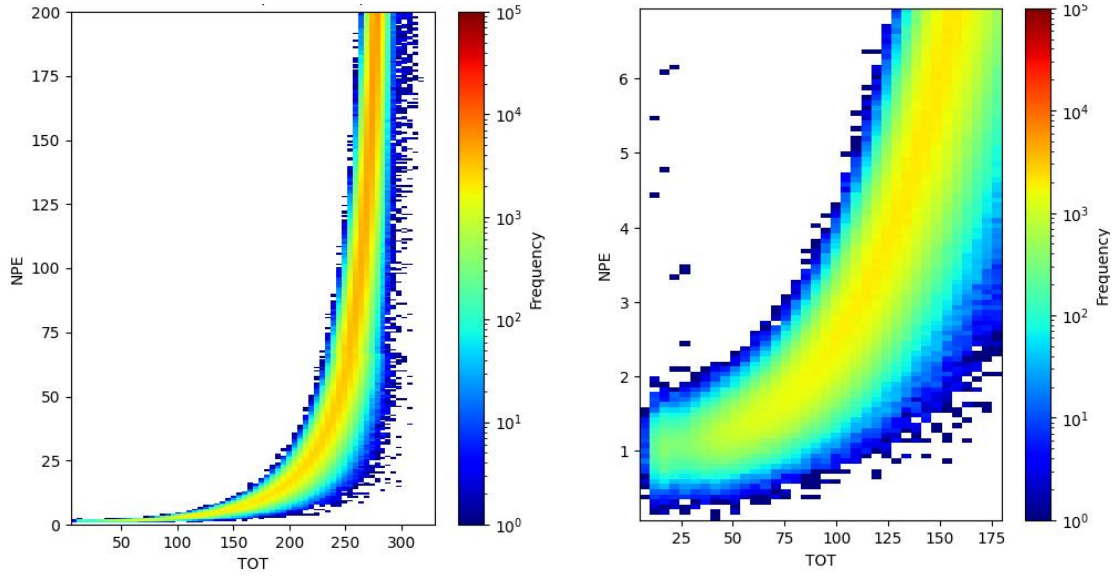

Fig. 4.17: (a) TOT-NPE events accumulation histogram for channel 0; (b) TOT-NPE events accumulation histogram for small NPE derived from (a).

Figure 4.18 presents the relationship between TOT and mean NPE for 64 individual channels, as evidenced by a series of scatter plots. Each channel is represented by a distinct color and symbol, and the data points for each channel form a curve that maps the increase in NPE with increasing TOT. The plots reveal a general trend where the NPE count remains low for smaller TOT values and begins to rise sharply as the TOT exceeds a certain value (about 180 ns), suggesting a nonlinear relationship. Remarkably, the consistency across the channels is evident, as most curves overlap or follow a similar trajectory, indicating homogenous

behavior in the conversion from TOT to NPE. This homogeneity is crucial for ensuring the reliability of the channels in detecting and quantifying the events, and suggests that the system is well-calibrated. The other figure will be provided in the annexes.

Capitalizing on this uniformity and homogeneity, I have conducted a comprehensive analysis to calculate the average response. This has culminated in the creation of a mean response curve, which is graphically represented in Figure 4.19. This mean curve embodies the collective behavior of the 64 channels, providing a centralized model of their performance and serving as a reference for expected outcomes under typical operating conditions.

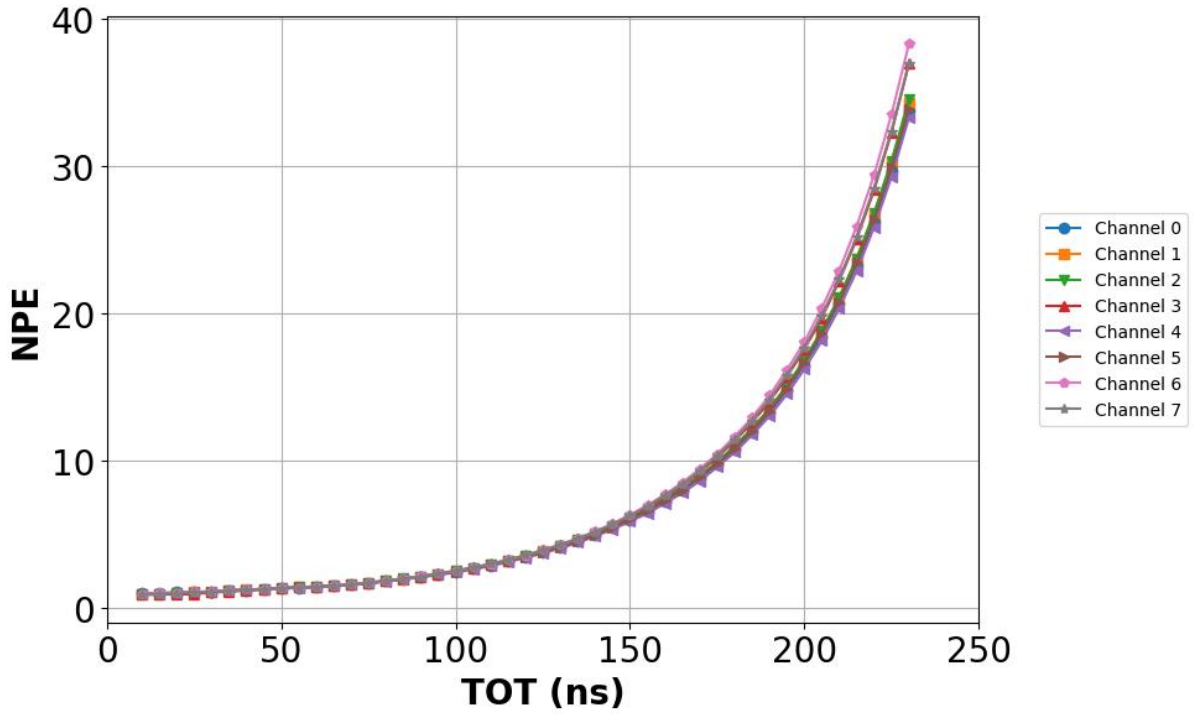

Fig. 4.18: TOT and NPE relationships for 8 first channels.

In our comprehensive analysis, as depicted in the collection of plots, we examined the deviations of individual channels from the mean curve, which represents the average TOT and the difference of NPE dividing by the mean NPE relationship for the 64 channels. These deviations, plotted as the difference in percentage for each channel against TOT, provide an insight into the channel-specific behavior against the collective norm. Across the spectrum of TOT values, most channels exhibit minimal divergence from the mean, maintaining a difference within ± 10%, which suggests a high level of consistency in the response characteristics of the PMT array. Notably, a few channels display more significant deviations, particularly in the higher TOT range, indicating areas where individual calibration may be

necessary to ensure uniformity across the array. These differences are crucial for identifying any channels that might require attention due to their anomalous behavior. The precise mapping of these deviations is pivotal for refining the calibration process and enhancing the accuracy of NPE measurements, which is essential for the reliability of subsequent analyses that depend on these data. Overall, the consistency of the PMT array's performance, with only sparse exceptions, reaffirms the robustness of the calibration methodology employed.

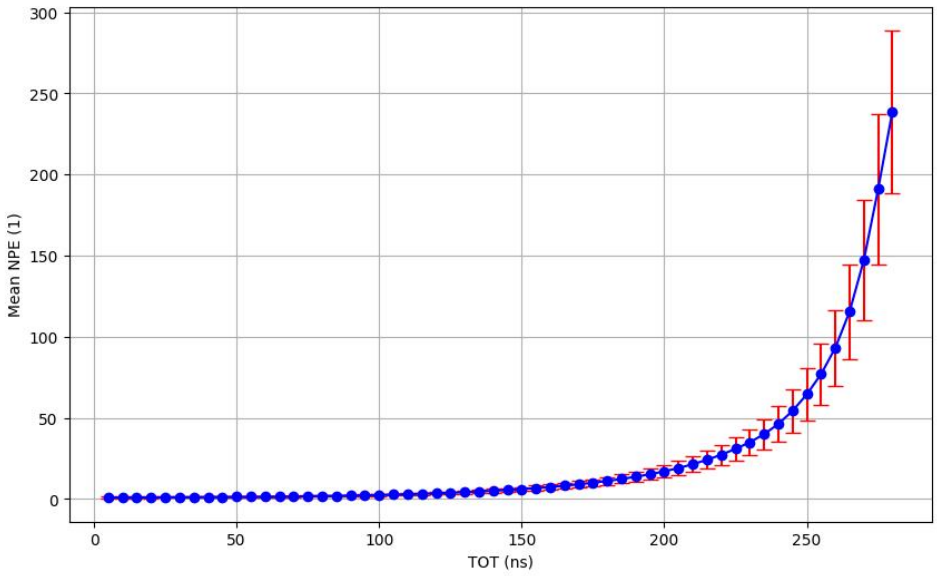

(a)

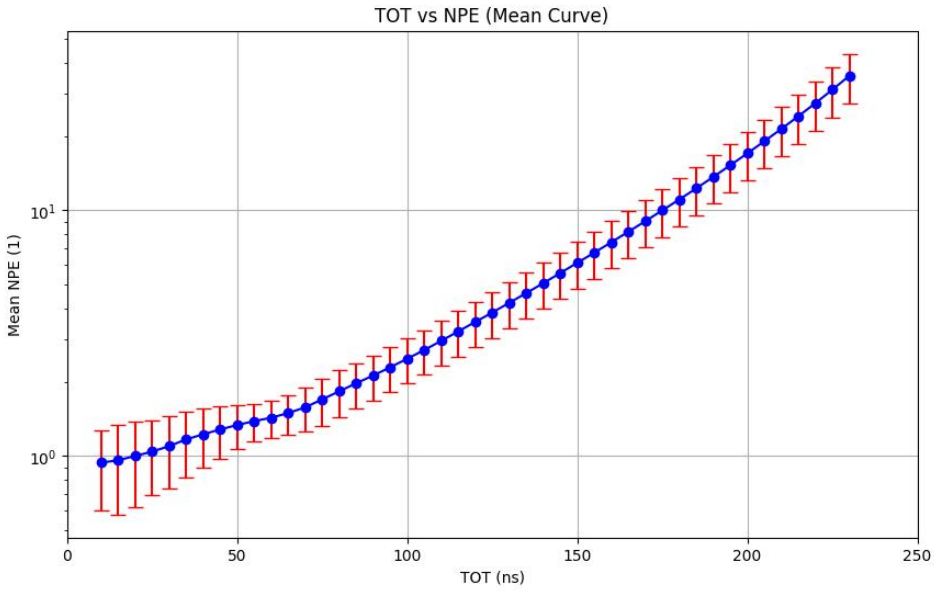

(b)

Fig. 4.19: (a) Mean curve of TOT and NPE relationships; (b) Mean curve of TOT and NPE relationships in log for small NPE derived from (a).

It's worth noting that the detection deviations are primarily driven by fluctuations in the gain of the PMTs, which exhibit a fluctuation of 50% [149]. Additionally, statistical data also reveals fluctuations consistent with the Poisson distribution, which is shown in the yellow curve in the Figure 4.20.

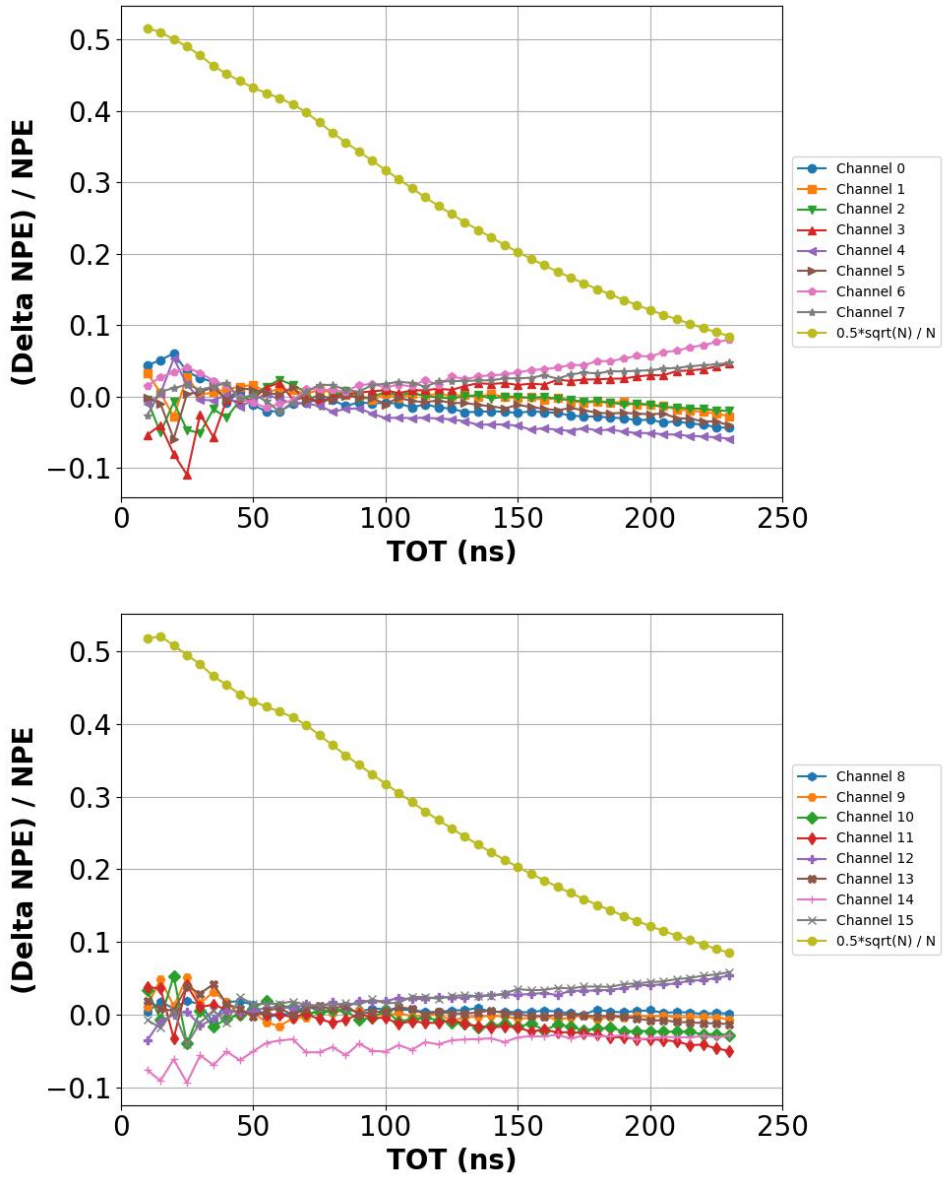

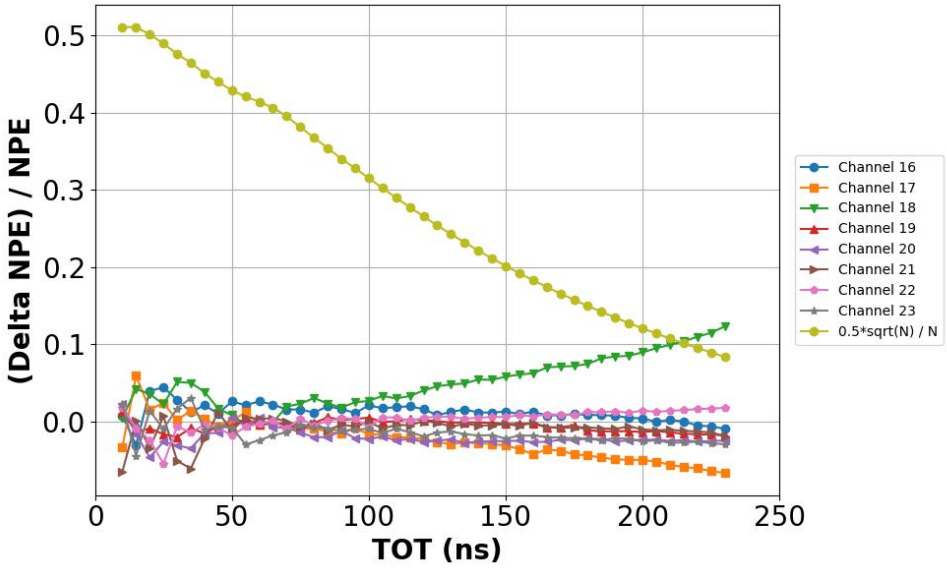
(Delta NPE) / NPE
TOT (ns)
Channel 16
Channel 17
Channel 18
Channel 19
Channel 20
Channel 21
Channel 22
Channel 23
0.5*sqrt(N) / N

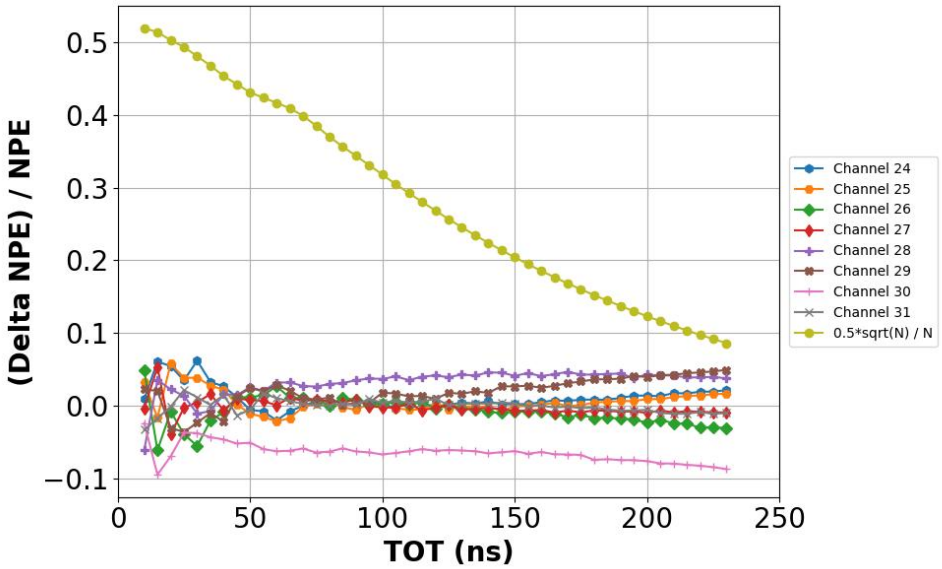
(Delta NPE) / NPE
TOT (ns)
Channel 24
Channel 25
Channel 26
Channel 27
Channel 28
Channel 29
Channel 30
Channel 31
0.5*sqrt(N) / N

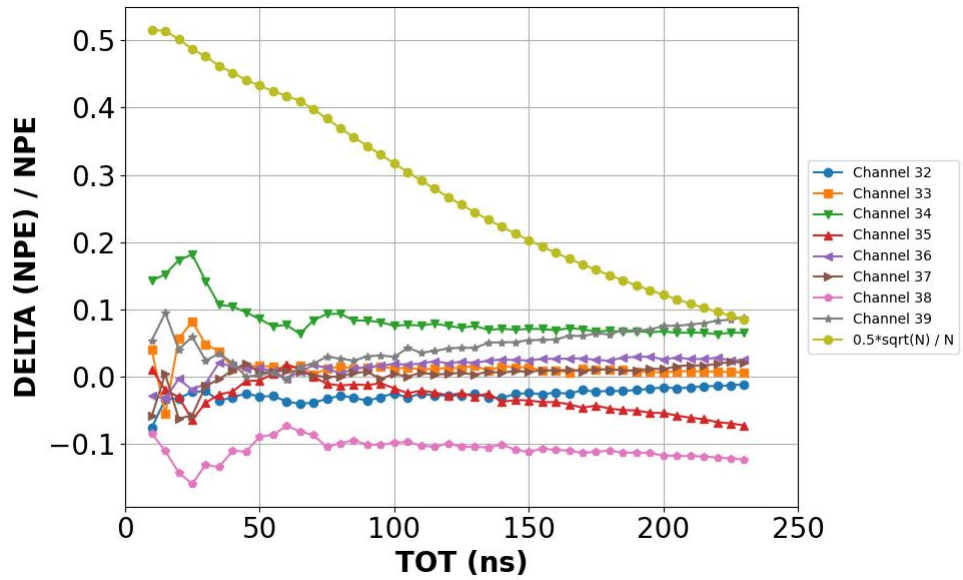
DELTA (NPE) / NPE
TOT (ns)
Channel 32
Channel 33
Channel 34
Channel 35
Channel 36
Channel 37
Channel 38
Channel 39
0.5*sqrt(N) / N

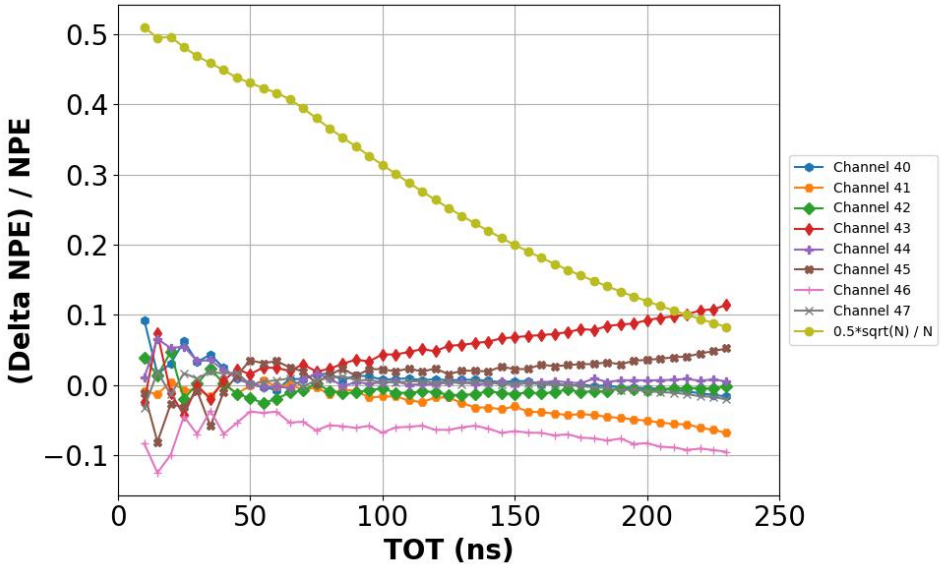
(Delta NPE) / NPE
TOT (ns)
Channel 40
Channel 41
Channel 42
Channel 43
Channel 44
Channel 45
Channel 46
Channel 47
0.5*sqrt(N) / N

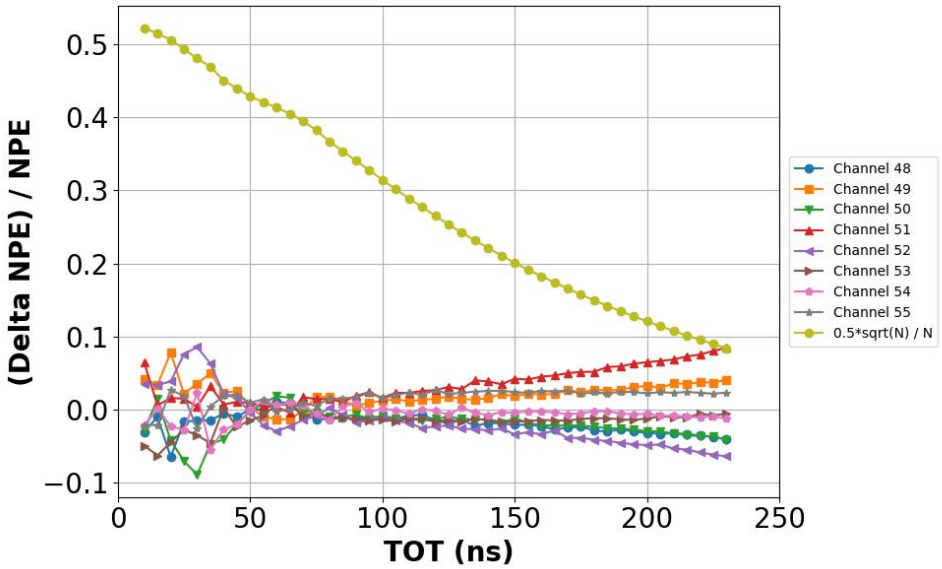
(Delta NPE) / NPE
TOT (ns)
Channel 48
Channel 49
Channel 50
Channel 51
Channel 52
Channel 53
Channel 54
Channel 55
0.5*sqrt(N) / N

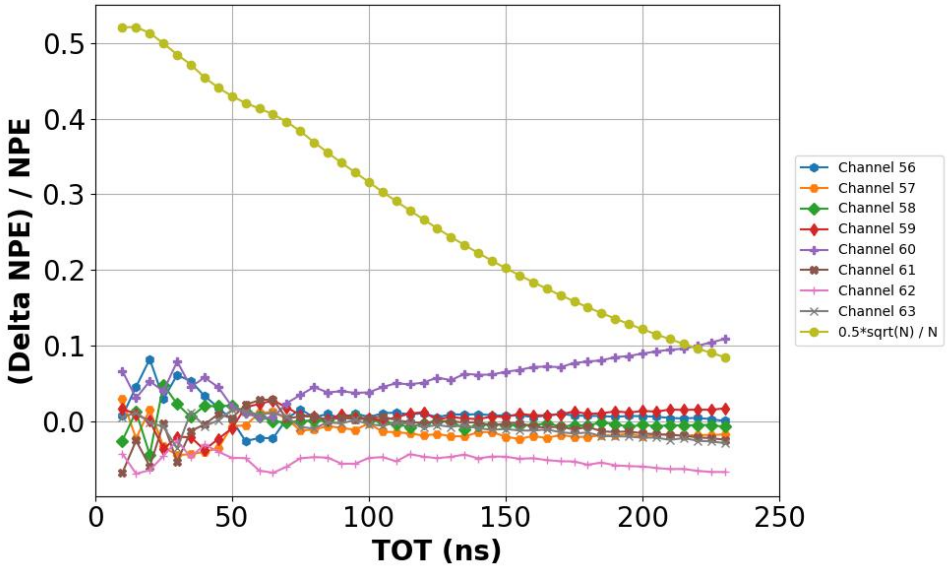
(Delta NPE) / NPE
TOT (ns)
Channel 56
Channel 57
Channel 58
Channel 59
Channel 60
Channel 61
Channel 62
Channel 63
0.5*sqrt(N) / N

Fig. 4.20: Deviations of individual channels from the mean curve.

Table 4.4 furnishes comprehensive details regarding the conversion from TOT to NPE of the mean curve of 64 channels , accompanied by associated standard errors. This tabulated data offers a precise and insightful depiction of how NPE varies as a function of TOT.

Table 4.4 TOT-NPE and TOT-NPE standard error relationships for the mean curve

TOTS Value (ns)	NPE	Standard Error of NPE	TOTS Value (ns)	NPE	Standard Error of NPE
5	1.0	0.5	130	4.2	0.9
10	1.0	0.4	135	4.6	1.0
15	1.0	0.4	140	5.1	1.1
20	1.0	0.4	145	5.6	1.2
25	1.1	0.4	150	6.1	1.3
30	1.1	0.4	155	6.8	1.5
35	1.2	0.4	160	7.4	1.6
40	1.2	0.3	165	8.2	1.8
45	1.3	0.3	170	9.1	2.0
50	1.4	0.3	175	10.0	2.2
55	1.4	0.3	180	11.1	2.5
60	1.5	0.3	185	12.3	2.7
65	1.5	0.3	190	13.7	3.1
70	1.6	0.3	195	15.3	3.4
75	1.7	0.4	200	17.1	3.8
80	1.9	0.4	205	19.1	4.3
85	2.0	0.4	210	21.5	4.9
90	2.1	0.4	215	24.2	5.5
95	2.3	0.5	220	27.3	6.2
100	2.5	0.5	225	30.9	7.1
105	2.7	0.6	230	35.0	8.1
110	3.0	0.6	235	40.0	9.3
115	3.2	0.7	240	46.2	11.1
120	3.5	0.7	245	54.4	13.4
125	3.9	0.8	250	64.6	15.9

4.3.4 Time measurement optimization

In XEMIS2, alongside quantifying incoming photons, we extract precise timestamps of photon arrivals from the scintillation signal. This temporal data assumes critical importance in various facets of our analysis and imaging procedures. As previously emphasized, scintillation signals play a pivotal role in deducing the interaction times of gamma rays. Furthermore, when correlated with ionization signals, they contribute to the initial spatial localization of gamma-ray interactions, thus facilitating the virtual delineation of the active volume. Given the extensive array of PMTs employed, efficient extraction of relevant signal information is essential for managing the data flow.

4.3.4.1 Time walk effect correction

The experimental setup for time measurement calibration is the same as that of the TOT calibration described in the previous section. As previously mentioned, the binary files recorded by the Spartan card contain data related to both TOT and trigger arrival times. In this section, we elucidate the data processing procedures integral to the time measurement calibration.

The leading edge of the logic pulse is defined as the moment when the PSA signal pass the LETD threshold. Instead of directly calculating this leading edge, we examine the time difference between the reference channel and the test channel. The reference channel receives a simulated PMT signal with a constant pulse height. By calculating the delay in the reference channel, we can deduce the delay in the test channel.

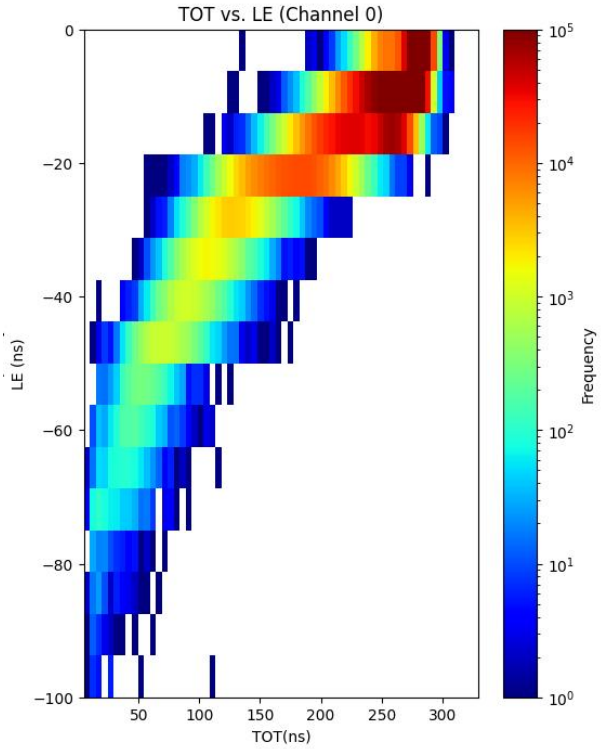

Fig. 4.21: TOT-Leading edge events accumulation histogram for channel 0.

Figure 4.21 presents a histogram that captures the accumulation of events based on their TOT and Leading Edge (LE) timings. The analytical focus on the leading edge, which is the initial part of the signal where the rise begins, is crucial for understanding the temporal dynamics of signal formation and propagation in the channel. This analysis can be pivotal for optimizing the timing resolution of the detection system and for investigating any potential systematic discrepancies that may affect the accuracy of charge collection and timing measurements.

The 64 channels demonstrate remarkably consistent behavior, allowing us to focus on a single representative curve that characterizes their collective response. Therefore, I have provided the mean curve, which encapsulates the average performance across all 64 channels. This synthesized curve offers a simplified yet precise overview, serving as a benchmark for the typical response pattern of the array. It is a composite reflection of the uniformity in timing and signal processing across the channels, which is instrumental for system-wide calibration and performance analysis.

Figure 4.22 (a) illustrates the mean curve of the Leading Edge (LE) versus TOT for 64 channels. This curve is the result of aggregating and averaging the individual measurements from each channel, and it displays a clear, consistent trend in how the leading edge of the signal correlates with the duration that the signal remains over a set threshold. The data points on the graph, marked with blue dots, are connected to form the mean curve, and the red error bars represent the standard deviation of the LE for each TOT value, providing a visual representation of the variability within the channels at each TOT. The curve demonstrates a non-linear relationship, with the LE times initially decreasing rapidly with small increases in TOT and then plateauing as the TOT extends.

Figure 4.22 (b) shows the difference between the average of each block and the overall average curve for 64 channels. We divide the 64 channels into 8 blocks. For example, block 1 includes the average of channels 0 to 7, and so on. We do this because during the experiment, we use channel 15 as a reference to measure the time for channels 0 to 7, and channel 0 as a reference to measure the time for channels 8 to 15, as explained earlier.

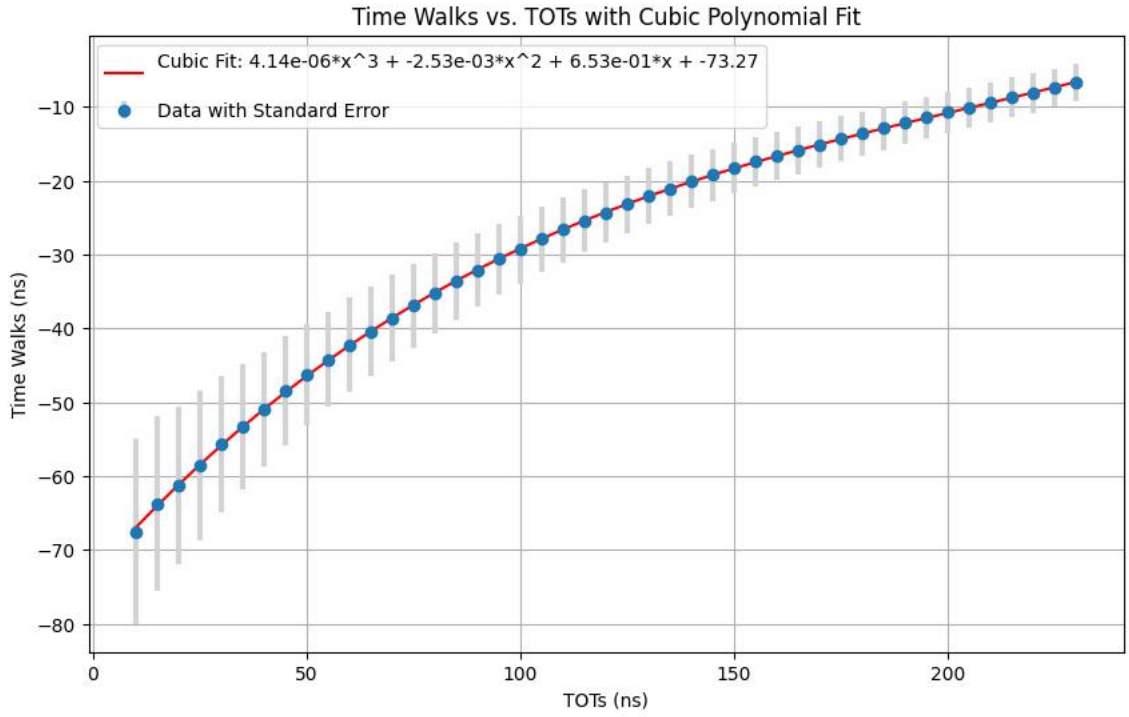

(a)

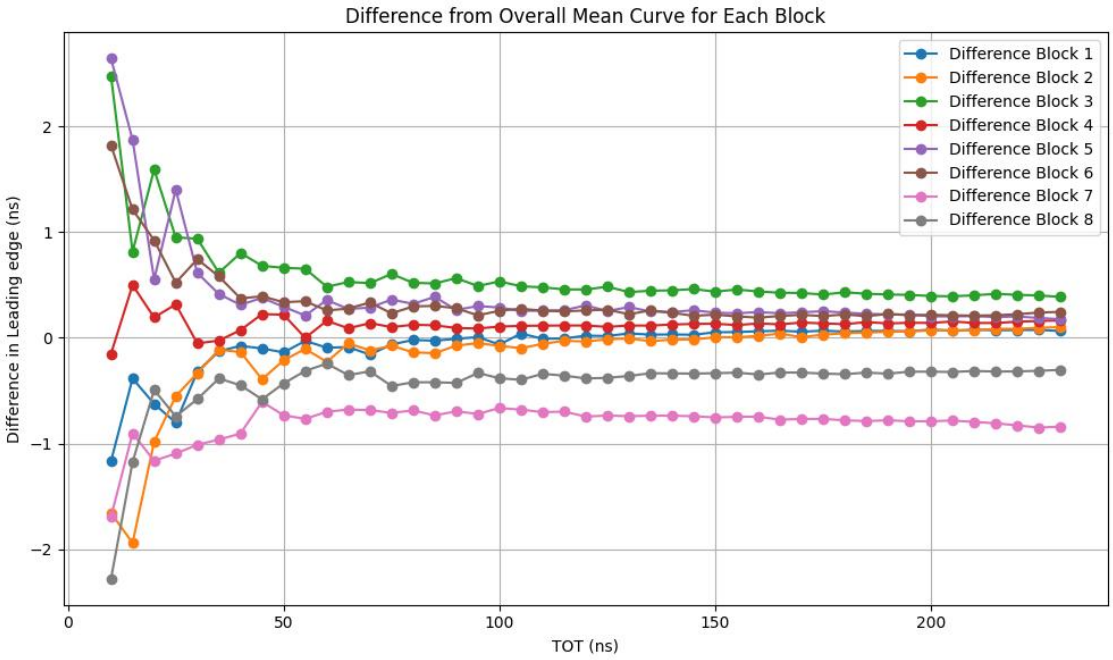

(b)

Fig. 4.22 (a) Mean curve of the Leading Edge vs TOT for 64 channels. (b) Difference between the average of each block and the overall average curve for 64 channels.

Table 4.5 furnishes comprehensive details regarding the conversion from TOT to leading edge of the mean curve for 64 channels, accompanied by associated standard errors. This tabulated data offers a precise and insightful depiction of how leading edge varies as a function of TOT.

Table 4.5 TOT vs Leading edge and standard error relationships for mean curve

TOTS Value (ns)	Leading edge (ns)	Standard Error of LE (ns)	TOTS Value (ns)	Leading edge (ns)	Standard Error of LE (ns)
10	-67.5	12.5	125	-23.2	3.9
15	-63.7	11.9	130	-22.1	3.8
20	-61.3	10.7	135	-21.1	3.7
25	-58.5	10.1	140	-20.1	3.6
30	-55.7	9.2	145	-19.2	3.5
35	-53.3	8.5	150	-18.3	3.4
40	-50.9	7.8	155	-17.4	3.3
45	-48.5	7.4	160	-16.6	3.2
50	-46.3	6.9	165	-15.9	3.2
55	-44.2	6.4	170	-15.1	3.1
60	-42.2	6.4	175	-14.3	3.1
65	-40.4	6.0	180	-13.6	3.0
70	-38.6	5.9	185	-12.9	3.0
75	-36.9	5.7	190	-12.1	2.9
80	-35.2	5.4	195	-11.4	2.8
85	-33.6	5.2	200	-10.7	2.8
90	-32.1	5.0	205	-10.1	2.7
95	-30.6	4.8	210	-9.4	2.7
100	-29.3	4.6	215	-8.7	2.7
105	-27.9	4.4	220	-8.1	2.7
110	-26.6	4.4	225	-7.4	2.6
115	-25.4	4.2	230	-6.7	2.6
120	-24.3	4.0			

Figure 4.23 provides a detailed analysis of the leading edge deviations of individual channels from the mean curve, plotted against the Time Over Threshold (TOT). Each line represents one of the 64 channels and traces the difference between its leading edge timing and the average of all channels for a given TOT. As can be seen from the graph, most of the channels follow the average curve closely in the medium to high TOT range. However, at lower TOT values there is a noticeable deviation, possibly due to the low signal-to-noise level. The deviations are contained within a narrow band, indicating a high degree of uniformity in channel behavior. This adherence to the mean suggests that the channels have similar timing characteristics and that the system is well-balanced.

However, the spread in the initial section where TOT is low reflects the individual characteristics or calibration differences among the channels. These variations diminish as

the TOT increases, which could be due to the signal's overcoming of the noise floor, leading to a more stable and uniform response. The tight clustering of lines around the zero deviation mark for the majority of the TOT range confirms the robustness of the mean curve as a reliable reference for the system's performance.

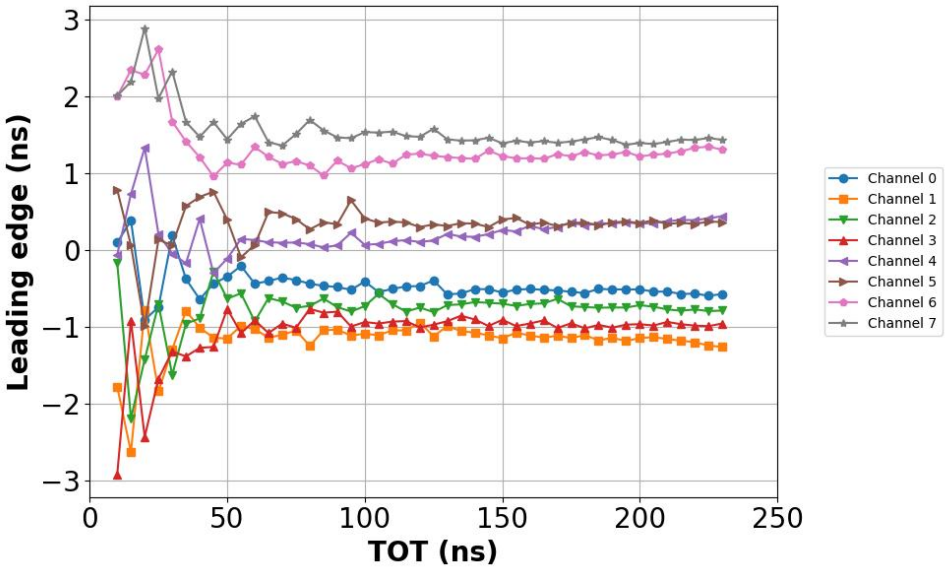

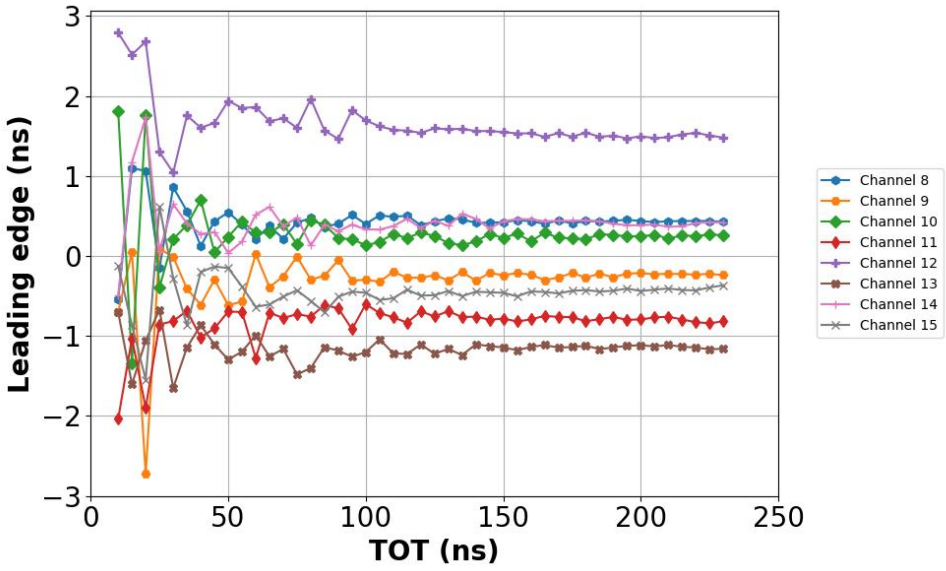

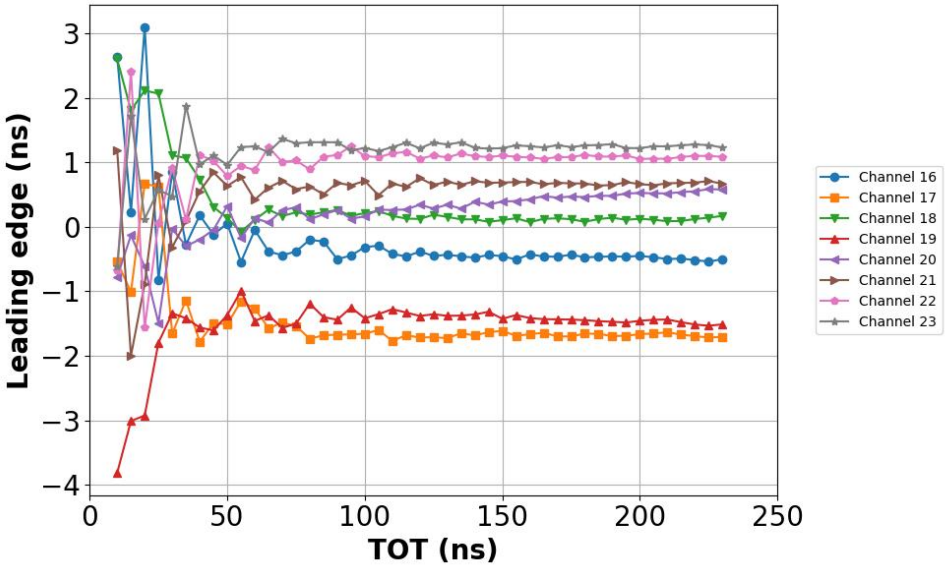
Leading edge (ns)
TOT (ns)
Channel 16
Channel 17
Channel 18
Channel 19
Channel 20
Channel 21
Channel 22
Channel 23

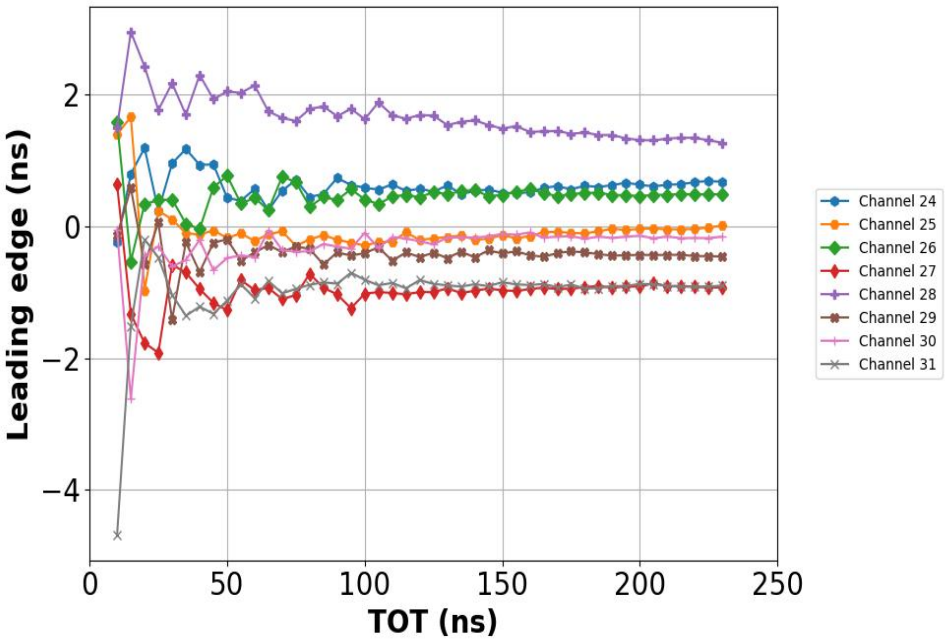
Leading edge (ns)
TOT (ns)
Channel 24
Channel 25
Channel 26
Channel 27
Channel 28
Channel 29
Channel 30
Channel 31

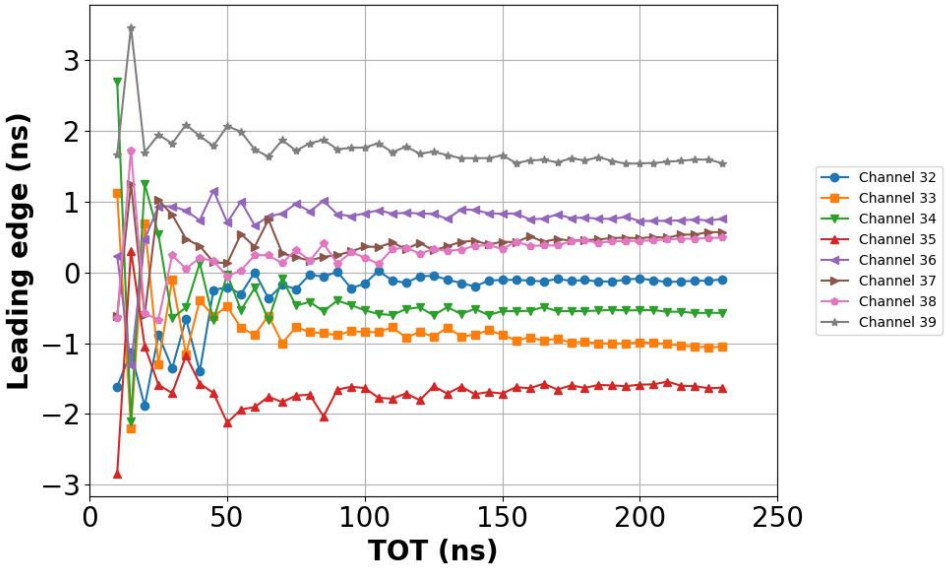
Leading edge (ns)
TOT (ns)
Channel 32
Channel 33
Channel 34
Channel 35
Channel 36
Channel 37
Channel 38
Channel 39

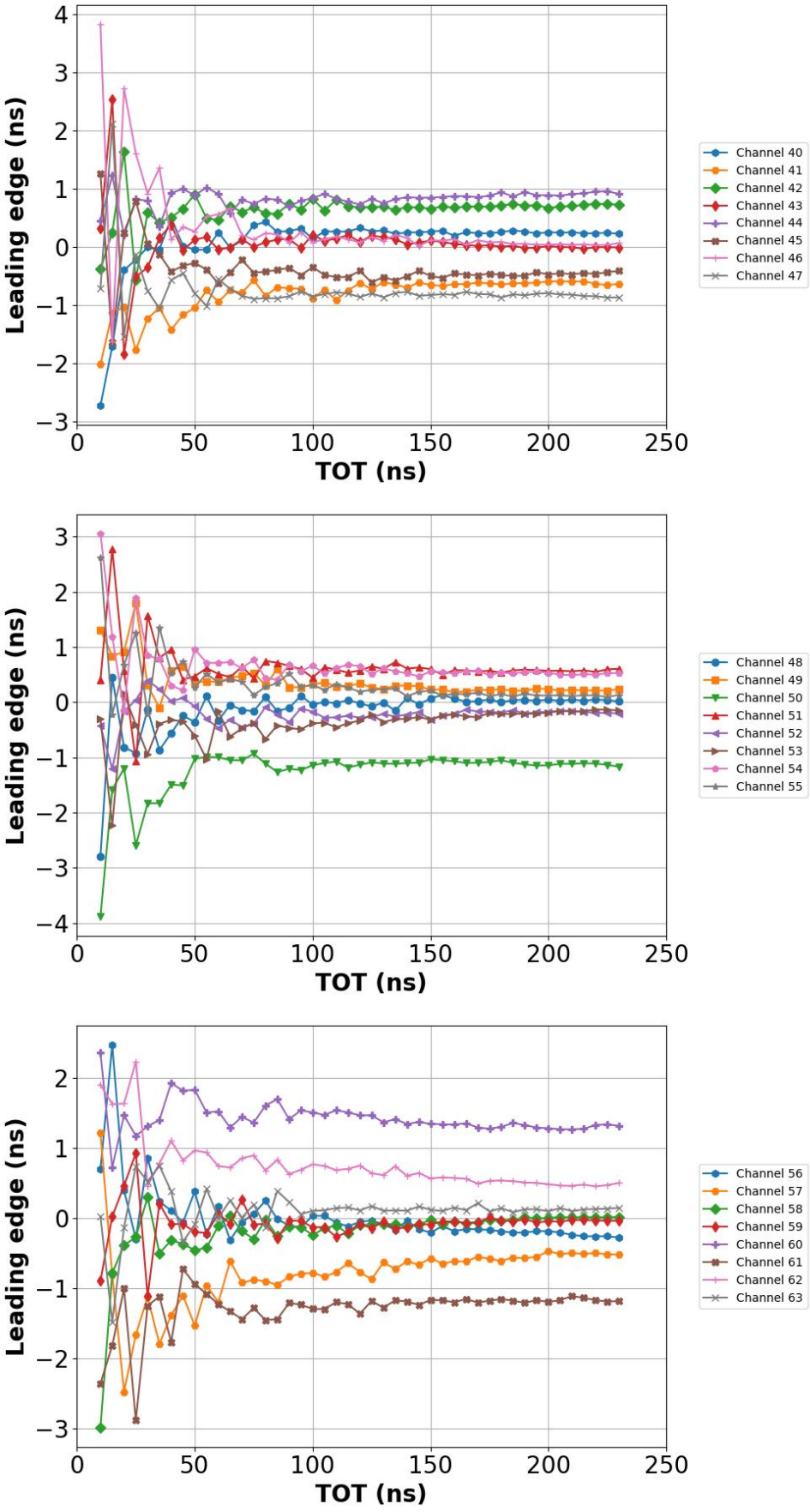

Figure 4.23: Leading edge deviations of individual channels from the mean curve.

Table 4.6 shows the delay for the 64 channels. We define the delay as the difference between the channel and the average curve of the 64 channels.

Table 4.6 Delay between the tested channel and the mean curve

Channel	Channel Delay (ns)	Block Delay (ns)	Delay Total (ns)	Channel	Channel Delay (ns)	Block Delay (ns)	Delay Total (ns)
0	-0.5	0.1	-0.4	32	-0.1	0.2	0.1
1	-1.1		-1.0	33	-1.0		-0.8
2	-0.7		-0.6	34	-0.5		-0.3
3	-1.0		-0.9	35	-1.6		-1.4
4	0.3		0.4	36	0.7		0.9
5	0.4		0.5	37	0.5		0.7
6	1.2		1.3	38	0.4		0.6
7	1.4		1.5	39	1.5		1.7
8	0.4	0.1	0.5	40	0.3	0.2	0.5
9	-0.2		-0.1	41	-0.6		-0.4
10	0.2		0.3	42	0.7		0.9
11	-0.8		-0.7	43	0.0		0.2
12	1.5		1.6	44	0.9		1.1
13	-1.1		-1.0	45	-0.5		-0.3
14	0.4		0.5	46	0.0		0.2
15	-0.4		-0.3	47	-0.8		-0.6
16	-0.5	0.4	-0.1	48	0.0	-0.8	-0.8
17	-1.7		-1.3	49	0.2		-0.6
18	0.1		0.5	50	-1.1		-1.9
19	-1.5		-1.1	51	0.6		-0.2
20	0.5		0.9	52	-0.2		-1.0
21	0.7		1.1	53	-0.2		-1.0
22	1.1		1.5	54	0.5		-0.3
23	1.2		1.6	55	0.1		-0.7
24	0.6	0.1	0.7	56	-0.2	-0.3	-0.5
25	0.0		0.1	57	-0.5		-0.8
26	0.5		0.6	58	0.0		-0.3
27	-0.9		-0.8	59	0.0		-0.3
28	1.3		1.4	60	1.3		1.0
29	-0.4		-0.3	61	-1.2		-1.5
30	-0.1		0	62	0.5		0.2
31	-0.9		-0.8	63	0.1		-0.2

4.3.4.2 Reference channel delay calculation

In precise timing measurements, especially within systems requiring tight synchronization across multiple channels, the leading edge of a logic pulse serves as a crucial parameter. This leading edge is typically defined as the temporal difference between a reference channel and a test channel.

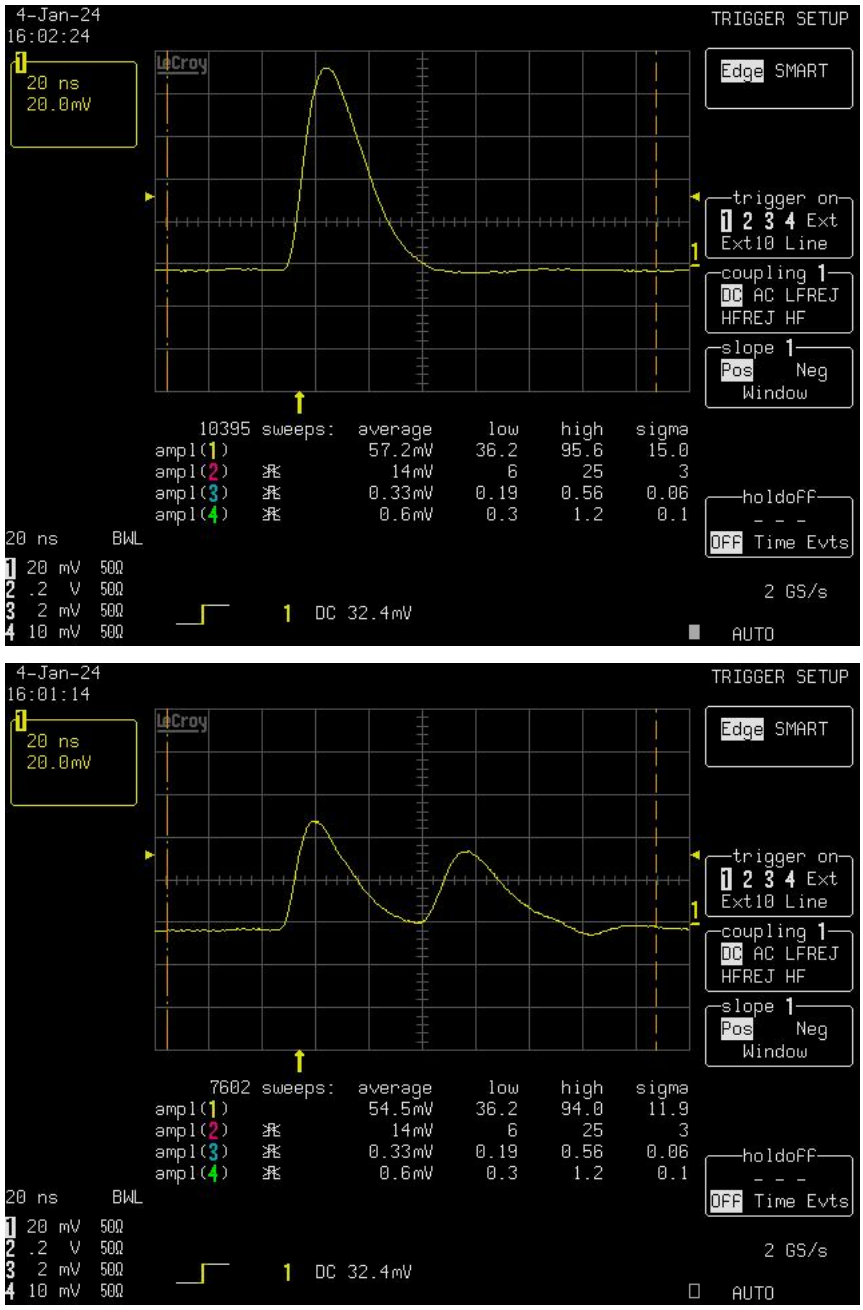

Fig. 4.24: (a) Oscilloscope traces for the input signal of the reference channel; (b) Response after passing through the reference channel.

In this case, the reference channel is crucial. Its task is to receive the analogue PMT signal, which has a constant pulse height. This uniformity is essential because it allows the reference channel to act as a calibration standard. The uniformity of the reference channel output ensures that any timing measurement is based on a stable and reliable reference.

When the test channel is evaluated, its performance is measured against this datum. The response time of a channel can be determined by measuring the time it takes for the pulse front to rise from a defined lower percentage of its maximum amplitude to a higher percentage (typically from 10% to 90%). The leading edge time is sensitive to a variety of factors, including signal propagation delays, channel-induced distortion, and the intrinsic time resolution of the detector used.

Based on the description provided for Figure 4.24 (a) and (b), the oscilloscope traces give us valuable information about the timing characteristics of the reference channel in a precision measurement system. (a) The input signal of the reference channel, as depicted in the oscilloscope trace. (b) The response of the signal after passing through the reference channel, as shown in the oscilloscope trace, is indicative of the inherent delay introduced by the channel itself. This is an expected phenomenon as every electronic component or channel introduces some delay due to its physical and electrical properties.

The deduction of a 55ns delay in the reference channel is a critical piece of information. This delay must be accounted for when comparing signals from different channels.

4.3.5 PMT Gain Calibration

In contemporary applications, Photomultiplier Tubes (PMTs) serve as ubiquitous light detection components within a spectrum of scintillation detectors, encompassing counters and calorimeters. The dependable functionality of these systems is contingent upon a comprehensive comprehension of pivotal PMT characteristics. Among these critical parameters are gain, time response, pulse linearity, angular response, aging, dark current, signal-to-noise ratio, and after-pulsing. Notably, the understanding of PMT gain assumes paramount significance as it directly influences the quantification of photoelectrons (p.e.s) released by the PMT photocathode and subsequently amplified by the dynode chain. While the scintillation signal isn't leveraged for precise energy determinations in XEMIS, the count of p.e.s assumes a pivotal role in the spatial pre-localization of γ-ray interactions within the active zone.

The gain of a photomultiplier tube is susceptible to variations in the supply voltage and may also fluctuate due to factors such as dynode aging and intrinsic background noise, which is intricately linked to the PMT's operational temperature. Lowering the operating temperature of the photomultiplier tube reduces thermionic electron emission, which reduces the dark current. In addition, the sensitivity of the photomultiplier is affected by temperature. The temperature coefficient of the photomultiplier is negative in the ultraviolet and visible regions and positive near the length cutoff wavelength. Because of the large temperature coefficient near the length cutoff wavelength, the operating temperature of the photomultiplier should be strictly controlled in some applications.

The intrinsic variability in PMT gain predominantly arises from statistical fluctuations in the secondary electron production on the dynode surfaces and disparities in electron trajectories within the electron multiplication system. Even among PMTs of identical models supplied with identical voltages, the average number of secondary electrons generated by the dynode structure in response to a single p.e. (i.e., the average gain of the PMT) may manifest variations. These divergences in gain emanate from discrepancies in the geometries of the dynode structures within the same PMT model, frequently traceable to imperfections in the fabrication process. In practical terms, gain fluctuations translate into alterations in the pulse height of the PMT output signal.

In the initial stage of XEMIS2, where scintillation signals are detected, the active volume is enveloped by 64 PMTs. To ensure uniform sensitivity to a single p.e. across various PMT channels, it is imperative to calibrate and harmonize the gain of each PMT to a consistent value. This necessitates the determination of an appropriate supply voltage for each PMT to enable the proper operation of XEMIS2 devices. In this experimental context, the average gain and gain fluctuations of two Hamamatsu R7600 PMTs, positioned within the XEMIS1 detector, were calibrated at varying supply voltages.

4.3.5.1 Experimental set-up

The figure 4.25 illustrates the calibration process for the 64 PMT gain. Initially, a high voltage of 730 V is applied to the PMT due to calibration at an ambient temperature of approximately 25 °C, exceeding 730V could risk damaging the PMTs because the Hamamatsu R7600 PMTs being designed for an operating temperature of -110°C. Subsequently, the PMT is illuminated with light from a blue LED. The PMT signal is then passed through the pulse shape amplifier and into a discriminator of the XRETOT set at a threshold of 1000 cps/s. The output from the Spartan enables the determination of the PMT's detection efficiency by comparing the known LED input frequency with the recorded signal. By gradually increasing the generator tension connected to the LED, the PMT's detection efficiency rises from 0% to approximately 1%, representing the single photoelectron (SPE) level. Maintaining this generator tension while systematically reducing the PMT's high voltage allows for the establishment of the relationship between detection efficiency and the applied PMT high voltage.

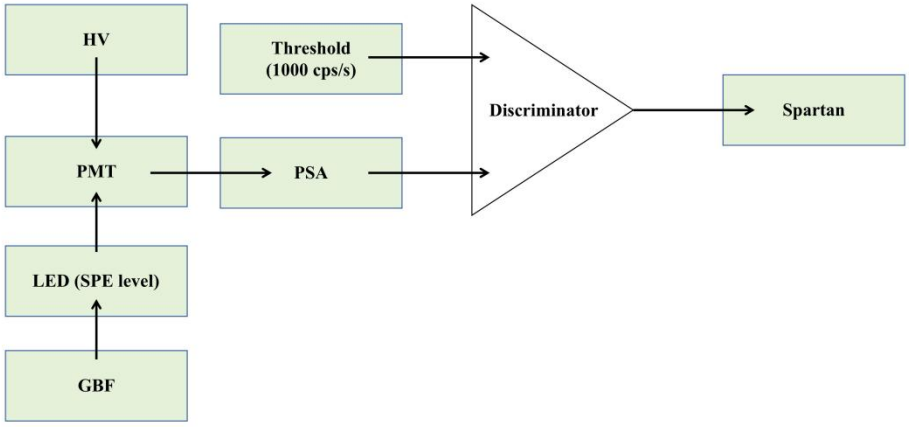

Fig. 4.25: Simplified schematic of experimental setup for PMT gain calibration.

4.3.5.2 Calibration results

The calibration results are divided into three parts. Firstly, we apply the time walk correction obtained in section 4.3.4 to the 64 PMTs. Secondly, we generate a histogram of TOT to verify that the LED operates at the single photon level. Finally, we illustrate the relationship between high voltage and detection efficiency.

4.3.5.2.1 Time windows method and Time walk correction

As previously discussed, the time windows method effectively reduces noise triggers. For an event rate of 50 kHz, corresponding to the generator frequency, we aim for a physical event detection rate of 0.5 kHz, representing a 1% detection efficiency. However, with a noise rate of 1000 cps/s, distinguishing physical events from noise becomes challenging.

Opening a time window of 100 ns, we calculate the percentage of time accounted for by each physical event, resulting in approximately 0.5%. By considering only events within the time windows, the noise rate is reduced to approximately 5 counts/s.

$$t_{windows} = 100\ \mathrm{ns} \tag{4.7}$$

The period of the physical events is about 20 µs :

$$t_{physical\ events} = \frac{1}{f} = \frac{1}{50kHz} = 20\ \mu s \tag{4.8}$$

For a time windows of 100 ns and the percentage of the time is about 0.5%:

$$\mu = \frac{100\ \mathrm{ns}}{20\ \mu s} = 0.5\% \tag{4.9}$$

In this case, the noise rate is about 5 cts/s.

$$\text{Noise rate}_{\,after\ windows} = 0.5\% \times 1000\ cts/s \ = 5\ cts/s \tag{4.10}$$

After applying the time window method, we achieve a 0.5% reduction in the noise rate. We anticipate that all physical events are perfectly aligned within the time windows, maintaining the physical event rate at approximately 5000 triggers/s, significantly higher than the reduced noise rate of 5 cts/s.

In order to correctly open a time window in the tested channel, we have to do the time walks correction for PMT. In the section 4.3.4, we get the relation between the time walk and TOT. After correcting the time walk, almost all the physical events are located near the synchronic channel.

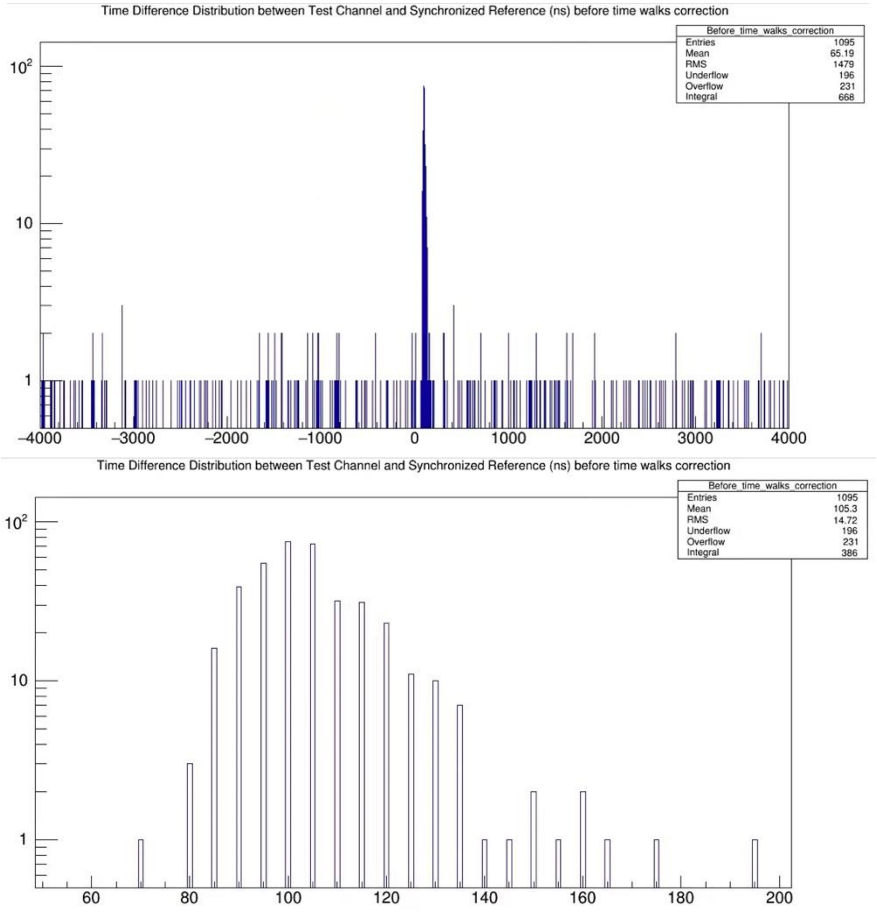

(a)

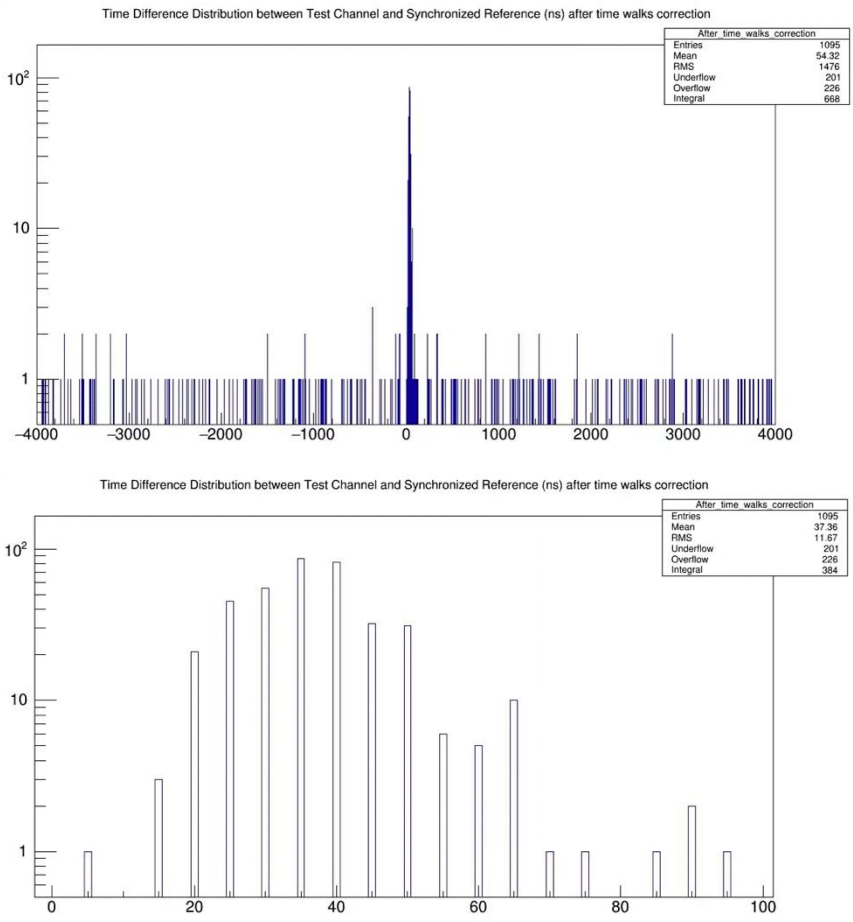

(b)

Fig. 4.26 (a) Distribution of difference time before time walk correction; (b) Distribution of difference time after time walk correction

The application of time walk correction significantly narrows the temporal window within which physical events are triggered, as evidenced by the transition from 80-140 ns before correction to 15-65 ns after correction, as depicted in Figure 4.26. This correction effectively aligns physical events closer to the synchronized trigger, enhancing temporal precision. Furthermore, the mean relation between each channel and the synchronizing signal, as outlined in Table 4.5, indicates a negligible difference ranging between -2 ns to 2 ns. In the context of a 100 ns time window chosen, this uniformity across channels supports the utilization of a mean relation for time walk and TOT values across all 64 PMTs, as illustrated in Figure 4.22.

4.3.5.2.2 TOT and NPE relation application

In section 4.3.3, we delve into the relationship between TOT and number of photoelectrons. During the gain calibration process, we operate under the assumption that the LED emits at the single photon electron level. This section aims to validate this assumption.

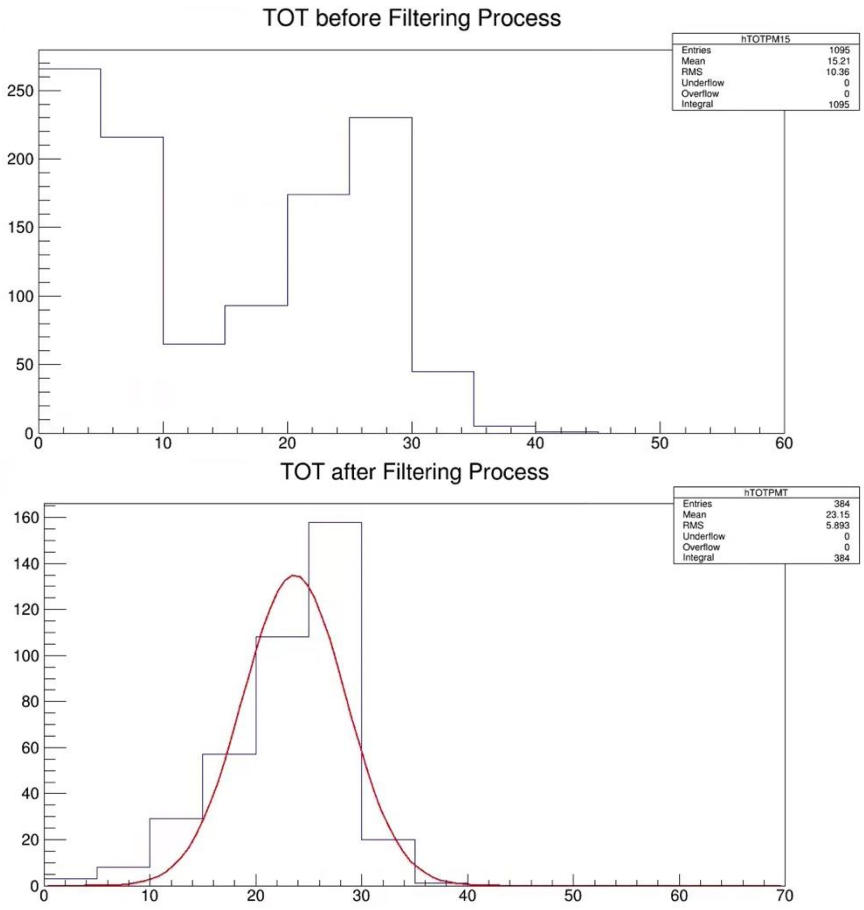

Fig. 4.27 (a) Histogram of TOT before time window filtering; (b) Histogram of TOT after time window filtering;

Figure 4.27 illustrates how the time window method effectively filters out small TOT values, indicative of noise, while retaining the majority of physical events with a mean TOT of 23 ns. Table 4.4 corroborates this finding by demonstrating that a TOT of 23 ns corresponds to approximately 1 NPE. Hence, the condition of single photon electron level is indeed verified.

4.3.5.2.3 Detection efficiency and high voltage of PMT

In this section, we meticulously examine the process of calibrating the high voltage applied to photomultiplier tubes to align the PMT gain with a predefined threshold as detailed in section 4.3.2. Our initial approach entails setting the PMTs to a starting voltage of 730 V and investigating the relationship between the generator voltage and detection efficiency.

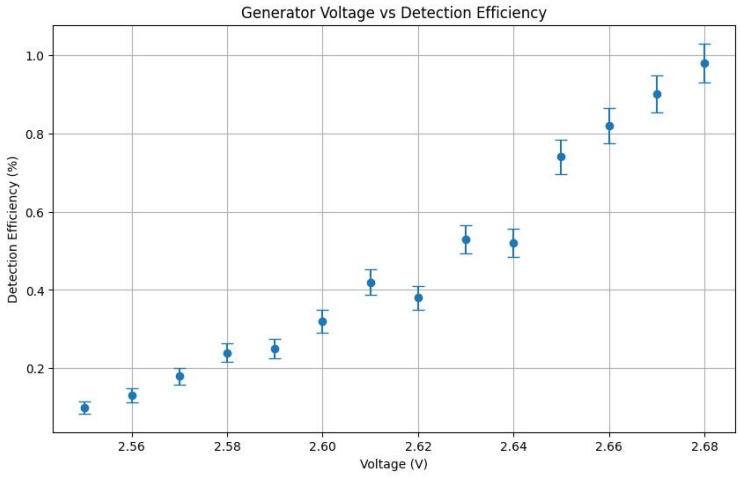

Fig. 4.28: Relation between the generator voltage applied to LED and the detection efficiency

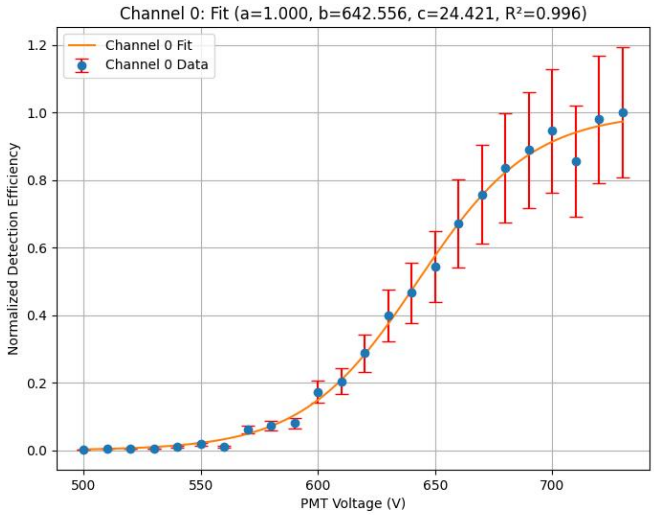

Fig. 4.29: Relation between the PMTs high voltage and the detection efficiency

The objective is to discern the optimal generator voltage that would ensure the LED operates at a single photon electron level. Upon determining the suitable generator voltage, we proceed to decrease the PMT high voltage from 730 V down to 500 V. This step is crucial for mapping out the curve that depicts the relationship between PMT high voltage and detection efficiency. Analyzing the characteristic 'S' curve enables us to extract the precise high voltage at which the PMT gain matches the threshold in electron units.

As illustrated in Figure 4.28, there is a discernible increment in detection efficiency corresponding with the rise in generator voltage. For this specific channel, we have identified 2.68 V as the optimal generator voltage for LED, achieving a detection efficiency close to 1%. Figure 4.29 further illustrates the dependency of detection efficiency on the high voltage applied to the PMT. For this channel, a high voltage of 642 V is recommended to equate the gain efficiency to the threshold efficiency. Figure 4.30 shows the distribution of high voltage for 64 PMTs. The Table 4.6 shows the high voltage applied to the 64 PMTs to maintain the gain equal to the threshold.

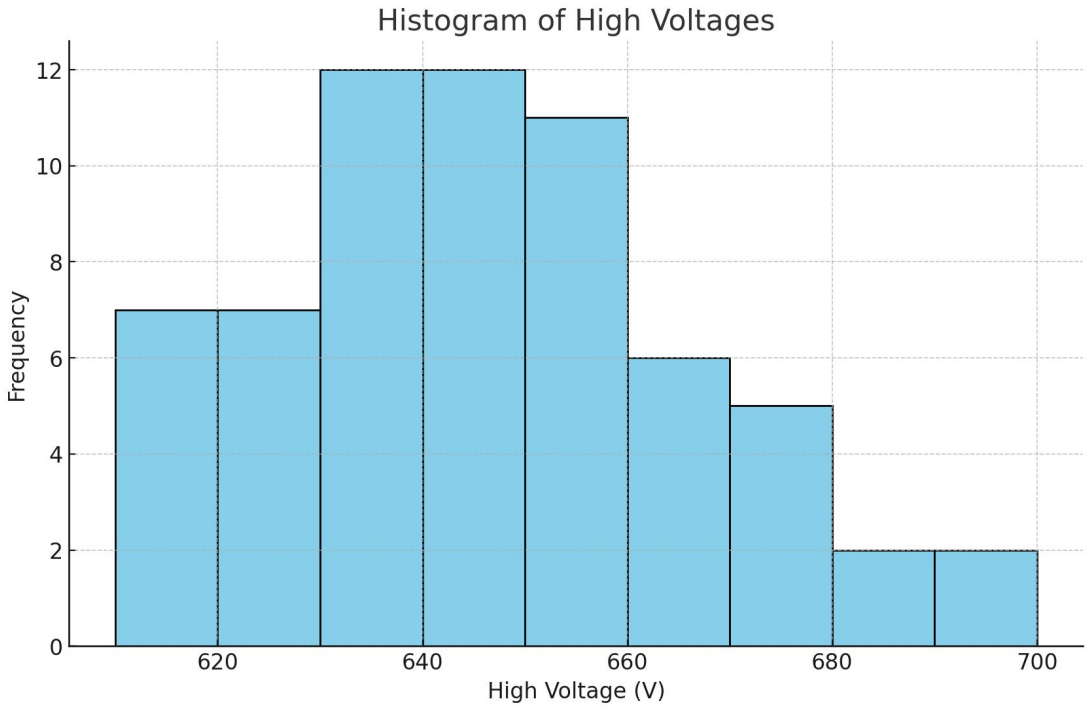

Fig. 4.30: PMTs high voltage distribution maintaining the the gain equal to the threshold.

Table 4.6: High voltage of PMTs(64 PMTS)

Channel	Threshold equivalent charge (e^-)	High Voltage (V)	Channel	Threshold equivalent charge (e^-)	High Voltage (V)
0	198000	642	32	188375	628
1	189750	619	33	189750	663
2	181500	677	34	196625	635
3	182875	647	35	181500	646
4	189750	625	36	187000	657
5	185625	649	37	182875	668
6	199375	629	38	177375	632
7	196625	663	39	193875	647
8	189750	680	40	198000	641
9	191125	622	41	189750	662
10	182875	619	42	199375	677
11	188375	656	43	184250	633
12	184250	700	44	196625	666
13	187000	680	45	178750	619
14	191125	654	46	195250	619
15	182875	646	47	191125	666
16	178750	650	48	178750	637
17	184250	690	49	192500	616
18	189750	647	50	174625	650
19	187000	636	51	184250	653
20	182875	655	52	195250	674
21	180125	636	53	177375	631
22	187000	658	54	178750	670
23	192500	644	55	184250	613
24	195250	629	56	193875	641
25	141625	642	57	171875	633
26	178750	636	58	181500	653
27	185625	655	59	170500	632
28	180125	615	60	185625	649
29	181500	674	61	173250	634
30	200750	625	62	196625	653
31	184250	628	63	178750	633

4.4 Conclusion

In summary, this chapter presents an exhaustive study of the scintillation detection process as it relates to the XEMIS2 system, a study that has both breadth and depth. We started the discussion with a panoramic view of the scintillation detection chain and delved into the urgent requirements for the design of an efficient readout system. Scintillation signal discrimination is essential for precise temporal localisation and spatial mapping of gamma-ray interactions within the sensitive volume of the detector. This recognition is not only academic, but is the basis for calibrating and improving the sensitivity of the detectors.

This chapter delves into the core issues of scintillation detection, starting with an in-depth study of threshold calibration, meticulously deconstructing the calibration process into its basic elements. This process is not just a procedural necessity; it is also key to fine-tuning the detector's responsiveness to incoming signals. The narrative then transitions to the nuances of threshold unit conversion, a pivotal moment that facilitates the translation of analogue nuances into a coherent digital vocabulary that enables accurate quantification and analysis of the detected signal.

The cornerstone of this exploration is a discussion of threshold time (TOT) calibration. This sophisticated method is an alternative to estimating the optoelectronic output triggered by scintillation events and is important for improving measurement accuracy. We reveal the subtleties of the calibration and clarify its integral role in the overall accuracy of the system.
The chapter also ventured into the domain of time measurement optimization. This segment elucidated various strategies that refine the temporal resolution and accuracy of the detector, ensuring that each scintillation event is recorded with the utmost fidelity. The calibration process also involves PMT gain calibration, the accuracy of which cannot be overemphasised as it directly affects the stability and uniformity of the signal amplification process, ensuring that the output of each channel is accurate and consistent.

In summary, this chapter provides a thorough compendium of the methodology and principles behind each calibration step, providing a comprehensive guide to the rigours of scintillation signal detection. The detailed exposition of the calibration procedure is an

important reference, emphasising the meticulous attention to detail required to achieve the high standards demanded by the XEMIS2 system.

In addition, this chapter not only sets the stage for the technical discussions that follow, but also emphasises the practical implications of these methods. Careful application of these calibration techniques is essential for the robust operation of the XEMIS2 system to ensure that it continues to be a model for scintillation signal detection. The principles and practices outlined here are indispensable and form the basis for future advances and innovations in the field. These fundamental insights will continue to guide the development and application of the XEMIS2 detector as we move forward, with the ultimate goal of reaching new heights of accuracy and reliability in scintillation detection.

5 Calibration results optimization

In this chapter, we embark on a meticulous journey to refine the calibration results of the scintillation detection in liquid xenon (LXe), an endeavour that is critical to the XEMIS2 project. The optimisation of these results is the basis for improving the accuracy and reliability of the detection system, which is essential for the accurate interpretation of the experimental data. This optimisation process not only demonstrates the robustness of the experimental setup, but also serves as a beacon for potential advances in the field.

Section 5.1 delves into the propagation and characterization of scintillation light within LXe. This exploration begins with the physical propagation mechanisms in 5.1.1, detailing how scintillation light traverses the medium of LXe, followed by a comprehensive characterization in 5.1.2, where the intricacies of scintillation signals within the XEMIS2 project are thoroughly analyzed.

Subsequently, Section 5.2 addresses the critical aspect of TOT calibration correction. Here, we dissect the characteristics of the shaper card response to single photoelectrons in 5.2.1 and proceed to validate this response for single-photon events in 5.2.2. We then examine TOT measurement simulations that incorporate scintillation signal mechanisms and PMT gain fluctuation in 5.2.3, leading to a rich discussion and conclusion in 5.2.4.

Section 5.3 shifts the focus to time measurement correction, a pivotal component in the calibration process. It commences with a comparison between simulation results and experimental findings in 5.3.1, moving on to more refined simulation results that take into account the scintillation signal mechanisms and PMT gain fluctuations in 5.3.2.

Finally, Section 5.4 synthesizes the findings and insights garnered from the preceding sections, culminating in a conclusive synthesis that ties together the overarching themes of calibration and optimization within the experimental framework. This chapter not only charts the path towards refined calibration but also unde

5.1 Propagation and characterization of scintillation light in Liquid Xenon

In this section, "TOT Calibration Results Correction," the narrative transitions from the foundational calibration methodologies delineated in Chapter 4 towards addressing a critical real-world application challenge inherent within the XEMIS2 camera. The pivot of this section is the reconciliation of the ideal conditions assumed during the calibration phase with the intrinsic variability of photon emission times in practical environments.

Chapter 4 meticulously outlines the calibration processes employed for scintillation detection within XEMIS2, including threshold calibration, conversion of threshold units, elucidation of the relationship between Time Over Threshold and the number of photoelectrons, optimization of time measurements, and calibration of PMT gain. These processes, albeit thorough, are predicated on a crucial assumption: the calibration generator provides a signal that mimics a uniform photon emission timing, a scenario seldom mirrored in the empirical reality of photon behavior.

Photon emission, by its very nature, exhibits stochasticity, with photons being emitted at non-uniform intervals, thereby introducing variability into TOT measurements that, if uncorrected, could undermine the fidelity and efficacy of scintillation signal detection efforts in XEMIS2. This deviation from the anticipated uniformity underscores the need for a sophisticated correction mechanism designed to recalibrate TOT results, ensuring they faithfully represent the nuanced dynamics of actual photon emission patterns.

To navigate this complexity, Section 5.1 articulates the development and implementation of advanced analytical strategies and algorithmic adjustments aimed at refining the calibration framework. This recalibration is essential to accommodate the inherent unpredictability of photon emission timing, striving to elevate the accuracy and robustness of scintillation detection. Such enhancements are pivotal for advancing the diagnostic precision of XEMIS2, underscoring the system’s contribution to the evolving landscape of medical imaging technologies where the exactitude of scintillation signal detection is paramount.

This recalibration effort not only highlights the importance of adaptive methodologies in the face of empirical challenges but also marks a significant step forward in the project's quest to

bridge the gap between theoretical calibration and real-world application, ensuring that XEMIS2 remains at the forefront of medical imaging innovation.

5.1.1 Propagation of scintillation light in liquid xenon

The propagation of scintillation light in liquid xenon is a key factor in the detection efficiency of VUV scintillation photons in LXe-based detectors. Although LXe is fundamentally transparent to the 178 nm scintillation light, the presence of impurities within the LXe significantly affects the propagation of these photons, leading to a decrease in the light yield. This attenuation effect is quantitatively described by an exponential function, dependent on the attenuation length (λ_{att}), which represents the mean free path of VUV scintillation photons.

$$I(z) = I_0 \, e^{-\frac{z}{\lambda_{att}}} \tag{5.1}$$

The equation 5.1 models this attenuation, where I_0 is the initial light intensity and z is the distance over which the scintillation light propagates in LXe.

The photon attenuation length in LXe is influenced mainly by two factors: absorption by impurities (notably water and oxygen) and the other factor is elastic scattering, primarily through Rayleigh scattering. The effective attenuation length is given by the equation :

$$\frac{1}{\lambda_{att}} = \frac{1}{\lambda_{abs}} + \frac{1}{\lambda_{scatter}} \tag{5.2}$$

where λ_{abs} and $\lambda_{scatter}$ are the absorption and scattering lengths, respectively.

Water is a critical contaminant in LXe due to its high absorption cross-section for VUV scintillation photons. Even at low concentrations, water significantly reduces the light yield. For example, a concentration of 10 ppm of water can absorb nearly 90% of scintillation light within just 2 cm. Oxygen also absorbs scintillation photons, albeit with a more pronounced effect on the ionization signal. The presence of these impurities at levels as low as a few ppm can adversely affect the scintillation properties of LXe, including light yield, emission

spectrum, and decay times. Effective purification systems are crucial for reducing these impurities, with advanced systems achieving absorption lengths greater than 100 cm, corresponding to water concentrations lower than 100 ppb.

Rayleigh scattering, the elastic scattering of photons without energy loss, also impacts the propagation of VUV scintillation light in LXe. The Rayleigh scattering length, dependent on the wavelength of scintillation light and the optical properties of LXe, such as the refractive index, determines how far a photon can travel before being scattered. Theoretically calculated and experimentally measured Rayleigh scattering lengths are in the range of 30 cm, indicating that for small volume detectors, this effect on light yield is negligible. However, in large volume detectors, Rayleigh scattering can significantly affect scintillation light collection.

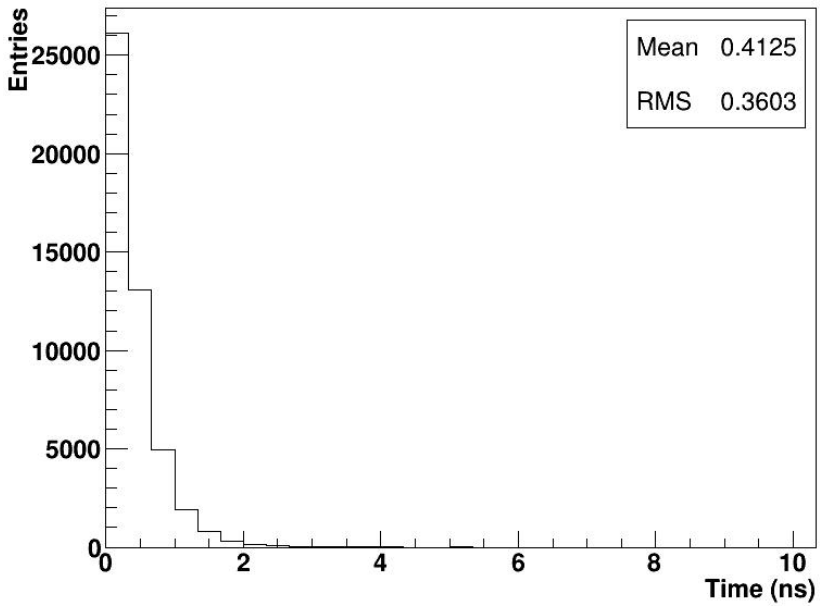

Fig 5.1 – Time distribution of photoelectrons (p.e.s) collected by all PMTs only considering the time propagation of VUV photons inside the detector.

The refractive index of LXe is crucial for simulating the propagation of scintillation light and determining the incident condition of VUV scintillation light. Reported values of the refractive index vary, influencing the precision of simulations and the understanding of light behavior in LXe. Lastly, the reflectivity of materials used in detector construction, such as aluminum and PTFE (Teflon), affects the efficiency of scintillation photon detection. Materials with high VUV reflectivity enhance the detection of scintillation photons. PTFE, in

particular, is favored for its high reflectivity, electrical insulation, and compatibility with LXe detectors' low radioactivity and high purity requirements.

In the thesis, it will be acknowledged that the visual data depicted in Figure 5.1 was adapted from an external source[149]. The figure illustrates the temporal distribution of photoelectrons collected by all PMTs, considering solely the propagation duration of vacuum ultraviolet photons within the detector's confines. The average propagation time is notably consistent, recorded at 0.4 ns.

5.1.2 Comprehensive Characterization of Scintillation Signals in XEMIS2

The scintillation light emission in liquid xenon can be characterized by three distinct decay components, primarily influenced by an external electric field of several kilo-volts per centimeter (kV/cm), as elaborated upon in Chapter 2:

- The fast component, characterized by a time constant τ_s of 2.2 ns, corresponds to the singlet excited state.
- The slow component, featuring a decay time τ_t of 27 ns, corresponds to the triplet excited state.
- The recombination component arises from electron-ion recombination and possesses a lifetime τ_r of 45 ns.

In the presence of an external electric field of 2 kV/cm, typically induced by electrons with an energy of 122 keV, the relative scintillation light yield ($R_{scintillation}$) compared to the maximum light yield is approximately 46%[197]. The ratio between the number of produced scintillation VUV photons from singlet excited states and triplet states is roughly 5% for electrons. The probabilities of emitting photons following these decay components are constrained by the requirement that their sum equals 1:

$$P_s + P_t + P_r = 1. \quad (5.3)$$

The values of these probabilities are as follows: P_s (3.15%), P_t (59.89%), and P_r (36.96%) using the equation 5.4.

$$P_s = \frac{R_{scintillation}(\infty) \times \frac{I_s}{I_t}}{R_{scintillation}}$$
$$P_t = \frac{R_{scintillation}(\infty) \times (1 - \frac{I_s}{I_t})}{R_{scintillation}}$$
$$P_r = \frac{R_{scintillation} - R_{scintillation}(\infty)}{R_{scintillation}} \quad (5.4)$$

where is equal to 29%, which is the percentage of non-quenched photons with infinite electric field.

Considering an initial total number of excited dimers N_0 for a deposited energy E_0, these dimers undergo de-excitation to the ground state through the three decay components. The number of exciters at a given time t can be mathematically represented as:

$$N(t) = P_s N_0 \times e^{-\frac{t}{\tau_s}} + P_t N_0 \times e^{-\frac{t}{\tau_t}} + P_r N_0 \times e^{-\frac{t}{\tau_r}} \quad (5.5)$$

The rate of excimer decays per unit time is defined as and can be expressed as:

$$f(t) = -\frac{dN(t)}{N_0 dt} = \frac{P_s}{\tau_s} \times e^{-\frac{t}{\tau_s}} + \frac{P_t}{\tau_t} \times e^{-\frac{t}{\tau_t}} + \frac{P_r}{\tau_r} \times e^{-\frac{t}{\tau_r}} \quad (5.6)$$

The probability density function (PDF) of de-excitation at time t, which represents the distribution of decay times for VUV photons in LXe, is denoted as f(t). Furthermore, the cumulative distribution function (CDF), indicating the probability that an excimer de-excites before time, is expressed as F(t).

$$F(t) = \int_{t0}^{t} f(t')dt' = -\left[P_s\left(e^{-\frac{(t-t_0)}{\tau_s}} - 1\right) + P_t\left(e^{-\frac{(t-t_0)}{\tau_t}} - 1\right) + P_r\left(e^{-\frac{(t-t_0)}{\tau_r}} - 1\right)\right] \quad (5.7)$$

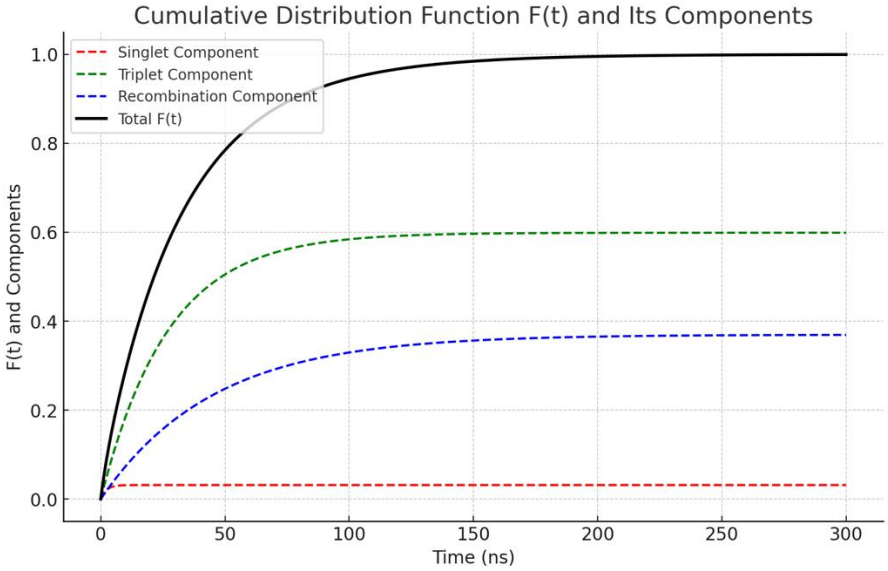

Fig 5.2: Probability distribution of excimer de-excitation prior to time t in liquid xenon under a 2 kV/cm electric field.

Figure 5.2 elucidates the probability distribution of excimer de-excitation occurring prior to a time t under an electric field of 2 kV/cm. The profound takeaway from this analysis is that a significant majority, approximately 78%, of photons are liberated in the first 50 ns.

In the equation 5.7, the function of F(t) is the cumulative distribution function, then the standard deviation can be found by calculating its corresponding probability density function. This is because for a continuous random variable, the F(t) is the integral of the PDF f(t), and the standard deviation is calculated using the PDF. Based on the calculated results, the mean of the probability density function corresponding to the cumulative distribution function is approximately 32.71 ns, the standard deviation is approximately 35.25 ns, and the variance is approximately 1242.41 ns.

The mean emission time for photons is markedly distinct from the average propagation time of vacuum ultraviolet photons within XEMIS2; the latter is a minimal 0.4 ns, as previously noted. The substantial difference between these two timescales is significant, to the extent

that the average propagation time may be considered negligible in comparison to the scintillation time. Therefore, in the subsequent simulation, we will solely consider the intrinsic scintillation time of xenon and disregard the propagation time.

5.2 TOT calibration correction

Section 5.2 delves into the detailed simulation of Time Over Threshold calibration by incorporating the mechanisms underlying scintillation signal generation. This approach is pivotal for refining the calibration process, ensuring that the TOT measurements accurately reflect the intrinsic behaviors of scintillation signals within the detection system.

At the core of this simulation is a comprehensive model that accounts for the dynamics of scintillation light production in liquid xenon, including the distinct decay times of singlet and triplet excited states and the impact of electron-ion recombination. By simulating the scintillation process, this section aims to more accurately predict the TOT response for various energy deposits. This simulation enhances the accuracy of energy measurement.

5.2.1 Characterization of shaper card response for one photoelectron

In the pursuit of establishing an accurate correlation between Time Over Threshold (TOT) and the count of photoelectrons, it is imperative to meticulously simulate and comprehend the electronic response of the shaping card to single photoelectron events. This understanding lays the groundwork for extrapolating the TOT response to multiple photoelectron scenarios, which are commonly encountered in practical applications of liquid xenon detectors.

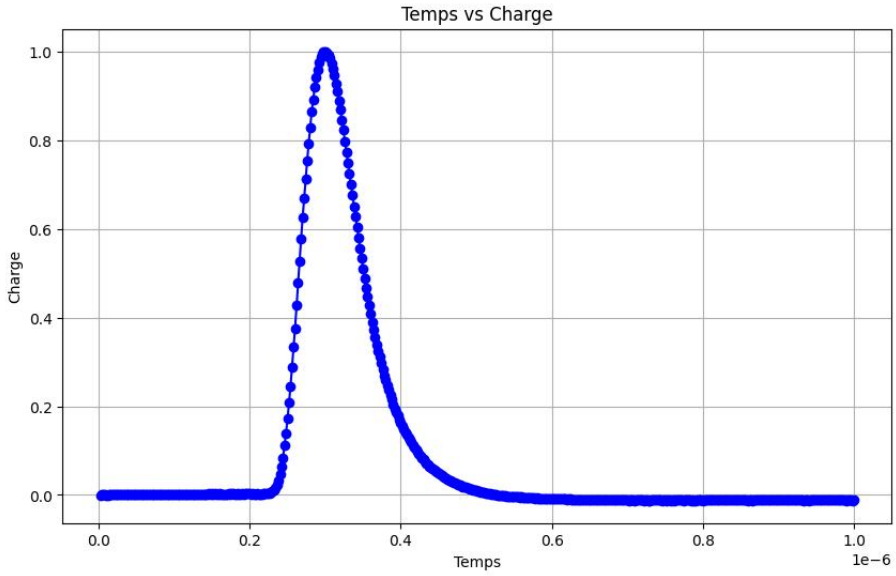

Fig 5.3: Normalized Response Curve of the Shaping Card to a Single Photoelectron Event

As elucidated in Figure 5.3, the response of the shaping card to a solitary photoelectron has been detected and characterized. The depicted curve is the culmination of averaging the outputs from 1000 such events, thereby ensuring a robust statistical foundation and mitigating the stochastic fluctuations inherent to single-event measurements. This approach yields a reliable representation of the typical response of the shaping card in a LXe detector system.

Normalization of the charge signal in the figure serves as a critical step in the simulation process. By scaling the charge to a unitary system, the data become independent of the absolute charge levels, thus offering a standardized comparison of the shaping card's response. Such normalization is essential for subsequent simulations that aim to model the detector's behavior across a spectrum of photoelectron counts. This standardized response serves as a pivotal reference for calibrating the detector's TOT response. It provides a detailed insight into the temporal evolution of the signal post-photoelectron detection, showcasing the characteristic peak and decay that are signatures of the shaping card's transformation of raw photodetection events into analyzable electronic signals.

Ultimately, the careful characterization of the shaping card's response, as encapsulated in Figure 5.3, underpin the accuracy of the TOT calibration process. This fundamental research enables the detector to precisely resolve the scintillation light signals, which is crucial for the accurate quantification of energy deposits within the LXe medium, a key performance metric for LXe-based detection systems. The integration of such detailed step into the calibration framework significantly enhances the detector's capability for precise and reliable

measurements, which are vital for advancing the frontiers of particle detection and instrumentation.

5.2.2 Validation of XRETOT response for single photon events

The calibration process outlined in Section 4 operates under the assumption that photon emissions are simultaneous and that the shaping card detects these photons concurrently. To validate the proposed model for the shaping card's response to single photon events, as introduced in the preceding section, it is imperative to employ a comparative approach. This involves the simulation outcomes, predicated on the notion of synchronous photon emission, against the empirical calibration results obtained using a controlled signal generator.

Such a validation strategy is critical for determining the veracity and applicability of the model within the operational framework of the detector system. By comparing the simulation predictions with the actual behavior as characterized by the generator-based calibration, we can evaluate the model's accuracy in replicating the temporal dynamics of photon detection.

This comparison not only tests the model's fidelity but also identifies potential discrepancies that may arise due to the idealized conditions assumed during the simulation. Any significant differences observed will prompt a re-examination and refinement of the simulation parameters, ensuring that the shaping card's model reflects the realistic conditions encountered during the detector's operation.

5.2.2.1 Simulation method

The simulation method adopted for validating the shaping card's response to single photon events integrates mathematical modeling with Monte Carlo simulation techniques to closely emulate the dynamics involved in photon detection and signal processing.

The core of the simulation is a function that models the decay processes associated with scintillation light, including the singlet, triplet, and recombination pathways. Each pathway is characterized by specific time constants and associated probabilities, reflecting the distinct temporal behaviors of these decay processes. But in this simulation, the assumption that photon emissions are simultaneous. To systematically explore the time over threshold (TOT)

for varying numbers of photoelectrons, the method iterates across a wide range of photoelectron counts. For each count:

1. Delayed Charge Simulation: The method simulates the time delays associated with each photoelectron's detection, based on the decay characteristics of the scintillation light. These delays are crucial for constructing a realistic temporal profile of the signal as it would be captured by the shaping card. However, for the purposes of this simulation, all photon emissions are assumed to be simultaneous, thereby setting the delay to zero.
2. Signal Construction: The cumulative effect of individual photoelectron signals is simulated by superimposing the delayed responses, thus forming a composite signal that represents the total response to the detected photoelectrons.
3. Noise Incorporation: To mimic the intrinsic electronic noise of the detection system, Gaussian noise is added to the composite signal. This step is essential for creating a realistic simulation of the signal that the shaping card processes, complete with the challenges posed by noise. Additionally, an uncertainty in the TOT recording, modeled by a Gaussian distribution with a standard deviation of ns, is included to account for timing inaccuracies.
4. TOT Analysis: The simulation then quantifies the TOT by identifying the duration over which the noisy composite signal exceeds a predefined threshold, In this context, the threshold is normalized to one photoelectron's signal strength. This analysis is critical for understanding how the shaping card's electronic characteristics influence the TOT measurement, a fundamental parameter in scintillation light detection.
5. Data Organization and Storage: The TOT data generated for each photoelectron count is meticulously saved for subsequent analysis. The method ensures systematic file naming and organization, facilitating easy access to the simulation results for comparison with empirical calibration data.

This comprehensive simulation approach aims to replicate the nuanced response of the shaping card to scintillation signals, from the initial photon detection to the electronic shaping and thresholding that define the TOT.

5.2.2.2 Simulation results

Figure 5.4 presents a comparative visualization of the TOT calibration process, juxtaposing the experimental results with those obtained from the simulation. Panel (a) displays the experimental results, while panel (b) shows the simulation results. The color-coded heatmaps represent the frequency of occurrences as a function of TOT against the number of photoelectrons (NPE). These heatmaps are pivotal in assessing the shaping card's performance and the efficacy of the simulation method.

In the experimental results (Figure 5.4a), a clear correlation between TOT and NPE is observable, with higher frequencies of longer TOT values at increased NPE. This trend is indicative of the expected physical behavior, where more photoelectrons result in a proportionally extended signal above the threshold. The simulation results (Figure 5.4b) aim to replicate this correlation. By employing the simulation method detailed in 5.3.2.1, the synthetic data seeks to capture the nuances of the shaping card's response to varying photon counts. The color gradient transitions from cooler to warmer hues denote ascending frequencies, providing an intuitive visualization of the TOT distribution's density. Crucially, the comparison between these two panels allows for a direct evaluation of the simulation model's fidelity. The degree of congruence between the experimental and simulated data sets speaks to the model's robustness and its potential utility in predicting the detector's behavior under different operational scenarios.

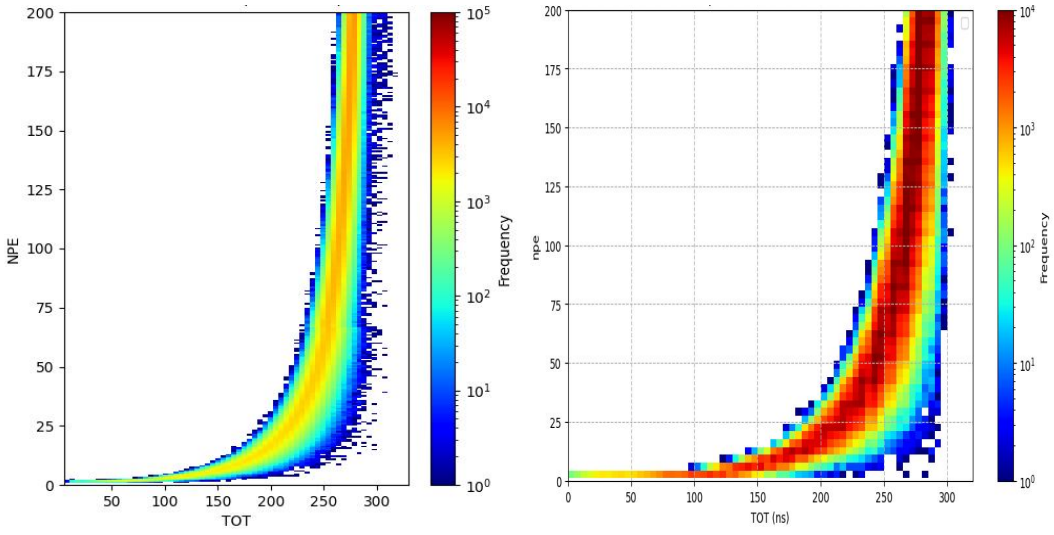

(a) Experimental results (b) Simulation results

Figure 5.4: Comparative analysis of NPE and TOT distributions: Experimental vs. Simulated Data

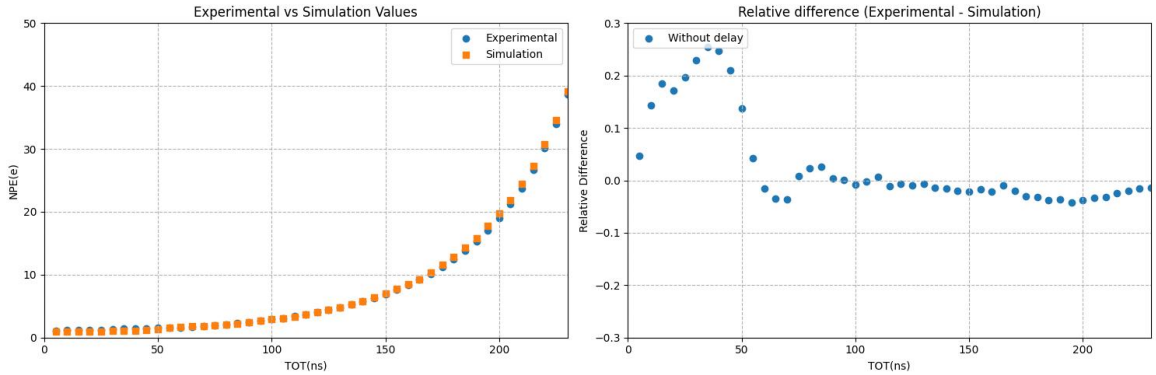

Fig 5.5: Mean number of photoelectrons as a function of TOT from experimental and simulated data.

Building upon the insights gleaned from Figure 5.4, Figure 5.5 serves to further elucidate the relationship between the TOT and the mean number of photoelectrons. This figure is integral to the discussion, showcasing the accuracy of the simulation model as it relates to the experimental data.

The left panel of Figure 5.5 depicts the mean npe values as a function of TOT, comparing the experimental findings (denoted by blue diamonds) with the simulation outputs (indicated by orange stars). The agreement between the two data sets across the spectrum of TOT values demonstrates the simulation's capability to closely mimic the actual shaping card response. The right panel offers a nuanced perspective on the model's precision, plotting the relative differences between the experimental data and the simulated outcomes. The distribution of data points around the zero line reveals the simulation's accuracy, with deviations providing critical feedback for model refinement.

The synthesis of the two panels in Figure 5.5 is indicative of a well-calibrated system where the simulation aligns with the empirical behavior of the detection process. This figure not only validates the simulation method discussed in Section 5.2.2.1 but also underscores the potential of the simulation to predict the shaping card's performance, which is vital for the calibration of time-resolved detectors in LXe-based detection systems.

5.2.3 TOT measurement simulation results by considering the scintillation signal mechanisms and PMT gain fluctuation

Building upon the methodologies established in the preceding sections, this portion of the study delves into the simulation results that account for the scintillation signal mechanisms. This simulation is more intricate as it incorporates the probabilistic nature of scintillation light production and its interaction with the detection system, thus offering a more nuanced view of the shaping card's performance.

The simulation integrates the physical processes that generate scintillation light in LXe, which is characterized by its singlet and triplet excitation states with distinct temporal decay profiles. The interaction of these states, alongside the electron-ion recombination dynamics, fundamentally influences the shaping card's response. By incorporating these mechanisms, the simulation aims to reflect the stochastic emission of scintillation photons and their subsequent detection, a departure from the simplified assumption of simultaneous photon emission used in prior models.

Section 5.2.3.1 will introduce considerations of simulation for the scintillation signal mechanisms within the LXe. Moreover, Section 5.2.3.2 will take into account the variations in the amplification process of PMTs. Finally, Section 5.2.3.3, will culminate the detailed simulation analyses by presenting the outcomes derived from the comprehensive models discussed previously.

5.2.3.1 Delayed Simulation

The simulation now provides a more detailed temporal resolution of the shaping card's response, capturing the variance in time delays associated with the stochastic nature of photon emission and detection, illustrated in Figure 5.6.

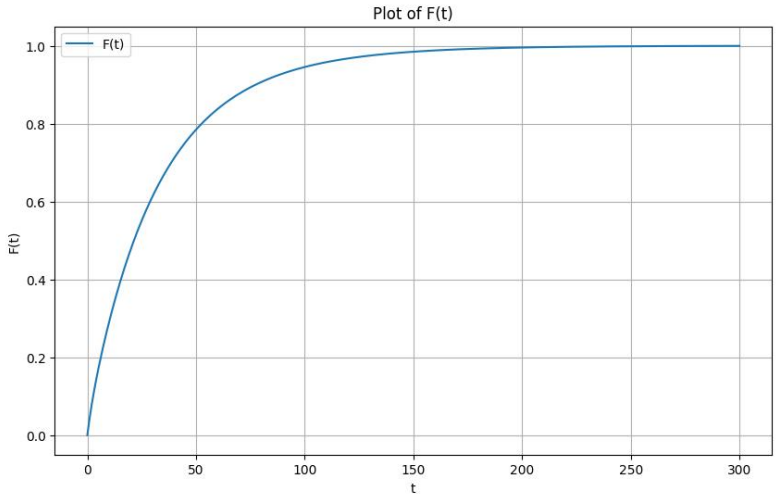

Fig.5.6: Simulated Probability Distribution of Excimer De-excitation Timings in Liquid Xenon at 2 kV/cm Electric Field

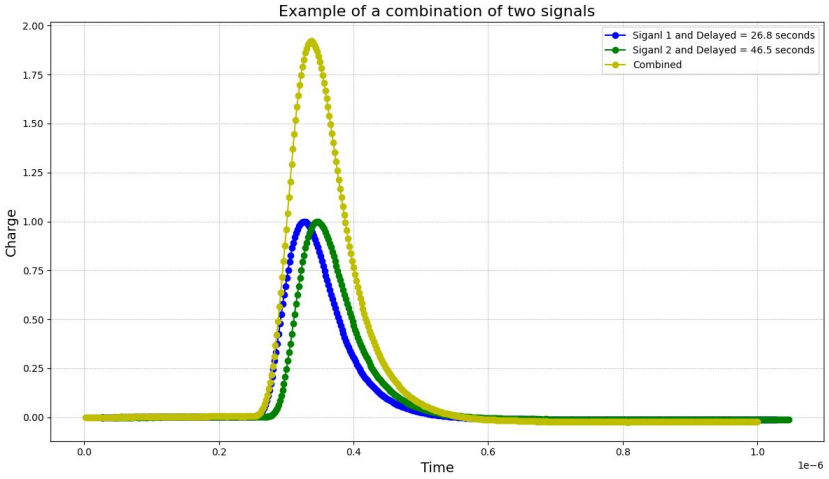

(a)

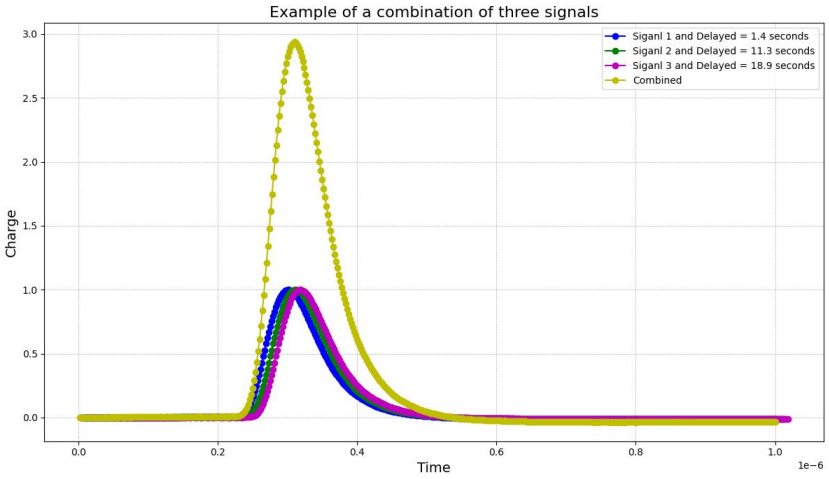

(b)

Figure 5.7: Example of composite signal formation from the superposition of (a)two individual events and (b)three distinct events.

Figures 5.7a and 5.7b exemplify the intricacies of signal composition within the context of multiple photonic interactions. These visual aids are pivotal in dissecting the shaping card's aptitude to discern and integrate multiple scintillation events that transpire in quick succession, a scenario typical in high-density photon environments. The elucidation of the shaping card's responsiveness to such events is critical for the precise calibration and consistent performance of scintillation detectors deployed in sophisticated experimental arrays. These figures underscore the importance of high-fidelity temporal resolution and the shaping card's role in the accurate reconstruction of overlapping scintillation events.

5.2.3.2 PMT gain fluctuation

In the experimental setup, utilizing LED illumination posed a significant challenge for exposing the PMTs to a singular stream of photons within the Liquid Xenon Time Projection Chamber.This complexity made it inherently difficult to isolate and study the PMT's response to single photoelectron events. The experimental data invariably included contributions from noise signals and occurrences of double photoelectron signals, necessitating their consideration in the analysis of the SPE (Single Photon Electron) spectrum.

To address this, a fitting approach involving a multi-Gaussian function was employed. This function was designed to model the distribution of the time-integrated PSA output signals, which correspond to the detection of a few photoelectrons. The mathematical representation of this fitting function is:

$$S_{PSA}(x) = A_{Noise} exp\left(-\frac{(x-\mu_{Noise})^2}{2{\sigma_{Noise}}^2}\right) + A_1 exp\left(-\frac{(x-\mu_{SE})^2}{2{\sigma_{SE}}^2}\right) + A_2 exp\left(-\frac{(x-2\mu_{SE})^2}{4{\sigma_{SE}}^2}\right) \tag{5.8}$$

The calculation of the average gain, which represents the current amplification, is formulated as follows:

$$G_{PMT} = \frac{\int V_{PSA}(t)dt}{k_{Q\_PSA}} = \frac{\mu_{SE}}{k_{Q\_PSA}} \tag{5.9}$$

where G_{PMT} denotes the average gain, $V_{PSA}(t)$ is the output voltage as a function of time, k_{Q_PSA} is a linear coefficient and μ_{SE} is the expected value associated with the single

photoelectronpeak. Moreover, the fluctuation in gain, quantified by the standard deviation during the electron amplification process, is provided by:

$$\Delta G_{PMT} = \frac{\sigma_{SE}}{k_{Q\_PSA}} \tag{5.10}$$

Here, ΔG_{PMT} signifies the gain fluctuation, and σ_{SE} stands for the standard deviation corresponding to the SPE peak distribution.

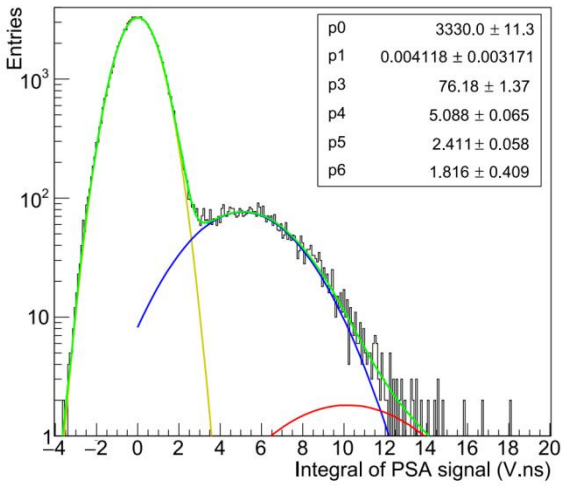

Fig. 5.8: Example of distribution of the integral over time of the PSA signal with LED-on for channel 1 with the PMT supply voltage set to 815 V.

Specifically, $p_0 = A_{noise}$ represents the amplitude of the noise component,
$p_1 = \mu_{noise}$ denotes the mean of the noise distribution,
$p_3 = A_1$ signifies the amplitude of the single electron peak,
$p_4 = \mu_{SE}$ is the mean of the single electron signal,
$p_5 = \sigma_{SE}$ stands for the standard deviation of the single electron signal,
and p_6=A2 reflects the amplitude of the second signal peak.

An example of the distribution of the integral over time of the PSA output signal in response to the SPEs for the PMT of XEMIS1 with the supply voltage set to 815 V is presented in Figure5.8. In the fitted model presented, parameters p_0, p_1, p_3, p_4, p_5 and p_6 correspond to the coefficients of the three-Gaussian function utilized to fit the integral of the PSA signal.

Additionally, it is important to note that within the context of the three-Gaussian fit function, the parameter σ_{Noise}, which would typically be denoted as p_2, is fixed[149]. This implies that

during the fitting process, σ_{Noise} does not vary and is set to a constant value, providing a constraint that shapes the noise component of the model while allowing the other parameters to adjust to best fit the empirical data. In this figure, we can calculate the ration of gain fluctuation over gain, which gives:

$$\frac{\Delta G_{PMT}}{G_{PMT}} = \frac{\sigma_{SE}}{\mu_{SE}} = \frac{p_5}{p_4} = 50\% \tag{5.11}$$

In the subsequent phase of our simulation, we will incorporate a refined model to simulate the gain variability inherent in PMTs, a critical component in the accurate rendering of scintillation detection processes. This model adopts a Gaussian distribution for the PMT gain, characterized by a mean of 1 and a standard deviation, set at 50% of the mean value. This parameterization is designed to emulate the observed fluctuations in PMT gain, thereby enhancing the realism and precision of the simulated detection signals. Given the physical impossibility of a negative gain in actual PMT operations, our model introduces a corrective mechanism whereby any gain values calculated to be negative—as an artifact of the Gaussian distribution—are reassigned a value of zero. This adjustment is crucial for preserving the physical validity of the simulation outcomes, ensuring that all simulated gain values remain within a plausible range.

5.2.3.3 Simulation results

Figure 5.9 presents a comparative analysis between experimental data and simulated TOT values under two distinct scenarios: one simulation accounts for the temporal delay in photon emission, and the other presupposes instantaneous photon emission. The left panel charts the average number of photoelectrons versus TOT, juxtaposing empirical results with those of the simulations. The simulation that incorporates photon emission delays is indicated by the orange curve, while the scenario assuming immediate emission is illustrated by the blue curve.

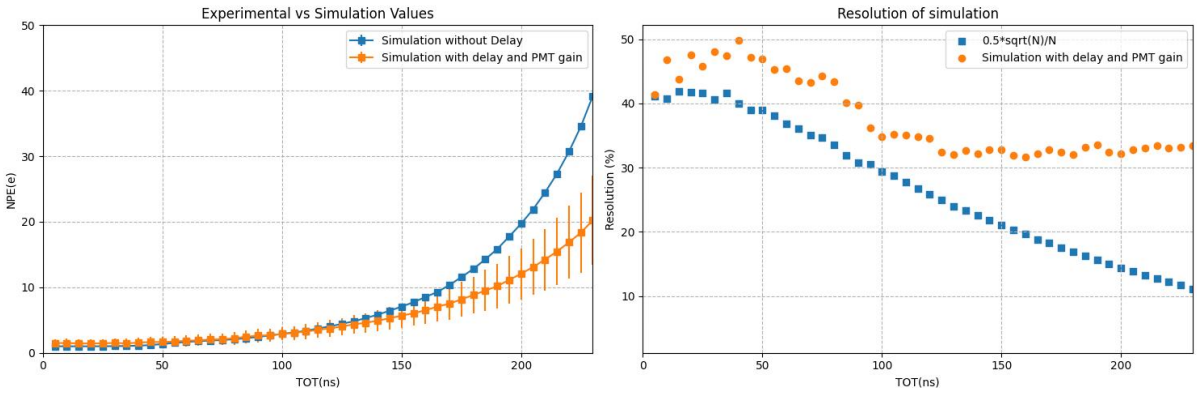

Fig 5.9 : Analysis of simulated TOT responses with delays considering the flutuaction of PMT gain and scintillation procedure.

We define the resolution for a given TOT as following:

$$\text{resolution} = \frac{\sigma_{TOT}}{\text{TOT}} \times 100\% \tag{5.12}$$

The right panel of figure 5.9 meticulously evaluates the resolution of the simulations, plotting the percentage resolution as a function of TOT. It draws a distinction between the advanced simulation that factors in both PMT gain variability and emission timing delays (depicted by the orange data points) and the hypothetical baseline resolution under perfect conditions (represented by the blue squares). This comparison is pivotal as it highlights the disparities in resolution that emerge upon introducing complex variables such as PMT gain fluctuations and photon emission delays into the simulation framework. Significantly, the graph accentuates that the resolution has a maximun of 50% and approaches a saturation point at 30%.

5.2.4 Discussion and Perspective

In summarizing the findings of Section 5.2, we must emphasize the rigour of the simulation work carried out to refine the TOT calibration, which included the complex physical processes of scintillation signal generation in liquid xenon (LXe) detectors. These simulations helped to elucidate the nuances of light generation, electron-ion recombination, and the behavior of the shaping card under different conditions. The properties of the

response of the shaping card to single photoelectron events are particularly critical, laying the foundational understanding and extending it to complex multi-photoelectron scenarios.

Nonetheless, a critical presupposition in these simulations must be brought to light. The methodologies employed have assumed a uniform probability distribution for the number of photons, which, while convenient for modeling purposes, does not necessarily reflect the true probabilistic nature of photon detection. In practical terms, the likelihood of photon detection is intrinsically linked to the characteristics of the XEMIS2 instrumentation—a factor that remains undefined until the system becomes operational.

Thus, the results presented within this chapter should be considered preliminary. They serve as an initial framework that will undoubtedly require recalibration once empirical data from the functioning XEMIS2 detector become available. At that juncture, the probability distribution for photon detection can be properly characterized, grounded in actual performance metrics rather than theoretical assumptions.

This acknowledgment does not diminish the value of the current simulation efforts but rather situates them appropriately within the iterative process of scientific inquiry. Once XEMIS2 is operational, the calibration strategies and simulation models will be revisited and refined, ensuring that the nuances of the actual photon detection probabilities are fully integrated, thereby enhancing the accuracy and reliability of the TOT calibration process.

5.3 Time measurement correction

In this section, we delve into the method of correcting time measurements within the context of scintillation signal detection, as applied in the XEMIS2 project. This correction is important for improving the precision of temporal data obtained from scintillation events, which contributes significantly to the overall accuracy and reliability of imaging in future medical applications.

5.3.1 Comparison of simulation results with experimental results

The main objective of this chapter is to evaluate the process of improving the time measurement methodology by comparing the simulation results with the experimental data. This comparison helps us to identify any differences caused by assumptions or

simplifications in the simulation process. By looking closely at these differences, we can identify parts of the time measurement process that need to be corrected or improved. This comparison also helps to confirm that the simulation model is accurate and reflects what happens in a real experiment.

Figure 5.10 exhibits a comparative analysis of Leading Edge (LE) and Time Over Threshold (TOT) distributions between (a) experimental and (b) simulated data. Panel (a) details the experimental data, depicting the correlation between the TOT and the LE. This color-coded heat map offers a visual representation of event frequency across the range of TOT values, which are seen to increase with longer LE times, indicating a relationship between the duration of signal and the time at which it's initially detected. Panel (b) parallels this with the simulated data, where similar patterns are expected to be observed. Disparities between these two panels would signal areas that require adjustment in the simulation parameters or highlight phenomena not adequately captured by the current simulation.

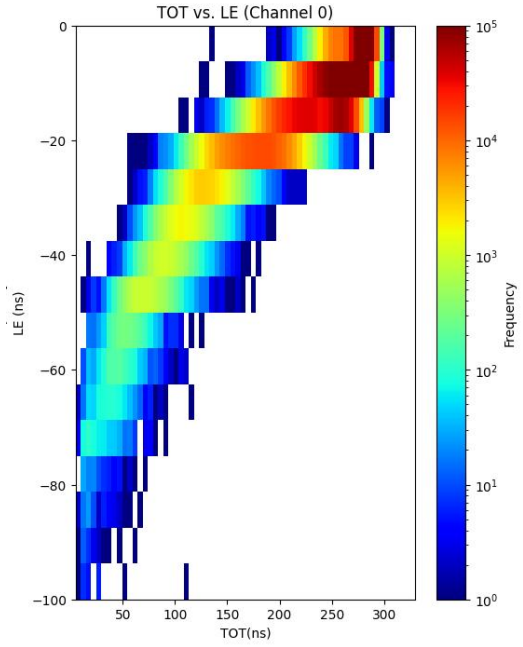

(a)

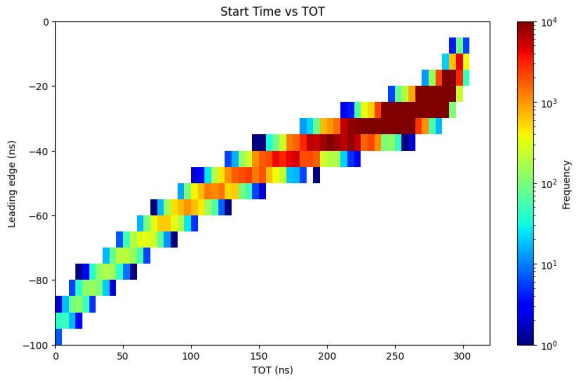

(b)

Fig 5.10 : Comparative analysis of Leadng edge and TOT distributions: (a) Experimental vs. (b) Simulated Data

Figure 5.11 offers an insightful visualization of the correlation between the Leading Edge and TOT, delineating the average values derived from empirical investigations alongside those generated by simulation. The graph is refined by a polynomial fit that not only smoothens the data trajectory but also enhances interpretability of the overarching trends.

A particular point of analytical interest within the lower TOT range, as highlighted in Figure 5.11, pertains to the signal-to-noise ratio. In this region, the noise component is relatively more significant compared to the signal, which can obscure the signal's true characteristics and complicate the precise emulation of experimental outcomes in the simulation environment. This is predominantly observed at reduced TOT values, where even minimal noise can disproportionately influence the results, thus presenting a challenge to accurately capture the fidelity of the empirical data.

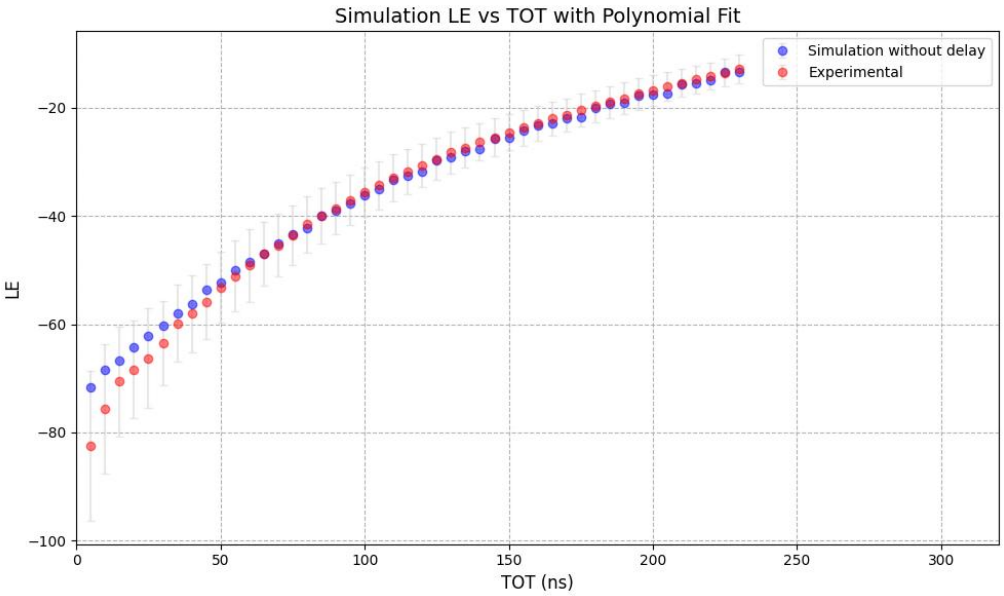

Fig 5.11 : Mean of Leadng edge and TOT.

Despite these complexities, the graph displays a notable correspondence between the mean LE times as a function of TOT, signified by the experimental data's red markers and the purple markers of simulation without delay effects. This matching suggests that the simulation model effectively can represente the essential dynamics of scintillation event detection.

5.3.2 Time measurement simulation results by considering the scintillation signal mechanisms and PMT gain fluctuation

In this subsection, we scrutinize the simulation results that integrate complex scintillation signal mechanisms and PMT gain fluctuation effects. Our simulations meticulously model the generation of scintillation light and its intricate interactions with the detection system, including phenomena such as photon absorption, reflection, and photoelectron generation by photomultiplier tubes (PMTs). Through these simulations, we aim to distill a clearer understanding of the temporal dynamics of scintillation signals, including rise and decay times, and how these influence time measurement accuracy within our detection apparatus.

These nuanced simulations are essential for uncovering and quantifying potential sources of timing errors. Delays within the signal processing chain, variability in PMT response, and extrinsic noise factors are among the considerations examined for their contribution to time

measurement discrepancies. Such detailed analysis is invaluable for developing targeted corrective strategies, enabling refinement of the time measurement techniques to ensure high precision in scintillation event detection. The overarching goal is to enhance the temporal accuracy of our measurements, thereby improving the fidelity of our experimental observations and the reliability of subsequent analyses within the scope of the XEMIS2 project.

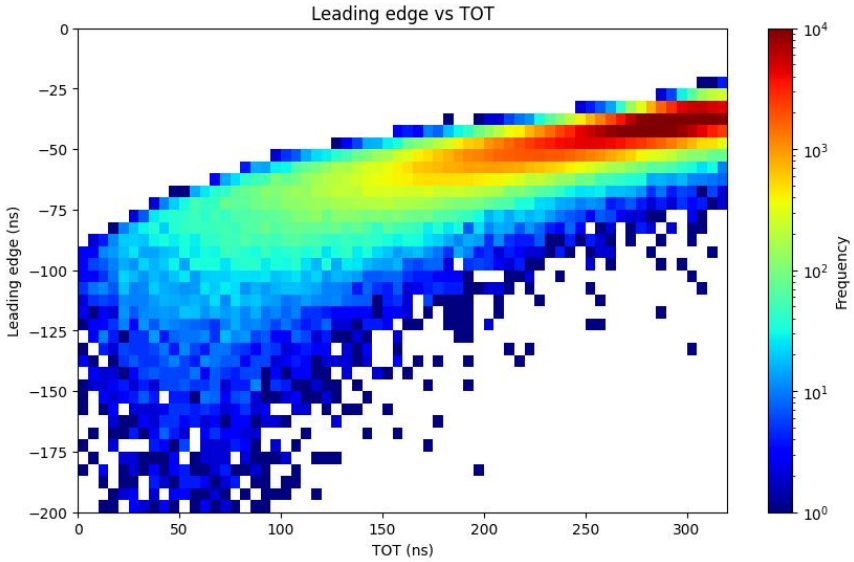

Fig 5.12 : Simulated Leadng edge vs TOT distribution considering scintillation signal mechanisms and PMT gain fluctuation

Figure 5.12 portrays the distribution of Leading Edge (LE) times versus Time Over Threshold (TOT) values while factoring in the intricacies of scintillation signal mechanisms and photomultiplier tube (PMT) gain fluctuations. The heat map vividly demonstrates the frequency of occurrences across various LE and TOT combinations, with cooler colors representing lower frequencies and warmer colors indicating higher frequencies. This visualization encapsulates the consequences of introducing realistic scintillation dynamics and PMT variability into the simulation.

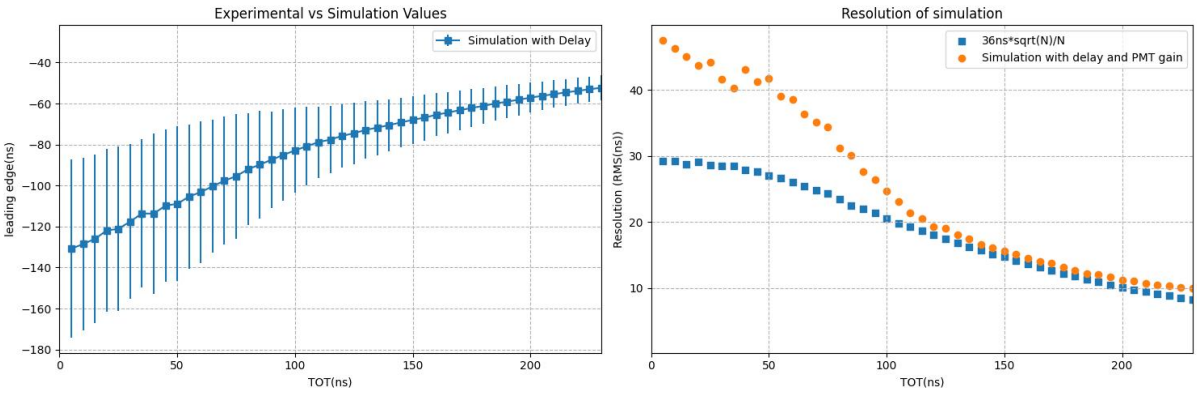

Fig 5.13 : Analysis of simulated Leading edge and TOT relation with delays considering the flutuaction of PMT gain and scintillation procedure.

Figure 5.13 provides the graphical analysis of the Leading Edge versus TOT relationship as influenced by the incorporation of delays reflective of PMT gain fluctuation and the scintillation process. The left panel of Figure 5.13 offers a precise illustration of the simulated mean Leading Edge (LE) values against Time Over Threshold (TOT). Error bars in this graph elucidate the range of variation present within the simulation. These error bars are particularly telling of the simulated data's consistency and the confidence levels associated with the mean values. Moving to the right panel, the graph meticulously quantifies the resolution of the simulation, articulating it as a percentage against TOT values. The figure presents a comparative analysis, juxtaposing the baseline resolution under idealized simulation conditions (blue) with a resolution that takes into account real-world complexities such as PMT gain fluctuations and the inherent randomness of the scintillation process (orange). The stark contrast between the two scenarios highlights the impact of these additional factors on the resolution of the system, and it is particularly noteworthy that the resolution is clearly affected for small TOT values.

As can be seen from the analysis in Figure 5.13, the temporal resolution of the simulations approaches the baseline resolution limit as the Time Over Threshold (TOT) value increases. The plot of resolution as a function of TOT value in the right panel illustrates this convergence; for larger TOT values, the orange data points representing simulations incorporating actual delay and PMT gain variations increasingly coincide with the blue points indicating ideal conditions.

5.3.3 Discussion and Perspective

The analyses presented in Sections 5.3.1 and 5.3.2 culminate in a critical reflection on the process of time measurement correction within the context of the XEMIS2 project. The correction of time measurements is a meticulous process that necessitates not only a deep understanding of the underlying scintillation phenomena but also an appreciation for the subtleties of the experimental apparatus involved.

With the comparative analysis provided in Figure 5.10, we see the gap between the experimental and simulated data in terms of the distribution of the leading edge (LE) and time over threshold (TOT). This allows us to detect discrepancies that may be caused by theoretical assumptions or simulation simplifications, thus identifying areas that need to be recalibrated.

Figure 5.11 reveals the complexity at low TOT values, when the signal-to-noise ratio will be a significant challenge. Here the ability of the simulation to reflect the empirical results is put to the test, highlighting the importance of the accuracy of the simulation execution and its subsequent interpretation.

Figure 5.12 illustrates the distribution of LE and TOT values, bringing into sharp focus the impact of PMT gain fluctuations and flicker signalling mechanisms. This intuitive evidence reinforces the importance of considering real-world variations when endeavouring to achieve high-precision time measurements.

This emphasis is reinforced in Figure 5.13, which compares the average LE value of the simulation and its resolution with the TOT value. As the TOT values increase, we find that the resolution of the simulation tends to converge towards the baseline limit, highlighting the inherent limitations of what can be achieved in terms of temporal resolution within the constraints of the system design and operating parameters.

In summarising these findings, we recognise that while our current simulations provide a detailed initial model, the reality of the XEMIS2 project operational data may require further refinement. The simulations assume a certain homogeneity in photon detection probabilities -

a simplification that will need to be re-evaluated as empirical data from the XEMIS2 in-service detectors become available.

With this in mind, the simulation results discussed in this thesis should be viewed as a foundational step - an important but preliminary step in calibrating the intricate dance between photons and electronics within the XEMIS2 instrument. As the system transitions from theoretical construction to real-world operation, these simulation models will be revisited and revised to ensure that our temporal measurement calibration strategy is as refined and accurate as possible, reflecting the true behaviour of scintillation events in liquid xenon.

5.4 Conclusion

This chapter has carefully explored the details of Time Over Threshold (TOT) calibration in the XEMIS2 liquid xenon (LXe) detection system. It presents a thorough correction method based on a deep understanding of how scintillation light travels and how signals are characterized within LXe. These calibration corrections are crucial for ensuring the accuracy and reliability of the XEMIS2 detector's measurements, which directly affect its scientific results.

The initial exploration of the propagation of scintillation light in LXe set the stage by identifying the critical parameters that influence photon transmission. This foundational knowledge informed the subsequent detailed characterization of scintillation signals and their impact on the TOT measurements. With the XEMIS2 system's requirements in mind, we developed and validated a model of the shaping card's response to individual photoelectrons. This model serves as a cornerstone in the calibration process, capturing the essential temporal response characteristics of the detector's electronic system.

Validation against empirical data established the credibility of our simulation approach, integrating complex scintillation signal mechanisms into the calibration process. The simulation results presented in Section 5.2.3 encapsulate this integration, offering a refined perspective on the scintillation signal detection. Our simulations, juxtaposed with experimental findings, provide critical insights into the detector's behavior, enabling us to fine-tune our calibration strategy to address real-world complexities such as stochastic photon emission delays.

The outcomes of this research have significant implications for LXe detector technology, enhancing XEMIS2's capability to deliver precise and reliable measurements. These advancements are not merely incremental; they represent a leap forward in our ability to probe the elusive nature of dark matter and investigate the properties of neutrinos.

Conclusion and perspective

In the intricate field of nuclear medicine imaging, the introduction of the XEMIS2 system marks a key advancement, not only a leap in technological sophistication, but also a thoughtful improvement in diagnostic accuracy and safety. This innovation, which utilizes liquid xenon (LXe) as the detection medium, ushers in a new era of imaging modalities, achieving both high sensitivity and a dramatic reduction in radiation exposure that significantly exceeds that of existing technologies. While fully recognizing the key developments in SPECT, PET and the nascent 3γ imaging technology, this thesis elegantly shifts its central focus to an in-depth exploration of the XEMIS2 system. Particular emphasis is placed on the refinement of the light calibration process and its improvement, and the role of the Frisch grid in optimizing detector performance is touched upon, albeit to a lesser extent.

Designed specifically for small animal imaging, the XEMIS2 system epitomizes the convergence of nuclear medicine innovation with real-world applications.The LXe's exceptional features will facilitate extraordinary clarity in imaging and will set a new benchmark for efficiency and safety in diagnostic practice. The choice of liquid xenon as the detection medium marks a significant paradigm shift from traditional methods, dramatically reducing the radiation dose and/or improving the quality and fidelity of captured images.

The key to the exemplary nature of the XEMIS2 system is its rigorous calibration process, particularly in the areas of scintillation signal detection and time over threshold (TOT) calibration. These intricate processes are fundamental, not only for program validation, but also critical to honing the system's responsiveness to radiated signals.Calibration of the XEMIS2 is a multilayered process, from threshold calibration and unit conversions to the subtle optimization of time measurement techniques, with each stage carefully designed to improve the system's diagnostic accuracy.

A particularly illuminating part of the thesis is the light calibration process. The calibration of the scintillation light in the system is crucial to accurately localize and quantify the interactions in the LXe medium. Through sophisticated calibration methods, including the innovative TOT calibration method, the XEMIS2 system achieves a level of accuracy and reliability. These improvements in the optical calibration process are not just incremental, but a major leap forward in our ability to perform subtle and precise diagnostics.

Looking ahead, advances in optical calibration and subtle improvements to the XEMIS2 system bode well for the future of nuclear medicine imaging. As the system transitions from the development phase to broader clinical applications, its potential to change the diagnostic standard is enormous. However, the path forward is accompanied by challenges, notably how to integrate this advanced imaging system into routine clinical practice and ensure that it is fully clinically validated. However, these obstacles also reveal opportunities for interdisciplinary collaboration, bringing together expertise from physics, engineering, biology and medicine to lead the future of diagnostics.

The impact of the XEMIS system, particularly its advancements in light calibration, extends well in the field of technology improvement. It promises to bring about a revolution in patient care, with the potential to detect diseases earlier and more accurately, and to tailor treatment to the varying needs of patients. This aligns seamlessly with the quintessential goal of medical diagnostics: enhancing patient outcomes and quality of life. As we stand on the brink of this new era, the comprehensive examination of the XEMIS system serves not just as an affirmation of progress in nuclear medical imaging but as a beacon for future exploration and innovation.

In essence, this thesis represents a harmonious blend of historical context, technological innovation, and a forward-looking perspective within the sphere of nuclear medical imaging. The meticulous study of the XEMIS2 system, especially its advanced light calibration processes, narrates a story of ongoing evolution and potential. Moving forward, the insights garnered and the foundation laid by this work promise to deepen our understanding and application of nuclear medical imaging, inspiring continued advancement and excellence in the quest for diagnostic tools that are more precise, safer, and inherently centered on patient care.

REFERENCE

(1) *Medical Image Processing: Techniques and Applications*; Dougherty, G., Ed.; Biological and Medical Physics, Biomedical Engineering; Springer New York: New York, NY, 2011. https://doi.org/10.1007/978-1-4419-9779-1.

(2) Kasban, H.; El-Bendary, M. A. M.; Salama, D. H. A Comparative Study of Medical Imaging Techniques. **2015**.

(3) *Biomedical Imaging*; Mudry, K. M., Plonsey, R., Bronzino, J. D., Eds.; Principles and applications in engineering; CRC Press: Boca Raton, Fla, 2003.

(4) R F., M. *A Century of X-Rays and Radioactivity in Medicine: With Emphasis on Photographic Records of the Early Years*; CRC Press; 1993.

(5) Magiorkinis, E.; Vladimiros, L.; Diamantis, A. The Early History of Military Radiology (1896-1916): From Wilhelm Conrad Röntgen to the First World War. *Balk. Mil. Med. Rev.* **2010**, *Vol. 13* (No. 4), 163–169.

(6) Artico, M.; Spoletini, M.; Fumagalli, L.; Biagioni, F.; Ryskalin, L.; Fornai, F.; Salvati, M.; Frati, A.; Pastore, F. S.; Taurone, S. Egas Moniz: 90 Years (1927–2017) from Cerebral Angiography. *Front. Neuroanat.* **2017**, *11*, 81. https://doi.org/10.3389/fnana.2017.00081.

(7) Kosyakovsky, L. B.; Austin, P. C.; Ross, H. J.; Wang, X.; Abdel-Qadir, H.; Goodman, S. G.; Farkouh, M. E.; Croxford, R.; Lawler, P. R.; Spertus, J. A.; Lee, D. S. Early Invasive Coronary Angiography and Acute Ischaemic Heart Failure Outcomes. *Eur. Heart J.* **2021**, *42* (36), 3756–3766. https://doi.org/10.1093/eurheartj/ehab423.

(8) Mustafi, D.; Saraf, S. S.; Shang, Q.; Olmos De Koo, L. C. New Developments in Angiography for the Diagnosis and Management of Diabetic Retinopathy. *Diabetes Res. Clin. Pract.* **2020**, *167*, 108361. https://doi.org/10.1016/j.diabres.2020.108361.

(9) Sudoł-Szopińska, I.; Martinoli, C.; Panas-Goworska, M. History Page: Leaders in MSK Radiology Karl Dussik, 1908–1968: Pioneer of MSK Ultrasonography. *Semin. Musculoskelet. Radiol.* **2021**, *25* (01), 184–185. https://doi.org/10.1055/s-0040-1722207.

(10) Newman, P. G.; Rozycki, G. S. THE HISTORY OF ULTRASOUND. *Surg. Clin. North Am.* **1998**, *78* (2), 179–195. https://doi.org/10.1016/S0039-6109(05)70308-X.

(11) Leighton, T. G. What Is Ultrasound? *Prog. Biophys. Mol. Biol.* **2007**, *93* (1–3), 3–83. https://doi.org/10.1016/j.pbiomolbio.2006.07.026.

(12) Chan, V.; Perlas, A. Basics of Ultrasound Imaging. In *Atlas of Ultrasound-Guided Procedures in Interventional Pain Management*; Narouze, S. N., Ed.; Springer New York: New York, NY, 2011; pp 13–19. https://doi.org/10.1007/978-1-4419-1681-5_2.

(13) Avola, D.; Cinque, L.; Fagioli, A.; Foresti, G.; Mecca, A. Ultrasound Medical Imaging Techniques: A Survey. *ACM Comput. Surv.* **2022**, *54* (3), 1–38. https://doi.org/10.1145/3447243.

(14) Hsieh, J.; Flohr, T. Computed Tomography Recent History and Future Perspectives. *J. Med. Imaging* **2021**, *8* (05). https://doi.org/10.1117/1.JMI.8.5.052109.

(15) Uldin, T. Virtual Anthropology – a Brief Review of the Literature and History of Computed Tomography. *Forensic Sci. Res.* **2017**, *2* (4), 165–173. https://doi.org/10.1080/20961790.2017.1369621.

(16) Liang, Z.-P.; Lauterbur, P. C. PRINCIPLES OF MAGNETIC RESONANCE IMAGING.

(17) Geva, T. Magnetic Resonance Imaging: Historical Perspective. *J. Cardiovasc. Magn. Reson.* **2006**, *8* (4), 573–580. https://doi.org/10.1080/10976640600755302.

(18) Soergel, D. W. Parahydrogen Hyperpolarized Metabolites and Spin Dynamics at High Magnetic Field.

(19) Anderson, C. J.; Ling, X.; Schlyer, D. J.; Cutler, C. S. A Short History of Nuclear Medicine. In *Radiopharmaceutical Chemistry*; Lewis, J. S., Windhorst, A. D., Zeglis, B. M.,

Eds.; Springer International Publishing: Cham, 2019; pp 11–26. https://doi.org/10.1007/978-3-319-98947-1_2.
(20) Carlson, S. A Glance At The History Of Nuclear Medicine. *Acta Oncol.* **1995**, *34* (8), 1095–1102. https://doi.org/10.3109/02841869509127236.
(21) Wheat, J.; Currie, G.; Davidson, R.; Kiat, H. An Introduction to Nuclear Medicine. *Radiographer* **2011**, *58* (3), 38–45. https://doi.org/10.1002/j.2051-3909.2011.tb00154.x.
(22) Hutton, B. F. The Origins of SPECT and SPECT/CT. *Eur. J. Nucl. Med. Mol. Imaging* **2014**, *41* (S1), 3–16. https://doi.org/10.1007/s00259-013-2606-5.
(23) Groch, M. W.; Erwin, W. D. SPECT in the Year 2000: Basic Principles. *J. Nucl. Med. Technol.* **2000**, *28* (4).
(24) Jaszczak, R. J. The Early Years of Single Photon Emission Computed Tomography (SPECT): An Anthology of Selected Reminiscences. *Phys. Med. Biol.* **2006**, *51* (13), R99–R115. https://doi.org/10.1088/0031-9155/51/13/R07.
(25) Khalil, M. M.; Tremoleda, J. L.; Bayomy, T. B.; Gsell, W. Molecular SPECT Imaging: An Overview. *Int. J. Mol. Imaging* **2011**, *2011*, 1–15. https://doi.org/10.1155/2011/796025.
(26) Arsanjani, R.; Xu, Y.; Dey, D.; Vahistha, V.; Shalev, A.; Nakanishi, R.; Hayes, S.; Fish, M.; Berman, D.; Germano, G.; Slomka, P. J. Improved Accuracy of Myocardial Perfusion SPECT for Detection of Coronary Artery Disease by Machine Learning in a Large Population. *J. Nucl. Cardiol.* **2013**, *20* (4), 553–562. https://doi.org/10.1007/s12350-013-9706-2.
(27) Jagust, W.; Thisted, R.; Devous, M. D.; Van Heertum, R.; Mayberg, H.; Jobst, K.; Smith, A. D.; Borys, N. SPECT Perfusion Imaging in the Diagnosis of Alzheimer's Disease: A Clinical-Pathologic Study. *Neurology* **2001**, *56* (7), 950–956. https://doi.org/10.1212/WNL.56.7.950.
(28) La Fougère, C.; Rominger, A.; Förster, S.; Geisler, J.; Bartenstein, P. PET and SPECT in Epilepsy: A Critical Review. *Epilepsy Behav.* **2009**, *15* (1), 50–55. https://doi.org/10.1016/j.yebeh.2009.02.025.
(29) Beheshti, M.; Langsteger, W.; Fogelman, I. Prostate Cancer: Role of SPECT and PET in Imaging Bone Metastases. *Semin. Nucl. Med.* **2009**, *39* (6), 396–407. https://doi.org/10.1053/j.semnuclmed.2009.05.003.
(30) Lerman, H.; Lievshitz, G.; Zak, O.; Metser, U.; Schneebaum, S.; Even-Sapir, E. Improved Sentinel Node Identification by SPECT/CT in Overweight Patients with Breast Cancer.
(31) Uematsu, T.; Yuen, S.; Yukisawa, S.; Aramaki, T.; Morimoto, N.; Endo, M.; Furukawa, H.; Uchida, Y.; Watanabe, J. Comparison of FDG PET and SPECT for Detection of Bone Metastases in Breast Cancer. *Am. J. Roentgenol.* **2005**, *184* (4), 1266–1273. https://doi.org/10.2214/ajr.184.4.01841266.
(32) Tjuvajev, J. G.; Macapinlac, H. A.; Daghighian, F.; Scott, A. M.; Ginos, J. Z.; Finn, R. D.; Kothari, P.; Desai, R.; Zhang, J.; Beattie, B.; Graham, M.; Larson, S. M.; Blasberg, R. G. Imaging of Brain Tumor Proliferative Activity with Iodine-131-Iododeoxyuridine. **1994**.
(33) Koral, K. F.; Zasadny, K. R.; Kessler, M. L.; Luo, J.-Q.; Buchbinder, S. F. Monoclonal Antibody Therapy of Lymphoma Patients.
(34) M W, H.; J M, F.; R A, B. Carcinoid Tumors: Iodine-131 MIBG Scintigraphy. *Radiology* **1989**, *172* (3), 699–703.
(35) M J, G. Imaging of Irradiated Liver with Tc-99m-Sulfur Colloid and Tc-99m-IDA. *Clin. Nucl. Med.* **1981**, *6* (9), 399–402.
(36) Yadav, N.; Taywade, S.; Kumar, R.; Prashanth, A.; Saxena, R. Role of 99mTc Sulphur Colloid Lymphoscintigraphy in a Rare Case of Chylothorax and Lymphocele

Formation Post Esophageal Duplication Cyst Excision. *Eur. J. Hybrid Imaging* **2021**, *5* (1), 17. https://doi.org/10.1186/s41824-021-00111-4.
(37) Drozdovitch, V.; Brill, A. B.; Callahan, R. J.; Clanton, J. A.; DePietro, A.; Goldsmith, S. J.; Greenspan, B. S.; Gross, M. D.; Hays, M. T.; Moore, S. C.; Ponto, J. A.; Shreeve, W. W.; Melo, D. R.; Linet, M. S.; Simon, S. L. Use of Radiopharmaceuticals in Diagnostic Nuclear Medicine in the United States: 1960–2010. *Health Phys.* **2015**, *108* (5), 520–537. https://doi.org/10.1097/HP.0000000000000261.
(38) Duatti, A. Review on 99mTc Radiopharmaceuticals with Emphasis on New Advancements. *Nucl. Med. Biol.* **2021**, *92*, 202–216. https://doi.org/10.1016/j.nucmedbio.2020.05.005.
(39) Crișan, G.; Moldovean-Cioroianu, N. S.; Timaru, D.-G.; Andrieș, G.; Căinap, C.; Chiș, V. Radiopharmaceuticals for PET and SPECT Imaging: A Literature Review over the Last Decade. *Int. J. Mol. Sci.* **2022**, *23* (9), 5023. https://doi.org/10.3390/ijms23095023.
(40) Tumeh S S, Rosenthal D S, Kaplan W D, et al. Lymphoma: Evaluation with Ga-67 SPECT. *Radiology* **1987**, *164* (2), 111–114.
(41) Maddahi, J.; Kiat, H.; Garcia, E. V.; Nichols, K.; Berman, D. S. Myocardial Perfusion Imaging with Technetium-99m Sestamibi SPECT in the Evaluation of Coronary Artery Disease.
(42) Taillefer, R.; DePuey, E. G.; Udelson, J. E.; Beller, G. A.; Latour, Y.; Reeves, F. Comparative Diagnostic Accuracy of Tl-201 and Tc-99m Sestamibi SPECT Imaging (Perfusion and ECG-Gated SPECT) in Detecting Coronary Artery Disease in Women. *J. Am. Coll. Cardiol.* **1997**, *29* (1), 69–77. https://doi.org/10.1016/S0735-1097(96)00435-4.
(43) Malkerneker, D.; Brenner, R.; Martin, W.; Sampson, U.; Feurer, I.; Kronenberg, M.; Delbeke, D. CT-Based Attenuation Correction versus Prone Imaging to Decrease Equivocal Interpretations of Rest/Stress Tc-99m Tetrofosmin SPECT MPI. *J. Nucl. Cardiol.* **2007**, *14* (3), 314–323. https://doi.org/10.1016/j.nuclcard.2007.02.005.
(44) P F, R. Breast Cancer Detection with Tc-99m Tetrofosmin. *Clin. Nucl. Med.* **1995**, *20* (8), 703–705.
(45) Levine, M.; Ahlberg, A.; Mann, A.; White, M.; Mcgill, C.; Deleon, C.; Piriz, J.; Waters, D.; Heller, G. Comparison of Exercise, Dipyridamole, Adenosine, and Dobutamine Stress with the Use of Tc-99m Tetrofosmin Tomographic Imaging1, 2. *J. Nucl. Cardiol.* **1999**, *6* (4), 389–396. https://doi.org/10.1016/S1071-3581(99)90004-1.
(46) Tsai, S.-Y.; Wang, S.-Y.; Shiau, Y.-C.; Wu, Y.-W. Benign Incidental Findings of Osteopoikilosis on Tc-99m MDP Bone SPECT/CT: A Case Report and Literature Review. *Medicine (Baltimore)* **2016**, *95* (23), e3868. https://doi.org/10.1097/MD.0000000000003868.
(47) Saeed, S.; Haq, S.; Sohaib, M.; Khan, A. N. Skull Base Involvement by a Nasopharyngeal Carcinoma Shown by Tc-99m MDP SPECT But Not by Computed Tomography: *Clin. Nucl. Med.* **2001**, *26* (11), 930–932. https://doi.org/10.1097/00003072-200111000-00008.
(48) Imran, M. B.; Kawashima, R.; Awata, S.; Sato, K.; Kinomura, S.; Ono, S.; Sato, M.; Fukuda, H. Tc-99m HMPAO SPECT in the Evaluation of Alzheimer's Disease: Correlation between Neuropsychiatric Evaluation and CBF Images. *J. Neurol. Neurosurg. Psychiatry* **1999**, *66* (2), 228–232. https://doi.org/10.1136/jnnp.66.2.228.
(49) Okuyaz, Ç.; Gücüyener, K.; Karabacak, N. İ.; AydIn, K.; SerdaroĞlu, A.; Cingi, E. Tc-99m-HMPAO SPECT in the Diagnosis of Brain Death in Children. *Pediatr. Int.* **2004**, *46* (6), 711–714. https://doi.org/10.1111/j.1442-200x.2004.01976.x.
(50) W., H.; P., C.; C., T.; A., K.; C., L. Objective Evidence of Abnormal Regional Cerebral Blood Flow in Patients with Systemic Lupus Erythematosus on Tc-99m ECD Brain SPECT. *Rheumatol. Int.* **2002**, *22* (5), 178–181. https://doi.org/10.1007/s00296-002-0224-9.

(51) R S, D. Tc-99m-ECD SPECT Brain Imaging in Children with Tourette's Syndrome. *Yonsei Med. J.* **2002**, *43* (4), 403–410.
(52) Eslamy, H. K.; Ziessman, H. A. Parathyroid Scintigraphy in Patients with Primary Hyperparathyroidism: ^{99m}Tc Sestamibi SPECT and SPECT/CT. *RadioGraphics* **2008**, *28* (5), 1461–1476. https://doi.org/10.1148/rg.285075055.
(53) Hsu, B.; Chen, F.-C.; Wu, T.-C.; Huang, W.-S.; Hou, P.-N.; Chen, C.-C.; Hung, G.-U. Quantitation of Myocardial Blood Flow and Myocardial Flow Reserve with 99mTc-Sestamibi Dynamic SPECT/CT to Enhance Detection of Coronary Artery Disease. *Eur. J. Nucl. Med. Mol. Imaging* **2014**, *41* (12), 2294–2306. https://doi.org/10.1007/s00259-014-2881-9.
(54) Kaneta, T.; Ogawa, M.; Daisaki, H.; Nawata, S.; Yoshida, K. SUV Measurement of Normal Vertebrae Using SPECT/CT with Tc-99m Methylene Diphosphonate.
(55) Pollard, J.; McNeely, P.; Menda, Y. Nuclear Imaging of Neuroendocrine Tumors. *Surg. Oncol. Clin. N. Am.* **2020**, *29* (2), 209–221. https://doi.org/10.1016/j.soc.2019.11.007.
(56) Batchala, P. P.; Dyer, A.; Mukherjee, S.; Rehm, P. K. Lateral Ectopic Thyroid Mimics Carotid Body Tumor on Indium-111 Pentetreotide Scintigraphy. *Clin. Imaging* **2019**, *58*, 46–49. https://doi.org/10.1016/j.clinimag.2019.05.012.
(57) Lange, C.; Seese, A.; Schwarzenböck, S.; Steinhoff, K.; Umland-Seidler, B.; Krause, B. J.; Brenner, W.; Sabri, O.; Kurth, J.; Hesse, S.; Buchert, R. CT-Based Attenuation Correction in I-123-Ioflupane SPECT. *PLoS ONE* **2014**, *9* (9), e108328. https://doi.org/10.1371/journal.pone.0108328.
(58) Jacobson, A. F.; Senior, R.; Cerqueira, M. D.; Wong, N. D.; Thomas, G. S.; Lopez, V. A.; Agostini, D.; Weiland, F.; Chandna, H.; Narula, J. Myocardial Iodine-123 Meta-Iodobenzylguanidine Imaging and Cardiac Events in Heart Failure. *J. Am. Coll. Cardiol.* **2010**, *55* (20), 2212–2221. https://doi.org/10.1016/j.jacc.2010.01.014.
(59) Emmett, L.; Willowson, K.; Violet, J.; Shin, J.; Blanksby, A.; Lee, J. Lutetium ^{177} PSMA Radionuclide Therapy for Men with Prostate Cancer: A Review of the Current Literature and Discussion of Practical Aspects of Therapy. *J. Med. Radiat. Sci.* **2017**, *64* (1), 52–60. https://doi.org/10.1002/jmrs.227.
(60) Zhang, H.; Chen, J.; Waldherr, C.; Hinni, K.; Waser, B.; Reubi, J. C.; Maecke, H. R. Synthesis and Evaluation of Bombesin Derivatives on the Basis of Pan-Bombesin Peptides Labeled with Indium-111, Lutetium-177, and Yttrium-90 for Targeting Bombesin Receptor-Expressing Tumors. *Cancer Res.* **2004**, *64* (18), 6707–6715. https://doi.org/10.1158/0008-5472.CAN-03-3845.
(61) Lepareur, N.; Lacœuille, F.; Bouvry, C.; Hindré, F.; Garcion, E.; Chérel, M.; Noiret, N.; Garin, E.; Knapp, F. F. R. Rhenium-188 Labeled Radiopharmaceuticals: Current Clinical Applications in Oncology and Promising Perspectives. *Front. Med.* **2019**, *6*, 132. https://doi.org/10.3389/fmed.2019.00132.
(62) Anger, H. O. Scintillation Camera. *Rev. Sci. Instrum.* **1958**, *29* (1), 27–33. https://doi.org/10.1063/1.1715998.
(63) Murayama, H.; Hasegawa, T. Hal Oscar Anger, D.Sc. (Hon.) (1920–2005): A Pioneer in Nuclear Medicine Instrumentation. *Radiol. Phys. Technol.* **2014**, *7* (1), 1–4. https://doi.org/10.1007/s12194-013-0252-z.
(64) Hal 0., A. Scintillation Camera with Multichannel Collimators. *J. Nucl. Med. 5* **1964**, *5*, 515–531.
(65) E. KUHL, D. Image Separation Radioisotope Scanning. *Radiology* **1963**, *80* (4), 653–662.
(66) G. A, M. Tomographic Scintillation Camera. *Phys. Med. Biol.* **1971**, *16* (1), 87.
(67) G, M.; R A, W. Section Imaging by Computer Calculation. *J Nucl Med* **1971**, *12*, 76–84.

(68) Budinger, T. F.; Gullberg, G. T. Three-Dimensional Reconstruction in Nuclear Medicine Emission Imaging. *IEEE Trans. Nucl. Sci.* **1974**, *21* (3), 2–20. https://doi.org/10.1109/TNS.1974.6499234.
(69) Mariani, G.; Bruselli, L.; Kuwert, T.; Kim, E. E.; Flotats, A.; Israel, O.; Dondi, M.; Watanabe, N. A Review on the Clinical Uses of SPECT/CT. *Eur. J. Nucl. Med. Mol. Imaging* **2010**, *37* (10), 1959–1985. https://doi.org/10.1007/s00259-010-1390-8.
(70) Schillaci, O. Hybrid SPECT/CT: A New Era for SPECT Imaging? *Eur. J. Nucl. Med. Mol. Imaging* **2005**, *32* (5), 521–524. https://doi.org/10.1007/s00259-005-1760-9.
(71) Chowdhury, F. U.; Scarsbrook, A. F. The Role of Hybrid SPECT-CT in Oncology: Current and Emerging Clinical Applications. *Clin. Radiol.* **2008**, *63* (3), 241–251. https://doi.org/10.1016/j.crad.2007.11.008.
(72) Bouziotis, P.; Fiorini, C. SPECT/MRI: Dreams or Reality? *Clin. Transl. Imaging* **2014**, *2* (6), 571–573. https://doi.org/10.1007/s40336-014-0095-6.
(73) Hutton, B. F.; Occhipinti, M.; Kuehne, A.; Máthé, D.; Kovács, N.; Waiczies, H.; Erlandsson, K.; Salvado, D.; Carminati, M.; Montagnani, G. L.; Short, S. C.; Ottobrini, L.; Van Mullekom, P.; Piemonte, C.; Bukki, T.; Nyitrai, Z.; Papp, Z.; Nagy, K.; Niendorf, T.; De Francesco, I.; Fiorini, C.; On behalf of the INSERT consortium. Development of Clinical Simultaneous SPECT/MRI. *Br. J. Radiol.* **2018**, *91* (1081), 20160690. https://doi.org/10.1259/bjr.20160690.
(74) Goetz, C.; Breton, E.; Choquet, P.; Israel-Jost, V.; Constantinesco, A. SPECT Low-Field MRI System for Small-Animal Imaging. *J. Nucl. Med.* **2008**, *49* (1), 88–93. https://doi.org/10.2967/jnumed.107.044313.
(75) Holen, V. Optimization of a Stationary Small Animal SPECT System for Simultaneous SPECTIMRI.
(76) Dorbala, S.; Park, M.-A.; Cuddy, S.; Singh, V.; Sullivan, K.; Kim, S.; Falk, R. H.; Taqueti, V. R.; Skali, H.; Blankstein, R.; Bay, C.; Kijewski, M. F.; Di Carli, M. F. Absolute Quantitation of Cardiac ^{99m} Tc-Pyrophosphate Using Cadmium-Zinc-Telluride–Based SPECT/CT. *J. Nucl. Med.* **2021**, *62* (5), 716–722. https://doi.org/10.2967/jnumed.120.247312.
(77) Fiechter, M.; Ghadri, J. R.; Kuest, S. M.; Pazhenkottil, A. P.; Wolfrum, M.; Nkoulou, R. N.; Goetti, R.; Gaemperli, O.; Kaufmann, P. A. Nuclear Myocardial Perfusion Imaging with a Novel Cadmium-Zinc-Telluride Detector SPECT/CT Device: First Validation versus Invasive Coronary Angiography. *Eur. J. Nucl. Med. Mol. Imaging* **2011**, *38* (11), 2025–2030. https://doi.org/10.1007/s00259-011-1877-y.
(78) Herzog, B. A.; Buechel, R. R.; Katz, R.; Brueckner, M.; Husmann, L.; Burger, I. A.; Pazhenkottil, A. P.; Valenta, I.; Gaemperli, O.; Treyer, V.; Kaufmann, P. A. Nuclear Myocardial Perfusion Imaging with a Cadmium-Zinc-Telluride Detector Technique: Optimized Protocol for Scan Time Reduction. *J. Nucl. Med.* **2010**, *51* (1), 46–51. https://doi.org/10.2967/jnumed.109.065532.
(79) Kim, H.; Furenlid, L. R.; Crawford, M. J.; Wilson, D. W.; Barber, H. B.; Peterson, T. E.; Hunter, W. C. J.; Liu, Z.; Woolfenden, J. M.; Barrett, H. H. SemiSPECT: A Small-Animal Single-Photon Emission Computed Tomography (SPECT) Imager Based on Eight Cadmium Zinc Telluride (CZT) Detector Arrays: A CZT SPECT System. *Med. Phys.* **2006**, *33* (2), 465–474. https://doi.org/10.1118/1.2164070.
(80) Bruyant, P. P. Analytic and Iterative Reconstruction Algorithms in SPECT.
(81) Sibille, L.; Chambert, B.; Alonso, S.; Barrau, C.; D'Estanque, E.; Al Tabaa, Y.; Collombier, L.; Demattei, C.; Kotzki, P.-O.; Boudousq, V. Impact of the Adaptive Statistical Iterative Reconstruction Technique on Radiation Dose and Image Quality in Bone SPECT/CT. *J. Nucl. Med.* **2016**, *57* (7), 1091–1095. https://doi.org/10.2967/jnumed.115.164772.
(82) Giovagnoli, D. Image Reconstruction for Three-Gamma PET Imaging.

(83) *Quantum Analysis in Nuclear Medicine Imaging*; Zaidi, H., Ed.; Springer: New York, NY, 2005.
(84) Zheng, W.; Li, S.; Krol, A.; Ross Schmidtlein, C.; Zeng, X.; Xu, Y. Sparsity Promoting Regularization for Effective Noise Suppression in SPECT Image Reconstruction. *Inverse Probl.* **2019**, *35* (11), 115011. https://doi.org/10.1088/1361-6420/ab23da.
(85) Bronnikov, A. V. SPECT Imaging With Resolution Recovery. *IEEE Trans. Nucl. Sci.* **2012**, *59* (4), 1458–1464. https://doi.org/10.1109/TNS.2012.2195675.
(86) Beekman, F. J.; De Jong, H. W. A. M.; Van Geloven, S. Efficient Fully 3-D Iterative SPECT Reconstruction with Monte Carlo-Based Scatter Compensation. *IEEE Trans. Med. Imaging* **2002**, *21* (8), 867–877. https://doi.org/10.1109/TMI.2002.803130.
(87) Dewaraja, Y. K.; Ljungberg, M.; Fessler, J. A. 3-D Monte Carlo-Based Scatter Compensation in Quantitative I-131 SPECT Reconstruction. *IEEE Trans. Nucl. Sci.* **2006**, *53* (1), 181–188. https://doi.org/10.1109/TNS.2005.862956.
(88) Apostolopoulos, I. D.; Papandrianos, N. I.; Feleki, A.; Moustakidis, S.; Papageorgiou, E. I. Deep Learning-Enhanced Nuclear Medicine SPECT Imaging Applied to Cardiac Studies. *EJNMMI Phys.* **2023**, *10* (1), 6. https://doi.org/10.1186/s40658-022-00522-7.
(89) Van Der Wildt, B.; Lammertsma, A. A.; Drukarch, B.; Windhorst, A. D. Strategies towards in Vivo Imaging of Active Transglutaminase Type 2 Using Positron Emission Tomography. *Amino Acids* **2017**, *49* (3), 585–595. https://doi.org/10.1007/s00726-016-2288-y.
(90) Torrico, E. V. CARACTERIZACIÓN, MEJORA Y DISEÑO DE ESCÁNERES PET PRECLÍNICOS.
(91) Reivich, M.; Kuhl, D.; Wolf, A.; Greenberg, J.; Phelps, M.; Ido, T.; Casella, V.; Fowler, J.; Hoffman, E.; Alavi, A.; Som, P.; Sokoloff, L. The [18F]Fluorodeoxyglucose Method for the Measurement of Local Cerebral Glucose Utilization in Man. *Circ. Res.* **1979**, *44* (1), 127–137. https://doi.org/10.1161/01.RES.44.1.127.
(92) Yap, C. S.; Czernin, J.; Fishbein, M. C.; Cameron, R. B.; Schiepers, C.; Phelps, M. E.; Weber, W. A. Evaluation of Thoracic Tumors With 18F-Fluorothymidine and 18F-Fluorodeoxyglucose-Positron Emission Tomography. *Chest* **2006**, *129* (2), 393–401. https://doi.org/10.1378/chest.129.2.393.
(93) Hatt, M.; Cheze-Le Rest, C.; Aboagye, E. O.; Kenny, L. M.; Rosso, L.; Turkheimer, F. E.; Albarghach, N. M.; Metges, J.-P.; Pradier, O.; Visvikis, D. Reproducibility of ^{18} F-FDG and 3′-Deoxy-3′- ^{18} F-Fluorothymidine PET Tumor Volume Measurements. *J. Nucl. Med.* **2010**, *51* (9), 1368–1376. https://doi.org/10.2967/jnumed.110.078501.
(94) Fendler, W. P.; Calais, J.; Eiber, M.; Flavell, R. R.; Mishoe, A.; Feng, F. Y.; Nguyen, H. G.; Reiter, R. E.; Rettig, M. B.; Okamoto, S.; Emmett, L.; Zacho, H. D.; Ilhan, H.; Wetter, A.; Rischpler, C.; Schoder, H.; Burger, I. A.; Gartmann, J.; Smith, R.; Small, E. J.; Slavik, R.; Carroll, P. R.; Herrmann, K.; Czernin, J.; Hope, T. A. Assessment of ^{68} Ga-PSMA-11 PET Accuracy in Localizing Recurrent Prostate Cancer: A Prospective Single-Arm Clinical Trial. *JAMA Oncol.* **2019**, *5* (6), 856. https://doi.org/10.1001/jamaoncol.2019.0096.
(95) Hope, T. A.; Goodman, J. Z.; Allen, I. E.; Calais, J.; Fendler, W. P.; Carroll, P. R. Metaanalysis of ^{68} Ga-PSMA-11 PET Accuracy for the Detection of Prostate Cancer Validated by Histopathology. *J. Nucl. Med.* **2019**, *60* (6), 786–793. https://doi.org/10.2967/jnumed.118.219501.
(96) Calais, J.; Ceci, F.; Eiber, M.; Hope, T. A.; Hofman, M. S.; Rischpler, C.; Bach-Gansmo, T.; Nanni, C.; Savir-Baruch, B.; Elashoff, D.; Grogan, T.; Dahlbom, M.; Slavik, R.; Gartmann, J.; Nguyen, K.; Lok, V.; Jadvar, H.; Kishan, A. U.; Rettig, M. B.; Reiter, R. E.; Fendler, W. P.; Czernin, J. 18F-Fluciclovine PET-CT and 68Ga-PSMA-11 PET-CT in Patients with Early Biochemical Recurrence after Prostatectomy: A Prospective, Single-

Centre, Single-Arm, Comparative Imaging Trial. *Lancet Oncol.* **2019**, *20* (9), 1286–1294. https://doi.org/10.1016/S1470-2045(19)30415-2.
(97) Tsuyuguchi, N.; Terakawa, Y.; Uda, T.; Nakajo, K.; Kanemura, Y. Diagnosis of Brain Tumors Using Amino Acid Transport PET Imaging With 18F- Fluciclovine: A Comparison Study With L-Methyl-11C-Methionine PET Imaging. *Asia Ocean. J. Nucl. Med. Biol.* **2017**, No. Online First. https://doi.org/10.22038/aojnmb.2017.8843.
(98) Liu, F.; Zhu, H.; Yu, J.; Han, X.; Xie, Q.; Liu, T.; Xia, C.; Li, N.; Yang, Z. ^{68} Ga/ ^{177} Lu-Labeled DOTA-TATE Shows Similar Imaging and Biodistribution in Neuroendocrine Tumor Model. *Tumor Biol.* **2017**, *39* (6), 101042831770551. https://doi.org/10.1177/1010428317705519.
(99) Von Eyben, F. E.; Kiljunen, T.; Joensuu, T.; Kairemo, K.; Uprimny, C.; Virgolini, I. 177Lu-PSMA-617 Radioligand Therapy for a Patient with Lymph Node Metastatic Prostate Cancer. *Oncotarget* **2017**, *8* (39), 66112–66116. https://doi.org/10.18632/oncotarget.19805.
(100) Pujara, A. C.; Kim, E.; Axelrod, D.; Melsaether, A. N. PET/MRI in Breast Cancer: PET/MRI in Breast Cancer. *J. Magn. Reson. Imaging* **2019**, *49* (2), 328–342. https://doi.org/10.1002/jmri.26298.
(101) Lamb, J.; Holland, J. P. Advanced Methods for Radiolabeling Multimodality Nanomedicines for SPECT/MRI and PET/MRI. *J. Nucl. Med.* **2018**, *59* (3), 382–389. https://doi.org/10.2967/jnumed.116.187419.
(102) Nutt, R. The History of Positron Emission Tomography. *Mol. Imaging Biol.* **2002**, *4* (1), 11–26. https://doi.org/10.1016/S1095-0397(00)00051-0.
(103) Jones, T.; Townsend, D. History and Future Technical Innovation in Positron Emission Tomography. *J. Med. Imaging* **2017**, *4* (1), 011013. https://doi.org/10.1117/1.JMI.4.1.011013.
(104) Mohammadi, I.; Castro, I. F. C.; Correia, P. M. M.; Silva, A. L. M.; Veloso, J. F. C. A. Minimization of Parallax Error in Positron Emission Tomography Using Depth of Interaction Capable Detectors: Methods and Apparatus. *Biomed. Phys. Eng. Express* **2019**, *5* (6), 062001. https://doi.org/10.1088/2057-1976/ab4a1b.
(105) Schmitz, R. E.; Alessio, A. M.; Kinahan, P. E. The Physics of PET/CT Scanners.
(106) Park, H.; Yi, M.; Lee, J. S. Silicon Photomultiplier Signal Readout and Multiplexing Techniques for Positron Emission Tomography: A Review. *Biomed. Eng. Lett.* **2022**, *12* (3), 263–283. https://doi.org/10.1007/s13534-022-00234-y.
(107) Patton, J. A.; Turkington, T. G. Coincidence Imaging with a Dual-Head Scintillation Camera.
(108) Wagner, H. N. A Brief History of Positron Emission Tomography (PET). *Semin. Nucl. Med.* **1998**, *28* (3), 213–220. https://doi.org/10.1016/S0001-2998(98)80027-5.
(109) K C., G. *Pets in America: A History*; UNC Press Books, 2006.
(110) Yamashita, T.; Watanabe, M.; Shimizu, K.; Uchida, H. High Resolution Block Detectors for PET. *IEEE Trans. Nucl. Sci.* **1990**, *37* (2), 589–593. https://doi.org/10.1109/23.106682.
(111) Conti, M. State of the Art and Challenges of Time-of-Flight PET. *Phys. Med.* **2009**, *25* (1), 1–11. https://doi.org/10.1016/j.ejmp.2008.10.001.
(112) Lewellen, T. K. Time-of-Flight PET. *Semin. Nucl. Med.* **1998**, *28* (3), 268–275. https://doi.org/10.1016/S0001-2998(98)80031-7.
(113) Surti, S. Update on Time-of-Flight PET Imaging. *J. Nucl. Med.* **2015**, *56* (1), 98–105. https://doi.org/10.2967/jnumed.114.145029.
(114) Karp, J. S.; Surti, S.; Daube-Witherspoon, M. E.; Muehllehner, G. Benefit of Time-of-Flight in PET: Experimental and Clinical Results. *J. Nucl. Med.* **2008**, *49* (3), 462–470. https://doi.org/10.2967/jnumed.107.044834.

(115) Vandenberghe, S.; Mikhaylova, E.; D'Hoe, E.; Mollet, P.; Karp, J. S. Recent Developments in Time-of-Flight PET. *EJNMMI Phys.* **2016**, *3* (1), 3. https://doi.org/10.1186/s40658-016-0138-3.
(116) Miyaoka, R. S.; Lewellen, T. K.; Yu, H.; McDaniel, D. L. Design of a Depth of Interaction (DOI) PET Detector Module. *IEEE Trans. Nucl. Sci.* **1998**, *45* (3), 1069–1073. https://doi.org/10.1109/23.681980.
(117) Tsuda, T.; Murayama, H.; Kitamura, K.; Yamaya, T.; Yoshida, E.; Omura, T.; Kawai, H.; Inadama, N.; Orita, N. A Four-Layer Depth of Interaction Detector Block for Small Animal PET. *IEEE Trans. Nucl. Sci.* **2004**, *51* (5), 2537–2542. https://doi.org/10.1109/TNS.2004.835739.
(118) Ito, M.; Hong, S. J.; Lee, J. S. Positron Emission Tomography (PET) Detectors with Depth-of- Interaction (DOI) Capability. *Biomed. Eng. Lett.* **2011**, *1* (2), 70–81. https://doi.org/10.1007/s13534-011-0019-6.
(119) Otte, A. N.; Barral, J.; Dolgoshein, B.; Hose, J.; Klemin, S.; Lorenz, E.; Mirzoyan, R.; Popova, E.; Teshima, M. A Test of Silicon Photomultipliers as Readout for PET. *Nucl. Instrum. Methods Phys. Res. Sect. Accel. Spectrometers Detect. Assoc. Equip.* **2005**, *545* (3), 705–715. https://doi.org/10.1016/j.nima.2005.02.014.
(120) Moehrs, S.; Guerra, A. D.; Herbert, D. J.; Mandelkern, M. A. A Detector Head Design for Small-Animal PET with Silicon Photomultipliers (SiPM). *Phys. Med. Biol.* **2006**, *51* (5), 1113–1127. https://doi.org/10.1088/0031-9155/51/5/004.
(121) Roncali, E.; Cherry, S. R. Application of Silicon Photomultipliers to Positron Emission Tomography. *Ann. Biomed. Eng.* **2011**, *39* (4), 1358–1377. https://doi.org/10.1007/s10439-011-0266-9.
(122) Cherry, S. R.; Jones, T.; Karp, J. S.; Qi, J.; Moses, W. W.; Badawi, R. D. Total-Body PET: Maximizing Sensitivity to Create New Opportunities for Clinical Research and Patient Care. *J. Nucl. Med.* **2018**, *59* (1), 3–12. https://doi.org/10.2967/jnumed.116.184028.
(123) Badawi, R. D.; Shi, H.; Hu, P.; Chen, S.; Xu, T.; Price, P. M.; Ding, Y.; Spencer, B. A.; Nardo, L.; Liu, W.; Bao, J.; Jones, T.; Li, H.; Cherry, S. R. First Human Imaging Studies with the EXPLORER Total-Body PET Scanner*. *J. Nucl. Med.* **2019**, *60* (3), 299–303. https://doi.org/10.2967/jnumed.119.226498.
(124) Delso, G.; Ziegler, S. PET/MRI System Design. *Eur. J. Nucl. Med. Mol. Imaging* **2009**, *36* (S1), 86–92. https://doi.org/10.1007/s00259-008-1008-6.
(125) Yamamoto, S.; Imaizumi, M.; Kanai, Y.; Tatsumi, M.; Aoki, M.; Sugiyama, E.; Kawakami, M.; Shimosegawa, E.; Hatazawa, J. Design and Performance from an Integrated PET/MRI System for Small Animals. *Ann. Nucl. Med.* **2010**, *24* (2), 89–98. https://doi.org/10.1007/s12149-009-0333-6.
(126) Zaidi, H.; Del Guerra, A. An Outlook on Future Design of Hybrid PET/MRI Systems: Design of Hybrid PET/MRI Scanners. *Med. Phys.* **2011**, *38* (10), 5667–5689. https://doi.org/10.1118/1.3633909.
(127) Zaidi, H.; Alavi, A. Current Trends in PET and Combined (PET/CT and PET/MR) Systems Design. *PET Clin.* **2007**, *2* (2), 109–123. https://doi.org/10.1016/j.cpet.2007.10.004.
(128) Mawlawi, O.; Townsend, D. W. Multimodality Imaging: An Update on PET/CT Technology. *Eur. J. Nucl. Med. Mol. Imaging* **2009**, *36* (S1), 15–29. https://doi.org/10.1007/s00259-008-1016-6.
(129) Tong, S.; Alessio, A. M.; Kinahan, P. E. Image Reconstruction for PET/CT Scanners: Past Achievements and Future Challenges. *Imaging Med.* **2010**, *2* (5), 529–545. https://doi.org/10.2217/iim.10.49.
(130) Basu, S.; Kwee, T. C.; Surti, S.; Akin, E. A.; Yoo, D.; Alavi, A. Fundamentals of PET and PET/CT Imaging: Fundamentals of PET and PET/CT. *Ann. N. Y. Acad. Sci.* **2011**, *1228* (1), 1–18. https://doi.org/10.1111/j.1749-6632.2011.06077.x.

(131) Hong, K. J.; Choi, Y.; Jung, J. H.; Kang, J.; Hu, W.; Lim, H. K.; Huh, Y.; Kim, S.; Jung, J. W.; Kim, K. B.; Song, M. S.; Park, H. A Prototype MR Insertable Brain PET Using Tileable GAPD Arrays: A MR Insertable PET for Simultaneous PET/MRI Imaging. *Med. Phys.* **2013**, *40* (4), 042503. https://doi.org/10.1118/1.4793754.
(132) Ramos, C. D.; Erdi, Y. E.; Gonen, M.; Riedel, E.; Yeung, H. W. D.; Macapinlac, H. A.; Chisin, R.; Larson, S. M. FDG-PET Standardized Uptake Values in Normal Anatomical Structures Using Iterative Reconstruction Segmented Attenuation Correction and Filtered Back-Projection. *Eur. J. Nucl. Med.* **2001**, *28* (2), 155–164. https://doi.org/10.1007/s002590000421.
(133) Rapisarda, E.; Bettinardi, V.; Thielemans, K.; Gilardi, M. C. Image-Based Point Spread Function Implementation in a Fully 3D OSEM Reconstruction Algorithm for PET. *Phys. Med. Biol.* **2010**, *55* (14), 4131–4151. https://doi.org/10.1088/0031-9155/55/14/012.
(134) Daube-Witherspoon, M. E.; Matej, S.; Karp, J. S.; Lewitt, R. M. Application of the Row Action Maximum Likelihood Algorithm with Spherical Basis Functions to Clinical PET Imaging. *IEEE Trans. Nucl. Sci.* **2001**, *48* (1), 24–30. https://doi.org/10.1109/23.910827.
(135) Chilcott, A. K.; Bradley, K. M.; McGowan, D. R. Effect of a Bayesian Penalized Likelihood PET Reconstruction Compared With Ordered Subset Expectation Maximization on Clinical Image Quality Over a Wide Range of Patient Weights. *Am. J. Roentgenol.* **2018**, *210* (1), 153–157. https://doi.org/10.2214/AJR.17.18060.
(136) Guobao Wang; Jinyi Qi. Penalized Likelihood PET Image Reconstruction Using Patch-Based Edge-Preserving Regularization. *IEEE Trans. Med. Imaging* **2012**, *31* (12), 2194–2204. https://doi.org/10.1109/TMI.2012.2211378.
(137) Teoh, E. J.; McGowan, D. R.; Macpherson, R. E.; Bradley, K. M.; Gleeson, F. V. Phantom and Clinical Evaluation of the Bayesian Penalized Likelihood Reconstruction Algorithm Q.Clear on an LYSO PET/CT System. *J. Nucl. Med.* **2015**, *56* (9), 1447–1452. https://doi.org/10.2967/jnumed.115.159301.
(138) Boellaard, R.; Hofman, M. B. M.; Hoekstra, O. S.; Lammertsma, A. A. Accurate PET/MR Quantification Using Time of Flight MLAA Image Reconstruction. *Mol. Imaging Biol.* **2014**, *16* (4), 469–477. https://doi.org/10.1007/s11307-013-0716-x.
(139) Cui, J.; Pratx, G.; Prevrhal, S.; Levin, C. S. Fully 3D List-Mode Time-of-Flight PET Image Reconstruction on GPUs Using CUDA: Fully 3D List-Mode Time-of-Flight PET on GPU-CUDA. *Med. Phys.* **2011**, *38* (12), 6775–6786. https://doi.org/10.1118/1.3661998.
(140) Akamatsu, G.; Ishikawa, K.; Mitsumoto, K.; Taniguchi, T.; Ohya, N.; Baba, S.; Abe, K.; Sasaki, M. Improvement in PET/CT Image Quality with a Combination of Point-Spread Function and Time-of-Flight in Relation to Reconstruction Parameters. *J. Nucl. Med.* **2012**, *53* (11), 1716–1722. https://doi.org/10.2967/jnumed.112.103861.
(141) Wagenknecht, G.; Kaiser, H.-J.; Mottaghy, F. M.; Herzog, H. MRI for Attenuation Correction in PET: Methods and Challenges. *Magn. Reson. Mater. Phys. Biol. Med.* **2013**, *26* (1), 99–113. https://doi.org/10.1007/s10334-012-0353-4.
(142) Catana, C.; Van Der Kouwe, A.; Benner, T.; Michel, C. J.; Hamm, M.; Fenchel, M.; Fischl, B.; Rosen, B.; Schmand, M.; Sorensen, A. G. Toward Implementing an MRI-Based PET Attenuation-Correction Method for Neurologic Studies on the MR-PET Brain Prototype. *J. Nucl. Med.* **2010**, *51* (9), 1431–1438. https://doi.org/10.2967/jnumed.109.069112.
(143) Kinahan, P. E.; Townsend, D. W.; Beyer, T.; Sashin, D. Attenuation Correction for a Combined 3D PET/CT Scanner. *Med. Phys.* **1998**, *25* (10), 2046–2053. https://doi.org/10.1118/1.598392.
(144) Donnard, J.; Chbib, D.; Chen, W.-T.; Cussonneau, J.-P.; Gallego-Manzano, L.; Lemaire, O.; Masbou, J.; Hadi, A. F. M.; Morteau, E.; Lavina, L. S.; Stutzmann, J.-S.; Thers, D.; Carlier, T.; Cherel, M.; Kraeber-Bodéré, F. XEMIS: The New Compton Camera with Liquid Xenon.

(145) Zhu, Y.; Acounis, S.; Beaupère, N.; Beney, J. L.; Bert, J.; Bouvier, S.; Cai, D.; Canot, C.; Carlier, T.; Cherel, M.; Cussonneau, J. P.; Diglio, S.; Giovagnoli, D.; Idier, J.; Kraeber-Bodéré, F.; Le Ray, P.; Lefèvre, F.; Masbou, J.; Morteau, E.; Stutzmann, J. S.; Visvikis, D.; Xing, Y.; Thers, D. Studies and Optimization of Scintillation Light Measurements for the Development of the 3-Gamma Medical Imaging XEMIS2 Liquid Xenon Compton Camera. *Nucl. Instrum. Methods Phys. Res. Sect. Accel. Spectrometers Detect. Assoc. Equip.* **2023**, *1047*, 167794. https://doi.org/10.1016/j.nima.2022.167794.
(146) Xing, Y.; Abaline, M.; Acounis, S.; Beaup, N.; Bert, J.; Bouvier, S.; Briend, P.; Butterworth, J.; Carlier, T.; Chanal, H.; Cherel, M.; Cussonneau, J. P.; Dahoumane, M.; Gallego-Manzano, L.; Giovagnoli, D.; Idier, J.; Kraeber-Bod, F.; Mathez, H.; Morteau, E.; Pillet, N.; Roy, D.; Royer, L.; Staemp, M.; Visvikis, D.; Zhu, Y.; Thers, D. XEMIS: Liquid Xenon Compton Camera for 3c Imaging.
(147) Cai, D. Studies of Frisch Grid Performance and Calibration of Light Measurement in Liquid Xenon Detector for Small Animal Medical Imaging. *JRJC2022* 137–140.
(148) Xing, Y. Studies and Optimization of Ionization Signal Measurement for the 3-Gamma Imaging XEMIS2 Liquid Xenon Compton Camera.
(149) Zhu, Y. Development of the XEMIS2 Liquid Xenon Compton Camera for 3-Gamma Imaging: Studies and Optimization of Scintillation Light Measurements.
(150) R W, T.; J M, N.; D B., E. A Proposed Gamma Camera. *Nature* **1974**, *251* (5471), 132–134.
(151) Takeda, S.; Aono, H.; Okuyama, S.; Ishikawa, S.; Odaka, H.; Watanabe, S.; Kokubun, M.; Takahashi, T.; Nakazawa, K.; Tajima, H.; Kawachi, N. Experimental Results of the Gamma-Ray Imaging Capability With a Si/CdTe Semiconductor Compton Camera. *IEEE Trans. Nucl. Sci.* **2009**, *56* (3), 783–790. https://doi.org/10.1109/TNS.2008.2012059.
(152) Gu, Y.; Matteson, J. L.; Skelton, R. T.; Deal, A. C.; Stephan, E. A.; Duttweiler, F.; Gasaway, T. M.; Levin, C. S. Study of a High-Resolution, 3D Positioning Cadmium Zinc Telluride Detector for PET. *Phys. Med. Biol.* **2011**, *56* (6), 1563–1584. https://doi.org/10.1088/0031-9155/56/6/004.
(153) Watanabe, S.; Tanaka, T.; Nakazawa, K.; Mitani, T.; Oonuki, K.; Takahashi, T.; Takashima, T.; Tajima, H.; Fukazawa, Y.; Nomachi, M.; Kubo, S.; Onishi, M.; Kuroda, Y. A Si/CdTe Semiconductor Compton Camera. *IEEE Trans. Nucl. Sci.* **2005**, *52* (5), 2045–2051. https://doi.org/10.1109/TNS.2005.856995.
(154) Hee Seo; Se Hyung Lee; Jong Hwi Jeong; Ju Hahn Lee; Chun Sik Lee; Jae Sung Lee; Chan Hyeong Kim. AID – A Novel Method for Improving the Imaging Resolution of a Table-Top Compton Camera. *IEEE Trans. Nucl. Sci.* **2008**, *55* (5), 2527–2530. https://doi.org/10.1109/TNS.2008.2000777.
(155) Sitarz, M.; Cussonneau, J.-P.; Matulewicz, T.; Haddad, F. Radionuclide Candidates for B+γ Coincidence PET: An Overview. *Appl. Radiat. Isot.* **2020**, *155*, 108898. https://doi.org/10.1016/j.apradiso.2019.108898.
(156) Jan, S.; Benoit, D.; Becheva, E.; Carlier, T.; Cassol, F.; Descourt, P.; Frisson, T.; Grevillot, L.; Guigues, L.; Maigne, L.; Morel, C.; Perrot, Y.; Rehfeld, N.; Sarrut, D.; Schaart, D. R.; Stute, S.; Pietrzyk, U.; Visvikis, D.; Zahra, N.; Buvat, I. GATE V6: A Major Enhancement of the GATE Simulation Platform Enabling Modelling of CT and Radiotherapy. *Phys. Med. Biol.* **2011**, *56* (4), 881–901. https://doi.org/10.1088/0031-9155/56/4/001.
(157) Strulab, D.; Santin, G.; Lazaro, D.; Breton, V.; Morel, C. GATE (Geant4 Application for Tomographic Emission): A PET/SPECT General-Purpose Simulation Platform. *Nucl. Phys. B - Proc. Suppl.* **2003**, *125*, 75–79. https://doi.org/10.1016/S0920-5632(03)90969-8.
(158) Manzano, L. G. Optimization of a single-phase liquid xenon Compton camera for 3 medical imaging.

(159) Aprile, E.; Doke, T. Liquid Xenon Detectors for Particle Physics and Astrophysics. *Rev. Mod. Phys.* **2010**, *82* (3), 2053–2097. https://doi.org/10.1103/RevModPhys.82.2053.
(160) Aprile, E.; Suzuki, M. Development of Liquid Xenon Detectors for Gamma Ray Astronomy. *IEEE Trans. Nucl. Sci.* **1989**, *36* (1), 311–315. https://doi.org/10.1109/23.34455.
(161) Ootani, W. Performance of the Liquid Xenon Scintillation Detector for the MEG Experiment. In *2006 IEEE Nuclear Science Symposium Conference Record*; IEEE: San Diego, CA, USA, 2006; pp 940–942. https://doi.org/10.1109/NSSMIC.2006.356001.
(162) Aprile, E.; Mukherjee, R.; Suzuki, M. Ionization of Liquid Xenon by 241Am and 210Po Alpha Particles. *Nucl. Instrum. Methods Phys. Res. Sect. Accel. Spectrometers Detect. Assoc. Equip.* **1991**, *307* (1), 119–125. https://doi.org/10.1016/0168-9002(91)90138-G.
(163) Jortner J, Meyer L, Rice S A, et al. Localized Excitations in Condensed Ne, Ar, Kr, and Xe. *J. Chem. Phys.* **1965**, *42* (12), 4250–4253.
(164) Solovov, V. N.; Hitachi, A.; Chepel, V.; Lopes, M. I.; Marques, R. F.; Policarpo, A. J. P. L. Detection of Scintillation Light of Liquid Xenon with a LAAPD. In *2000 IEEE Nuclear Science Symposium. Conference Record (Cat. No.00CH37149)*; IEEE: Lyon, France, 2000; Vol. 1, p 7/58-7/62. https://doi.org/10.1109/NSSMIC.2000.949288.
(165) Hitachi, A.; Takahashi, T.; Funayama, N.; Masuda, K.; Kikuchi, J.; Doke, T. Effect of Ionization Density on the Time Dependence of Luminescence from Liquid Argon and Xenon. *Phys. Rev. B* **1983**, *27* (9), 5279–5285. https://doi.org/10.1103/PhysRevB.27.5279.
(166) Doke, T.; Hitachi, A.; Kikuchi, J.; Masuda, K.; Okada, H.; Shibamura, E. Absolute Scintillation Yields in Liquid Argon and Xenon for Various Particles. *Jpn. J. Appl. Phys.* **2002**, *41* (Part 1, No. 3A), 1538–1545. https://doi.org/10.1143/JJAP.41.1538.
(167) Takahashi, T.; Konno, S.; Hamada, T.; Miyajima, M.; Kubota, S.; Nakamoto, A.; Hitachi, A.; Shibamura, E.; Doke, T. Average Energy Expended per Ion Pair in Liquid Xenon. *Phys. Rev. A* **1975**, *12* (5), 1771–1775. https://doi.org/10.1103/PhysRevA.12.1771.
(168) Miller, L. S.; Howe, S.; Spear, W. E. Charge Transport in Solid and Liquid Ar, Kr, and Xe. *Phys. Rev.* **1968**, *166* (3), 871–878. https://doi.org/10.1103/PhysRev.166.871.
(169) Young A T. Rayleigh Scattering. *Phys Today* **1982**, *35* (1), 42–48.
(170) Damashek, M.; Gilman, F. J. Forward Compton Scattering. *Phys. Rev. D* **1970**, *1* (5), 1319–1332. https://doi.org/10.1103/PhysRevD.1.1319.
(171) Joseph, J.; Rohrlich, F. Pair Production and Bremsstrahlung in the Field of Free and Bound Electrons. *Rev. Mod. Phys.* **1958**, *30* (2), 354–368. https://doi.org/10.1103/RevModPhys.30.354.
(172) McEachran, R. P.; Stauffer, A. D. Elastic Scattering of Electrons from Krypton and Xenon. *J. Phys. B At. Mol. Phys.* **1984**, *17* (12), 2507–2518. https://doi.org/10.1088/0022-3700/17/12/018.
(173) Rosenbluth, M. N. High Energy Elastic Scattering of Electrons on Protons. *Phys. Rev.* **1950**, *79* (4), 615–619. https://doi.org/10.1103/PhysRev.79.615.
(174) Takatsuka, K.; McKoy, V. Theory of Electronically Inelastic Scattering of Electrons by Molecules. *Phys. Rev. A* **1984**, *30* (4), 1734–1740. https://doi.org/10.1103/PhysRevA.30.1734.
(175) Bunkin, F. V.; Fedorov, M. V. BREMSSTRAHLUNG IN A STRONG RADIATION FIELD.
(176) Herren, Ch.; Dousse, J.-Cl. Experimental Evidence for the K - LM Radiative Auger Effect in Medium-Mass Atoms. *Phys. Rev. A* **1997**, *56* (4), 2750–2758. https://doi.org/10.1103/PhysRevA.56.2750.
(177) Johansson, F. O. L.; Berggren, E.; Cornetta, L. M.; Céolin, D.; Fondell, M.; Ågren, H.; Lindblad, A. Resonant Auger Spectroscopy on Solid Xenon on Gold, Silver, and Copper Substrates. *Phys. Rev. A* **2023**, *107* (3), 032802. https://doi.org/10.1103/PhysRevA.107.032802.

(178) Partanen, L. Auger Cascade Processes in Xenon and Krypton Studied by Electron and Ion Spectroscopy.
(179) Doke, T. A Historical View on the R&D for Liquid Rare Gas Detectors. *Nucl. Instrum. Methods Phys. Res. Sect. Accel. Spectrometers Detect. Assoc. Equip.* **1993**, *327* (1), 113–118. https://doi.org/10.1016/0168-9002(93)91423-K.
(180) Nygren, D. R. Origin and Development of the TPC Idea. *Nucl. Instrum. Methods Phys. Res. Sect. Accel. Spectrometers Detect. Assoc. Equip.* **2018**, *907*, 22–30. https://doi.org/10.1016/j.nima.2018.07.015.
(181) Rubbia, C. A. The Liquid-Argon Time Projection Chamber : A New Concept for Neutrino Detectors. *CERN-EP-INT-77-81977 - 15 P* **1977**.
(182) Curioni, A. Laboratory and Balloon Flight Performance of the Liquid Xenon Gamma Ray Imaging Telescope (LXeGRIT).
(183) Aprile, E.; Curioni, A.; Giboni, K.-L.; Kobayashi, M.; Ni, K.; Oberlack, U. G. A New Light Readout System for the LXeGRIT Time Projection Chamber. *IEEE Trans. Nucl. Sci.* **2003**, *50* (5), 1303–1308. https://doi.org/10.1109/TNS.2003.818235.
(184) Wamba, K. *EXO: The Enriched Xenon Observatory for Double Beta Decay*; SLAC-PUB-9548, 808701; 2002; p SLAC-PUB-9548, 808701. https://doi.org/10.2172/808701.
(185) O'Sullivan, K.; Collaboration, T. E. The Enriched Xenon Observatory. *J. Phys. Conf. Ser.* **2008**, *120* (5), 052056. https://doi.org/10.1088/1742-6596/120/5/052056.
(186) Angle, J.; Aprile, E.; Arneodo, F.; Baudis, L.; Bernstein, A.; Bolozdynya, A.; Brusov, P.; Coelho, L. C. C.; Dahl, C. E.; DeViveiros, L.; Ferella, A. D.; Fernandes, L. M. P.; Fiorucci, S.; Gaitskell, R. J.; Giboni, K. L.; Gomez, R.; Hasty, R.; Kastens, L.; Kwong, J.; Lopes, J. A. M.; Madden, N.; Manalaysay, A.; Manzur, A.; McKinsey, D. N.; Monzani, M. E.; Ni, K.; Oberlack, U.; Orboeck, J.; Plante, G.; Santorelli, R.; Dos Santos, J. M. F.; Shagin, P.; Shutt, T.; Sorensen, P.; Schulte, S.; Winant, C.; Yamashita, M. First Results from the XENON10 Dark Matter Experiment at the Gran Sasso National Laboratory. *Phys. Rev. Lett.* **2008**, *100* (2), 021303. https://doi.org/10.1103/PhysRevLett.100.021303.
(187) XENON100 Collaboration; Aprile, E.; Arisaka, K.; Arneodo, F.; Askin, A.; Baudis, L.; Behrens, A.; Brown, E.; Cardoso, J. M. R.; Choi, B.; Cline, D.; Fattori, S.; Ferella, A. D.; Giboni, K. L.; Kish, A.; Lam, C. W.; Lang, R. F.; Lim, K. E.; Lopes, J. A. M.; Undagoitia, T. M.; Mei, Y.; Fernandez, A. J. M.; Ni, K.; Oberlack, U.; Orrigo, S. E. A.; Pantic, E.; Plante, G.; Ribeiro, A. C. C.; Santorelli, R.; Santos, J. M. F. dos; Schumann, M.; Shagin, P.; Teymourian, A.; Tziaferi, E.; Wang, H.; Yamashita, M. The XENON100 Dark Matter Experiment. *Astropart. Phys.* **2012**, *35* (9), 573–590. https://doi.org/10.1016/j.astropartphys.2012.01.003.
(188) Aprile, E.; Aalbers, J.; Agostini, F.; Alfonsi, M.; Althueser, L.; Amaro, F. D.; Anthony, M.; Arneodo, F.; Baudis, L.; Bauermeister, B.; Benabderrahmane, M. L.; Berger, T.; Breur, P. A.; Brown, A.; Brown, A.; Brown, E.; Bruenner, S.; Bruno, G.; Budnik, R.; Capelli, C.; Cardoso, J. M. R.; Cichon, D.; Coderre, D.; Colijn, A. P.; Conrad, J.; Cussonneau, J. P.; Decowski, M. P.; De Perio, P.; Di Gangi, P.; Di Giovanni, A.; Diglio, S.; Elykov, A.; Eurin, G.; Fei, J.; Ferella, A. D.; Fieguth, A.; Fulgione, W.; Gallo Rosso, A.; Galloway, M.; Gao, F.; Garbini, M.; Geis, C.; Grandi, L.; Greene, Z.; Qiu, H.; Hasterok, C.; Hogenbirk, E.; Howlett, J.; Itay, R.; Joerg, F.; Kaminsky, B.; Kazama, S.; Kish, A.; Koltman, G.; Landsman, H.; Lang, R. F.; Levinson, L.; Lin, Q.; Lindemann, S.; Lindner, M.; Lombardi, F.; Lopes, J. A. M.; Mahlstedt, J.; Manfredini, A.; Marrodán Undagoitia, T.; Masbou, J.; Masson, D.; Messina, M.; Micheneau, K.; Miller, K.; Molinario, A.; Morå, K.; Murra, M.; Naganoma, J.; Ni, K.; Oberlack, U.; Pelssers, B.; Piastra, F.; Pienaar, J.; Pizzella, V.; Plante, G.; Podviianiuk, R.; Priel, N.; Ramírez García, D.; Rauch, L.; Reichard, S.; Reuter, C.; Riedel, B.; Rizzo, A.; Rocchetti, A.; Rupp, N.; Dos Santos, J. M. F.; Sartorelli, G.; Scheibelhut, M.; Schindler, S.; Schreiner, J.; Schulte, D.; Schumann, M.; Scotto Lavina, L.; Selvi, M.; Shagin, P.; Shockley, E.; Silva, M.; Simgen, H.; Thers, D.; Toschi, F.; Trinchero, G.; Tunnell, C.; Upole, N.;

Vargas, M.; Wack, O.; Wang, H.; Wang, Z.; Wei, Y.; Weinheimer, C.; Wittweg, C.; Wulf, J.; Ye, J.; Zhang, Y.; Zhu, T.; XENON Collaboration 7. Dark Matter Search Results from a One Ton-Year Exposure of XENON1T. *Phys. Rev. Lett.* **2018**, *121* (11), 111302. https://doi.org/10.1103/PhysRevLett.121.111302.
(189) The XENON collaboration; Aprile, E.; Aalbers, J.; Agostini, F.; Alfonsi, M.; Althueser, L.; Amaro, F. D.; Antochi, V. C.; Angelino, E.; Angevaare, J. R.; Arneodo, F.; Barge, D.; Baudis, L.; Bauermeister, B.; Bellagamba, L.; Benabderrahmane, M. L.; Berger, T.; Brown, A.; Brown, E.; Bruenner, S.; Bruno, G.; Budnik, R.; Capelli, C.; Cardoso, J. M. R.; Cichon, D.; Cimmino, B.; Clark, M.; Coderre, D.; Colijn, A. P.; Conrad, J.; Cussonneau, J. P.; Decowski, M. P.; Depoian, A.; Di Gangi, P.; Di Giovanni, A.; Di Stefano, R.; Diglio, S.; Elykov, A.; Eurin, G.; Ferella, A. D.; Fulgione, W.; Gaemers, P.; Gaior, R.; Galloway, M.; Gao, F.; Grandi, L.; Hasterok, C.; Hils, C.; Hiraide, K.; Hoetzsch, L.; Howlett, J.; Iacovacci, M.; Itow, Y.; Joerg, F.; Kato, N.; Kazama, S.; Kobayashi, M.; Koltman, G.; Kopec, A.; Landsman, H.; Lang, R. F.; Levinson, L.; Lin, Q.; Lindemann, S.; Lindner, M.; Lombardi, F.; Long, J.; Lopes, J. A. M.; Fune, E. L.; Macolino, C.; Mahlstedt, J.; Mancuso, A.; Manenti, L.; Manfredini, A.; Marignetti, F.; Undagoitia, T. M.; Martens, K.; Masbou, J.; Masson, D.; Mastroianni, S.; Messina, M.; Miuchi, K.; Mizukoshi, K.; Molinario, A.; Morå, K.; Moriyama, S.; Mosbacher, Y.; Murra, M.; Naganoma, J.; Ni, K.; Oberlack, U.; Odgers, K.; Palacio, J.; Pelssers, B.; Peres, R.; Pienaar, J.; Pizzella, V.; Plante, G.; Qin, J.; Qiu, H.; García, D. R.; Reichard, S.; Rocchetti, A.; Rupp, N.; Santos, J. M. F. dos; Sartorelli, G.; Šarčević, N.; Scheibelhut, M.; Schreiner, J.; Schulte, D.; Schumann, M.; Lavina, L. S.; Selvi, M.; Semeria, F.; Shagin, P.; Shockley, E.; Silva, M.; Simgen, H.; Takeda, A.; Therreau, C.; Thers, D.; Toschi, F.; Trinchero, G.; Tunnell, C.; Valerius, K.; Vargas, M.; Volta, G.; Wang, H.; Wei, Y.; Weinheimer, C.; Weiss, M.; Wenz, D.; Wittweg, C.; Xu, Z.; Yamashita, M.; Ye, J.; Zavattini, G.; Zhang, Y.; Zhu, T.; Zopounidis, J. P. Projected WIMP Sensitivity of the XENONnT Dark Matter Experiment. *J. Cosmol. Astropart. Phys.* **2020**, *2020* (11), 031–031. https://doi.org/10.1088/1475-7516/2020/11/031.
(190) Aalbers, J.; Agostini, F.; Alfonsi, M.; Amaro, F. D.; Amsler, C.; Aprile, E.; Arazi, L.; Arneodo, F.; Barrow, P.; Baudis, L.; Benabderrahmane, M. L.; Berger, T.; Beskers, B.; Breskin, A.; Breur, P. A.; Brown, A.; Brown, E.; Bruenner, S.; Bruno, G.; Budnik, R.; Buetikofer, L.; Calven, J.; Cardoso, J. M. R.; Cichon, D.; Coderre, D.; Colijn, A. P.; Conrad, J.; Cussonneau, J. P.; Decowski, M. P.; Diglio, S.; Drexlin, G.; Duchovni, E.; Erdal, E.; Eurin, G.; Ferella, A.; Fieguth, A.; Fulgione, W.; Rosso, A. G.; Di Gangi, P.; Di Giovanni, A.; Galloway, M.; Garbini, M.; Geis, C.; Glueck, F.; Grandi, L.; Greene, Z.; Grignon, C.; Hasterok, C.; Hannen, V.; Hogenbirk, E.; Howlett, J.; Hilk, D.; Hils, C.; James, A.; Kaminsky, B.; Kazama, S.; Kilminster, B.; Kish, A.; Krauss, L. M.; Landsman, H.; Lang, R. F.; Lin, Q.; Linde, F. L.; Lindemann, S.; Lindner, M.; Lopes, J. A. M.; Undagoitia, T. M.; Masbou, J.; Massoli, F. V.; Mayani, D.; Messina, M.; Micheneau, K.; Molinario, A.; Mora, K. D.; Morteau, E.; Murra, M.; Naganoma, J.; Newstead, J. L.; Ni, K.; Oberlack, U.; Pakarha, P.; Pelssers, B.; de Perio, P.; Persiani, R.; Piastra, F.; Piro, M. C.; Plante, G.; Rauch, L.; Reichard, S.; Rizzo, A.; Rupp, N.; Santos, J. M. F. D.; Sartorelli, G.; Scheibelhut, M.; Schindler, S.; Schumann, M.; Schreiner, J.; Lavina, L. S.; Selvi, M.; Shagin, P.; Silva, M. C.; Simgen, H.; Sissol, P.; von Sivers, M.; Thers, D.; Thurn, J.; Tiseni, A.; Trotta, R.; Tunnell, C. D.; Valerius, K.; Vargas, M. A.; Wang, H.; Wei, Y.; Weinheimer, C.; Wester, T.; Wulf, J.; Zhang, Y.; Zhu, T.; Zuber, K. DARWIN: Towards the Ultimate Dark Matter Detector. *J. Cosmol. Astropart. Phys.* **2016**, *2016* (11), 017–017. https://doi.org/10.1088/1475-7516/2016/11/017.
(191) Thomas, J.; Imel, D. A.; Biller, S. Statistics of Charge Collection in Liquid Argon and Liquid Xenon. *Phys. Rev. A* **1988**, *38* (11), 5793–5800. https://doi.org/10.1103/PhysRevA.38.5793.

(192) Zhu, Y.; Acounis, S.; Beaupere, N.; Beney, J.-L.; Bert, J.; Bouvier, S.; Canot, C.; Carlier, T.; Cherel, M.; Cussonneau, J.-P.; Diglio, S.; Giovagnoli, D.; Idier, J.; Kraeber-Bodere, F.; Ray, P. L.; Lefevre, F.; Masbou, J.; Morteau, E.; Stutzmann, J.-S.; Visvikis, D.; Xing, Y.; Thers, D. XEMIS2 Liquid Xenon Compton Camera for Small Animal 3γ Medical Imaging: Scintillation Light Measurement. In *2019 IEEE Nuclear Science Symposium and Medical Imaging Conference (NSS/MIC)*; IEEE: Manchester, United Kingdom, 2019; pp 1–4. https://doi.org/10.1109/NSS/MIC42101.2019.9059638.
(193) HAMAMATSU. *PHOTOMULTIPLIER TUBES*.
(194) Arnaboldi, C.; Calvi, M.; Fanchini, E.; Giachero, A.; Gotti, C.; Maino, M.; Matteuzzi, C.; Perego, D. L.; Pessina, G. Characterization of a Hamamatsu R7600 Multi-Anode Photomultiplier Tube with Single Photon Signals. In *IEEE Nuclear Science Symposuim & Medical Imaging Conference*; IEEE: Knoxville, TN, 2010; pp 1124–1129. https://doi.org/10.1109/NSSMIC.2010.5873942.
(195) Akgun, U.; Funk, G.; Corso, J.; Jia, Z.; Southwick, D.; Adams, L.; Kingyon, J.; Tiras, E.; Munhollon, T.; Troendle, E.; Bruecken, P.; Khristenko, V.; Onel, Y. Characterization of 1800 Hamamatsu R7600-M4 PMTs for CMS HF Calorimeter Upgrade. *J. Instrum.* **2014**, *9* (06), T06005–T06005. https://doi.org/10.1088/1748-0221/9/06/T06005.
(196) Sorokin, I. E.; Мйiier, W. F. J.; Schmidt, C. J. RICE FORMULA APPLICABILITY FOR NOISE RATE ESTIMATION IN THE CBM AND OTHER EXPERIMENTS WITH SELF-TRIGGERED ELECTRONICS: COMPARING THE CALCULATION TO A MEASUREMENT ON EXMAPLE OF N-XYTER CHIP.
(197) Aprile, E.; Dahl, C. E.; DeViveiros, L.; Gaitskell, R.; Giboni, K. L.; Kwong, J.; Majewski, P.; Ni, K.; Shutt, T.; Yamashita, M. Simultaneous Measurement of Ionization and Scintillation from Nuclear Recoils in Liquid Xenon as Target for a Dark Matter Experiment. *Phys. Rev. Lett.* **2006**, *97* (8), 081302. https://doi.org/10.1103/PhysRevLett.97.081302.

Résumé de la Thèse en Français

Dans le paysage complexe de l'imagerie médicale nucléaire, l'introduction du système XEMIS2 marque une avancée cruciale, signalant non seulement un bond en avant dans la sophistication technologique mais aussi une amélioration réfléchie de la précision et de la sécurité diagnostiques. Cette innovation, avec son utilisation du xénon liquide (LXe) comme moyen de détection, inaugure une nouvelle ère pour les modalités d'imagerie qui allient une haute sensibilité à une réduction significative de l'exposition aux radiations, réalisant une diminution bien supérieure à celle des technologies existantes. Bien que cette thèse reconnaisse respectueusement les développements cruciaux de la SPECT, de la PET et les prometteuses avancées de l'imagerie 3γ, son intérêt principal se tourne élégamment vers une exploration approfondie du système XEMIS2. Elle met particulièrement en lumière le raffinement des processus de calibration de la lumière et leur amélioration, tout en abordant légèrement le rôle de la grille de Frisch dans l'optimisation des performances du détecteur.

Le système XEMIS2, spécifiquement conçu pour l'imagerie de petits animaux, incarne la fusion de l'innovation et de l'application pratique en médecine nucléaire. Les caractéristiques exceptionnelles du LXe facilitent non seulement une clarté d'image remarquable mais établissent également de nouveaux standards pour l'efficacité et la sécurité des pratiques diagnostiques. Le choix du xénon liquide comme moyen de détection marque un changement de paradigme significatif par rapport aux méthodes traditionnelles, offrant des réductions substantielles des doses de radiation tout en améliorant simultanément la qualité et la fidélité des images capturées.

Au cœur du fonctionnement exemplaire du système XEMIS2 se trouve son processus de calibration rigoureux, particulièrement prononcé dans les domaines de la détection du signal de scintillation et de la calibration du Temps de Séjour (TOT). Ces processus complexes sont fondamentaux, servant non seulement à la validation procédurale mais surtout à affiner la réactivité du système aux signaux de radiation. La calibration du XEMIS2 est un voyage en couches, se déplaçant méticuleusement de la calibration du seuil et de la conversion des unités à une optimisation nuancée des techniques de mesure du temps, chaque phase étant délibérément conçue pour augmenter la précision diagnostique du système.

Un segment particulièrement éclairant de la thèse est consacré au processus de calibration de la lumière. La calibration de la lumière de scintillation dans le système est essentielle pour identifier et quantifier avec précision les interactions au sein du milieu LXe. Cela garantit non seulement la fiabilité des signaux détectés mais joue également un rôle crucial dans la performance globale du système. Grâce à des méthodologies de calibration sophistiquées, y compris des approches innovantes de la calibration TOT, le système XEMIS2 atteint un niveau de précision et de fiabilité. Ces améliorations des processus de calibration de la lumière représentent un bond significatif dans notre capacité à effectuer des diagnostics nuancés et précis.

En regardant vers l'avenir, les avancées dans la calibration de la lumière et les améliorations nuancées au sein du système XEMIS2 annoncent une trajectoire prometteuse pour l'imagerie médicale nucléaire. Alors que ce système passe de sa phase de développement à une application clinique plus large, son potentiel à transformer les normes diagnostiques est immense. Cependant, ce chemin vers l'avant est accompagné de défis, notamment l'intégration de tels systèmes d'imagerie avancés dans la pratique clinique routinière et

l'assurance de leur validation clinique complète. Pourtant, ces obstacles dévoilent également des opportunités de collaboration interdisciplinaire, invitant à un confluent d'expertise de la physique, de l'ingénierie, de la biologie et de la médecine pour naviguer collectivement dans l'avenir du diagnostic.

L'impact du système XEMIS, en particulier ses avancées dans la calibration de la lumière, s'étend bien dans le domaine de l'amélioration technologique. Il promet une transformation dans les soins aux patients, avec le potentiel de détecter les maladies plus tôt, de manière plus précise et d'adapter les traitements aux besoins individuels des patients. Cela s'aligne parfaitement avec l'objectif quintessentiel du diagnostic médical : améliorer les résultats pour les patients et la qualité de vie. Alors que nous nous tenons au bord de cette nouvelle ère, l'examen complet du système XEMIS sert non seulement de confirmation des progrès réalisés en imagerie médicale nucléaire mais aussi de phare pour de futures explorations et innovations.

En essence, cette thèse représente un mélange harmonieux de contexte historique, d'innovation technologique et de perspective prospective dans le domaine de l'imagerie médicale nucléaire. L'étude minutieuse du système XEMIS2, en particulier ses processus avancés de calibration de la lumière, raconte une histoire d'évolution continue et de potentiel. En allant de l'avant, les informations recueillies et les fondations établies par ce travail promettent non seulement d'approfondir notre compréhension et notre application de l'imagerie médicale nucléaire, mais aussi d'inspirer une avancée et une excellence continues dans la quête d'outils diagnostiques plus précis, plus sûrs et intrinsèquement centrés sur le soin du patient.

Chapitre 1 nous a emmenés dans un voyage captivant à travers le développement de l'imagerie médicale, retraçant l'évolution historique et les avancées récentes de la SPECT, de la TEP, ainsi que de la nouvelle modalité d'imagerie 3γ émergente. Au cours de plus d'un siècle, le travail acharné de nombreux pionniers a ouvert la voie à l'intégration réussie de la SPECT et de la TEP dans la pratique médicale. Ces modalités d'imagerie ont révolutionné le diagnostic, permettant aux professionnels de la santé d'acquérir des informations cruciales sur diverses conditions médicales et d'améliorer les résultats pour les patients. Le dévouement continu des chercheurs dans ce domaine reflète l'engagement inébranlable à améliorer la qualité et l'efficacité de l'imagerie, faisant de celle-ci un outil indispensable dans la médecine moderne. Au milieu de ces techniques d'imagerie bien établies, l'émergence de l'imagerie 3γ se présente comme un développement prometteur. Avec une période de développement relativement courte de 20 ans, l'imagerie 3γ a le potentiel d'inaugurer une nouvelle ère de l'imagerie médicale nucléaire. Bien qu'elle soit encore en cours de validation et de réalisation, les principes et l'instrumentation derrière l'imagerie 3γ ont suscité un grand enthousiasme au sein de la communauté scientifique. En regardant vers l'avenir, la perspective que l'imagerie 3γ remplace la SPECT et la TEP en tant que modalité principale pour l'imagerie médicale nucléaire est une possibilité intrigante. Le perfectionnement continu et la validation de cette nouvelle technique pourraient potentiellement conduire à une meilleure résolution spatiale, une sensibilité accrue et une réduction de l'exposition aux radiations, révolutionnant ainsi les pratiques d'imagerie médicale. À mesure que notre compréhension de ces modalités d'imagerie s'approfondit, et que de nouvelles technologies comme le Xemis2, la caméra Compton au xénon liquide, émergent, nous sommes confrontés à d'innombrables opportunités pour repousser les limites de l'imagerie médicale. La fusion des connaissances historiques et des innovations de pointe a le potentiel de remodeler le diagnostic médical, permettant une

détection plus précise et plus précoce des maladies, et, en fin de compte, d'offrir de meilleurs soins aux patients du monde entier.

Chapitre 2 offre une discussion complète et approfondie sur XEMIS2, une caméra Compton au xénon liquide de pointe développée spécifiquement pour l'imagerie des petits animaux dans la recherche en médecine nucléaire. Cette section commence par explorer les propriétés physiques et les avantages du xénon liquide, démontrant son potentiel en tant que milieu de détection efficace pour capturer les signaux de radiation. Les interactions uniques des photons et des particules chargées avec le xénon liquide sont étudiées en profondeur, révélant les processus de génération de signaux qui font du xénon liquide un candidat idéal pour l'imagerie haute résolution. Section 2 présente une discussion détaillée sur la chambre à projection temporelle au xénon liquide (LXeTPC). Les principes des chambres à projection temporelle au xénon liquide sont soigneusement expliqués, montrant comment cette technique permet un suivi et une imagerie précis des événements radiatifs. Un aperçu historique de la LXeTPC fournit des informations de base sur les progrès réalisés dans ce domaine, culminant avec le développement de XEMIS2.

Chapitre 3 présente la grille de Frisch qui est une pierre angulaire dans le domaine des détecteurs de radiation gonflables et joue un rôle clé dans l'assurance de l'uniformité et de la précision de la détection des signaux, en particulier dans les chambres d'ionisation utilisées pour la quantification des radiations ionisantes. En expliquant les principes fondamentaux de fonctionnement de la grille de Frisch et en explorant les techniques de simulation avancées adaptées aux architectures de détecteurs contemporaines telles que XEMIS2, cette étude éclaire la dynamique complexe de la grille de Frisch et son impact sur la performance des détecteurs. Les fondations théoriques établies par la discussion du théorème de Shockley-

Ramo fournissent une compréhension fondamentale des mécanismes d'induction de charge au sein des détecteurs d'ionisation. En examinant les interactions complexes entre le mouvement des charges et le champ électrique, ce théorème sert de principe directeur pour comprendre les signaux induits dans le détecteur et prépare le terrain pour la discussion ultérieure sur la fonctionnalité de la grille de Frisch. Dans les applications pratiques, la chambre d'ionisation à grille de Frisch s'est imposée comme une solution sophistiquée pour résoudre le problème de variabilité de l'amplitude des impulsions inhérente aux chambres d'ionisation traditionnelles. En divisant conceptuellement la région active du détecteur en zones distinctes et en protégeant efficacement l'anode des charges générées dans la région intermédiaire, la grille de Frisch garantit que les signaux induits à l'anode sont uniquement influencés par le nombre total d'ions créés, plutôt que par leur position initiale dans le détecteur. Cette caractéristique non seulement améliore la résolution énergétique du détecteur, mais facilite également la quantification précise des radiations ionisantes sur l'ensemble de son volume. En outre, la simulation de la grille de Frisch pour XEMIS2, englobant des conceptions innovantes telles que le Micro-Mesh pour chambre d'ionisation liquide (MIMELI) et la géométrie de grille modifiée par GEM, a offert des informations précieuses sur leurs caractéristiques de performance. Grâce à une analyse minutieuse facilitée par un ensemble d'outils de simulation, incluant GMSH, Elmer, Paraview, Garfield++, et COMSOL Multiphysics, les chercheurs ont acquis une compréhension globale de la dynamique des électrons, des distributions de champ électrique, et de l'efficacité de la grille. Ces connaissances sont essentielles pour optimiser les paramètres de conception des détecteurs, améliorer la précision de détection, et faire progresser les capacités des systèmes de détection de nouvelle génération comme XEMIS2. Cette étude met en lumière l'importance de la grille de Frisch dans le détecteur XEMIS2, en soulignant son rôle dans la réduction de la variabilité des signaux et l'amélioration de la performance du détecteur. En combinant des principes théoriques avec des techniques de

simulation avancées, les chercheurs peuvent ouvrir de nouvelles voies d'innovation, ouvrant la voie au développement de systèmes de détection des radiations plus sensibles, précis et efficaces. À mesure que la technologie continue d'évoluer, la grille de Frisch demeure un composant intégral, alimentant les progrès dans des domaines allant de la physique nucléaire et des particules à l'imagerie médicale et la sécurité intérieure. Avec des efforts continus en R&D, le potentiel des grilles de Frisch pour révolutionner la détection des radiations dans une variété d'applications est infini.

ce chapitre présente une étude exhaustive du processus de détection par scintillation en lien avec le système XEMIS2, une étude qui allie à la fois ampleur et profondeur. Nous avons commencé par une vue panoramique de la chaîne de détection par scintillation et nous sommes penchés sur les exigences urgentes pour la conception d'un système de lecture efficace. La discrimination des signaux de scintillation est essentielle pour une localisation temporelle précise et une cartographie spatiale des interactions des rayons gamma au sein du volume sensible du détecteur. Cette reconnaissance n'est pas seulement théorique, mais constitue également la base pour calibrer et améliorer la sensibilité des détecteurs.

Chapitre 4 aborde les questions fondamentales de la détection par scintillation, en commençant par une étude approfondie de la calibration des seuils, en décomposant méticuleusement le processus de calibration en ses éléments de base. Ce processus n'est pas simplement une nécessité procédurale; il est également crucial pour affiner la réactivité du détecteur aux signaux entrants. La discussion évolue ensuite vers les nuances de la conversion des unités de seuil, un moment clé qui facilite la traduction des nuances analogiques en un vocabulaire numérique cohérent, permettant une quantification et une analyse précises du signal détecté. Le point central de cette exploration est la discussion sur la calibration du temps de seuil (TOT). Cette méthode sophistiquée constitue une alternative

pour estimer la sortie optoélectronique déclenchée par les événements de scintillation et est cruciale pour améliorer la précision des mesures. Nous révélons les subtilités de cette calibration et clarifions son rôle intégral dans la précision globale du système. Le chapitre s'aventure également dans le domaine de l'optimisation de la mesure du temps. Cette partie explique diverses stratégies qui affinent la résolution temporelle et la précision du détecteur, garantissant que chaque événement de scintillation est enregistré avec la plus grande fidélité. Le processus de calibration comprend également la calibration du gain des PMT, dont l'importance ne peut être surestimée, car elle affecte directement la stabilité et l'uniformité du processus d'amplification des signaux, assurant ainsi que la sortie de chaque canal est précise et cohérente. En résumé, ce chapitre fournit un compendium détaillé des méthodologies et des principes sous-jacents à chaque étape de la calibration, offrant un guide complet sur les rigueurs de la détection des signaux de scintillation. L'exposition détaillée de la procédure de calibration constitue une référence importante, soulignant l'attention méticuleuse aux détails nécessaire pour atteindre les normes élevées exigées par le système XEMIS2. De plus, ce chapitre ne se contente pas de poser les bases des discussions techniques à venir, mais met également en lumière les implications pratiques de ces méthodes. L'application rigoureuse de ces techniques de calibration est essentielle pour le fonctionnement robuste du système XEMIS2, garantissant qu'il reste un modèle de détection des signaux de scintillation. Les principes et pratiques énoncés ici sont indispensables et constituent le socle des avancées et innovations futures dans ce domaine. Ces insights fondamentaux continueront de guider le développement et l'application du détecteur XEMIS2 alors que nous avançons, avec pour objectif ultime d'atteindre de nouveaux sommets en matière de précision et de fiabilité dans la détection par scintillation.

Chapitre 5 a minutieusement exploré les détails de la calibration du Temps au-dessus du Seuil (TOT) dans le système de détection au xénon liquide (LXe) XEMIS2. Il présente une méthode de correction approfondie basée sur une compréhension profonde de la propagation de la lumière de scintillation et de la caractérisation des signaux dans le LXe. Ces corrections de calibration sont cruciales pour assurer la précision et la fiabilité des mesures du détecteur XEMIS2, qui ont un impact direct sur ses résultats scientifiques. L'exploration initiale de la propagation de la lumière de scintillation dans le LXe a permis d'identifier les paramètres critiques qui influencent la transmission des photons. Ces connaissances de base ont ensuite informé la caractérisation détaillée des signaux de scintillation et leur impact sur les mesures de TOT. En tenant compte des exigences du système XEMIS2, nous avons développé et validé un modèle de réponse de la carte de mise en forme aux photoélectrons individuels. Ce modèle constitue une pierre angulaire du processus de calibration, capturant les caractéristiques temporelles essentielles de la réponse du système électronique du détecteur. La validation par rapport aux données empiriques a établi la crédibilité de notre approche de simulation, intégrant des mécanismes complexes de signaux de scintillation dans le processus de calibration. Les résultats de simulation présentés dans la section 5.2.3 illustrent cette intégration, offrant une perspective affinée sur la détection des signaux de scintillation. Nos simulations, mises en parallèle avec les résultats expérimentaux, fournissent des insights critiques sur le comportement du détecteur, nous permettant d'affiner notre stratégie de calibration pour traiter les complexités du monde réel, telles que les retards stochastiques dans l'émission de photons. Les résultats de cette recherche ont des implications significatives pour la technologie des détecteurs LXe, améliorant la capacité de XEMIS2 à fournir des mesures précises et fiables. Ces avancées ne sont pas simplement incrémentielles ; elles représentent un bond en avant dans notre capacité à sonder la nature insaisissable de la matière noire et à étudier les propriétés des neutrinos.

COLLEGE DOCTORAL PAYS DE LA LOIRE
ED MATIERE, MOLECULES MATERIAUX ET GEOSCIENCES

IMT Atlantique
Bretagne-Pays de la Loire
École Mines-Télécom

Titre : **Contributions aux développements instrumentaux de la caméra XEMIS2, aux mesures embarquées de l'ionisation et de la scintillation**

Mots clés : Xénon liquide, PMTs, lumière de scintillation, imagerie médicale, imagerie 3-gamma, Time Projection Chamber

Résumé : Les travaux décrits dans cette thèse sont centrés sur l'évolution de l'imagerie médicale nucléaire, des techniques d'imagerie fondamentales aux innovations actuelles, avec un focus particulier sur la caméra XEMIS2. Cette caméra Compton au xénon liquide est conçue pour l'imagerie 3-gamma des petits animaux à faible activité. L'objectif principal de XEMIS2 est de localiser en trois dimensions un radiopharmaceutique marqué avec un radionucléide spécifique, tel que le Scandium-44, tout en réduisant l'activité administrée sans compromettre la qualité de l'image.

La thèse se concentre ensuite sur le développement et les performances de la caméra XEMIS2. Elle couvre les principes opérationnels des chambres de projection temporelle au xénon liquide (LXeTPCs), l'utilisation de la grille de Frisch pour améliorer les performances des chambres d'ionisation, et le processus complexe de la calibration des signaux de scintillation dans XEMIS2 en utilisant la méthode Time over Threshold (TOT). Les efforts d'optimisation des résultats de calibration sont également abordés. En résumant ces avancées technologiques et méthodologiques, la thèse offre une perspective historique et une analyse prospective des impacts potentiels de ces technologies sur les diagnostics médicaux et la recherche.

Title : **Contributions to instrumental developments for the XEMIS2 camera, and on-board ionization and scintillation measurements**

Keywords : Liquid xenon, PMTs, scintillation light, medical imaging, 3-gamma imaging, Time Projection Chamber

Abstract : The work described in this thesis focuses on the evolution of nuclear medical imaging, from fundamental imaging techniques to current innovations, with a particular focus on the XEMIS2 camera. This liquid xenon Compton camera is designed for 3-gamma imaging of small, low-activity animals. The main objective of XEMIS2 is to localize in three dimensions a radiopharmaceutical labeled with a specific radionuclide, such as Scandium-44, while reducing the administered activity without compromising image quality.

The thesis then focuses on the development and performance of the XEMIS2 camera. It covers the operational principles of the liquid xenon time projection chambers (LXeTPCs), the use of the Frisch grid to improve the performance of the ionization chambers, and the complex process of calibrating the scintillation signals in XEMIS2 using the Time over Threshold (TOT) method. Efforts to optimize calibration results are also discussed. By summarizing these technological and methodological advances, the thesis provides a historical perspective and a prospective analysis of the potential impact of these technologies on medical diagnostics and research.